

Numerical simulation of the rheological behavior of fresh concrete

Numerische Simulation des rheologischen Verhaltens von Frischbeton

An der Fakultät Bauingenieurwesen der Technischen Universität Dresden
zur Erlangung der Würde eines Doktor-Ingenieurs (Dr.-Ing.)
eingereichte

DISSERTATION

vorgelegt von
Dipl.-Ing. Sergiy Shyshko
aus Charkiw (Ukraine)

eingereicht am 12. Juni 2013.

Tag der mündlichen Prüfung: 23. September 2013.

Gutachter:
Prof. Dr.-Ing. V. Mechtcherine,
Prof. Dr. L. Ferrara.

ABSTRACT

This thesis reports recent numerical investigation of the rheological behavior of fresh concrete using the Discrete Element Method (DEM). Some relevant questions of the concrete rheology e.g. the influence of the concrete composition on the rheological behavior of the fresh concrete, the experimental determination of the Bingham rheological constants as well as the use of these constants in the numerical simulation were discussed thoroughly. An important topic of the performed investigation was the development of the numerical model for fresh concrete which enables simple, fast and stable predictive simulation of different technological operations with fresh concrete.

Firstly, in a literature survey, the state-of-the-art of the numerical simulation of fresh concrete was presented and critically discussed in order to show advantages and disadvantages of other methods and modeling approaches. Open (unsolved) questions were highlighted and the basis for their investigation is created within this thesis. Fundamental concepts of the rheology were then presented and the basic rheological models of viscoelastic materials were considered; the rheological behaviors of different types of concretes were presented and its influencing factors were discussed. Additionally main methods for scientific investigation and testing of the fresh concrete were shown. The test methods were critically discussed in order to select the test, which has been used as a reference experimental test for the numerical simulations.

Chosen reference experimental test was the slump flow test. The slump flow test was thoroughly analyzed and an analytical solution was developed which helps to interpret the results of measurements and provides a link between rheological constants and measured quantities.

In a further step an extensive experimental program was carried out in order to investigate the rheological behavior of fresh concrete and get the input data for numerical simulation. Firstly, the experiments on macrolevel were performed. Here the rheological behavior of the fresh concrete flow in different tests was investigated (slump and slump flow tests, L-Box). Further, the experiments on mesolevel with polymer on Carbopol basis and mortar were developed and performed in order to investigate the interaction between discrete particles suspended in a fluid matrix. The necessary material parameters, especially those representative of the fluid suspension micromechanical behavior, i.e. the force-displacement relationship, yield force and bond strength, were determined by these experiments. The slump flow test was used as the basic test to calibrate the model for fresh concrete (key data: slump value, slump flow diameter (for concretes with a soft consistency) and the time of spreading). Thus, the decisive phenomena of the fresh concrete flow were highlighted, control points for a contact model were selected and the initial input data for the development of the contact model was obtained.

Next, the user-defined contact model was developed and implemented into the Particle Flow Code ITASCA. The contact model was completely described and its limitations discussed. Then, the set of numerical tools was developed, which enable simplified and stable numerical simulation of the fresh concrete with particular behavior, i.e. automatic generation of the concrete with given particle grading, amount of fibers and air, automatic recalculation of the micromechanical parameters of the contact model from given initial yield stress and plastic viscosity. The model was calibrated by slump flow test simulations and validated by corresponding analytical approach. Further, the role of different model parameters was investigated by simulating the slump flow test. Furthermore, for verification of the model several additional experiments were simulated, i.e. L-Box and LCPC-box

test. The results of modeling were compared with experimental results and discussed in detail. All numerical simulations provide qualitatively as well as quantitatively correct results and hence adequately represent the phenomena observed in real experiments.

The thesis closes with general conclusions and outlook of the work. In the future, the developed contact model and tools of the “Virtual concrete laboratory” could be modified in order to extend the potential of the laboratory to cover such properties as thixotropic behavior of fresh concrete or simulating hardening of the concrete and behavior of the hardened concrete.

KURZFASSUNG

In dieser Doktorarbeit wird eine neue numerische Simulationsmethode zur Beschreibung des rheologischen Verhaltens von Frischbeton unter Nutzung der Diskrete Element Methode (DEM) vorgestellt. Das Hauptziel der durchgeführten Untersuchungen war die Entwicklung eines numerischen Modells für Frischbeton, das eine einfache, schnelle und stabile prädiktive Simulation verschiedener betontechnologischer Vorgänge ermöglicht.

In der Literaturanalyse wird der Kenntnisstand zu numerischen Simulationen von Frischbeton vorgestellt und kritisch diskutiert, um Vor- und Nachteile anderer Methoden und Modellierungsansätze aufzudecken. Offene Fragen werden hervorgehoben und die Grundlagen zu deren Untersuchung im Rahmen dieser Doktorarbeit umfassend dargestellt. Die Grundbegriffe der Rheologie werden vorgestellt und die elementaren rheologischen Modelle von viskoelastischen Materialien betrachtet. Des Weiteren werden die rheologischen Verhalten verschieden zusammengesetzter Frischbetone vorgestellt und Einflussfaktoren auf deren Rheologie diskutiert. Ebenso werden die Basismethoden für die wissenschaftliche Untersuchung und Prüfung von Frischbeton vorgestellt. Diese werden kritisch diskutiert, um eine experimentelle Methode, die als Referenz für die numerischen Simulationen dienen soll, auswählen zu können.

Als experimentelle Referenz wurde das Setzmaß- bzw. Setzfließmaßversuch (Slump or Slump Flow Test) ausgewählt. Dieser Test wurde grundlegend studiert und dafür eine analytische Lösung entwickelt, mit der die Ergebnisse der experimentellen Messungen interpretiert und in einen Zusammenhang mit den rheologischen Konstanten des Bingham-Modells gestellt werden konnten.

In einem weiteren Schritt wurde ein umfassendes experimentelles Programm auf der makroskopischen Untersuchungsebene ausgeführt, um das rheologische Verhalten frischer Betone zu untersuchen und damit Eingangsdaten für numerische Simulationen zu generieren. Hier wurde das rheologische Verhalten der frischen Betone mit Hilfe verschiedener Tests (Slump Test, Slump Flow Test, L-Box Test) untersucht. Das Setzfließmaßversuch wurde dann verwendet, um das numerische Modell für den frischen Beton zu kalibrieren. Als essentielle Kennwerte wurden Slump Flow, Slump Flow Time und die Form des „Betonkuchens“ genutzt. Damit konnten die entscheidenden Phänomene beim Fließen von frischem Beton klar dargestellt, die Kontrollpunkte für ein Kontaktmodell ausgewählt und die initialen Eingangsdaten für die Entwicklung des Kontaktmodells erhalten werden.

Anschließend wurden neuartige Experimentieranordnungen auf der Mesoebene entwickelt, erprobt und angewendet, um die Wechselwirkung zwischen zwei diskreten Partikeln in einer flüssigen Matrix zu untersuchen. Als Matrix wurde ein transparentes Polymer auf Carbopol-Basis sowie verschiedene zementhaltige Feinststoffsuspensionen eingesetzt. Mit diesen Experimenten wurden die Materialparameter bestimmt, welche mesomechanische Verhalten (Kraft-Weg-Gesetz, Fließgrenze, Bindungskraft) widerspiegeln.

Auf Grundlage der experimentellen Ergebnisse auf der Makro- und Mesoebene wurde das benutzerdefinierte Kontaktmodell entwickelt und in einen Partikel Flow Code implementiert. Das Kontaktmodell wurde hierbei komplett beschrieben und seine Beschränkungen diskutiert. Es wurde ein Satz von numerischen Werkzeugen entwickelt, mit dem automatisch Betone mit vorgegebener Partikelgrößenverteilung generiert sowie die Neuberechnung der Parameter des mesomechanischen

Kontaktmodells bei gegebener Fließgrenze und plastischer Viskosität durchgeführt werden konnten. Mit diesen Werkzeugen wurde eine robuste numerische Simulation verschieden zusammengesetzter frischer Betone möglich.

Das Modell wurde mit Hilfe der Simulation von Setzfließmaßversuchen kalibriert und durch die entsprechende analytische Methode validiert. Mit dem kalibrierten und validierten Modell wurde der Einfluss verschiedener Modellparameter analysiert. Außerdem wurden für die Überprüfung des Modells mehrere zusätzliche Experimente simuliert. Die Ergebnisse der Modellierung wurden mit den experimentellen Ergebnissen verglichen und detailliert diskutiert. Die numerischen Simulationen lieferten qualitativ als auch quantitativ korrekte Ergebnisse und spiegelten die in realen Experimenten beobachteten Phänomene angemessen wieder.

Die Arbeit endet mit allgemeinen Schlussfolgerungen und einem Ausblick.

In der Zukunft könnten das entwickelte Kontaktmodell und die Werkzeuge des "virtuellen Betonlabors" modifiziert werden, um auch solche Eigenschaften wie das thixotrope Verhalten von Frischbeton, das Aushärten von frischem Beton oder das mechanische Verhalten erhärteten Betons abzubilden und damit das Potenzial des Labors zur Erfassung solcher Eigenschaften zu steigern.

VORWORT DES HERAUSGEBERS

Die zielsichere Gestaltung der Herstellungs-, Verarbeitungs- und Applikationsprozesse von Beton und anderen Werkstoffen auf der Basis von mineralischen Bindemitteln ist die Voraussetzung für wirtschaftliche, energie- und zeitsparende Lösungen zahlreicher Herausforderungen im heutigen und künftigen Baugeschehen. Heute beruht die Gestaltung dieser Prozesse überwiegend auf empirischem Wissen beteiligter Fachleute. In der Folge werden – trotz z. T. hohen experimentellen Aufwandes – oft keine optimalen Prozessgestaltungen erzielt. Der Grund dafür ist eine sehr hohe Komplexität des vorliegenden Systems bestehend aus Frischmaterial – dichtgepackter, thixotroper Suspension aus Wasser und einer immensen Anzahl von Feststoffpartikeln sehr unterschiedlicher Größe, Form, Oberflächenladung und chemischer Zusammensetzung – sowie Verarbeitungstechnik mit diverser Geometrie und Arbeitsregimes. Die Verwendung numerischer Simulation kann das tiefgreifende Verständnis der ablaufenden Prozesse wie Mischen, Transport und Einbringen in die Form fördern und zur Findung optimaler Lösungen verhelfen. Besonders Erfolg versprechend sind hierbei Modellansätze, die die Heterogenität des Materials auf der Mesoebene direkt abbilden und hiermit eine eingehende Analyse solcher Vorgänge wie Durchmischen, Verdichten sowie Faserverteilung und -orientierung ermöglichen.

In der vorliegenden Arbeit wird ein solches Simulationsmodell auf der Basis der Discrete Element Method (DEM) entwickelt, welche eine quantitative Beschreibung und Vorhersage des Fließverhaltens von Frischbeton gestattet. Zwar liegen einige Studien zur Simulation des Fließverhaltens von Frischbeton mit Hilfe der DEM vor, keine der Arbeiten davon bietet jedoch weder eine Methodik zur physikalisch begründeten Festlegung der Modellparameter noch eine quantitative Vorhersage des Betonfließens. Mit seiner Arbeit schließt Herr Dr. Shyshko einen großen Teil dieser Lücke. Besonders hervorzuheben sind zunächst die Setzfließversuche mit automatischer Erfassung der Voränderung des Betonkuchens und der eigens entwickelte Algorithmus für die Ableitung der rheologischen Kennwerte aus diesen Daten. Auch die experimentellen Untersuchungen zur Interaktion zwischen benachbarten Feststoffpartikeln mit einer viskosen Zwischenschicht sind in Bezug auf Frischbeton einmalig. Sie gewähren einen sehr guten Einblick in die maßgebenden Mechanismen und liefern eine zuverlässige Datenbasis zur Ableitung der Stoffgesetze für die DEM.

Einen weiteren wichtigen wissenschaftlichen Beitrag leistet die Entwicklung eines Modells, welches das Zusammenwirken der das Betongemenge abbildenden diskreten Elemente beschreibt. Schließlich ist der Algorithmus zur Bestimmung des Hauptparameters des Modells aus der vorgegebenen Schergrenze des Frischbetons hoch originell und überaus nützlich für eine zielsichere Simulation von Fließvorgängen. Die entwickelten Modelle und Algorithmen tragen beträchtlich zur Verbesserung der Qualität der Abbildung und Vorhersage des Frischbetonverhaltens bei und bilden eine ausgezeichnete Grundlage für die Weiterentwicklung der ausgearbeiteten Ansätze. Vorteilhaft war für die Dissertation auch die aktive Mitarbeit von Herrn Shyshko im RILEM Technical Committee 222-SCF “Simulation of fresh concrete flow” (Chair: Dr. N. Roussel) sowie seine Forschungsaufenthalte beim Institutspartner Politecnico di Milano, Italien (Prof. L. Ferrara).

Ich freue mich, dass sich Herr Dr. Shyshko auch nach Abschluss seiner Promotion und zwar im Rahmen seiner heutigen Tätigkeit am Institut für Angewandte Bauforschung in Weimar weiter mit der DEM-Simulation von Betongemengen beschäftigen kann. Für seine berufliche Karriere wünsche ich ihm viel Erfolg!

Viktor Mechtcherine

ACKNOWLEDGEMENTS

At this memorable moment of the successful accomplishment of my doctoral research work, I would like to acknowledge all those who have, in one way or another, been very helpful throughout the period of my research and subsequent writing of this dissertation.

First of all I would like to express my heartfelt gratitude to my major professor, Prof. Dr.-Ing. Viktor Mechtcherine, Director of the Institute for Construction Materials at the TU Dresden indeed for providing me with an enormous opportunity; for his wonderful support, technical, financial, and moral, and encouragement; for his kindness; and for the unfathomable and overwhelming confidence he showed me. The amount of knowledge and academic/scientific maturity I was able to gain in my work under his supervision is simply beyond measure. For these I am, and will always be, truly grateful.

My special thanks go as well to Prof. Liberato Ferrara, who travelled all the way from Milano, Italy to be available for this work: he gave important hints in improving the thesis and will write a report on it.

I shall always be thankful to my colleagues at TU Dresden, and in particular to Prof. Dr. rer. nat. habil. Michael Schiekkel, Dr. Marko Butler, and Dr. Christof Schröfl. No amount of words would suffice to describe the sort of assistance and guidance I received from them.

To all my colleagues at the laboratory, I wish to extend my thanks for your friendship, eager willingness to assist, and the perfect atmosphere I have had the pleasure of experiencing throughout. Because of all of you, my entire time has been smooth, enjoyable, and cheerful.

In particular, I would like to thank my colleagues and friends Egor Secieru and Venkatesh Nerella for the grand time we spent together in our shared office, the enlightening discussions we carried out, and for the collaborative research work we accomplished there.

I also want to express my special thanks to the secretaries at the Institute of Construction Materials, Ms. Verena Damme and Ms. Martina Awasi for taking care of all my administrative needs throughout the time of my doctoral work.

I take great pleasure in expressing my gratitude to my colleagues at the TU Kaiserslautern, Cornelia Ziegler, Dr. rer. nat. Joachim Schulze, Robert Adams, and Karl Leidner, who also helped facilitate my stay in Kaiserslautern. I shall always appreciate the cheerful words of encouragement and advice they offered so faithfully.

Finally, I would at this point like to thank my parents, Mr. Evgeniy Shyshko and Mrs. Galina Shyshko for their unconditional support and love and would also like to express my heartfelt thanks to my brothers Alexander and Andriy Shyshko, my friends, well-wishers, and each and every individual who directly or indirectly contributed to my growth.

Sergiy Shyshko, Dresden, June, 2013

TABLE OF CONTENTS

CHAPTER 1

INTRODUCTION

1

1.1	Introduction.....	1
1.2	Problem and goal definition.....	1
1.3	Chosen approach.....	2
1.4	Structure of the thesis.....	2

CHAPTER 2

LITERATURE REVIEW

5

2.1	Introduction.....	5
2.2	Basics of rheology.....	5
	2.2.1 Newtonian fluids.....	7
	2.2.2 Non-Newtonian fluids.....	7
	2.2.3 Viscoelastic fluids.....	8
2.3	Rheological Models.....	10
	2.3.1 Basic rheological elements and principles of a model construction.....	10
	2.3.2 Basic viscoelastic models.....	12
	2.3.3 Basic models with yield stress.....	13
2.4	Rheology of concretes.....	15
	2.4.1 Concrete components affecting rheological properties.....	18
	2.4.2 Methods of the rheological investigation of fresh concrete.....	20
	2.4.2.1 Free flow test methods.....	21
	2.4.2.2 Confined Flow Tests.....	28
	2.4.2.3 Vibration test methods.....	32
	2.4.2.4 Rheometers.....	34
2.5	Methods for numerical simulation of flow process.....	36
	2.5.1 Continuous body approach (Single fluid simulations).....	37
	2.5.2 Simulation of discrete particle flow.....	40
	2.5.3 Simulation of suspension flow.....	46
	2.5.4 Comparison and discussion of numerical methods.....	50
2.6	Summary.....	51

CHAPTER 3

EXPERIMENTAL INVESTIGATION OF THE FRESH CONCRETE RHEOLOGY

(MACROLEVEL)

53

3.1	Introduction.....	53
3.2	Materials, methods and test results.....	53
	3.2.1 Composition of the concretes.....	53
	3.2.2 Slump test.....	55
	3.2.3 Slump flow test.....	56

3.2.4	L-Box test	59
3.3	Analytical approach for a slump flow test	60
3.3.1	Evaluation of the yield stress value	61
3.3.1.1	Analysis of deformation due to dead weight for ordinary concretes	61
3.3.1.2	Analysis of deformation due to dead weight for highly flowable concretes	66
3.3.2	Evaluation of the plastic viscosity	68
3.3.2.1	Analysis of the spreading process	68
3.3.2.2	Finding the velocity profile	71
3.3.2.3	Transition from the dynamic to the plastic viscosity	73
3.4	Analysis and discussion of the experimental results using analytical approach	74
3.4.1	Influence of the cone orientation	74
3.4.2	Influence of the cone lifting velocity and height of lifting	75
3.4.3	Influence of the moisture on the table on slump flow measurement	76
3.4.4	Calculation of the yield stress	78
3.4.5	Calculation of the plastic viscosity	79
3.5	Summary	82

CHAPTER 4

MESOLEVEL - INVESTIGATION OF THE INTERACTION BETWEEN DISCRETE PARTICLES

		85
4.1	Introduction	85
4.2	Discretization of meso-structure of fresh concrete	85
4.3	Viscoelastic materials used in the investigation	87
4.4	Interaction between neighbouring entities with viscoelastic material between them	89
4.5	Experimental equipment	90
4.6	Arrangements of solid spheres and viscoelastic material and measurement procedure	91
4.7	Evaluating the force-displacement diagrams	96
4.8	The program of the tests	98
4.9	Results and discussions of the tests with Carbopol solutions	98
4.10	Results and discussion of the tests with mortar for fresh SCC and UHPC	105
4.10.1	Investigation of the time-dependence of the rheological behaviour	105
4.10.2	Discussion of the results of the tests with mortars with ball-wall contact	107
4.11	Material model for interaction between entities in DEM	111
4.12	Summary and conclusions	115

CHAPTER 5

MATERIAL MODEL AND NUMERICAL SIMULATIONS

		117
5.1	Introduction	117
5.2	Numerical Model	117
5.2.1	The Particle Flow Code Itasca	117
5.2.1.1	Basic concepts of the method	117
5.2.1.2	Characteristics of the elements	118
5.2.1.3	The force-displacement law	119
5.2.1.4	Law of Motion	121
5.2.1.5	Modelling of the contact bond	123

5.2.1.6	Dissipation the kinetic energy.....	126
5.2.1.7	User-defined contact model.....	127
5.2.2	Developing of the material model for numerical simulation	128
5.2.2.1	Normal direction.....	128
5.2.2.2	Tangential direction.....	130
5.2.3	Implementation of the contact model into PFC program.....	133
5.2.3.1	Description of the parameters of contact model.....	133
5.2.3.2	Limitations of the contact model.....	135
5.2.4	Additional tools for “Virtual Concrete Laboratory”.....	136
5.2.4.1	Modelling of the equipment and boundary conditions.....	136
5.2.4.2	Procedure for generation of particles representing fresh concrete.....	137
5.2.4.3	Procedure for generating of fibres and non-spherical aggregates.....	128
5.2.4.4	Compensating of the volume of components which cannot be discretised ..	139
5.2.4.5	Layer of fine mortar for material model.....	141
5.2.4.6	Procedures for time-controlling function.....	142
5.2.4.7	Procedure for obtaining the shape of simulated concrete specimen.....	143
5.3	Numerical simulations.....	143
5.3.1	Parameter study and calibration of the UDM using the slump flow test.....	143
5.3.1.1	Effect of the characteristic distances.....	145
5.3.1.2	Effect of the characteristic forces.....	146
5.3.1.3	Link between contact bond strength in the simulation and yield stress of the fresh concrete in the experiment.....	147
5.3.1.4	Effect of internal friction and viscosity.....	149
5.3.1.5	Effect of the particle size.....	149
5.3.1.6	Compensation the particle size effect.....	151
5.3.1.7	Choose of the initial model parameters and calibrating of the numerical model.....	153
5.3.2	Verification of the material model.....	154
5.3.2.1	Simulation of the slump-flow test.....	154
5.3.2.2	Simulation of the LCPC-box test.....	159
5.3.2.3	Simulation of the L-box test.....	161
5.4	Summary and conclusions.....	162
CHAPTER 6		
GENERAL CONCLUSIONS AND OUTLOOK.....		165
BIBLIOGRAPHY.....		169
Appendix A	Abbreviations, Symbols and Indices.....	179
Appendix B	Mixing procedures for fresh concretes.....	182
Appendix C	Results of the slump flow tests.....	184
Appendix D	Results of meso-level tests on Carbopol polymer 0.3%M.....	188
Appendix E	Results of meso-level tests on Carbopol polymer 0.5%M.....	198
Appendix F	Results of meso-level tests on SCC mortar.....	208
Appendix G	Results of meso-level tests on UHPC.....	210

CHAPTER 1

GENERAL INTRODUCTION

1.1 Motivation

The behaviour of fresh concrete during transport, placement, and compacting can have a significant effect on the mechanical performance, the durability, and on other properties of the hardened concrete. Many problems arise out of the improper filling of formworks, insufficient de-airing, separation of constituents, etc. The importance of this issue has increased year by year since formworks are becoming ever more complex, steel reinforcements ever denser, and the ranges of workability considerably broadened, including the use of Self-Compacting Concrete (SCC). A consequence of this, on the one hand, is the notion that modern material design must meet particular geometrical and technological demands. On the other hand, the concrete working techniques and, in some cases the geometry of the structures as well, can be optimized in considering the using of concretes with particular rheological properties.

Computer simulation of fresh concrete behaviour and processing could provide a powerful tool in optimising concrete construction and in the developing of new concrete technologies such as those bound up in the development of SCC. Practical applications of technologies of this variety clearly show the need for a better understanding of the defining mechanisms and for predicting not only the process of concrete flow, but possibly the effects of de-airing, segregation, and fibre orientation as well.

1.2 Problem and goal definition

Concrete is a composite material with a complex internal structure consisting of several phases. In principle it is known how individual parameters such as mixture composition, rheological behaviour of concrete in its fresh state, and the compacting process may influence material structure and material performance; see, for example, [80, 135].

Comprehensive investigations of fresh concrete are very complex and laborious. The main components of concrete are not transparent; thus, the end product is not transparent at all. As a result, the experimental, non-destructive investigation of its internal structure and variations thereof are very difficult tasks; it is not possible to look through the concrete and observe its distinct constituents with respect to their positions, movements, interactions, and their possible separation/accumulation, e.g., as air, fibres or coarse aggregates. Furthermore, many phenomena and processes, such as cluster building, air blockage in the de-airing process, formation of obstructions during casting, component distribution during mixing, and casting in formworks with complex geometries always occur in concrete production, and indeed many of these process have still not been investigated adequately.

In order to make possible the analysis of the complex behaviour of fresh concrete as affected by different combinations of rheological properties and boundary conditions, adequate modelling tools are required.

The overarching aim of this thesis is, for the rheological behaviour of fresh concrete, the development of a “numerical simulation laboratory” which at the macro-level provides for the modelling of the most significant phenomena observed and is based on a reliable physical footing.

1.3 Approach chosen

There is already a great deal of work treating the computational modelling of fresh concrete. In most of these studies fresh concrete is regarded as a homogenous fluid with given properties, but there has been relatively little work done on simulating concrete as a heterogeneous, multiphase system. When simulating the flow behaviour of concrete using the “single fluid” approach, the parameters of the Bingham model can be directly used as input parameters for the simulation software.

However, in many instances the single fluid approach is not an appropriate tool in simulating the behaviour of the material since many phenomena occurring during concrete processing and casting are the results of its heterogeneity, which cannot be reproduced adequately unless a sufficient degree of material meso-structure is modelled explicitly. The Distinct Element Method (DEM) provides a better basis indeed for simulating such important phenomena as, for example, passing among reinforced steel bars, blockage, separation, fibre orientation, and rebounding of shotcrete. However, the parameters of models based on DEM are not rheological constants and cannot be obtained by experimentation directly.

Accordingly, a specific, numerical simulation tool has been developed based on DEM. Particle Flow Code ITASCA (PFC ITASCA) was used in this investigation as the basic programme [59], enabling the modelling of the movement (translation and rotation) of distinct particles, including their interactions and their separation and automatic contact detection as well [66]. The interaction between distinct, individual particles in contact with one another is defined by constitutive relationships, which are represented diagrammatically as a force-displacement relationship. The characteristic force-displacement diagrams have to be obtained in the series of the tests for investigation of the interaction between neighbouring solid particles with some viscoelastic material between them. Since the constitutive relation depends on the rheological properties of the material, the constitutive relation obtained can be directly introduced in numerical codes based on the Distinct Element Method.

1.4 Structure of the thesis

This thesis is comprised of 6 chapters.

The introduction (Chapter 1) of the thesis is followed by a literature review (Chapter 2). The state-of-the-art of numerical simulation of fresh concrete is presented and critically discussed in this chapter in order to show the advantages, disadvantages, and limitations of the different methods of numerical simulation, specify the open questions to be investigated, and create a basis for their treatment within this thesis. Further, the survey of the literature presents the basic concepts of rheology and considers the basic rheological models of viscoelastic materials. The rheological behaviour of different types of concretes is presented and factors influencing such behaviour in fresh concrete are discussed, and the chief methods for the scientific investigation and testing of

fresh concrete are shown. The test methods are critically discussed and the slump flow test was selected to be used as the primary reference for numerical simulations.

In order to obtain the input data for numerical simulation, an extensive experimental program was carried out, which consisted of two parts: investigation of the rheological behaviour of the fresh concretes (Chapter 3) and investigation of the interaction and contact behaviour between distinct particles with some viscoelastic material in between (Chapter 4). Obtained from the experiments, the phenomena of fresh concrete flow and control points required to be reproduced in a numerical simulation have been highlighted.

For the simulation of the fresh concrete, a PFC ITASCA was used as the basis program. Chapter 5 describes how this simulation method works and briefly outlines the algorithms applied. Since the interactive forces between the particles play a significant role in the simulation of heterogeneous media, the applicable laws and their implementation are provided. Forces both normal and tangential at contact points have been treated. This chapter presents the steps in the development of the user-defined contact model and describes the parameters of the contact model. Subsequently, a parameter study was performed in order to quantify the effects of individual parameters of the model on the results of the numerical simulation of slump tests using Abram's cone. The analysis of the results obtained provided a basis for initial considerations concerning an algorithm for the choice of the model parameters when concretes with various rheological properties have to be simulated. An algorithm for determining the yield-stress parameter using the analytical approach as developed in Chapter 3 is presented. Furthermore, for the "virtual concrete laboratory" a set of tools necessary for the correct modelling of the actual experiments was developed and implemented into the PFC. This set of tools includes the following: a procedure for generating the particles from the composition of the concrete; a further procedure for compensating for the volume of the components which cannot be modelled directly using DEM (liquids, fine sand, cement paste), a procedure for generating fibres and non-spherical components, and finally procedures which monitor important characteristics in the modelling and process data, etc. Using this set of tools, the calibrated virtual concrete was used in simulation of the L-Box and LCPC-Box tests, which are regarded as a verification of the model. Finally, the results of numerical simulation were compared to the experimental data and analytical model. It was found that all the simulation agreed both qualitatively and quantitatively with results representing the essential phenomena correctly, as observed in the corresponding experiments.

The thesis closes with general conclusions and prospects for work to follow; see Chapter 6.

CHAPTER 2

LITERATURE REVIEW

2.1 Introduction

This review of the literature consists of two parts; the first part (“Rheology” Sections 2.2 – 2.4) is split further into three subparts. Section 2.2 presents basics of rheology as the science of the deformation and flow of matter. Basic rheological models are presented in Section 2.3. For purposes of this work, the behaviour of fresh concrete is analysed accordingly in rheological terms, see Section 2.4. The factors influencing the rheological behaviour of fresh concrete and the test methods used in identifying the rheological parameters of fresh concrete are presented. The second part (“Numerical simulation”, Section 2.5) presents a literature survey in respect of existing methods for the numerical simulation of flow processes. Methods of numerical simulation are classified; the most favoured methods are presented, and their advantages and disadvantages are discussed critically.

2.2 Basics of rheology

As noted above, rheology is the science of the deformation and flow of matter. This definition was adopted when the American Society of Rheology was founded in 1929 [8]. This organisation has since then fostered the study of the relationship between force, time, and deformation rate. The experimental characterisation of a material's rheological behaviour is known as “rheometry”, although the term “rheology” is frequently used synonymously, particularly by experimentalists. From a broad perspective, rheology includes almost every aspect of behaviour having to do with the deformation of materials as a result of applied stresses [71].

The basic theoretical concepts of rheology are kinematics, dealing with geometrical aspects of deformation and flow; conservation laws, dealing with forces, stresses, and energy interchanges; and constitutive relations specific to classes of bodies, for example, elastic or viscoelastic bodies. The constitutive relations serve to link motion and force to complete the flow process’ description, which may then be applied in solving engineering problems arising in concrete production, polymer processing, food technology, and many other fields [123].

One of the basic properties important in rheology is viscosity, defined as the resistance to flow. This resistance acts against the motion of any solid object through the fluid and also against motion of the fluid itself past stationary obstacles. Viscosity also acts internally on the fluid between slower and faster moving adjacent layers. If the resistance is high the viscosity has a high value. Figure 2.1 shows a fluid sheared between two plates with ‘A’ indicating their surface area.

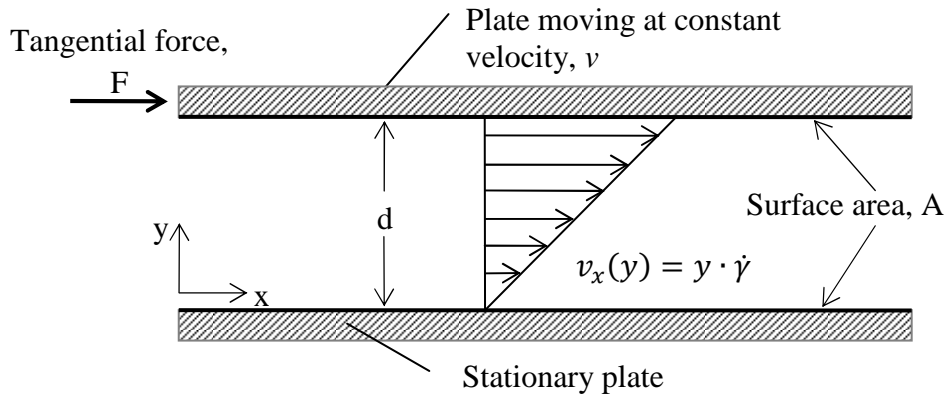


Figure 2.1: Simple shearing; fluid is contained between two parallel plates separated by a distance d ; the top plate moves with a constant velocity v in the x direction [123]

For many fluids the tangential, or shearing, stress which causes flow is directly proportional to the rate of shear strain, or rate of deformation. In other words, the shear stress divided by the rate of shear strain is constant for a given fluid at a fixed temperature. This constant is called the dynamic or absolute viscosity, or often simply the viscosity. Fluids that behave in this way are called Newtonian fluids. Formally, dynamic viscosity is represented by the symbol η "eta" [123].

When a shear force F is applied to the top plate, this will result in a shear stress τ (see Eq. 2.1).

$$\tau = F/A \quad (2.1)$$

Viscosity is defined mathematically as the ratio of the shear stress to the velocity gradient in a fluid (see Eq. 2.2).

$$\eta = (F/A) \div \left(\frac{dv_x}{dy} \right) \quad (2.2)$$

The dimensions of viscosity are force multiplied by time divided by area. The SI-unit of viscosity, accordingly, is Newton-second per square meter or Pascal-second.

The more usual form of this relationship, called Newton's equation, states that the resulting shear of a fluid is directly proportional to the force applied and inversely proportional to its viscosity.

$$F/A = \eta \cdot \left(\frac{dv_x}{dy} \right)$$

When shifting this plate horizontally, the applied stress will result in a displacement, x of the "top" plate during a time period t . This displacement can also be described by an angle γ , called shear strain. When its derivative with respect to the time increment, dt is calculated, the rate of shear is obtained (see Eq. 2.3).

$$\dot{\gamma} = d\gamma/dt \quad (2.3)$$

From the shear stress (Eq. 2.1) and the rate of shear (Eq. 2.3) the viscosity η follows (see Eq. 2.4):

$$\eta(\dot{\gamma}) = \tau/\dot{\gamma} \quad (2.4)$$

Depending on their flow properties, fluids can be classified into three groups [7, 123]:

- Newtonian fluids,
- Non-Newtonian fluids, and
- Viscoelastic fluids.

2.2.1 Newtonian fluids

A Newtonian fluid is a fluid whose stress at each point is linearly proportional to its strain rate at that point. For Newtonian fluids the viscosity remains constant at any shear rate. As the viscosity is constant the viscosity function for Newtonian fluids is the simplest that can occur (see Eq. 2.5).

$$\tau = \eta \cdot \dot{\gamma} \quad (2.5)$$

Flow and viscosity curves of Newtonian fluids are shown below in Figure 2.2.

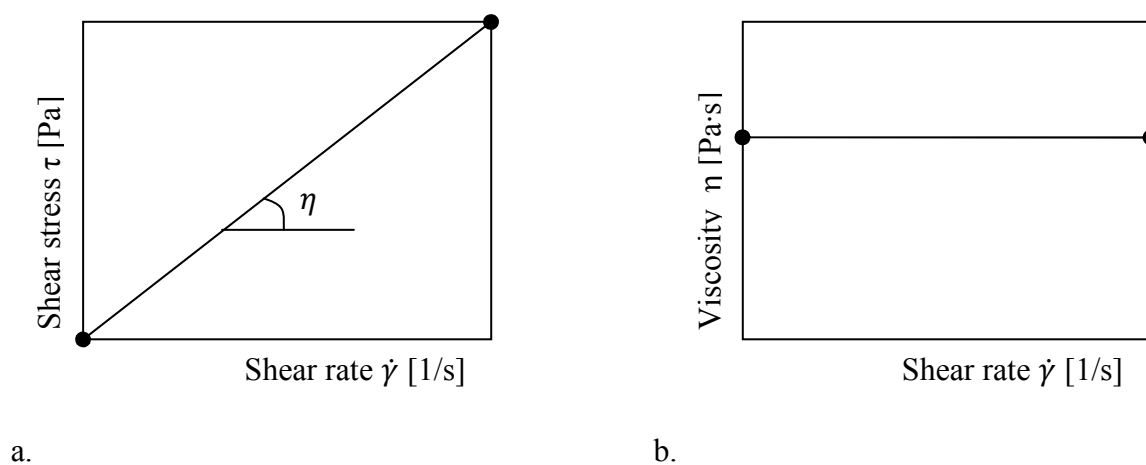


Figure 2.2: Flow a) and viscosity b) curves of Newtonian fluids [123]

Fluids with Newtonian flow are simple, single-phase fluids and solutions of fluids, for example, water, glycerol, petrol and oil.

For a Newtonian fluid, the viscosity depends by definition only on temperature and pressure, and also the chemical composition of the fluid if the fluid is not a pure substance, and expressly not on the forces acting upon it.

2.2.2 Non-Newtonian fluids

A non-Newtonian fluid is one in which the viscosity is a function of a mechanical variable like shear stress or time (see Eq. 2.6).

$$\eta = \eta(\dot{\gamma}, t) \quad (2.6)$$

The classification of non-Newtonian fluids is presented in Table 2.1.

Table 2.1: Classification of non-Newtonian fluids [123]

	Shear-thinning	Shear-thickening
Time-dependent (memory materials)	<u>thixotropic</u> fresh mortar and concrete, honey	<u>rheopectic</u> printer's ink
Time-independent (non-memory materials)	<u>pseudoplastic</u> styling gel, paint	<u>dilatants</u> viscous coupling fluids (fluid armour)
With yield stress	<u>Bingham plastic</u> toothpaste, molten chocolate, fresh concrete	-

Some gels and pastes behave as fluids when worked or agitated and then settle into a nearly solid state when at rest. Such materials are examples of **shear-thinning fluids**. Shear-thinning fluids are characterised by a viscosity decreasing with an increasing shear rate. The diagrams for shear thinning fluids are presented in Figure 2.3a.

Shear-thinning fluids can be classified into one of three general groups. A material that has a viscosity that decreases under shear stress but stays constant over time is said to be **pseudoplastic**. A material that has a viscosity that decreases under shear stress and then continues to decrease with time is said to be **thixotropic**. If the transition from high viscosity (or nearly semisolid) to low viscosity (or essentially fluid) takes place only after the shear stress exceeds some minimum value then the material is said to be a **Bingham plastic**.

Materials which thicken when worked or agitated are called **shear-thickening fluids**. Shear-thickening fluids are also divided into two groups: those with a time-dependent viscosity (memory materials) and those with a time-independent viscosity (non-memory materials). If the viscosity increases over time, the material is said to be **rheopectic**. If the increase is roughly directly proportional to the shear stress and does not change over time, the material is said to be **dilatant**. Shear-thickening or dilatancy is the property of increasing fluid viscosity with increasing shear rate. This is shown in Figure 2.3b.

Materials that have a yield stress start flowing when the shear stress exceeds a certain value, called the yield stress τ_0 . If the yield stress has not yet been reached, the material behaves as a solid. When the yield stress is exceeded, the sample can display Newtonian, shear thinning, or shear thickening properties.

Materials having a yield point and showing Newtonian behaviour are called **Bingham plastic**. The Bingham model is described by the following equation (see Eq. 2.7):

$$\tau = \tau_0 + \eta \cdot \dot{\gamma}, \quad (2.7)$$

where τ is the shear stress applied to the material, $\dot{\gamma}$ is the shear strain rate (also called the strain gradient), τ_0 is the yield stress and η is the viscosity.

Materials which have a yield stress and show shear thinning or shear thickening behaviour when the yield stress is exceeded can be described by the **Hershel-Bulkley** model (see Eq. 2.8):

$$\tau = \tau_0 + \eta \cdot \dot{\gamma}^n \quad (2.8)$$

For $n > 1$ the model describes shear thickening and for $n < 1$ shear thinning is described. If n is 1 the Bingham model is described. Figure 2.3c shows the different models with yield stress.

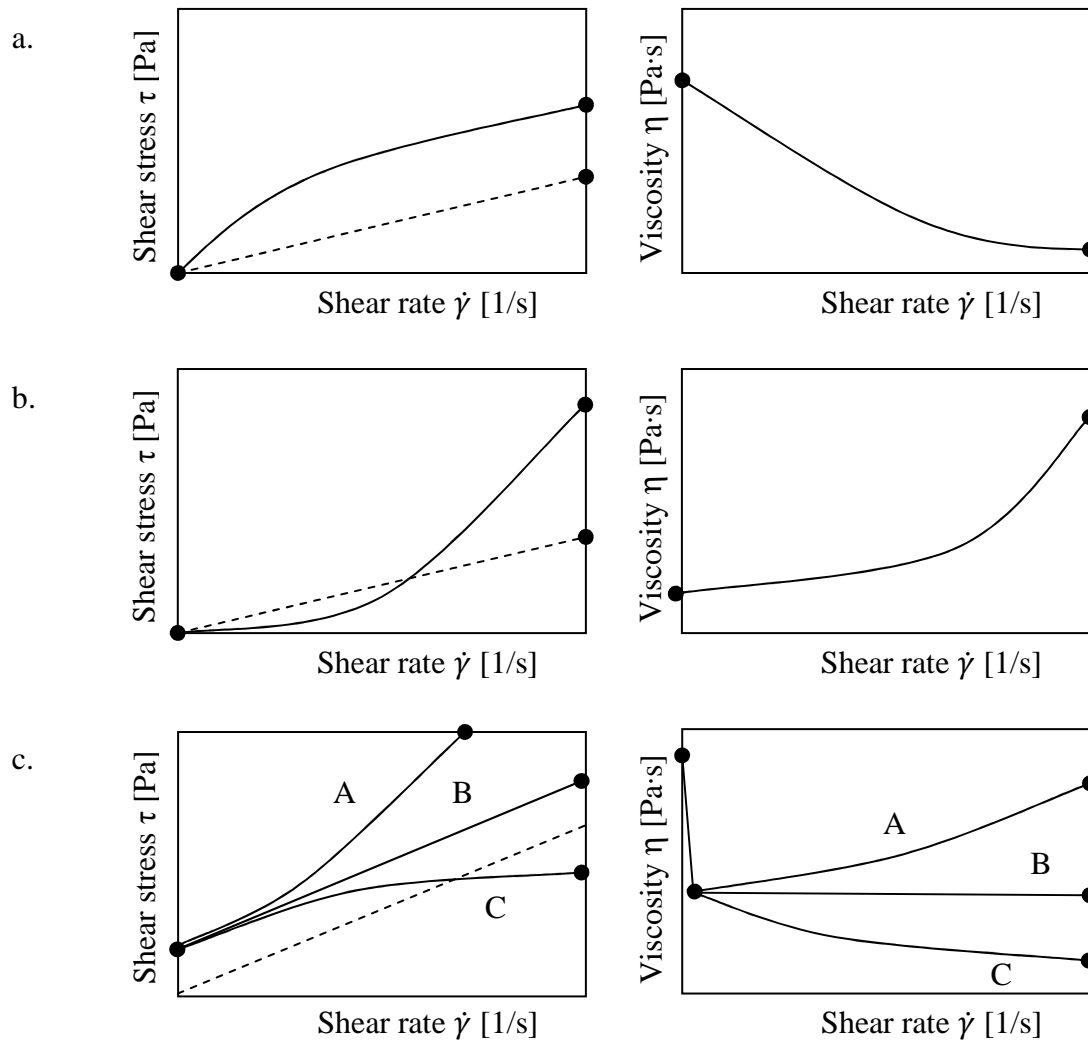


Figure 2.3: Flow (left) and viscosity (right) curves, a) for shear thinning materials, b) for shear thickening materials, c) for material having a yield stress: A) visco-plastic, shear thinning, B) Bingham plastic, C) visco-plastic, shear thickening [123]

2.2.3 Viscoelastic fluids

Viscoelastic fluids comprise the last group. Unlike purely elastic substances a viscoelastic substance has, as the name suggests, both an elastic and a viscous component. Also, when strain is applied and removed, the viscoelastic substance loses energy, in most cases in the form of heat. The lost energy is represented by the space enclosed in the hysteresis loop as shown in Figure 2.4. An example of a viscoelastic substance is bitumen.

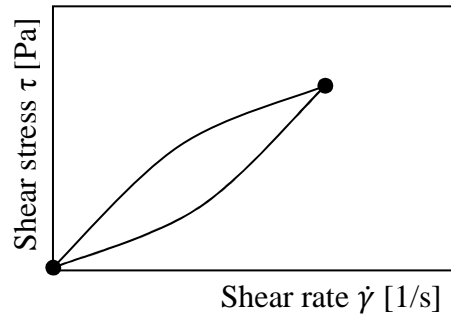


Figure 2.4: *Hysteresis loop of viscoelastic fluid [123]*

2.3 Rheological Models

Depending on the relations between deformation, stress, and time scale, all materials, from gases to solids, can be divided into the following four categories of rheological behaviour [7, 43, 71, 79]:

- **Viscous materials:** In a purely viscous material (such as water) all energy added is dissipated into heat.
- **Elastic materials:** In a purely elastic material (such as steel at stresses below the yield stress) all energy added is stored in the material.
- **Viscoelastic materials:** A viscoelastic material exhibits viscous as well as elastic behaviour. Typical examples of viscoelastic materials are bread dough, polymer melts, and artificial or natural gels and fresh concrete.
- **Materials with yield stress:** To such materials external stress must be applied to make them begin to flow, indeed to yield. Typical examples are toothpaste, mayonnaise, and fresh concrete.

2.3.1 Basic rheological elements and principles of a model construction

The rheological behaviour of viscoelastic materials can be successfully described by the creation of rheological models based on two fundamental elements: the linear spring and the linear viscous dashpot. For the linear spring the relationship between stress and strain is given by Hooke's law (see Eq. 2.9):

$$\sigma(t) = E \cdot \varepsilon(t) \quad (2.9)$$

where E is the modulus of elasticity (Young's modulus).

The response \mathcal{E} of such a spring to a stress σ is instantaneous, without any time dependency, and the recovery after release of the stress is also instantaneous and complete.

The viscous dashpot can be visualized as a piston displacing a Newtonian fluid in a cylinder with a perforated bottom. Eq. 2.10 gives the Newton's law of viscosity:

$$\sigma(t) = \eta \cdot \dot{\varepsilon}(t) \quad (2.10)$$

where $\dot{\varepsilon}(t) = d\varepsilon/dt$ is the strain rate and η is the viscosity coefficient.


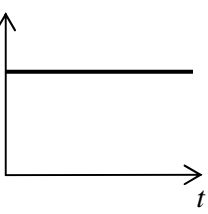
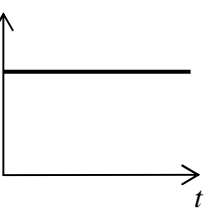
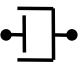
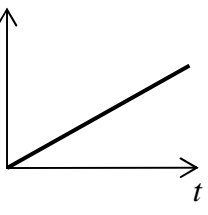
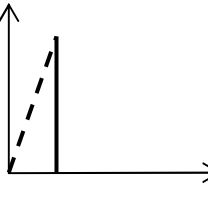
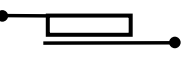
There is no instantaneous response; the deformation is directly proportional to time, and no recovery takes place.

The rheological behaviour of viscoelastic materials with yield stress cannot be estimated accurately by rheological models which are based on only two fundamental elements. Therefore an additional element is needed to represent the yield stress phenomenon. This is the so-called St.-Venant element. The deformation of this element is possible only after the achievement of some critical stress value, called yield stress (see Eq. 2.11):

$$\varepsilon = \begin{cases} 0 & \sigma < \sigma_y \\ \varepsilon(t) & \sigma \geq \sigma_y \end{cases} \quad (2.11)$$

The outlined representation of basic rheological elements is shown in Table 2.2.

Table 2.2: Representation of basic rheological elements

Name	Representation	Creep	Relaxation
Spring			
Dashpot			
St.-Venant Element		$\varepsilon = 0, \sigma < \sigma_y$ $\varepsilon = \varepsilon(t), \sigma \geq \sigma_y$	$\varepsilon = 0, \sigma < \sigma_y$ $\varepsilon = \varepsilon(t), \sigma \geq \sigma_y$

Complex formulations can be obtained by combining basic elements in different configurations. One of the simplest combinations is assembling them in series or in parallel.

When two elements are combined in series (as shown in Figure 2.5), the total stress is equal to both the stress of the spring and to the stress of the dashpot, while the total deformation is the sum of the deformation of the spring and the deformation of the dashpot (see Eqs. 2.12 and 2.13).



Figure 2.5: Two elements combined in series

$$\sigma = \sigma_1 = \sigma_2 \quad (2.12)$$

$$\varepsilon = \varepsilon_1 + \varepsilon_2 \quad (2.13)$$

When two elements are combined in parallel (as shown in Figure 2.6), the total stress is the sum of the stress in the spring and the stress in the dashpot, while the total deformation is equal to both the deformation of the spring and the deformation of the dashpot (see also Eqs. 2.14 and 2.15).

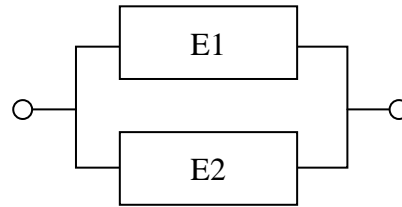


Figure 2.6: Two elements combined in parallel

$$\sigma = \sigma_1 + \sigma_2 \quad (2.14)$$

$$\varepsilon = \varepsilon_1 = \varepsilon_2 \quad (2.15)$$

Using these simple rules (Eqs. 2.12-2.15) any rheological model can be built or analysed.

2.3.2 Basic viscoelastic models

The list of the most well-known models is presented in Table 2.3.

The **Maxwell** viscoelastic model consists of a spring and a dashpot in series. As the elements are connected in series, same stress acts on both elements, and so the total strain is equal to the sum of the strain of the two elements. The elongation of the spring is given by $\varepsilon_s = \sigma/E$ and the extension of the dashpot obeys the relationship $\dot{\varepsilon}_d = \sigma/\eta$. Eq. 2.16 gives the rheological equation for Maxwell model:

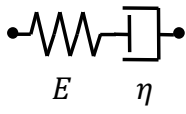
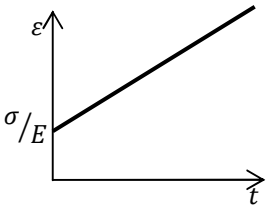
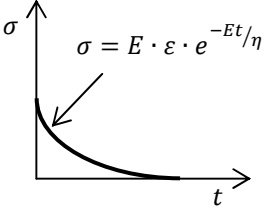
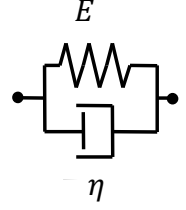
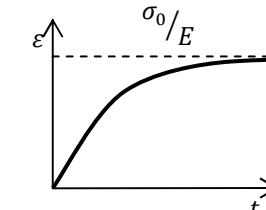
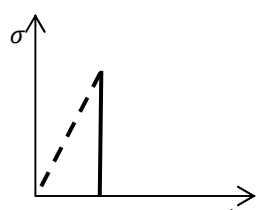
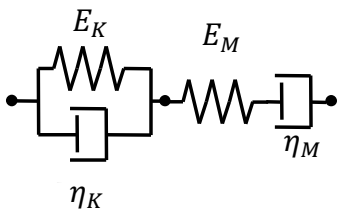
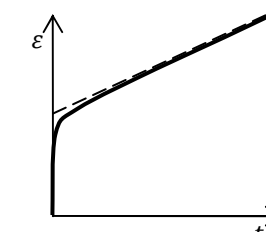
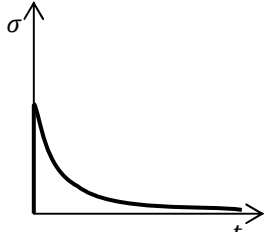
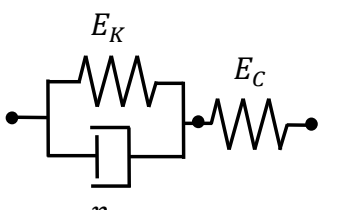
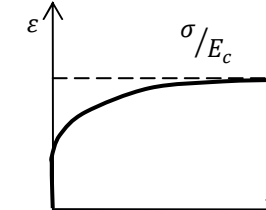
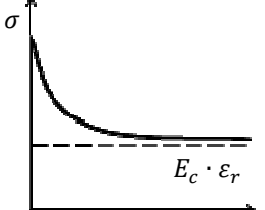
$$\sigma + \frac{\eta}{E} \cdot \dot{\sigma} = \eta \cdot \dot{\varepsilon} \quad (2.16)$$

The **Kelvin** viscoelastic model consists of a spring and a dashpot in parallel. This model does not allow for instantaneous deformation since the stress on the dashpot would be infinite. In this case, the elongation in each element remains the same. Therefore, $\sigma_s = E \cdot \varepsilon$ and $\sigma_d = \eta \cdot \dot{\varepsilon}$. The Kelvin model also does not describe stress relaxation. Eq. 2.17 gives the rheological equation for Kelvin model:

$$\sigma = E \cdot \varepsilon + \eta \cdot \dot{\varepsilon} \quad (2.17)$$

Both models, Maxwell and Kelvin, are limited in their representation of actual viscoelastic behaviour; the former is able to describe stress relaxation, but only irreversible flow; the latter can represent creep, but without instantaneous deformation, and it cannot account for stress relaxation. A combination of both models, like the Burgers model, enables a realistic description of the materials with more complex behaviour.

Table 2.3: Common viscoelastic models [41, 78, 98]

Name	Representation	Creep	Relaxation
Maxwell			
Kelvin			
Burgers			
Standard Solid (Poynting)			

The **Burgers** viscoelastic model consists of the Maxwell (spring and dashpot in series) and the Kelvin (spring and dashpot in parallel) section connected in series. Therefore, the creep curve of Burgers model under the creep stress provides the superposition of Kelvin and Maxwell models (see Eq. 2.18).

$$\sigma + \left(\frac{E_K \cdot \eta_K + E_K \cdot \eta_M + E_M \cdot \eta_K}{E_K \cdot E_M} \right) \cdot \dot{\sigma} + \frac{\eta_K \cdot \eta_M}{E_K \cdot E_M} \cdot \ddot{\sigma} = \eta_K \cdot \dot{\varepsilon} + \frac{\eta_K \cdot \eta_M}{E_M} \cdot \ddot{\varepsilon} \quad (2.18)$$

The **standard Solid (Poynting)** contact model consists of the Kelvin (spring and dashpot in parallel) section and an additional spring connected in series. This contact model shows the creep and relaxation behaviour and also the instantaneous elasticity.

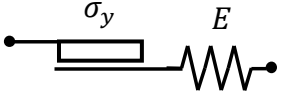
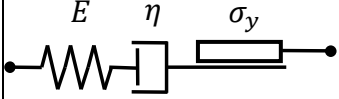
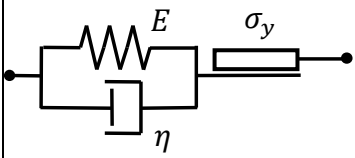
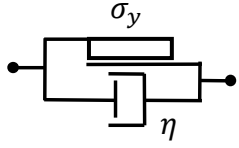
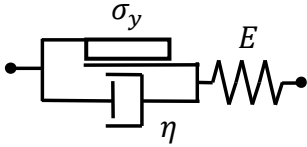
Eq. 2.19 gives the equation of the Poynting model:

$$\sigma + \frac{\eta}{E_K} \cdot \dot{\sigma} = E_C \cdot \varepsilon + \frac{\eta_K \cdot (E_K + E_C)}{E_K} \cdot \dot{\varepsilon} \quad (2.19)$$

2.3.3 Basic models with yield stress

Table 2.4 shows the outlined representation of common viscoelastic models with yield stress and the response of these models before and after achievement of the yield stress value σ_y .

Table 2.4: Common viscoelastic models with yield stress [97, 98, 142]

Name	Representation	$\sigma < \sigma_y$	$\sigma \geq \sigma_y$
Prandtl		$\sigma = E \cdot \varepsilon$	$\sigma = \sigma_y$
Maxwell - St.-Venant		$\sigma + \frac{\eta}{E} \cdot \dot{\sigma} = \eta \cdot \dot{\varepsilon}$	$\sigma + \frac{\eta}{E} \cdot \dot{\sigma} = \eta \cdot (\dot{\varepsilon} - \dot{\varepsilon}_p)$
Kelvin - St.-Venant		$\sigma = E \cdot \varepsilon + \eta \cdot \dot{\varepsilon}$	$\sigma = E \cdot (\varepsilon - \varepsilon_p) + \eta \cdot (\dot{\varepsilon} - \dot{\varepsilon}_p)$
Bingham		$\sigma = 0$	$\sigma = \sigma_y + \eta \cdot \dot{\varepsilon}$
Bingham - Hooke		$\sigma = \varepsilon \cdot E$	$\sigma + \frac{\eta}{E} \cdot \dot{\sigma} = \eta \cdot \dot{\varepsilon} + \sigma_y$

The **Prandtl** model consists of a Saint-Venant element and a spring element in series (as shown in Table 2.4). The behaviour of that material is characterised by linear elasticity for stress values below the yield strength. When yield stress is attained, the body exhibits pure plasticity.

The serial connection of all the basic rheological elements can be presented as the **Maxwell model with St.-Venant element in series**. Prior to attaining yield stress the system shows behaviour similar to the ordinary Maxwell model. The behavior of the Saint-Venant element is characterized by function $\varepsilon_p(t)$ for stress values above the yield strength.

The **Kelvin model with St.-Venant element in series** gives another alternative in representing plastic deformation, as shown in Table 2.4. The system shows the behaviour of the Kelvin model below the yield stress σ_y .

The **Bingham** model consists of a Saint-Venant element and a dashpot in parallel (as shown in Table 2.4). Deformation of the model is not possible before reaching yield stress through the Saint-Venant element. When yield stress is achieved, the model exhibits visco-plastic deformation.

The **Bingham-Hooke** model consists of a Bingham model and a spring in series. Bingham's material exhibits linear elasticity for stress values lower than the yield stress, as in the Saint-Venant model, but flows linearly above that value, as in the Maxwell model. The strain rate is proportional to the difference between the applied stress σ and the yield strength σ_y .

2.4 Rheology of concretes

Considering concrete as a composite, multi-scale material, it is meaningful to study the properties of the material on various observation levels, i.e., the micro-, meso-, and macro-levels. At the micro- and meso-levels of observation concrete is heterogeneous; only at the macro-level the material can be considered to be homogeneous. In general, the homogeneity of the material is desired since it means a uniform distribution of properties over the volume of a structural element. In more detail, however, important influences of the meso-structure on the mechanical and durability-associated transport properties of concrete have been identified [3, 141]. At the meso-structural level, concrete is assumed to be a composite material formed by a mortar matrix, a coarse, aggregate fraction, an interfacial transition zone, and fibres, if one is dealing with fibre-reinforced concrete.

Since concrete is defined as a composite material, it can be represented as a concentrated suspension consisting of solid particles (aggregates) dispersed in a viscous fluid (cement pastes). Interactions among the finest particles in the mixture may lead to a macroscopic thixotropic behaviour [104].

Several attempts have been made to relate fresh concrete properties to measurable quantities efficiently. Ritchie's work [99] was the first that attempted to define the flow of concrete by associating it with various effects such as bleeding, sedimentation, and density (see Figure 2.7). Consequently, he subdivided the rheology of fresh concrete into three fundamental properties, namely: stability, compatibility, and mobility. Stability is linked to bleeding and segregation; compatibility is equivalent to relative density, and mobility is linked to the internal friction angle, bonding force, and viscosity. Although Ritchie's approach was innovative when developed, it had one major drawback. Even though the major parameters associated with the rheology of fresh concrete had been identified, there was no apparent relationship among them. For instance, the three factors that influence the mobility of a mix may affect compatibility as well.

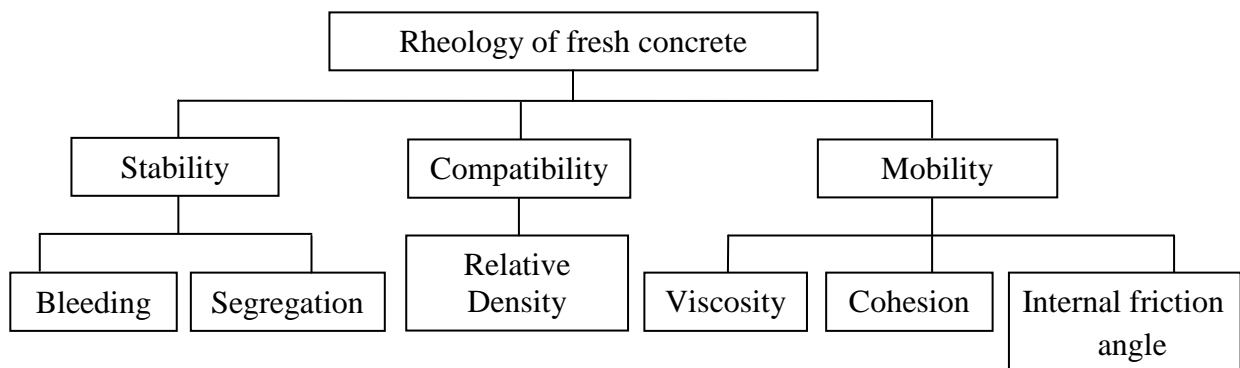


Figure 2.7: *Rheology of fresh concrete according to Ritchie [99]*

From the late 1970s many researchers started treating fresh concrete as a fluid and used methods assuming fluid rheology to describe concrete flow [124]. Concrete in its fresh state can be considered to be a fluid, provided that a certain degree of flow can be achieved and that the concrete is homogeneous. As mentioned above, the type of flow that characterises concrete flow is shear flow. To demonstrate the shear behaviour of fresh concrete, a sample has to be subjected to shear deformations, either under conditions of controlled stress or controlled strain rate.

2 Literature review

Concrete as a fluid is most often assumed to behave like a Bingham fluid. In this case, its flow is defined by two parameters: yield stress τ_0 and plastic viscosity μ (see Eq. 2.7). There are two possibilities of determining the Bingham parameters [36]:

1. The stress applied to the material is increased slowly and the shear rate is measured. When the stress is high enough, the concrete will start flowing. The stress at which the materials flow is the yield stress, and the slope of the shear stress - shear rate curve for values above this stress is the plastic viscosity;
2. The fresh concrete is sheared at a high rate before the rheological test. Then the shear rate is decreased gradually and the stress is measured. The relationship between the stress and shear rate is plotted, the intercept at zero-shear rate being the yield stress and the slope the plastic viscosity.

The yield stress and plastic viscosity of fresh concrete can be measured with the help of a viscometer or a Tattersall two-point workability test apparatus [127]. Such workability test equipment records the shear resistance, or stresses, of the concrete at two or more flow rates.

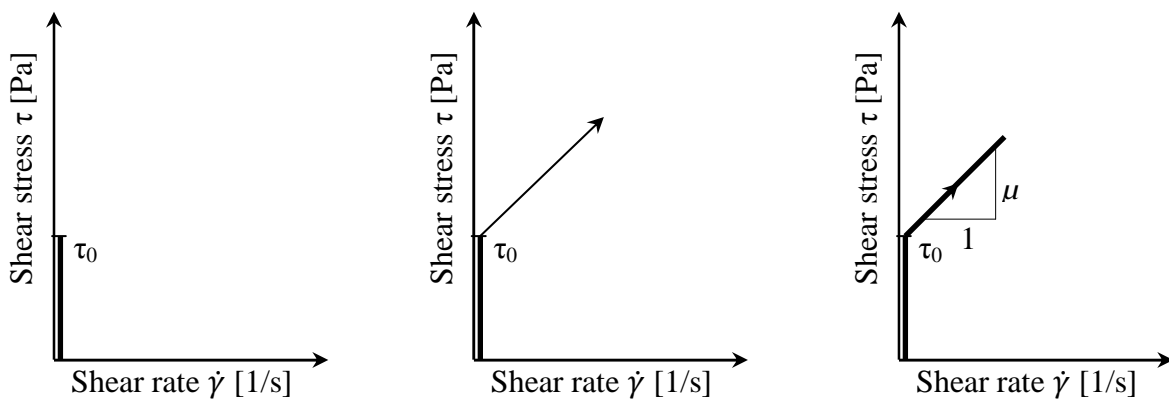


Figure 2.8: *Development of resistance or shear stresses when starting movement in fresh concrete; a simple flow-curve for fresh concrete [136]*

Figure 2.9 indicates the desired values of yield stress and plastic viscosity for a concrete mix in different applications. For instance, for up-hill casting, as high a yield stress as is possible is preferred. And in order to make the mix workable, it should have as low a viscosity as possible; the lower the plastic viscosity the higher is the allowed yield stress, obtaining a workable mix. When casting using a slip-form it is better not to have too viscous a mix as slippage between concrete and slip-form is preferred. As regards the slip-form, the adhesion properties and generation of slippage layer of the fresh concrete can be most relevant parameters [136].

For ordinary concrete which has to be pumped, the yield stress value must exceed a certain value to ensure that the concrete will flow into the pipe without segregation.

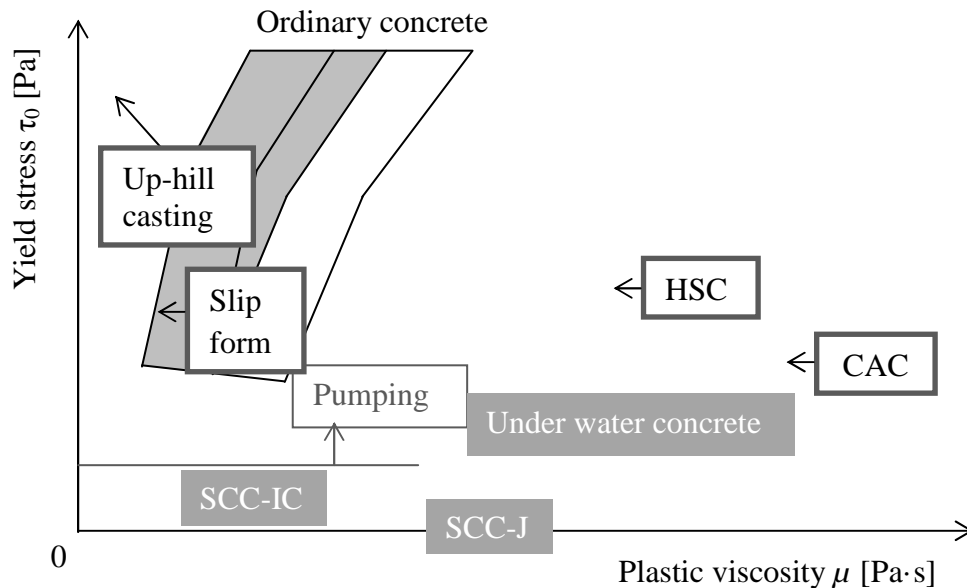


Figure 2.9: Typical τ_0 and μ values for different concrete types [136]

The art of making workable, high-strength concrete depends on the ability to reduce plastic viscosity as minimum as possible, because high viscosity normally causes problems with workability. Problems with the plastic viscosity limit the strength potential of the concrete if it is to remain workable. The better one masters this, the lesser the volume of water (or water-to-cement ratio) which needs to be used. The same applies for “calcium aluminate concrete” (CAC) which often exhibits extremely high plastic viscosity, even at a w/c of 0.5. A w/c < 0.4 is often required for CAC, and even then measures should be taken to reduce the viscosity by the use of rounded aggregates or some silica fume. An easy way to reduce plastic viscosity is to increase the water content, but a given low w/c in the CAC could lead to very high cement content; therefore, it is more economical to use silica fume as a viscosity-reducing agent [138].

Underwater concrete needs higher plastic viscosity since otherwise shearing, to wit: flowing, can be excessive, and undue washout of the cement paste will deteriorate the concrete. Also, higher plastic viscosity means, in general, increase the cohesiveness of the fresh concrete. It is recommended that the yield stress be lower (about 150 Pa) to obtain the necessary consolidation of the concrete under water [136].

The rheology of self-compacting concrete differs from that of ordinary concrete, as can be seen in Figure 2.9. SCC has almost no yield stress, or about zero to 60 Pa, where for ordinary concrete it ranges from a few hundred to several thousand Pa. The viscosity of SCC is very variable, especially from country to country, from 20 Pa·s to well over 100 Pa·s [136]. Figure 2.10 shows schematic flow-curves for a high-strength concrete of the strength class C100 and an ACC relative to ordinary concrete.

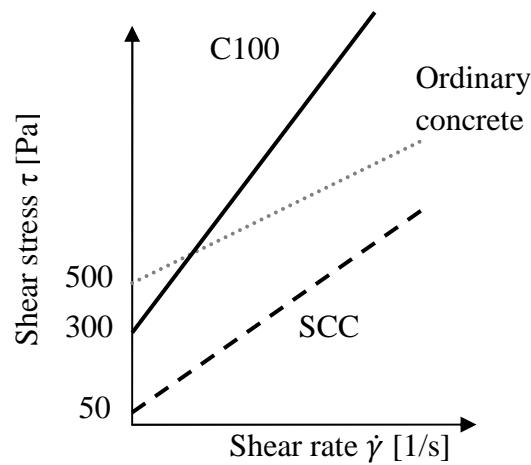


Figure 2.10: *Flow-curve of ordinary, high-strength and self-compacting concrete (schematically) [136]*

Rheological studies of fresh SCC have shown that to achieve self-compacting characteristics, an adequate combination of yield stress and plastic viscosity is necessary. If the viscosity is relatively low, an increase in yield stress is recommended to avoid segregation. On the other hand, if viscosity is too high, a lower yield stress would be necessary. Thus, an adequate balance of the fundamental rheological parameters, i.e. as yield stress and plastic viscosity, define the recommended behaviour of SCC [136].

2.4.1 Concrete components affecting rheological properties

There are various parameters which strongly influence the rheological properties of fresh concrete. In order to describe the effects of the individual constituents of concrete, one can plot the relationship between the yield stress τ_0 and the plastic viscosity μ . Figure 2.11 illustrates the qualitative significance of τ_0 and μ in simplified form.

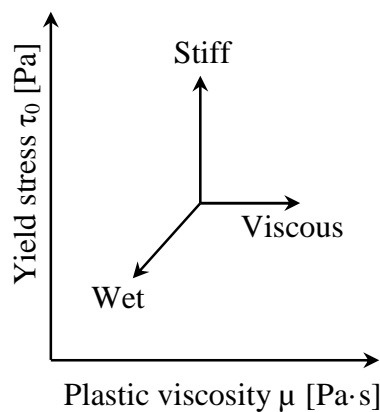


Figure 2.11: *A τ_0 - μ -diagram showing the qualitative significance of these rheological parameters with respect to properties of fresh concrete [136]*

Water is a major factor in reducing both plastic viscosity and yield stress. If one adds water to the concrete, it “moves” toward the origin in the τ_0 - μ diagram [136].

When the w/c is lowered, it is possible either to lower the water content, which will increase the plastic viscosity rapidly, or to add **cement** to the mix, which will increase the plastic viscosity only

moderately. Changes in the content of water have a more pronounced effect on plastic viscosity than do changes in the volume of powder [137, 138].

The addition of **air** to fresh concrete will primarily reduce its plastic viscosity. Yield stress might also decrease, in particular in the absence of plasticizer (relatively stiff mix) or in the presence of a high amount of fines. For a very fluid mix the yield stress can even increase slightly, but it is not likely to be significant [125].

If the slump (see Section 2.4.2.1) is held constant while the water is reduced and, correspondingly, the dosage of **superplasticizer** is increased, the plastic viscosity increases. In this case the yield stress remains nearly constant. The concrete becomes more viscous because of the reduction in water content with increased dosage of superplasticizer [125].

Stabilisers often used are high-molecular-weight cellulose, the first of which to be used being carboxyl-methyl-cellulose, bio-polymers, even poly-carboxyl based materials, or silica-sol. There are numerous such products on the market, and they influence the rheology of the fresh concrete very differently to each other. Some increase plastic viscosity, others reduce viscosity, some have little influence on yield stress; and others rapidly increase it. The often observed increase in yield stress will need measures to compensate for the reduction in fluidity. This being the case, when the concrete has been brought to a similar yield stress as with the mix without stabilizers, the increase in plastic viscosity is very often lost; so, in such a case there is no viscosity enhancement for a given yield stress [125, 137].

Silica fume acts in a way similar to that of stabilisers and should perhaps be characterised as such in respect of its influence on the behaviour of fresh concrete. This is due to the significant effect of silica fumes in reducing the mobility of the water in fresh concrete. Substitution of cement with silica fume up to a certain threshold value reduces the plastic viscosity by up to 50%. This threshold value depends on the cement content of the concrete (and will probably decrease with decreasing water content). Yield stress is nearly constant until the threshold value of the silica fume itself is reached. Further substitutions of silica fume above the threshold level increase yield stress. Thus, a silica fume concrete will have a slightly higher yield stress and much lower plastic viscosity than a concrete of the same slump without silica fume [28, 137].

It is difficult to provide as complete a description of the effects of **aggregate** as for the other parameters because many of the parameters change simultaneously. These include the relation between amounts of aggregates and binder, aggregate grading, grain shape, and different types and amounts of fines (< 0.125 mm). The very important parameter of the aggregates is their shape: crushed or rounded. It is known from the experiments that concrete made of rounded kies will have a significantly lower plastic viscosity as well as a considerably lower yield stress than concrete containing crushed aggregates. The yield stress increases when the proportion of coarse aggregate is reduced from 55 to 40% of the total aggregate content.

By increasing the **sand** fraction in a reference mix having crushed, coarse aggregate, the yield stress will increase and the plastic viscosity will decrease significantly [137].

2.4.2 Methods of rheological investigation of fresh concrete

Since the early 20th century, the concrete industry has recognized the need to monitor concrete workability to ensure that concrete can be properly placed and can eventually achieve adequate strength when hardened [34, 67].

The term workability is broadly defined; no single test method measures all aspects of workability. The American Concrete Institute describes workability as “that property of freshly mixed concrete or mortar that determines the ease with which it can be mixed, placed, consolidated, and finished to a homogenous condition” [2]. The Japanese Association of Concrete Engineers defines workability as “that property of freshly mixed concrete or mortar that determines the ease and homogeneity with which it can be mixed, placed, and compacted due to its consistency, the homogeneity with which it can be made into concrete, and the degree with which it can resist separation of materials” [37]. Neville [87] succinctly defines workability as “the amount of useful internal work necessary to produce full compaction”. Workability not only depends on the properties of the concrete, but also on the nature of the application. A very dry concrete mixture may seem to have very low workability when it may be, in fact, entirely appropriate for a given application [66].

The multitude of test methods for workability can be divided into categories based on several different classification schemes. Tattersall [125] broadly splits the assessment of workability into three classes, as shown in Table 2.5. The majority of workability test methods fall into Class II and Class III.

Table 2.5: *Classes of workability measurements [125]*

Class I Qualitative Workability, Flowability, Compactability, Finishability, Pumpability, etc.	To be used only in a general descriptive way without any attempt to quantify
Class II Quantitative Empirical Slump, Compacting Factor, Vebe Time, Flow Table Spread, etc.	To be used as a simple quantitative statement of behaviour in a particular set of circumstances
Class III Quantitative Fundamental Viscosity, Mobility, Fluidity, Yield stress, etc.	To be used strictly in conformity with standard definitions

Similar to Tattersall’s scheme, most test methods for workability have traditionally been split between single-point tests and multi-point tests. The concept of single- versus multipoint tests is based on the flow curve relating shear stress to shear rate. A single-point test measures only one point on the flow curve and, thus, provides an incomplete description of workability. For instance, the slump test can provide only one point on the flow curve, close to the yield stress. Multi-point tests, by contrast, provide additional points of the flow curve, typically by varying the shear rate, in order to give a more complete description of concrete rheology. Single-point tests generally fall into Class II of Tattersall’s scheme, whereas multi-point tests fall into Class III. Single-point tests can provide a direct or indirect measurement of yield stress, plastic viscosity, or some other property. Multi-point tests typically measure yield stress and plastic viscosity or closely related material parameters [125].

Single-point workability tests are generally intended to be simple and quick. In some cases, a single-point test may be appropriate for a certain type of concrete mix or a certain application even

though the test represents only one fundamental rheological parameter. The trade-off between single-point tests and multi-point tests is generally that single-point tests are simpler, yet less complete.

A distinction can also be made between dynamic tests and static tests. In dynamic tests, energy is induced into the concrete through such actions as vibrating, jolting, or applying a shear force to the concrete. In contrast, static tests do not add such energy and mostly on the concrete to flow under its own weight. Dynamic tests are particularly appropriate for low- and moderate-workability-concretes that are commonly vibrated in the field and for highly thixotropic concretes where energy is required to overcome the initially high at-rest yield stress.

Workability test methods have also been classified in terms of the type of flow produced during the test. In an effort to establish a uniform and widely accepted nomenclature for concrete rheology, the National Institute of Standards and Technology (NIST) divided existing rheology test methods as belonging to four broad categories [48, 64], see Table 2.6.

The NIST classification scheme is most consistent with the current understanding of concrete rheology and workability. Confined flow, free-flow, and vibration test methods generally attempt to simulate field placement flow conditions, whereas rotational rheometers attempt to apply the concepts of traditional rheometers to concrete.

Table 2.6: *NIST categorization of concrete rheology tests [48, 64]*

Category	Definition	Example
Free-flow Tests	The material either flows under its own weight, without any confinement, or an object penetrates the material by gravitational settling.	Slump Test, Slump flow Test, Cone Penetration Test, J-Ring Test, etc.
Confined Flow Tests	The material flows under its own weight or under an applied pressure through a narrow orifice.	L-Box Test, Compaction Factor Test, V-Funnel Test, etc.
Vibration Tests	The material flows under the influence of applied vibration. The vibration is applied by using a vibrating table, dropping the base supporting the material, an external vibrator, or an internal vibrator.	Flow Table Test, Compaction Test, Vibropenetrator, etc.
Rotational Rheometers	The material is sheared between two parallel surfaces, one or both of which are rotating.	BML Viscometer, BTRHEOM Rheometer, IBB Rheometer, etc.

2.4.2.1 Free-flow test methods

Free-flow test methods are generally simple to perform and provide a clear, direct result. The slump test is the best known of these. Other free-flow test methods represent attempts to improve on the slump test. Free-flow tests generally give results that are closely related to yield stress. Additionally, a few tests have been developed in order to assess plastic viscosity. Although many of the free-flow tests can be used on concretes with a wide range of workability, none of the free-flow

tests includes vibration. Tests that do not include vibration may not be the most appropriate test methods for characterising low-workability and highly thixotropic concrete mixtures [64].

Slump test

The **slump test** is the most well-known and widely used test method to characterise the workability of fresh concrete. This inexpensive test, which measures consistency, is used on job sites to determine rapidly whether a concrete batch should be accepted or rejected. The method is widely standardized throughout the world, including in ASTM C143 [4] in the United States and EN 12350 in Europe [33] part 2 (for OC) and 8 (for SCC).

The apparatus consists of a mould in the shape of a cone frustum with a base diameter of 20 cm, a top diameter of 10 cm, and a height of 30 cm. The mould has to be filled with concrete in three layers of equal volume. The slump cone mould has to be lifted vertically upward and the change in the height of the concrete has to be measured. Four types of slumps are commonly encountered, as shown in Figure 2.12. The only type of slump permissible under ASTM C143 is frequently referred to as the “true” slump, where the concrete remains intact and retains a symmetric shape. A zero slump and a collapsed slump are both outside the range of workability which can be measured by the slump test. Specifically, ASTM C143 advises caution in interpreting test results of less than ½ inch and greater than 9 inches. If part of the concrete shears from the mass, the test must be repeated with a different sample of concrete. A concrete that exhibits a shear slump in a second test is not sufficiently cohesive and should be rejected.

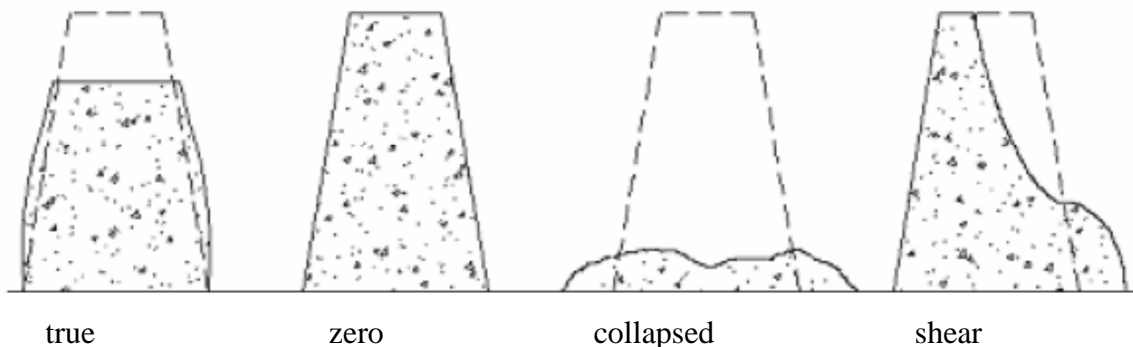


Figure 2.12: *Four types of slump [64]*

Additional qualitative information on the mobility of fresh concrete can be obtained after reading the slump measurement. Concretes with the same slump can exhibit different behaviour when tapped with a tamping rod. A harsh concrete with few fines will tend to fall apart when tapped and be appropriate only for applications such as pavements or mass concrete. Alternatively, the concrete may be very cohesive when tapped, and thus be suitable for difficult placement conditions.

Slump is influenced by both yield stress and plastic viscosity; however, in most cases the effect of plastic viscosity on slump is negligible or rather neglected. Equations have been developed for calculating yield stress in terms of slump, based on either analytical or experimental analyses. Since different rheometers measure different absolute values for the yield stress of identical samples of concrete, the experimental equations are largely dependent on the specific device used to measure yield stress.

In the literature several attempts can be found whose purpose was to relate slump to yield stress. Some authors, i.e., Kurokawa *et al.* [69], Tanigawa and Mori [119], Tanigawa *et al.* [122], and Christensen [17], proposed a complete description of the Abrams slump cone test based on finite element simulations by assuming that concrete is a Bingham fluid. Although they use different assumptions of the slip between concrete and the cone and table surface, these models show that the main parameter governing slump is the yield stress of the concrete.

The yield stress value can be expressed as the function of slump value or slump-flow value based on the static equilibrium of external forces and resistance stress [69, 83]. Kurokawa *et al.* [69] proposed a general formula relating the slump S and slump-flow Sf to the yield stress τ_0 in the following form (see Eqs. 2.20 and 2.21):

$$\tau_0(S) = \frac{7 \cdot \rho \cdot g}{1200 \cdot \sqrt{3}} \cdot (30 - S) \quad (2.20)$$

$$\tau_0(Sf) = \frac{\rho \cdot g \cdot V_c}{25 \cdot \pi \cdot \sqrt{3} \cdot Sf^2} \times 10^8 \quad (2.21)$$

where g is the acceleration of gravity ($=9,8067 \text{ m/s}^2$), S is the slump value in cm, Sf is the slump flow in mm, and V_c is the volume of the slump cone in m^3 .

In the case of a high-slump material whose $\tau_0(S)$ is lower than 200 Pa, the final shape becomes almost flat, such that the measured slump-flow value is lower than the theoretical result obtained on the assumption of a cut cone shape, and $\tau_0(Sf)$ becomes higher than $\tau_0(S)$. Contrarily, in the case of the material whose $\tau_0(S)$ is higher than 200 Pa, the measured slump-flow value becomes higher than the theoretical result, and $\tau_0(Sf)$ becomes lower than $\tau_0(S)$. The yield stress decreases linearly with increasing slump-flow value [69].

Kurokawa *et al.* [69] made the assumption that the sample keeps a truncated conic form with a diameter of the upper face equal to half of the one of the lower face. This leads to the Eq. 2.22:

$$Sf = \sqrt{\frac{12 \cdot 10^6}{S - 300}} \quad (2.22)$$

where Sf is the slump flow in mm.

The slump value is almost inversely proportional to the square of the slump-flow value Sf because of the constant volume of the material. The theoretical curve obtained on the assumption that the final shape of the material in the slump test is a simple cut cone of which the top radius is half of the bottom radius. The experimental results are in good agreement with the analytical curve when $Sf > 300 \text{ mm}$.

Helmuth *et al.* [50] developed a slump model based on Murata's [84] force-balance approach (see Eq. 2.23).

$$\tau_0 = \frac{\rho \cdot g \cdot V_c}{2 \cdot \pi \cdot r_s^2} \quad (2.23)$$

where V_c is the volume of the slump cone and r_s is the radius of the slumped material.

The radius of the base of the slumped material was assumed to be a function of the final slump height S , see Eq. 2.24.

2 Literature review

$$r_s = \left(\frac{336}{(12 - S)} - 3 \right)^{-\frac{1}{2}} - 1 \quad (2.24)$$

More precisely, dimensional analysis shows that the slump is controlled by the term $\tau_0/g\rho$ where τ_0 is the shear yield stress in Pa, ρ the density of concrete in kg/m^3 and g the acceleration due to gravity. This relation is in fact relatively intuitive because the slump measures the equilibrium of the concrete and then mainly describes static properties like the yield stress. Tattersall [125] measured, by analogy to the flow behaviour of the concrete, a yield torque with its two point workability apparatus and had verified long ago the existence of such a relationship between the slump and the yield torque. The relationship to shear yield stress has been shown more directly with the BTRHEOM rheometer (see Section 2.4.2.4) developed at LCPC by Hu [55] and de Larrard and Ferraris [25].

Based on a finite element model of a slump test, Hu *et al.* [56] developed an expression for yield stress in terms of slump and density, as shown in Eq. 2.25. The finite element calculations were performed for concretes with slumps ranging from zero to 25 cm. The equation is not appropriate for concretes with a plastic viscosity greater than 300 Pa·s, above which viscosity sufficiently slows flow which causes thixotropy, in turn resulting in a reduction of the actual slump value. An experimental study to verify the results of the finite element model showed “satisfactory” agreement between Eq. 2.25 and yield stress measurements from the BTRHEOM rheometer. It should be noted that the finite element calculations were performed for concrete starting with slumps as low as zero, while the BTRHEOM rheometer can only measure concretes with slumps greater than 10 cm approximately.

$$\tau_0 = \frac{\rho}{270}(300 - S) \quad (2.25)$$

where τ_0 is yield stress in Pa, S is slump in mm, and ρ = density in kg/m^3 .

Murata and Kikukawa [79] used a coaxial-cylinders rheometer to develop an empirical equation for yield stress in terms of slump for concretes with slumps ranging from 12.5 cm to 26 cm, as shown in Eq. 2.26:

$$\tau_0 = 714 - 473 \log(S) \quad (2.26)$$

where τ_0 is yield stress in Pa, S is slump in cm.

Schwalter and Christensen [108] developed a simple analytical equation to relate slump to yield stress and the height of the unyielding region of the slump cone, defined as the region where the weight of concrete above a given point is insufficient to overcome the yield stress. Other, more complex analytical analyses have been developed. Additionally, Tattersall and Banfill [127] presented experimental data showing a relationship between slump and yield stress.

There is also an analytical approach which predicts the shape of the concrete sample after deformation: the fluid depth at stoppage as a function of the distance $h(r)$ from the centre [102]. The flow turns from three-dimensional (with cylindrical symmetry) to one dimensional flow as the fluid height becomes much smaller than its radial extent.

The cone shape at stoppage is not conical any more but is described by the following expression (see Eq. 2.27):

$$h(r) = \left(\frac{2 \cdot \tau_0 \cdot (Sf - r)}{\rho \cdot g} \right)^{1/2} \quad (2.27)$$

The advantages and disadvantages of the slump flow test can be summarised as follows:

Advantages:

- The slump test is the most widely used test in concrete rheology worldwide.
- The slump test is simple and inexpensive to perform. Results are obtained immediately.
- The test is robust and repeatable.
- The results of the slump test can be converted to yield stress in fundamental units based on various analytical treatments and experimental studies of the slump test.
- Compared to other commonly used concrete tests, the slump test provides acceptable precision.
- The specimen size is small.

Disadvantages:

- The slump test does not give any indication of plastic viscosity.
- The slump test is a static test; therefore, results are influenced by concrete thixotropy. The test does not provide an indication of the ease with which concrete can be moved under dynamic placing conditions, such as vibration.
- The slump test is less relevant for new advanced concrete mixes than for more conventional mixes.

Modified slump test

The modified slump test [37, 39, 40, 69] is intended for use as a field test to measure both the plastic viscosity and yield stress of concrete mixtures. The test adds the parameter of time to the standard slump test in order to measure plastic viscosity. The time can be measured for two cases: vertical slump or horizontal slump flow of the specimen. The starting points for time measurements are same in both cases – beginning of the slump cone motion. The time measurements end when the slump reaches specified value (100 mm) in the first case and when the slump flow reaches 50 cm in the second case.

The apparatus for the modified slump test (time measurement for vertical slump) consists of a vertical rod that extends from a horizontal base plate through the center of the standard slump cone. The slump cone has to be filled in accordance with ASTM C143 [4] and a sliding disk is placed atop the fresh concrete. Once the slump cone is removed, the time for the disk to slide a distance of 100 mm has to be measured. The sliding disk comes to rest on a stop located on the vertical rod. After the disk comes to rest, the concrete continues on to reach its final position. The final slump measurement must be recorded not later than 60 seconds after the slump cone is removed. A schematic of the test procedure is shown in Figure 2.13.

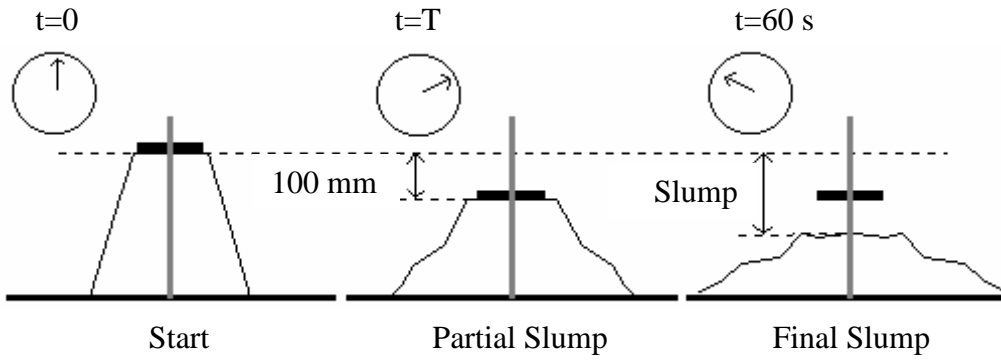


Figure 2.13: Schematic of the Modified Slump Test [40]

The rheological parameters of yield stress and plastic viscosity can be expressed in fundamental units using equations based on the results of the test. Yield stress (τ_0 , Pa) is expressed in terms of final slump (S , mm) and concrete density (ρ , kg/m³), while plastic viscosity (μ , Pa·s) is a function of final slump, slump time (T , s), and concrete density. The proposed expression for yield stress is the modified form of Eq. 2.25 and repeated below (see Eq. 2.28) [40]:

$$\tau_0 = \frac{\rho}{347}(300 - S) + 212 \quad (2.28)$$

The equation for plastic viscosity is based on a semi-empirical model developed by using the results of the modified slump test (see Eq. 2.29) [40]:

$$\begin{aligned} \mu &= \rho \cdot T \cdot 1.08 \cdot 10^{-3} \cdot (S - 175) && \text{for } 200 \text{ mm} < S < 260 \text{ mm;} \\ \mu &= 25 \cdot 10^{-3} \cdot \rho \cdot T && \text{for } S < 200 \text{ mm} \end{aligned} \quad (2.29)$$

Due to the need to measure the time for a slump of 100 mm to be achieved, the test only applies to concrete with slumps ranging from 120 to 260 mm. It has been shown that the rod has a negligible effect on the final slump and that there is no risk of the concrete falling faster than the plate. Other researchers have eliminated the sliding plate and shortened the rod so that it terminates 100 mm below the top of the slump cone [37]. And there is the possibility of operator error in determining the precise instants to start and stop the measurement of slump time.

Additional experimental testing needs to be carried out on a wider range of concrete mixtures in order to verify the validity of the test. Ferraris and Brower [39] found poor correlations between the results of the modified slump test and plastic viscosity as measured with five rotational rheometers.

During the slump flow test, it is possible to measure the time T_{50} from the moment the cone is lifted to the moment the spread is 50 cm in diameter. For the same slump flow, the more viscous the concrete, the longer it will take it to flow and the greater T_{50} . So, viscosity should be related to the spreading time. Kurokawa *et al.* [69] analysed the flow of a concrete versus time with a visco-plastic finite elements model. They deduced from their simulation a relationship between T_{50} on one hand and the viscosity and the final spread on the other hand.

Assuming that the concrete sample retains the geometry of a truncated cone with a lower diameter twice the upper one, they deduced the following equation:

$$\mu = 0.0545 \cdot \rho \cdot \left(1 - \frac{40000}{Sf^2}\right) \cdot \left(1 - \frac{25000}{Sf^2}\right) \cdot T_{50} \quad (2.30)$$

where Sf is the slump flow in mm, T_{50} is the time from the moment the cone is left up to the moment the spread is 50 cm in diameter.

If the concrete does not flow at the same rate in all directions, which is common, all concrete will not reach the 50 cm line at the same time. Therefore, it is important to specify whether T_{50} should be determined when concrete first touches the 50 cm line or completely reaches the entire 50 cm slump flow. The mean error is 35 Pa·s for viscosities between 50 and 350 Pa·s which is the order of the repeatability of the measurements with the BTRheom (see Section 2.4.2.4). The advantages and disadvantages of the modified slump flow test can be summarised as follows:

Advantages:

- The test is simple to conduct and only requires a bit more equipment than the slump test.
- The test gives an indication of both yield stress and plastic viscosity.

Disadvantages:

- The test is not a dynamic test and accounts neither for the thixotropy of concrete nor for the ability of concrete to flow under vibration.
- Further testing is required to validate the test.

J-ring test

This test is currently standardized in Europe as EN 12350 [33] part 12. The J-ring test [9, 32, 64] extends common filling ability test methods to characterise passing ability. The J-ring, as shown in Figure 2.14, is a steel ring of rectangular cross-section (30 mm by 25 mm) with a 300 mm diameter. Vertical holes drilled in the ring allow standard reinforcing bars to be attached to the ring. Each reinforcing bar is 100 mm long. The spacing of the bars is adjustable, although 3 times the maximum aggregate size is typically recommended.

To conduct the J-ring test in conjunction with the slump flow test, the slump cone has to be placed in the center of the J-ring and has to be filled with concrete in accordance with ASTM C143 [4]. After filling, the slump cone has to be lifted vertically upward and concrete is allowed to spread horizontally through the gaps between the bars.

The J-ring flow spread S_J is the average of diameters d_{max} (maximal diameter of the slump cake) and d_{perp} (diameter of the slump cake in the direction which is perpendicular to the d_{max}), as shown in Eq. 2.31. S_J is expressed in mm to the nearest 5 mm [109]. S_J characterised a horizontal spread of the concrete sample.

$$S_J = \frac{d_{max} - d_{perp}}{2} \quad (2.31)$$

The J-ring blocking step B_J is calculated using Eq. 2.32 and expressed in mm to the nearest mm. B_J characterises passing ability of the concrete sample.

2 Literature review

$$B_J = \frac{(\Delta h_{x1} + \Delta h_{x2} + \Delta h_{y1} + \Delta h_{y2})}{4} - \Delta h_0 \quad (2.32)$$

where Δh_0 is the relative height differences between the lower edge of the straight rod and the concrete surface at the central position; Δh_{x1} , Δh_{x2} - positions outside the J-ring in x -direction; Δh_{y1} , Δh_{y2} - positions outside the J-ring in y -direction (perpendicular to x), as shown in Figure 2.14 [109].

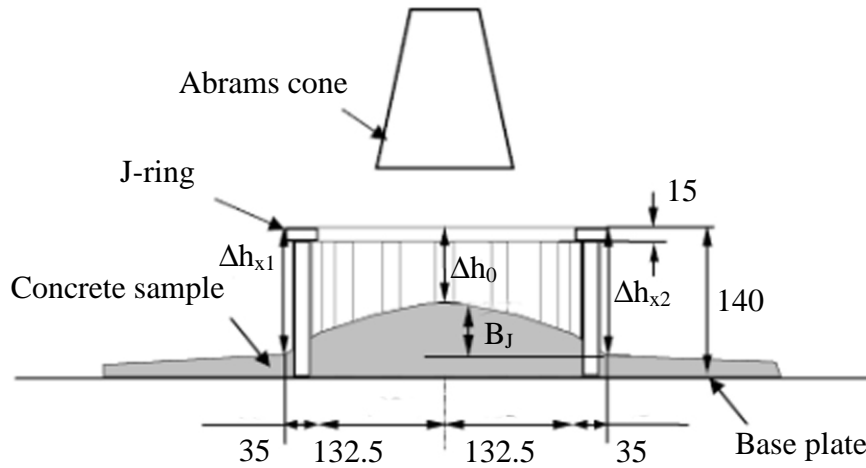


Figure 2.14: Dimensions of J-ring and positions for measurement of height differences; all dimensions in mm [109]

Various interpretations of the test results have been suggested. The measures of passing ability and filling ability are not independent of each other. To characterise the filling and passing abilities, the horizontal spread of the concrete sample is measured after the concrete passes through the gaps in the bars of the J-ring and comes to rest. Also, the difference in the height of the concrete just inside and immediately outside the bars is measured at four locations. The smaller this difference in heights is, the greater the passing ability of the concrete will be. Alternatively, horizontal spread with and without the J-ring can be compared as a measure of passing ability.

The concrete's cohesiveness and the tendency to segregation can also be evaluated with this test by examining the extended circle of concrete formed, i.e., is it homogeneous or disintegrated, is there paste at the perimeter, has it settled over the depth of the extended circle, etc. [109].

2.4.2.2 Confined Flow Tests

Many of the tests available for self-compacting concrete are confined flow tests. Generally confined flow tests are not suitable for low to moderate slump concretes, which are not sufficiently fluid to flow readily under confined conditions and produce meaningful test results.

The slump test also can be considered to be a confined flow test. However, the confined flow tests presented below provide additional information not provided by the slump test.

V-funnel test

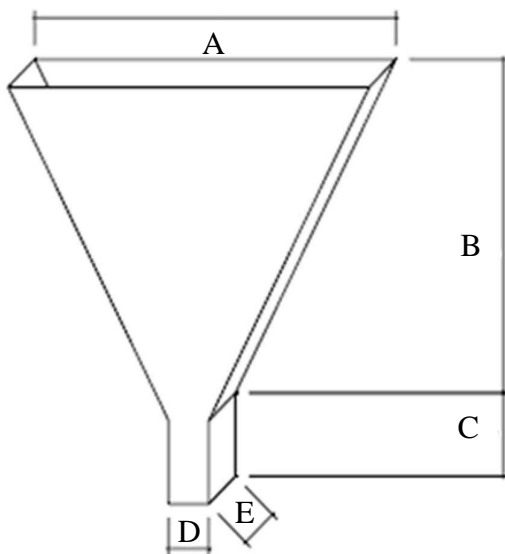
The V-funnel test [9, 32] is used to measure the filling ability of self-compacting concrete and can also be used to evaluate segregation resistance. The test is currently standardized in Europe as

EN 12350 [33] part 9. The test method is similar to the concept of the flow cone test used for cement paste.

The test apparatus consists of a V-shaped funnel with dimensions as given in Figure 2.15. Alternatively, an O-shaped funnel with a circular cross-section can be used. The inside walls of the funnel should be wetted before starting the test, and the funnel must be stable and leveled. With the valve closed, the entire funnel is filled with concrete without tamping or vibration. Within 10 seconds after leveling the top, the valve is opened. Time measurement is started by opening the bottom of the funnel. The mixture then falls freely through the bottom of the funnel. The stopwatch is stopped when light can be seen coming through the bottom opening of the funnel. The flow time for all of the concrete to exit the funnel is then recorded as a measure of filling ability.

The time measured is called flow time. For self-compacting concrete the flow time should be less than 10 seconds [32].

To measure segregation resistance, the V-funnel is refilled with concrete and allowed to settle for 5 minutes. The valve is opened again and the flow time is recorded. The greater the increase in flow time after the concrete has remained at rest for five minutes, the greater is the concrete's susceptibility to segregation. Further, non-uniform flow of the concrete from the funnel suggests a lack of segregation resistance [32].



Funnel dimensions in mm				
	Max. aggregate size in mm			
Type	4	8	16	32
A	270	390	515	600
B	240	350	450	515
C	60	105	150	195
D	30	40	65	85
E	30	40	75	95
(liters)	1.13	3.27	10.51	18.3

Figure 2.15: V-funnel test apparatus [109]

The average flow-through speed, V_m , is calculated in terms of the flow through time t_0 (see Eq. 2.33) [109]:

$$V_m = \frac{0.01}{(0.065 \cdot 0.075) \cdot t_0} = \frac{2.05}{t_0} (m/s) \quad (2.33)$$

To quantify segregation resistance, the flow through index, S_{flow} , is calculated in terms of initial flow through time (see Eq. 2.34), t_0 , and the flow through time after 5 minutes, t_5 :

$$S_{flow} = \frac{t_5 - t_0}{t_0} \quad (2.34)$$

2 Literature review

The funnel time t_0 is often used to estimate the apparent viscosity of a mixture. The time value obtained does not measure the viscosity but is related to it by describing the rate of flow. It is evident that concrete of low viscosity will have a very quick initial flow. Highly viscous concrete may continue to creep forward over an extended time [9, 32].

The advantages and disadvantages of the V-funnel test can be summarised as follows:

Advantages:

- The V-funnel test is simple and inexpensive to perform. Results are available immediately.
- The test gives an indication of apparent viscosity.
- The V-funnel test permits quantifying segregation resistance.

Disadvantages:

- The V-funnel test does not indicate yield stress.
- The test is not a dynamic test and does not account for the thixotropy of concrete, nor does it measure the ability of concrete to flow under vibration.
- Further work is required to validate the test.

L-box and LCPC-box flow tests

The L-box test [9, 32, 64] measures the filling and passing ability of self-compacting concrete and the extent to which it is subjected to blocking by reinforcement. Originally developed in Japan for underwater concrete, the test is also applicable for highly flowable concrete. The L-box test is currently standardized in Europe as EN 12350 [33] part 10.

As the test name implies, the apparatus consists of an L-shaped box, shown in Figure 2.16a. The concrete has to be initially placed in the vertical section of the box, which measures 600 mm in height and 100 mm by 200 mm in its cross-section. The vertical and horizontal sections are separated by a movable gate, in front of which reinforcing bar obstacles are placed. The vertical section is filled with concrete and left to rest for one minute. Then, the gate is lifted and concrete flows under its own weight through the reinforcement into the horizontal section (600 mm long, 200 mm wide and 150 mm tall). The concrete is allowed to flow through a line of vertical reinforcing bars. In the most common arrangement of reinforcing bars, three 12 mm bars are spaced with clear gaps of 35 mm each. Generally the spacing of the reinforcing bars should be three times the maximum aggregate size.

The time for concrete to reach marks 200 mm (T_{200}) and 400 mm (T_{400}) down the horizontal section of the box must be recorded in L-box test. T_{200} and T_{400} times can give some indication of ease of flow, but no suitable reference values have met with general agreement. After the concrete comes to rest in the L-box test apparatus, the heights of the concrete at the end of the horizontal section, h_2 , and in the vertical section, h_1 , must be measured as shown in Figure 2.16a.

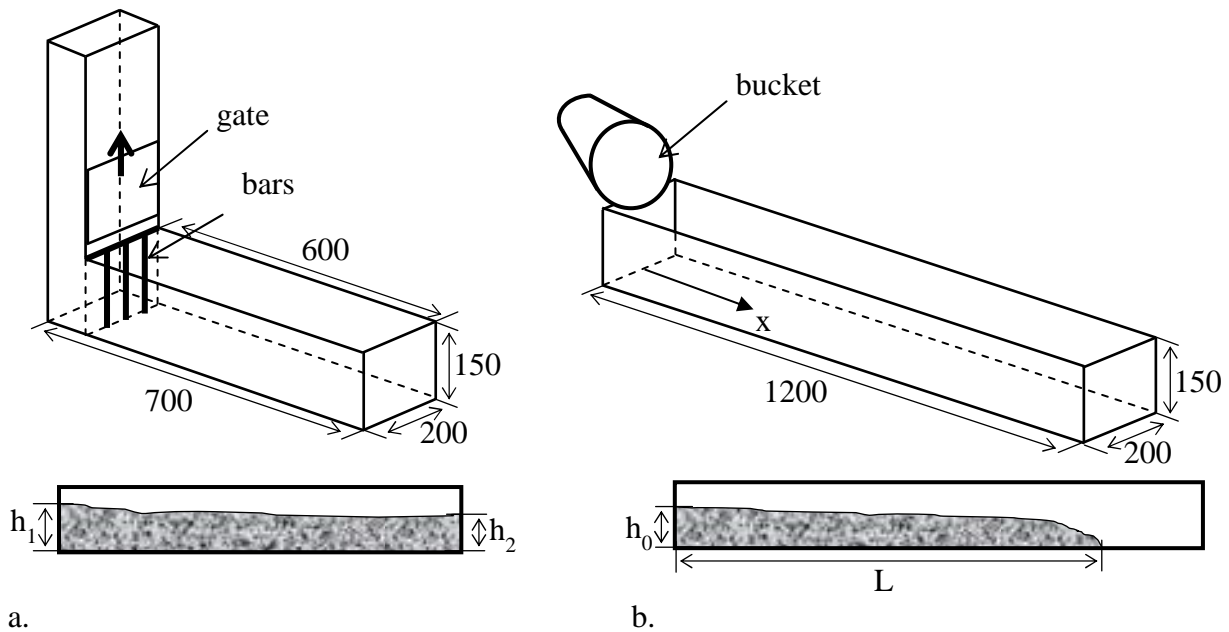


Figure 2.16: Test apparatuses and measured quantities for a) L-box [109] and b) LCPC-box [102] tests

The passing ratio (PA) for the L-box test is calculated using the following equation (see Eq. 2.35), and is expressed dimensionless to the nearest 0.01.

$$PA = h_2/h_1 \quad (2.35)$$

The passing ratio for most tests should be 0.80 to 0.85. In addition, both blocking and stability can be detected visually. Segregation resistance can also be evaluated visually. A concrete sample with coarse aggregate particles that reach the far end of the horizontal part of the box demonstrates good resistance to segregation. The L-box can be disassembled after the concrete has hardened. By cutting out samples of the hardened concrete, additional information about the concrete's resistance to segregation can be determined, as shown by Tanaka *et al.* [118].

The LCPC box is an alternative new test developed at *Laboratories Central des Ponts et Chaussées* (LCPC), France. It fulfils all the conditions needed to correlate the measured empirical value to the yield stress of the SCC tested [102]. The LCPC test apparatus consists of bucket and channel, shown in Figure 2.16b. The width of the channel is 200 mm, the length 1200 mm. The volume of SCC is the same as that used in the slump flow test as it is sufficient to be representative of the tested concrete. The SCC has to be poured slowly at the one end of the box, i.e., emptying the bucket should take about 30 s [102]. The spread length L in the box and height of the concrete in the vertical section h_0 are measured after the concrete comes to rest in the LCPC-box test apparatus (see Figure 2.16b).

The measured spreading length L in the LCPC-box apparatus, as shown in Figure 2.16b, correlates with the yield stress of the concrete; this is the correlation between the spread length and the yield stress. The analysis of this flow and its stoppage can be found in [88, 102].

2 Literature review

There is also an analytical approach to predict the shape of the concrete sample after stoppage in the LCPC-box test. The fluid depth at stoppage can be calculated as a function of the distance $h(x)$ using following equation (see Eq. 2.36) [88]:

$$h_0 - h + \frac{l_0}{2} \ln \left(\frac{l_0 + 2h}{l_0 + 2h_0} \right) = \frac{2\tau_y}{\rho g l_0} x \quad (2.36)$$

where h_0 is the thickness of the deposit at $x=0$, h is the thickness of the deposit at the distance x , l_0 is the width of the channel ($l_0=200$ mm, as shown in Figure 2.16).

The advantages and disadvantages of L-box and LCPC-box tests can be summarised as follows:

Advantages:

- The L-box test is a widely used test, suitable for laboratory and, perhaps, use on site.
- The L-box test assesses the filling and passing ability of SCC, and serious lack of stability (segregation) can be detected visually.
- The LCPC-box test is a new, alternative way to measure the yield stress of the SCC.
- The LCPC-box test is simpler than the L-box test; just one operator is required.

Disadvantages:

- The L-box and the LCPC-box tests do not indicate plastic viscosity.
- The L-box test does not give an indication of yield stress.
- The tests are not dynamic tests and do not account for the thixotropy of concrete nor does it measure the ability of concrete to flow under vibration.
- There are no standardized dimensions for tests, results from different test apparatuses cannot be compared directly.
- Two operators are required for L-box test if times are measured, and some operator errors are inevitable.

2.4.2.3 Vibration test methods

Due to the wide use of vibration and other methods of compacting in placing concrete, many test methods now measure the flow of concrete under vibration. Vibration test methods typically feature free or confined flow and are generally simple to perform. However, none of them, except flow-table test, has been widely accepted. Although vibration test methods can be used for a wide range of workability, they are most appropriate for low and moderate slump concretes, which in the field are commonly vibrated.

In evaluating the results of vibration test methods, it is important to recognise the role of several vibration parameters in influencing the flow properties of concrete. It has been experimentally established [29, 127] that vibration alters the Bingham parameters of concrete. The flow properties of vibrated concrete are related not just to the flow properties of the unvibrated concrete but also to the nature of the applied vibration. In [29] it was shown that the flow of concrete under vibration is most significantly influenced by the frequency of the vibration. When the frequency of vibration is above a minimum threshold value, concrete can be considered as a Newtonian fluid, at least for low shear rates. In general, based on this information the results obtained from the same test method with different types of vibration should not be compared directly.

Flow table test

The flow table test [125] measures the horizontal spread of a concrete cone specimen after being subjected to jolting. Multiple versions of the test have been proposed since its original introduction in Germany in the 1930s. The test is currently standardized in Europe as EN 12350 [33] part 5.

The apparatus consists of a 700 mm square wooden top plate lined with a thin metal sheet, as shown in Figure 2.17. The plate has to be hinged on one end to a base, while on the other end; clips allow the plate to be lifted to a vertical distance of 40 mm. Two perpendicular lines which cross in the center of the plate and a 200 mm circle (concentric with the center of the plate) are etched into the metal sheet. The frustum of a cone used as mould for the concrete is, with a top diameter of 130 mm and both bottom diameter and height of 200 mm [64], shorter than the slump cone.

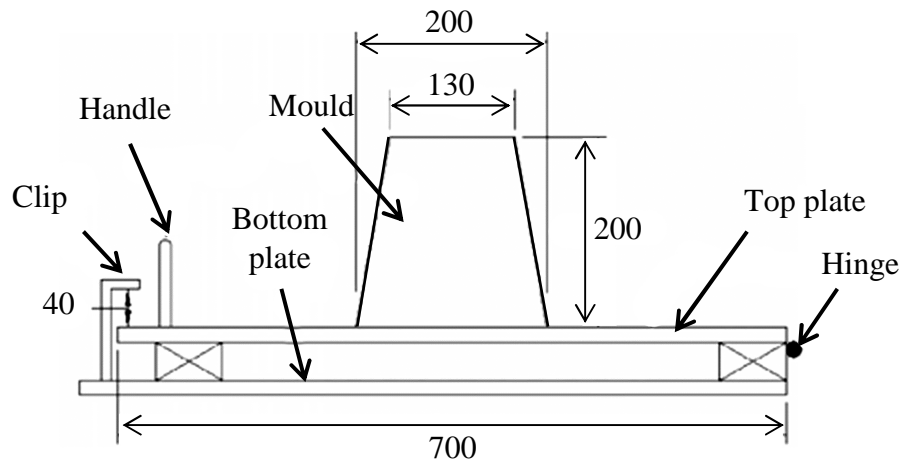


Figure 2.17: Flow table test apparatus; all dimensions are in mm [9]

To perform the test, the cone mould has to be placed in the center of the plate and has to be filled with concrete of two layers, each of which must be compacted with a tamping rod. The plate has to be lifted with the attached handle to a distance of 40 mm and then has to be dropped a total of 15 times. The horizontal spread of the concrete must be measured. Resistance to segregation can be assessed qualitatively: in concrete mixes that are susceptible to segregation, the paste will tend to separate from the coarse aggregate around the perimeter of the concrete mass.

The test is applicable to fresh concrete of a wide range of workability and is also appropriate for OC mixes which collapse during the slump process. The results of the flow table test can be correlated to slump, although it has been suggested that the initial horizontal spread, prior to jolting, correlates better to slump [60]. Despite its simplicity, the test apparatus is large and must be placed on firm and flat ground. The jolting of the concrete does not accurately simulate field practices and cannot easily be treated analytically. In fact, the further the concrete spreads, the thinner the layer of concrete becomes, and this thin layer represents the bulk properties of the concrete. Research has suggested that spread measurements for different concrete mixtures converge with an increasing number of drops of the top plate [125].

Advantages:

- The test is simple and can be used in the field.
- The test quickly provides a direct result.
- The test is dynamic, making it especially appropriate for highly thixotropic concrete mixtures.

Disadvantages:

- The test procedure does not represent actual placement conditions; concrete is typically vibrated, not jolted.
- The test results tend to converge as the number of drops is increased. Near the end of the test, the properties of the thin layer of concrete do not reflect the bulk properties of the concrete.
- The results are not given in terms of fundamental units. An analytical treatment of the test would be difficult.

2.4.2.4 Rheometers

Several instruments have been designed to determine the workability or flow properties of concretes [37], some in an empirical manner, and some attempting to apply absolute physical measurements to concrete rheology, i.e., fluid rheology. The devices attempting to use methods of fluid rheology to measure the flow of concrete by measuring shear stress at varying shear rates are called rheometers [47]. They all measure the resistance to flow of concrete at varying shear rate conditions.

The majority of commercially available rheometers were originally developed to test polymer systems. These rheometers apply different geometries, such as the parallel plates, coaxial cylinders, and vane configurations using one machine by simply changing fixtures. However, rheometers designed for polymers or neat fluids with no solid particles are, due to the presence and size of the solid aggregates, not suitable for measuring concrete. For these rheometers the sample sizes must be small and the torque capacity should be low, limiting the testing of concrete to relatively fluid cement paste and mortar systems, typically without fibre reinforcement. In response to these limitations, a number of researchers have developed rheometers for evaluating the rheology of highly fluid concrete materials. Custom-designed and built rheometers include mixer-type setups like the IBB [10] (Canada) and Two-Point (UK) [29], coaxial cylinder configurations such as the BML (Iceland) [140] and CEMAGREF-IMG (France) [17], parallel plate geometries, including the BTRHEOM (France) [26, 27, 56], and the rheometer developed at the University of Illinois at Champaign-Urbana [115]. The Tattersall two-point rheometer, IBB and BTRHEOM rheometers are schematically illustrated in Figure 2.18.

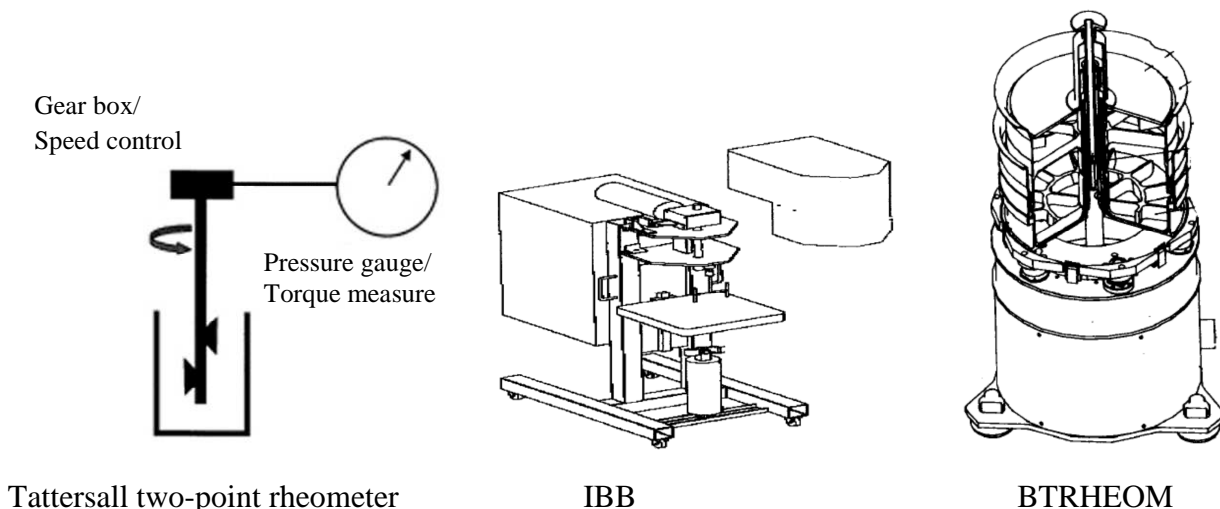


Figure 2.18: Schematic representation of different rheometers [37]

The IBB and two-point rheometers are based on rotating an impeller in fresh concrete contained within a cylindrical vessel. The shape of the vane varies with the rheometer. The speed of rotation of the blade is first increased and then decreased while the concrete resistance or torque is measured. The BTRHEOM is a parallel plate rheometer. The concrete is placed in a cylindrical container with a fixed bottom plate. A top plate embedded in the concrete is rotated at increasing and then decreasing speeds and the torque is measured. The CEMAGREF-IMG and the BML are coaxial cylinder rheometers in which one cylinder, the inner cylinder for the CEMAGREF-IMG and the outer for the BML, is rotated at increasing and decreasing speed and the torque induced by the concrete on the inner cylinder is measured. The flow pattern of the concrete in the IBB and Two-Point rheometers cannot be assessed or modelled easily, while the flow can be mathematically modelled for the coaxial rheometers (BML, CEMAGREF-IMG) and for the parallel-plate rheometer (BTRHEOM). For these three rheometers (BML, BTRHEOM, CEMAGREF-IMG), rheological characteristics in fundamental units can be calculated. The Two-Point test rheometer requires indirect methods using calibrating fluids of known viscosity to convert quantitative data into the fundamental units. The IBB is not calibrated with a fluid and therefore, the results are not reported in fundamental units [39].

A considerable amount of research has been conducted on the rheology of cementitious materials using both commercial and custom-designed rheometers. Unfortunately, the results from independent studies are not quantitatively comparable due to differences in materials, shear history (mixing/handling procedures), age (hydration), rheology-measuring protocols and the rheometers used [6, 34, 107, 127]. In addition, testing artifacts such as plug flow, wall slip, sedimentation, and edge effects, can significantly influence rheological measurements. When reviewing the values reported in the literature, Tattersall and Banfill found a 20- and 50-fold range for yield stress and viscosity measurements, respectively [127]. More recently, custom-built concrete rheometers were compared in a survey at LCPC [6]. They found that even with the same materials and mixing procedures, large variations of yield stress and viscosity values were measured. It was noted, however, that a qualitative comparison could be made and that there was a good correlation between the rheometers.

Advantages:

- The rheometers measure both plastic viscosity and yield stress.
- The rheometers are applicable to concretes with wide range of workability.
- Rheometers have been used widely in research, particularly when compared to other rheometers.
- The operation of the rheometers can be automated.
- The device can be used to measure the effects of vibration on concrete rheology and thixotropy.

Disadvantages:

- The devices are complex and expensive.
- The devices are not suitable to be used at construction site.
- The devices must be calibrated.

2.5 Methods for numerical simulation of the flow process

Computational modelling of flow is a powerful tool for understanding the rheological behaviour of concrete. Numerical simulation of flow could be used for simulation of, for example, form filling and detailed flow behaviour as particle migration and formation of granular arches between reinforcements (“blocking”). Numerical simulation of the casting process could allow specifying a minimum workability of the fresh concrete that could ensure the proper filling of a given formwork.

Fresh concrete is a suspension of particles in a matrix. Depending on the purpose of the simulation and behaviour of the concrete, the scales vary at which the solid components of the concrete, i.e., cement, fine and coarse aggregates, fibres or other binders, are considered as particles or belonging to the matrix. The techniques found in the literature may be divided into three main families:

- single fluid simulations;
- numerical modelling of discrete particles flow;
- numerical modelling of particles suspended in a fluid.

As the relevant length scales in suspensions differ by several orders of magnitude, it is not possible to simulate them by including details at all these length scales. All numerical methods are based on one chosen particular length scale.

Few numerical flow analysis methods have been proposed for fresh concrete. The majority of them and their characteristics are shown in Figure 2.19. They can be classified into two types: continuous body models and discontinuous body models.

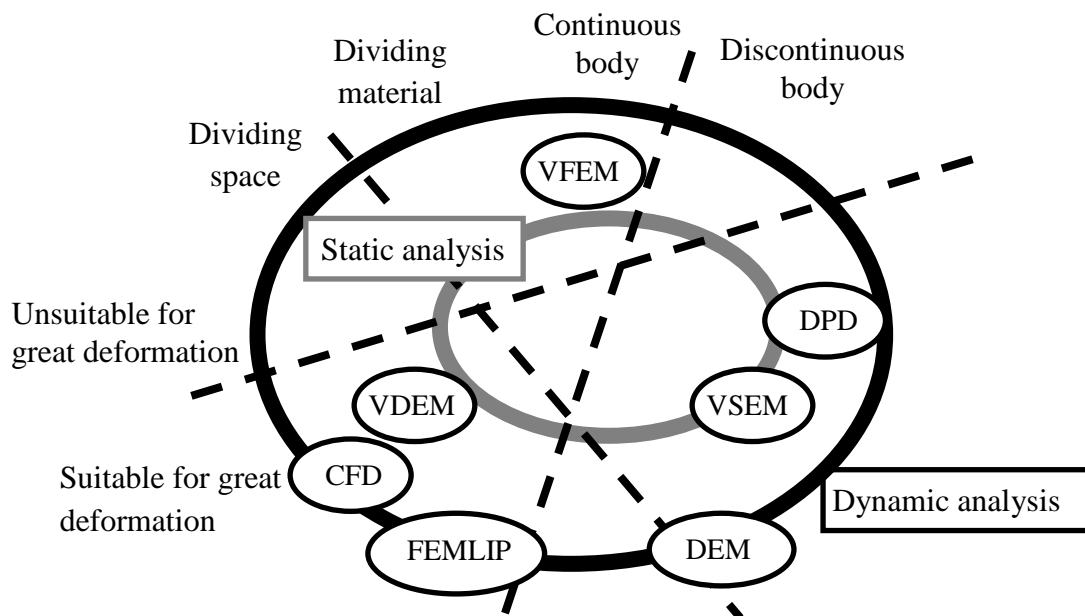


Figure 2.19: Numerical flow analysis methods for fresh concrete [146]

This chapter shows the general conception of the methods for numerical simulation and gives the comparative analysis of potentials of these methods.

2.5.1 Continuous body approach (Single fluid simulations)

Single fluid simulations have been used chiefly to model the flow of fresh concrete during testing [102, 105, 100, 131]. However, few examples of computational modelling of full-scale castings assuming single fluid behaviour are given [62, 63, 129, 130].

The single fluid simulations have two main numerical difficulties: modelling of the yield stress behaviour of the material and displacement of the free surface [105]. Indeed, it is the apparent viscosity of the material that is, most of time, applied in the Navier-Stokes equations in order to obtain a numerical solution of the problem. However, the apparent viscosity of a yield-stress fluid approaches infinity when the shear rate, or more generally in 3D the strain rate, approaches zero. It is necessary to avoid this in determination of the deformation state below the yield stress in zones where flow stops or starts, which are the primary zones of interest [105]. Moreover, as with many continuum methods, single fluid simulations require a clear definition of the boundary conditions. Fresh concrete displaying a moving free boundary is thus particularly difficult to simulate.

The most popular methods of the continuous body approach are **Computational Fluid Dynamics (CFD)** in Europe, **Viscoplastic Finite Element Method (VFEM)** and **Viscoplastic Divided Element Method (VDEM)** in Japan.

Computational Fluid Dynamics is a method of modelling fluid flows by the numerical solution of the governing partial differential equations or other mathematical equations of motion [143]. The fundamental basis of any CFD problem is the Navier-Stokes equations, which defines any single-phase fluid flow. The most fundamental consideration in CFD is how one treats a continuous fluid in a fashion made discrete for a computer. One method is to divide, make discrete, the spatial domain into small cells to form a volume mesh or grid, and then apply a suitable algorithm to solve the equations of motion (Euler equations for non-viscous, and Navier-Stokes equations for viscous flow). Such a mesh can be either irregular (for instance consisting of triangles in 2D, or pyramidal elements in 3D) or regular. The distinguishing characteristic of the former is that each cell must be stored separately in memory.

In many instances, other equations are solved simultaneously using the Navier-Stokes equations. These other equations can include those describing species concentration, chemical reactions, heat transfer, etc. More advanced codes allow the simulation of more complex cases involving multi-phase flows, e.g., fluid/gas, solid/gas, and fluid/solid, or non-Newtonian fluids (such as concrete) [143].

A single fluid approach assuming Bingham behaviour was used in [129, 131] to simulate the flow of SCC during slump flow and L-box tests. The simulation approach applied was based on the Galerkin FEM formulation of the Navier-Stokes equation, and it allowed for moving boundaries. Combined simulations and experiments indicated that the slump flow test and the flow in an L-box with reinforcement can be simulated assuming ideal Bingham behaviour and rheological properties measured in a BML rheometer.

Further, a form-filling experiment and corresponding 3D simulations are presented in [130]. This simulation was also based on a FEM formulation of the Navier-Stokes equations, and a Bingham model was applied. The results show good correlation between the flow behaviour observed in the experiment and the simulation with respect to detection of the free surface location, dead zones, and paths of single point of flow during simulation. The simulation was undertaken using the code

FIDAP. The geometries of the form and filling process at different times are illustrated in Figure 2.20.

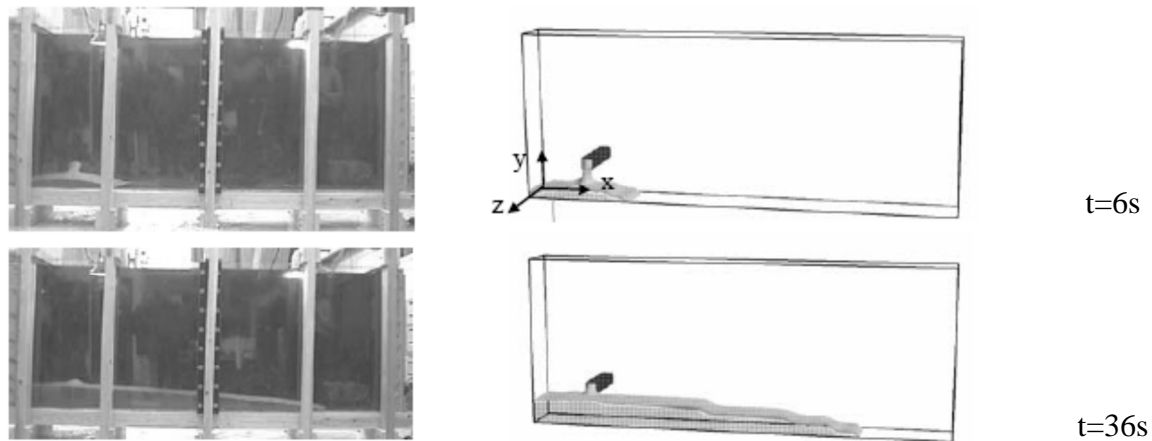


Figure 2.20: Location of the free surface in the experiment and in the simulation at different times [130]

Numerical simulation of the flow in different rheometers was given by Wallevik J.E. [135]. The simulations are based on the assumption of a viscoplastic material, flowing either at steady state or under time dependent (“transient”) conditions. Wallevik used a combination of several different techniques and both self-developed and freely available numerical software to describe the viscoplastic behaviour of concrete. The computational modelling was used for the comparison of rheometers, among others, with regard to variations in shear rate and migration of single points of flow. He simulated velocity and shear stress profiles for various viscometer configurations.

The CFD approach was also used by Roussel [100, 103] for numerical simulation of various slump flow test methods. The fresh concrete was assumed to be incompressible, elastic solid up to the yield stress, and a Bingham fluid beyond that. It was assumed that no sliding takes place at the base. Therefore, an elasto-viscoplastic model was used to describe the fluid behaviour of concrete with yield stresses between 25 and 5500 Pa. Good agreement between numerical and experimental results for the mini-cone slump test and for the ASTM tests was obtained. The computational fluid mechanics code Flow 3D was used to perform 3D simulations.

The numerical results obtained were compared to two analytical solutions valid in two asymptotic cases: when there is a very small slump, or purely extensional flow – extension of the specimen without shearing flow, and when there is a large spread, or purely shearing flow. Examples of three-dimensional predicted shapes for the ASTM Abrams cone are shown in Figure 2.21. The presence of an unyielding zone, usual in this type of simulation, is to be noted. The calculated values of the slump confirmed the fact that slump, i.e., final shape, only depends on yield stress and density.

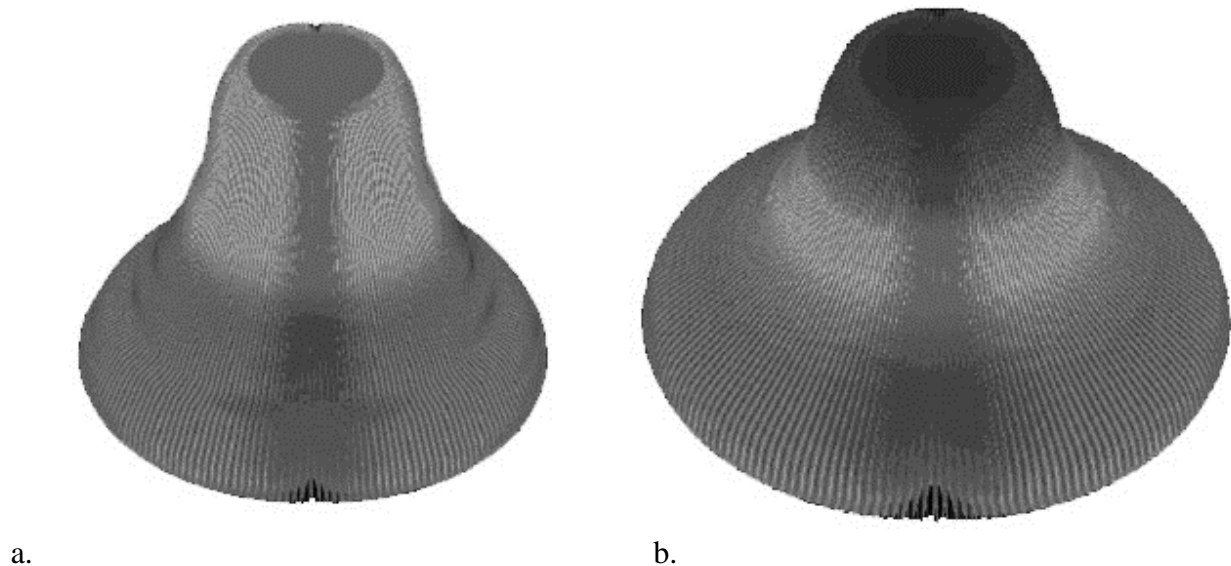


Figure 2.21: Examples of obtained shapes for the ASTM Abrams cone a) yield stress = 2600 Pa, b) yield stress = 2000 Pa; density = 2500 kg/m³ for both simulations [100]

Numerical simulations of an industrial casting of a very high strength concrete pre-cambered composite beam were also performed by Roussel *et al.* [106]. Simulation helped determine optimal values of the rheological parameters needed to accomplish the casting process successfully. Fluidity is proportional to the spread of the slump flow cake. Therefore, minimum fluidity means that such set of rheological parameters which provide modelling of the concrete with minimal spread are needed to cast the element successfully.

Viscoplastic Finite Element Method (VFEM) and Viscoplastic Divided Element Method (VDEM) were used by Mori and Tanigawa [81] to simulate flow of fresh concrete. Both of them assumed concrete as a single-phase homogeneous fluid with given rheological properties.

In VFEM the fresh concrete is divided into elements in which the deformation is calculated, and the flow is described by displacement of nodal points. However, the fixed position of nodal points allows reinforcement and complicated boundary conditions to be simulated.

VFEM was used by Kurokawa *et al.* [70] to evaluate factors affecting the slump flow of fresh concrete. They used the Bingham model and fitted the rheological properties to experimental results.

The dynamic VFEM can treat the volume elasticity of fluid to make it possible to reproduce the propagation phenomenon of vibration numerically. The VFEM is possibly applicable to three-dimensional problems, but it is difficult to be used for practical problems such as simulation of casting fresh concrete in a mould with cross-placed steel bars because of the complexity of the boundary conditions and the limitations of the freedom of the nodes.

In the analysis process of the viscoplastic divided element method (VDEM) [120], the space, in which fresh concrete is cast, rather than the fresh concrete is divided into many elements, and the characteristics of the individual elements vary with the inflow of fresh concrete. The strain rate at each node is obtained by iterative calculations with time steps. The movement of an imaginary ball cock, called a marker, depicts the flow of fresh concrete during casting.

Although this numerical method is based on a continuous body model, it can reproduce the phenomena of large deformation; break-up, the breaking up into several pieces or sections; massing, gathering of moving pieces or sections together; collision, a violent impact of moving pieces or sections; etc. of fresh concrete. Simulation of concrete casting on an industrial scale becomes possible by using the VDEM, although a large calculation capacity is needed for computing. The VDEM is suitable for making concrete flow visible.

However, the VDEM has not been used in three-dimensional analysis until now because of the high computer capacity demand of the model. Furthermore, in outline the filling of fresh concrete into a mould is relatively easily clarified by using this numerical analysis method, but the flow in small-scale spaces such as the mould's corners, and the finishing state of fresh concrete are difficult to simulate.

Mori and Tanigawa demonstrated the applicability of VDEM in simulating the flow of concrete in a reinforced beam section and the filling of a reinforced wall (2 m high, 3 m long); and Kitaoji *et al.* [62] confirmed the applicability of 2D VDEM to simulate the flow of fresh concrete cast into an unreinforced wall (1 m high, 2 m long). Kitaoji *et al.* approximated the slipping behaviour on the wall surface near the inlet by thin layer elements. The simulations were based on a single fluid approach assuming ideal Bingham behaviour.

Both methods (VFEM and VDEM) were applied in simulating various test methods at reasonable computation time. The main advantages and disadvantages of the continuous body approaches can be summarised as follows:

Advantages:

- They enable investigations of form-filling behaviour on a large scale.
- The extensive choice of behaviour laws allows the modelling of many phenomena such as thixotropy.
- The calculation time and memory used are relatively small; it is indeed the fastest way to simulate the casting of concrete.

Disadvantages:

- Particle blocking and segregation cannot be predicted.

2.5.2 Simulation of discrete particles flow

Many phenomena during fresh concrete flows, e.g., passing through reinforced steel bars, segregation, and blockage, are associated with concrete workability. These phenomena arise out of the heterogeneity of concrete.

Concrete is by nature dominated by its fluid-like behaviour or by its granular media-like behaviour, according to its workability. In the case of SCC for example, the amount of coarse particles in the mixture is low, and this modern concrete behaves as a fluid suspension whereas, in the case of ordinary concrete with a greater amount of coarse particles, behaviour is dominated by its granular nature.

Various techniques have been used for the computational modelling of the movement and interaction of aggregate particles in concrete. The numerical methods are powerful tools for detailed studies of the movement and interaction of particles in a fluid, e.g., SCC. Furthermore, visualization

of particle movement can assist in the design of improved numerical simulations and ways to evaluate the physical behaviour of systems.

Numerical mesoscopic particle flow models have been proposed in simulating concrete: the standard **Discrete (or Distinct) Element Method (DEM)** [89, 92] and **Dissipative Particle Dynamics (DPD)** [72].

The **Distinct Element Method** has been introduced into the flow analysis of fresh concrete as a numerical method using the discontinuous body model [85, 92].

This method is based on a motion equation of rigid elements and the transmission of forces among these rigid elements. Each calculation cycle includes two steps: the determination of the contact forces between solid particles and the calculation of the motion of each particle determined by the application of Newton's second law. During deposition of particles, for example, DEM can track motions and reveal all the dynamic behaviour until all the particles come to a state of rest. The static state then takes on emergent properties such as shear strength, porosity and permeability, all of which vary locally. Each property is the result of every single particle's experience of interaction forces up to that moment.

When the DEM is applied in concrete flow analysis, each contact point between particles is replaced by a set of normal and shear springs, normal and shear dashpots, normal and shear no tension-joints and shear sliders to express viscous resistance and inter-frictional resistance of concrete; see Figure 2.22. However, the dashpot and the spring have no dimension, and there is the mayor problem that the input data used are imaginary values not directly related to the measured rheological constants – yield stress and plastic viscosity of matrix mortar.

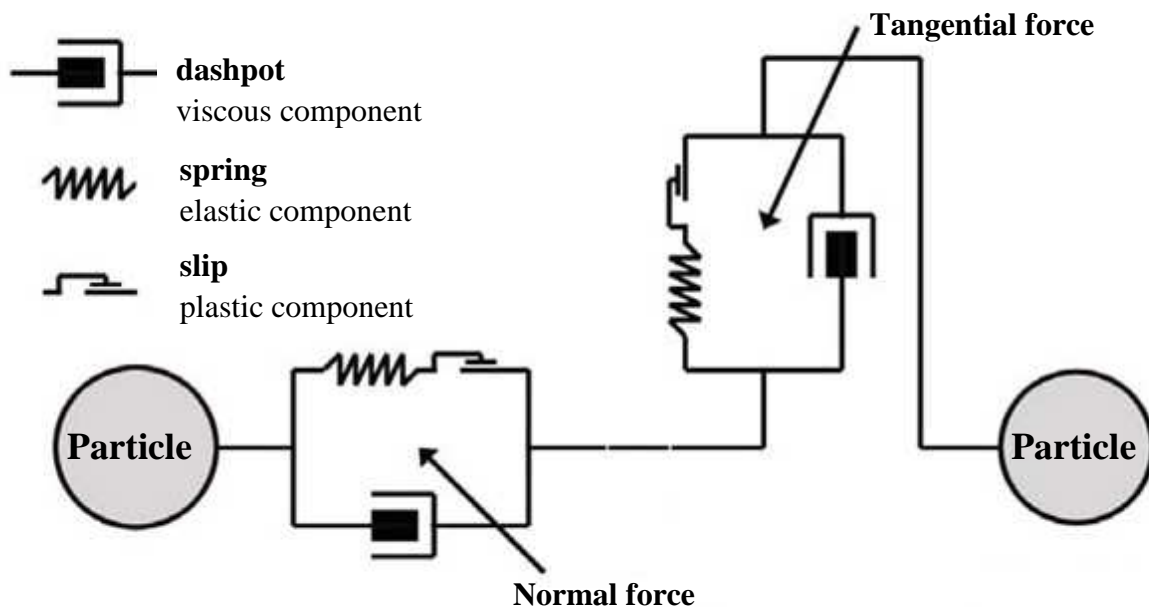


Figure 2.22: Model for particle interaction for normal and for tangential direction [105]

As a complement to laboratory experiments, discrete numerical simulation applied to granular materials gives access to the microstructure at the scale of the grains and contacts and improves our understanding of the microscopic origin of macroscopic mechanical behaviour.

2 Literature review

The various discrete simulation methods found in the literature, considered as numerical experimentation tools, are presented in relation to mechanical models of inter-granular contacts. DEM was selected by the authors to reproduce the qualitative behaviour in fresh concrete. As a compromise between modelling aggregate movement and limiting computational time, the material was mostly divided into mortar and coarse aggregates larger than 4 mm [45, 110].

Based on work by Chu *et al.* [18], a 3D DEM using a 3D **Particle Flow Code (PFC)** program, was applied in a preliminary study by Noor and Uomoto [91] in order to simulate the flow of SCC during various standard tests: slump flow test, L-box and V-funnel. PFC was originally developed and applied by engineers, who have worked in the field of geomechanics and processing engineering. The method proposed by Noor and Uomoto was also adopted by Petersson and Hakami [92] and Petersson [91] in order to simulate SCC flow during L-box and slump flow testing, and J-ring and L-box testing, respectively. They found 3D and, depending on the type of problem, 2D simulations to be appropriate.

PFC^{2D} and PFC^{3D}, Particle Flow Code in two and in three dimensions, respectively, are discontinuum codes used in analysis, testing, and research in any field where a description of the interaction of many discrete objects characterised by large-strain and/or fracturing is required.

PFC models the movement and interaction of stressed assemblies of rigid spherical (3D) and circular (2D) particles using DEM. DEM was introduced by Cundall [20] for the analysis of rock-mechanics problems and then applied to soils by Cundall and Strack [22]. A thorough description of the method is given in the two-part paper of Cundall [21] and Hart *et al.* [49] and in the UDEC manual [59]. PFC^{3D} is classified as a discrete element code based on the definition in the review of Cundall and Hart [23] since it allows finite displacements and rotations of discrete bodies, including complete detachment, and recognizes new contacts automatically as the calculation progresses. PFC^{3D} can be viewed as a simplified implementation of the DEM because of the restriction to rigid spherical particles.

In the PFC particle interaction is modelled as a dynamic process with states of equilibrium developing whenever the internal forces balance. The contact forces and displacements of a stressed assembly of particles are found by tracing the movements of the individual particles. Movements result from the propagation through the particle system of disturbances caused by specified wall and particle motion and/or body forces. This is a dynamic process in which the speed of propagation depends on the physical properties of the discrete system [59].

Dynamic behaviour is represented numerically by a timestepping algorithm in which it is assumed that the velocities and accelerations are constant within each timestep [59]. The solution scheme is identical to that used by the explicit finite-difference method for continuum analysis. The DEM is based on the idea that the timestep chosen may be so small that, during a single timestep, disturbances cannot propagate from any particle further than its immediate neighbours. Then, at all times the forces acting on any particle are determined exclusively by its interaction with the particles with which it is in contact. Since the speed at which a disturbance can propagate is a function of the physical properties of the discrete system, the timestep can be chosen to satisfy the above constraint. The use of an explicit, as opposed to an implicit, numerical scheme makes it possible to simulate the nonlinear interaction of a large number of particles without excessive memory requirements or the need for an iterative procedure.

The calculations performed in the PFC alternate between the application of Newton’s second law to the particles and a force-displacement law at the contacts. Newton’s second law is used to determine the motion of each particle arising from the contact and body forces acting upon it, while the force-displacement law is used to update the contact forces arising from the relative motion at each contact. The presence of walls in PFC^{3D} requires only that the force-displacement law account for ball-wall contacts. Newton’s second law is not applied to walls, since the wall motion is specified by the user [59].

The core of the method is the spring and dashpot contact force model shown in Figure 2.22. In the normal direction the spring models the repulsive force, and a dashpot models the inelasticity in the collision. In the tangential direction the spring models the tangential elastic deformation of the contacting surfaces and a dashpot models plastic deformation. The tangential force is limited by the Coulomb friction. This is the limiting friction that can be withstood by the contact before sliding of one particle over the other. The friction is the prime generator of particle spin, which is an important but often unconsidered part of these flows.

In [45] the PFC code was used in order to simulate and predict physical particle blocking in the J-Ring test (Figure 2.23). The modelled particle size distribution was represented by the actual grading curve. In order to speed up computations, a cutoff line, 2 mm between the aggregates and the mortar phase, was considered. Each particle was represented as piece of rock enclosed by a paste layer. A user-defined contact model (based on the Bingham model) was applied to the paste layer of each particle.

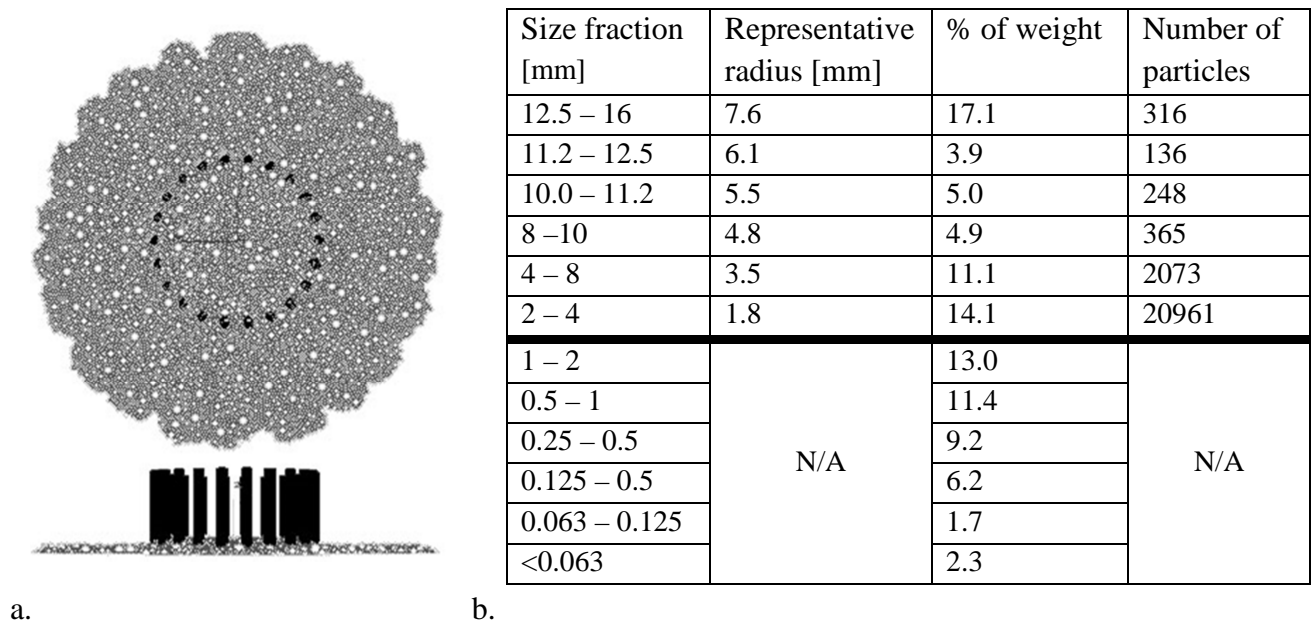


Figure 2.23: Results of numerical simulation (a) and numerical aggregate size distribution (b) for modelling particle blocking in J-Ring test [45]

The numerical results obtained show the good correspondence between laboratory tests and the numerical simulation.

The particle simulation was successfully used for the construction design of mixers [67, 110]. The concrete mix was represented by a multiplicity of particles which are in contact with each other and with the model walls by contact laws. In this way restructuring and mixing processes were studied (Figure 2.24).

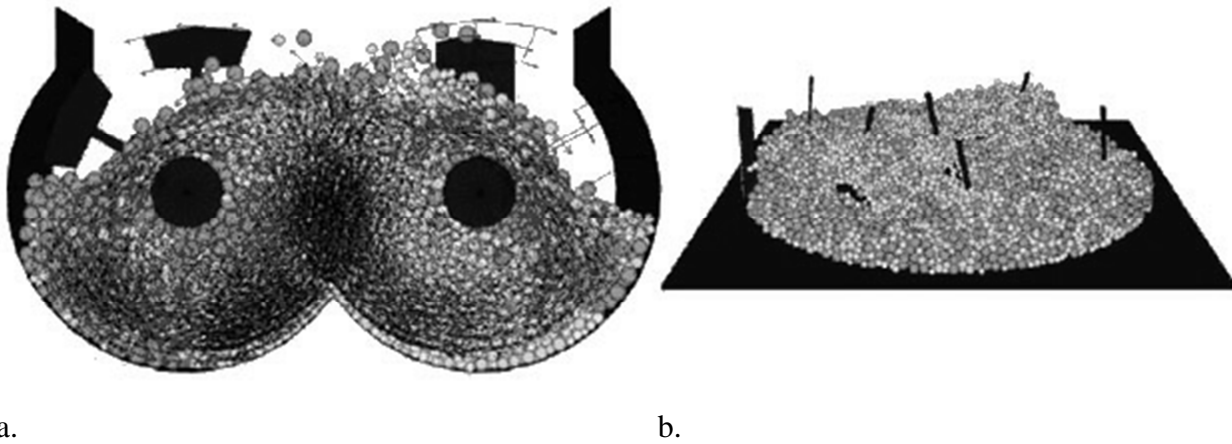


Figure 2.24: Particle model used to simulate mixing processes: a) double shaft batch mixer, b) planetary counter flow mixer [110]

The Particle Flow Code was also used to simulate transportation and form-filling processes. Figure 2.25 shows the PFC-Model of the form-filling process with concrete with the aim of optimizing the casting process.

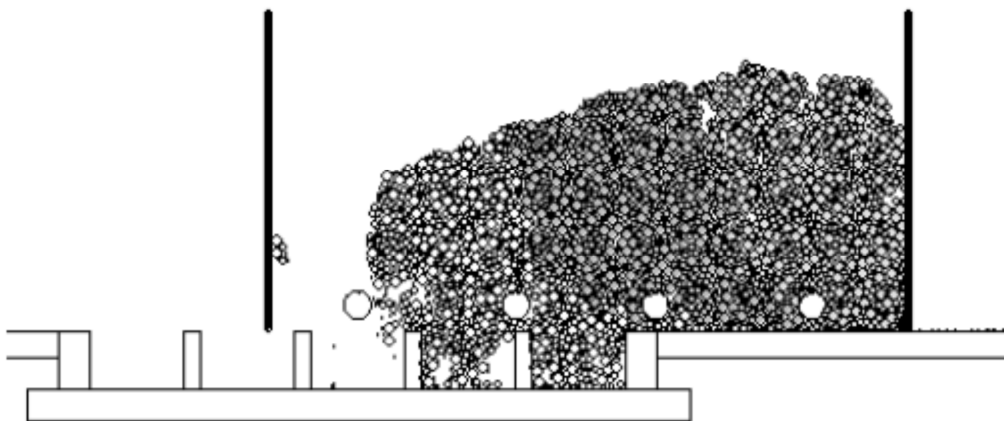


Figure 2.25: Particle model used to simulate a form-filling process [67]

The particle simulation helped visualise the observable movement of mixture and analyse the influence of various parameters; for instance, the geometry of form or particle-related issues, i.e., grading of the particles, their density, stiffness etc.

The PFC allows the user to write his or her own code in the C++ language. The constitutive behaviour of a material is simulated in *PFC* by associating a contact model for each contact. The alternative contact models can be written and implemented using the User-Defined contact Model (UDM) facility.

The **Dissipative Particle Dynamics** method was introduced by Hoogerbrugge & Koelman [52]. The particles within the DPD scheme are ill defined “mesoscopic” quantities of the underlying fluid, which evolve in a way similar to molecular dynamics (MD) particles but with different interparticle forces. DPD particles are assumed to have internal degrees of freedom: the forces between them have both fluctuating and dissipative components in addition to the conservative

forces. However, Newton's third law is still satisfied. Consequently, momentum conservation along with mass conservation produces hydrodynamic behaviour at the macroscopic level [74].

This method is applicable on time and length scales between those typical for molecular modelling and continuum mechanics. These features make DPD an interesting tool in the area of multiphase flows.

The original DPD algorithm used properties of symmetry such as conservation of mass, momentum, and Galilean invariance to construct a set of equations for updating the position of particles, which can be thought of as representing clusters of molecules or "clumps" of fluid and a leap-frog algorithm for updating the positions of the solid inclusions [112].

The mesoscopic particles, which in the context of DPD are called rigid bodies, are not to be confused with particles in suspension. The particles are subjected pair-wise to forces which include soft repulsion, stochastic noise, and dissipation, conceptually similar to viscous drag [105].

Based on work by Koelman and Hoogerbrugge [65], the mesoscopic models have been extended to cover rigid bodies by "freezing" a part of the fluid particles (the fluid phase). In [76] a so-called velocity Verlet algorithm for a DPD-based model describing the motion of rigid body inclusions is proposed. Compared to the Euler algorithm originally used, the velocity Verlet algorithm is claimed to improve significantly the numerical accuracy at little computational cost.

The DPD technique has been successfully applied to SCC technology in [35, 36, 73]. DPD has been used to model the spherical movement and interaction of mono-sized [36] and poly-sized spheres, between 200 and 500 spheres depending on the solid fraction [35]. The viscosity of the suspensions was calculated based on the average stresses for a given strain rate. The relative viscosities were observed to correlate well with measured data. Compared to analytical composite models, DPD should, in combination with knowledge on the forces between the colloidal particles in the matrix, allow modelling of the actual viscosity of the suspension.

In [73] the flow under the influence of gravity between two rebars of mono-sized aggregates of either 1/2 or 1/5 of the free space between the rebars (see Figure 2.26) was described.

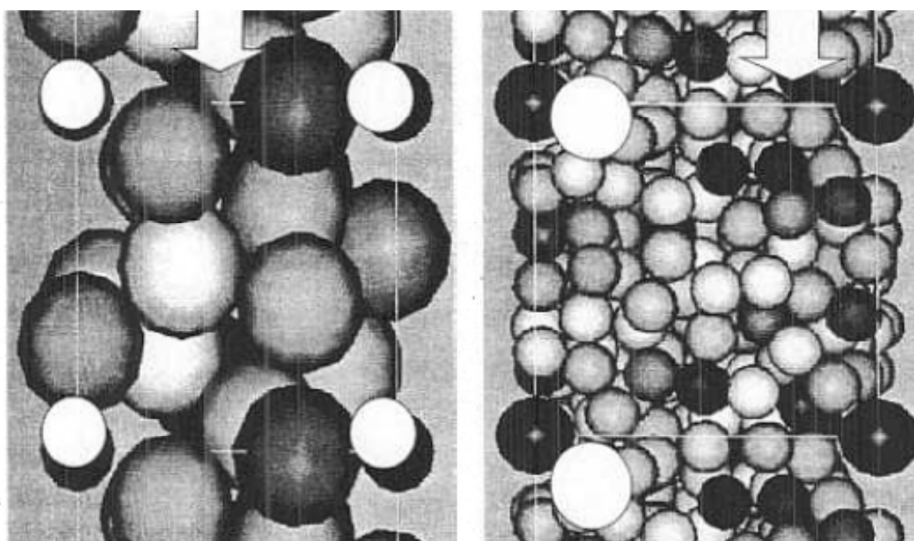


Figure 2.26: *Simulation of flow of aggregates between reinforcement bars by Dissipative Particle Dynamics (DPD) [73]*

Modelling of the flow of monosize spheres between sets of rebars demonstrated a tendency toward the blocking of spheres with diameter 1/2 of the free space, whereas smaller spheres were observed to flow unhindered.

Using the DPD technique in [42] two key aspects of concrete rheology are highlighted: (1) the agglomeration of finer particles and the role of dispersants to counteract this agglomeration and (2) the granular nature of concrete and the role of particle size distributions on the rheological properties of concrete.

The main advantages and disadvantages of the discrete particle flow approaches can be summarised as follows:

Advantages:

- Limiting cases in which the scale of observation is of the same order as the size of coarsest elements can be treated.
- The moving free surface of the flowing material can be modelled in detail.
- The trajectories of selected species in the mixture can be studied.

Disadvantages:

- The DEM parameters have no clear physical meaning when applied to fresh concrete. It is indeed difficult to define direct contact between solid particles assumed to represent the mortar phase and solid particles assumed to represent the coarse grains. Moreover, the parameters of the contact law are impossible to measure and can only be fitted in order to get the best comparison between numerical predictions and experiments. The high computational costs are at present too great to be used for simulations of full-scale casting [105].
- Although the DPD approach is very promising in understanding the correlation between the rheological behaviour of the material and its mix proportioning, the number of particles that can be dealt with prevent the use of this technique when prediction of real casting is the objective [105].

2.5.3 Simulation of suspension flow

In this method concrete is assumed to consist of particles suspended in a fluid matrix. The most popular methods for simulation of suspension flow are **Visco-plastic Suspension Element Method (VSEM)** and **Finite Element Method with Lagrangian Integration Point (FEM-LIP)**.

Visco-plastic Suspension Element Method is the first numerical analysis method using a discontinuous-body model for the flow analysis of concrete [121]. It adopts the two-phase model and is based on the extremely bold simplification that fresh concrete is a three-dimensional truss structure with node points of spherical coarse aggregates, as shown in Figure 2.27.

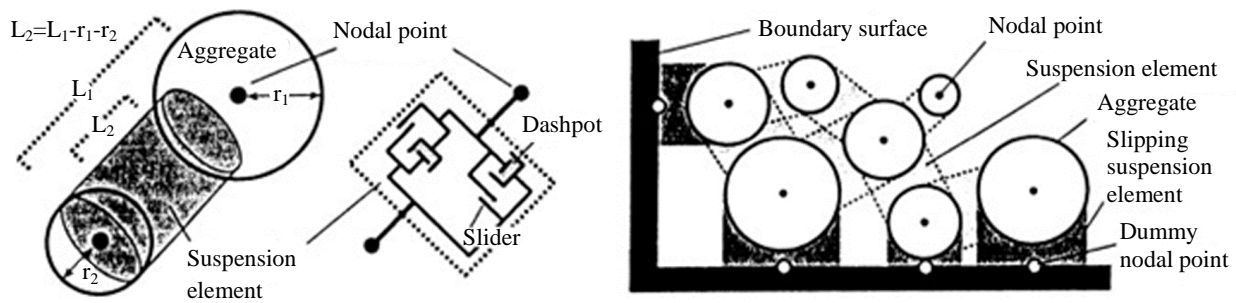


Figure 2.27: Nodes (aggregate) and elements (matrix mortar or cement paste) of suspension element method [63]

The calculation process of dynamic VSEM is similar to that of the DEM described earlier [63]. However, the dynamic VSEM and the DEM have opposite concepts of node and element, and the visco-deformation elements in the dynamic VSEM have dimensions. Moreover, the DEM is used mainly to predict the failure or yield behaviour of fresh concrete, whereas the principal object of the VSEM is to simulate the behaviour of flows after yielding.

The VSEM can be applied to three-dimensional flow analysis, and due to the simplicity of boundary conditions, it has already been used to simulate many flow phenomena of fresh concrete [63, 82]. However, because it requires huge computing capacity, the VSEM is now only used for flow analyses on relatively small scales.

Mori and Tanigawa [81] used VSEM to simulate the flow of concrete in various tests. The concrete was divided into mortar and coarse aggregates, and the aggregates were approximated as monosize spheres. The rheological properties of the concrete (suspension) were numerically predicted from the rheological properties of the matrix and the coarse aggregate volume fraction. The motion of stiff spheres in a viscoplastic body was simulated by introducing viscoplastic interactions between pairs of particles which are closer than a given distance. Kurokawa *et al.* [70] simulated in 2D, measured, and compared flow in L-box and slump flow testing for concretes with yield stresses between 50 and 300 Pa. They found that the numerical approach, in general, overestimated the initial rate and underestimated the final flow. Mori and Tanigawa tested concretes with minimum yield stress of 100 Pa and claimed the method applicable for the simulation of complex behaviour of concrete such as mixing, collapse, and separation during compacting [81, 105].

The **Finite Element Method with Lagrangian Integration Point** was developed recently, based on the Material Point Method originally developed by Sulsky and Schreyer [117] and belonging to the broad family of Particle-In-Cell methods, Moresi *et al.* [80].

This method is based on an Eulerian finite element mesh with Lagrangian particles carrying material properties and time variables. Thus, large deformation limits have been abolished, and history variables can be carried through the mesh. The implicit description of material interfaces gives the possibility to model fluid-solid interactions by assigning special rheological properties to particles in space.

Particles (or Tracers in FEMLIP) carry material properties and time variables, as shown in Figure 2.28. At the same time, tracers may carry different material properties depending on their initial location in the finite element grid, and heterogeneous structures can easily be handled [80].

2 Literature review

Unknowns, i.e., velocity fields, are computed at the mesh nodes, and the Lagrangian particles carry history variables, including material properties, during the large deformation process. From the material properties point of view, unlike in a pure Eulerian method, material interfaces are not subject to convection during computations since fictitious lines representing interfaces are preserved during flow between two adjacent particles with different properties. From a computational point of view, interfaces are taken into account in one finite element for which rheological properties are averaged for integration. The consequence is that the modelling of heterogeneous material needs very fine meshes with the FEM-LIP, as is for any numerical method based on integration over volumes [30].

In contrast to Gaussian points in classical FEM, shape functions need to be recalculated for each particle configuration as their positions change over time within the elements. At the end of each step, tracer positions are updated. Tracer velocities are computed from the nodal velocity field. Tracer displacements are computed according to a timestep chosen because a tracer cannot cross one element within one timestep (Figure 2.28c).

All time-dependent properties stored on particles move with the particles and must be rotated if they are tensor variables, e.g., an elastic stress tensor [29]. At the end of the computational step the grid contains no information at all; it is a pure computational grid. And one can choose a totally different mesh for the new particle configuration. The grid is usually kept fixed except in the case of moving boundary conditions.

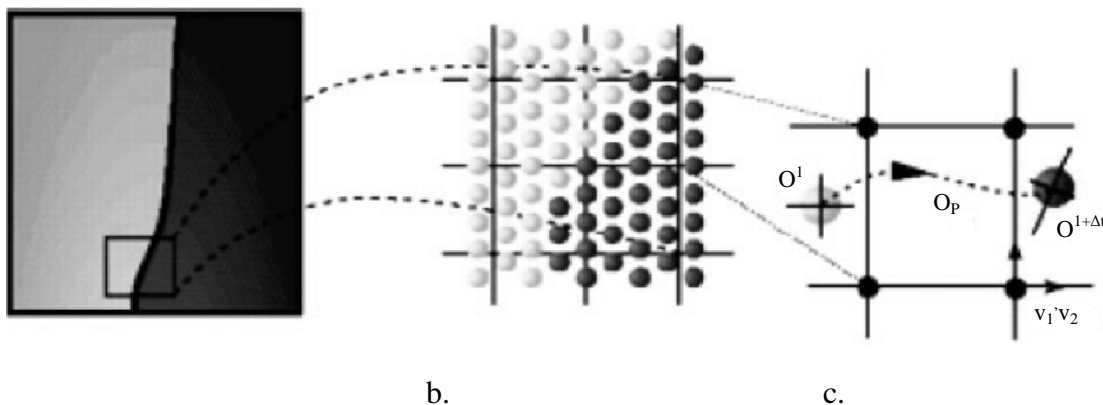


Figure 2.28: Schematic representation of a) FEM-LIP interfaces are set by applying different behaviour to material in space; b) a set of Lagrangian particles is used as integration points and to track material properties; c) particles are moved according to nodal velocities and history dependant variables are stored on particles [30]

The capacity of FEM-LIP to simulate very large deformation processes with interfaces and free surfaces has been demonstrated for a wide range of material properties in several types of applications, including concrete flow within and into forms. In [29] concrete flow, either with a homogeneous or a heterogeneous approach within the classical continuum framework, was modelled. In the first approach, information about material microstructure is clearly missing, e.g., material locking between bars cannot be modelled, whereas the second approach is very demanding of computer resources and cannot be used for large scale applications.

This method was applied by Dufour and Pijaudier-Cabot [30] on two different types of concrete, self-compacting and ordinary concrete. They calibrated the two Bingham parameters based on experimental results from a simple slump test with flow time measurement.

When modelling concrete as a heterogeneous material made of mortar and aggregate (see Figure 2.29 (right)), the scale should be smaller than the form scale since aggregates must be made discrete into several finite elements in order to be modelled properly as rigid when compared to mortar.

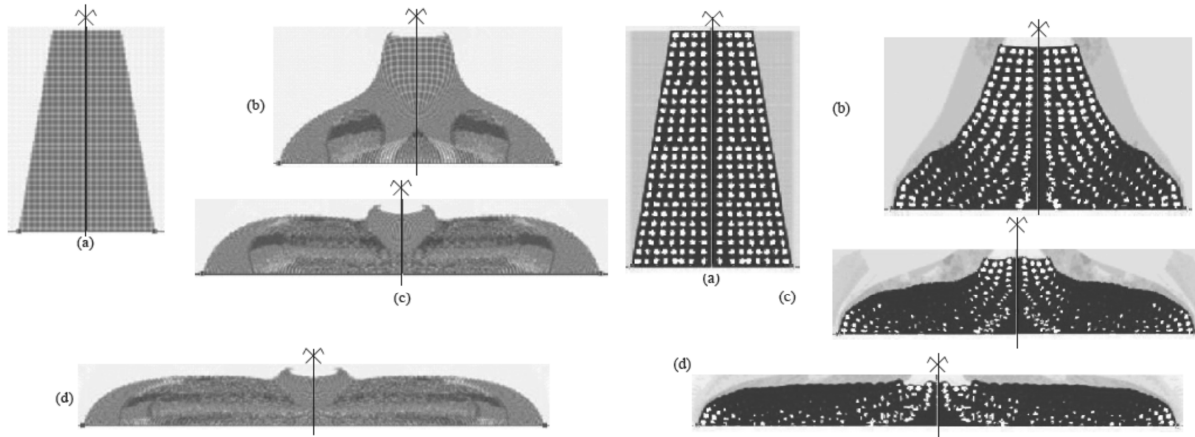


Figure 2.29: Numerical simulation of the slump flow test by using a homogeneous approach (left) and a heterogeneous approach (right) [29]

The main advantages and disadvantages of the suspension flow approaches can be summarised as follows:

Advantages:

- These methods capture the real nature of the material.
- The computational time remains reasonable.
- Any rheological law (Newton, Bingham, Herschel-Bulkley, etc.) can be used for the matrix.
- The VSEM can consider the effect of aggregates, segregation, and more complex behaviours of concrete such as collapse, separation and mixing, but in such cases long computation times and high memory capacity are necessary.
- Anisotropic viscous model may even be used to represent concrete flow reinforced with fibres [105].

Disadvantages:

- In FEMLIP the entire space which is occupied by the material and where the material is assumed to move must be made discrete. It makes a larger demand on memory and computational time for taking particles into account which have no effect on the flow. However, the Levelset method could be used to define explicitly the interface between the material of interest and air, which need not be modelled anymore. The integration domain could be reduced to one side of the levelset, e.g., the half-space of positive isovalues, even when the levelset runs through a finite element, as it does in crack propagation problems. Thus, it will efficiently reduce the computational cost in time and memory. The key point of such an approach is to define the velocity field along the levelset in order to propagate the interface properly [105].

2.5.4 Comparison and discussion of numerical methods

In future, computational modelling of concrete flow could be used for simulation of, for example, total form filling and detailed flow behaviour such as particle migration and formation of granular arches between reinforcement (“blocking”). But computational modelling of flow could also be a potential tool for understanding the rheological behaviour of concrete as a function of its mix proportioning.

The computational modelling techniques found in the literature may be divided into three main families: single fluid simulations, numerical modelling of discrete particle flow and numerical techniques allowing the modelling of particles suspended in a fluid.

Table 2.7 summarises the efficiency of these techniques as a function of the targeted application. The commercial codes listed in Table 2.7 are the ones that can be found in the literature. Other methods unknown to the author may be equally or even more efficient. The physical meaning column expresses the fact that the input parameters can be easily measured and that no fitting of these parameters is needed in order to obtain a result that can be compared to experimental results.

Table 2.7: *Applicability of the available numerical methods in the cementitious materials field [105]*

Method	Single fluid simulation	Distinct Element Method	Suspension simulation
Simulation of testing	Yes (except blocking)	Yes	Yes
Full-scale simulation of casting	Yes	No (too many particles)	No (too many particles)
Blocking prediction	No	Yes	Yes
Segregation under flow	No	Yes	Yes
Thixotropy	Yes	No	Yes
Physical meaning	Adequate	Poor	Adequate
Commercial code	FLOW3D © FIDAP ©	PFC3D ©	No

It must be noted here that this field is still a very “young” research area, the first paper dating from 1994. However, it can be expected that in the coming years computational modelling could become the tool which will bring rheology from research and development into the field of practical applications [105].

DEM was selected by the authors to reproduce qualitative behaviour in fresh concrete. This approach uses simple basic elements – spheres and walls, which makes the computation relatively simple and fast. The great advantage of DEM is that it provides an opportunity to display the movement of the concrete mixture as a whole as well as its individual components discretely.

The concrete mixture is formed by a large number of particles connected among each other and to the model walls in accordance with laws of the defined contact behaviour. Thus, concrete

technology's relevant processes and phenomena, such as mixing, compacting, de-airing, sedimentation, fibre distribution, orientation, etc. could be analysed and taken into account in solving various problems.

2.6 Summary

Rheology is the science of the **deformation** and **flow of matter**, and the emphasis on flow means that it is concerned with relationship between stress, strain, rate of strain, and time. Flow is concerned with the relative movements of adjacent elements of fluid and has two basic types, shear and extensional flow. In shear flows fluid elements flow over or past each other, while in extensional flows, elements flow toward or away from each other. In the case of **cementitious composites**, shear flow is of primary interest. In a **shear flow**, imaginary parallel layers of fluid move in response to a shear stress to produce a velocity gradient. This velocity gradient is referred to as the shear rate, equivalent to the rate of increase in shear strain.

Concrete is defined as a composite material, and in rheological terms it can be regarded as a **concentrated suspension** of solid particles, or aggregates, in a viscous fluid, i.e., cement paste.

On a macroscopic scale, concrete flows as a fluid. Interactions among the finest particles in the mixture may lead to a network structure of the finest particles in the suspension, i.e., like a gel or a colloidal glass, which generates a macroscopic thixotropic behaviour [104].

The rheology of **fresh concrete** is very complex due to its composition and the accompanying chemical changes. Various researchers have already described fresh concrete as a **complex non-Newtonian fluid** that has a yield stress and a viscosity dependent on the shear rate, seeing that both change with time. As the concrete hardens yield stress and viscosity increase.

Most researchers agree that the flow of concrete can be described reasonably well using a **Bingham model**. Therefore, it has been meaningful to use the Bingham rheological model as a basic rheological model in recent investigations. The equation of this rheological model is a linear function of the shear stress, the concrete response, versus shear rate once a threshold is overcome. Two parameters characterise the Bingham equation, namely the yield stress and the plastic viscosity. The **yield stress** is the above mentioned threshold which has to be overcome to initiate the flow. The yield stress correlates reasonably well with the slump value, but the plastic viscosity cannot be measured accurately using the slump test. **Plastic viscosity** governs concrete flow behaviour after flow has started, i.e., after the yield stress is overcome. The existence of plastic viscosity helps explain why concretes with the same slump may behave differently during placement.

The main property of the fresh concrete is its **workability**. In the concrete industry, workability is defined as “the ease and homogeneity for which the concrete or mortar can be placed, consolidated and finished”. Ideally, concrete workability should be characterised by its **rheological properties** – yield stress and plastic viscosity.

Since the early 20th century, the concrete industry has recognized the need to **monitor** concrete **workability** to ensure that concrete can be properly placed and can achieve adequate strength in hardened state. Unfortunately, the technology used to measure the properties of fresh concrete has not changed significantly. Hundreds of test procedures for determining workability have been

developed for research, mix proportioning, and field use. The vast majority of these test methods have never found any use beyond one or two initial studies, with the exception of the widely used tests such as the slump test or flow-table test. Even with the increase in knowledge of concrete rheology, the slump test remains the predominately used test method for measuring concrete workability. Hence, the **slump test** is chosen as a reference test for numerical modelling. An analytical solution for slump test is required in order to characterise the flow of the fresh concrete during experiments taking into account the concrete's rheological properties – yield stress and plastic viscosity.

There are various parameters which strongly influence the rheological properties of fresh concrete. In order to describe the effects of the individual constituents of concrete, one can plot the relation between yield stress τ_0 and plastic viscosity μ . Water, air entrainment agent, superplasticizer, and silica fume have significantly different influences on the flow behaviour of fresh concrete.

Computational modelling of flow is a powerful tool for understanding the rheological behaviour of concrete. Few **methods of numerical flow analysis** have been proposed for fresh concrete. They can be classified into two types according to the analytical models used — **continuous** body models and **discontinuous** body models. The continuous body assumption facilitates the calculation procedure, but the evaluation and modelling of material properties becomes complicated, and the boundary conditions are difficult to set up in large deformation analysis. Many phenomena during fresh concrete flows, e.g., passing through reinforced steel bars, segregation, and blockage, are associated with the non-homogeneity of concrete. The discontinuous body approach helps to visualise and characterise these phenomena.

Fresh concrete is a **suspension** of particles in a matrix. Depending on the purpose of the simulation and behaviour of the concrete, the scales vary at which the solid components of the concrete such as cement, fine and coarse aggregates, fibres or other binders are considered as particles or belonging to the matrix. Since the relevant **length scales** in suspensions differ by several orders of magnitude, it is not possible to simulate them by including details at all these length scales. All numerical methods are based on one particular length scale selected.

The **Distinct Element Method** has recently been introduced into the flow analysis of fresh concrete as a numerical method using a discontinuous body model. This method is based on motion equations of rigid elements and the transmission of forces between the rigid elements. When the DEM is applied to the flow analysis, to express viscous resistance and inter-frictional resistance of concrete, at first dashpots, springs and St.-Venant elements must be set up between the rigid elements; simulating coarse particles in fresh concrete. However, the dashpot and the spring have no dimension, and at present there is the significant problem that the input data in use are imaginary values which are not directly related to the measured rheological constants – yield value and plastic viscosity – of the matrix mortar.

The problem with input data can be solved using the analytical approach adopted for the reference slump test and a user-defined contact model, which corresponded to the Bingham rheological model. A corresponding **user-defined contact model** can be potentially developed on the basis of experimental investigation of the interaction between discrete particles with some viscoelastic material between them. In any case, set of the experiments on the macro-level for verification of the results of numerical modelling is required.

CHAPTER 3

EXPERIMENTAL INVESTIGATION OF FRESH CONCRETE RHEOLOGY (MACROLEVEL)

3.1 Introduction

The experimental research into the rheology of fresh concrete is carried out on two levels of consideration: the macro- and meso-levels. The rheological behaviour of fresh concrete is considered to be a macrolevel investigation, while interaction between neighbouring entities is considered to be on the mesolevel.

This chapter treats the macrolevel. The slump flow test is used as a reference flow test for the relevant modelling. Parameters such as composition of the concrete and grading of the aggregates are input values for the modelling. In addition an analytical solution for the slump flow test, which allows estimation of the Bingham rheological parameters, yield stress and plastic viscosity, is presented.

Still further, this analytical solution is implemented later in the modelling process for calculating the yield stress in the slump flow test modelling. The slump test output data, such as final spreading and slump, shape of the sample after the slump test, flow rate, and velocity profiles are used in verifying the results of modelling, see Chapter 5. The L-Box test is also used for verification of the results of modelling as an additional test.

3.2 Materials, methods and test results

The experimental investigation at the macrolevel has been performed with reference to simple test methods for fresh concrete, i.e., the slump and slump flow tests as well as the L-Box test. The following concrete types were chosen for experimental investigation: ordinary concrete (OC), self-compacting light-weight concrete (SCLC), high-strength concrete (UHPC), and normal-weight self-compacting concrete (SCC). These concretes, quite naturally, have different rheological behaviour.

3.2.1 Composition of the concretes

Four mixes, all with different water-to-cement ratios, were prepared in order to obtain ordinary concretes with different yield stress values. OC1 is the reference mix. Mixes OC2 and OC3 differ from reference mix by the amount of water only. It should be noted that mixes OC2 and OC4 have same w/c; however, mix OC4 contains some amount of superplasticizer (Naphthalinsulfonat). The respective compositions of the ordinary concretes are presented in Table 3.1.

3 Experimental investigation of fresh concrete rheology (Macrolevel)

Table 3.1: Mixture composition of the ordinary concretes

Concrete type	OC1 – Reference	OC2	OC3	OC4
Cement CEM I 32.5R [kg/m ³]	340	340	340	340
Water [kg/m ³]	187	204	221	189
w/c (free water)*	0.55	0.60	0.65	0.61
Quartz sand 0/2 [kg/m ³]	544.1	540.2	536.3	543.6
Gravel 2/8 [kg/m ³]	634.8	630.2	625.7	634.2
Gravel 8/16 [kg/m ³]	634.8	630.2	625.7	634.2
Superplasticizer FMBV-30 [kg/m ³]	-	-	-	1.77*

* w/c includes water from superplasticizer (the solid content of SP was 35%).

The compositions of the investigated flowable concretes are presented in Table 3.2.

Table 3.2: Mixture composition of the flowable concretes

	SCC	UHPC1	UHPC2	SCLC
Cement CEM I 42.5R HS-NA Holcim [kg/m ³]	-	853.4	666.4	-
Cement CEM II 32.5 [kg/m ³]	350.47 (A-F 32.5R Schwenk)	-	-	315.3 (A-LL 32.5 Heidelberg)
Silica fume [kg/m ³]	-	138.5	181.4	-
Fly-ash [kg/m ³]	273.48	-	-	214.8
Water [kg/m ³]	160.18	170.3	162	159.0
Stabilizer [kg/m ³]	-	-	-	0.47
w/c (free water)*	0.46	0.22	0.27	0.51
Quartz powder [kg/m ³]	-	212.3	467.5	-
Quartz sand 0.125/0.5 [kg/m ³]	-	1000.1	362.9	-
Quartz sand 0/2 [kg/m ³]	689.0	-	-	618.8
Gravel 2/8 [kg/m ³]	419.36	-	-	-
Gravel 8/16 [kg/m ³]	419.36	-	-	-
Expanded clay 2/10 [kg/m ³]	-	-	-	460.2
Basalt split 2/8 [kg/m ³]	-	-	612.1	-
Superplasticizer PCE [kg/m ³]	3.71 Glenium ACE-30	30.2* Viscocrete 20 gold (Sika)	31.2* Viscocrete 20 gold (Sika)	3.0 Glenium ACE-30

* w/c includes water from superplasticizer (the solid content of SP was 35%).

The mixing procedure began after preparing and weighing of all components of the concrete. A special mixing procedure was used for each type of concrete, see Appendix B.

3.2.2 Slump test

The slump test according to EN 12350 part 2 [33] was used to determine the consistency of ordinary concretes.

To describe the test, before lifting the cone the concrete inside is at equilibrium. On lifting the cone the system is under stress, loses its equilibrium, and evolves toward a new equilibrium without the cone. The deformation process starts at the bottom of sample because the stress level is at a maximum there and continues from bottom to top of the sample. Some representative examples of the deformed samples after the cone lifting are presented in Figure 3.1.

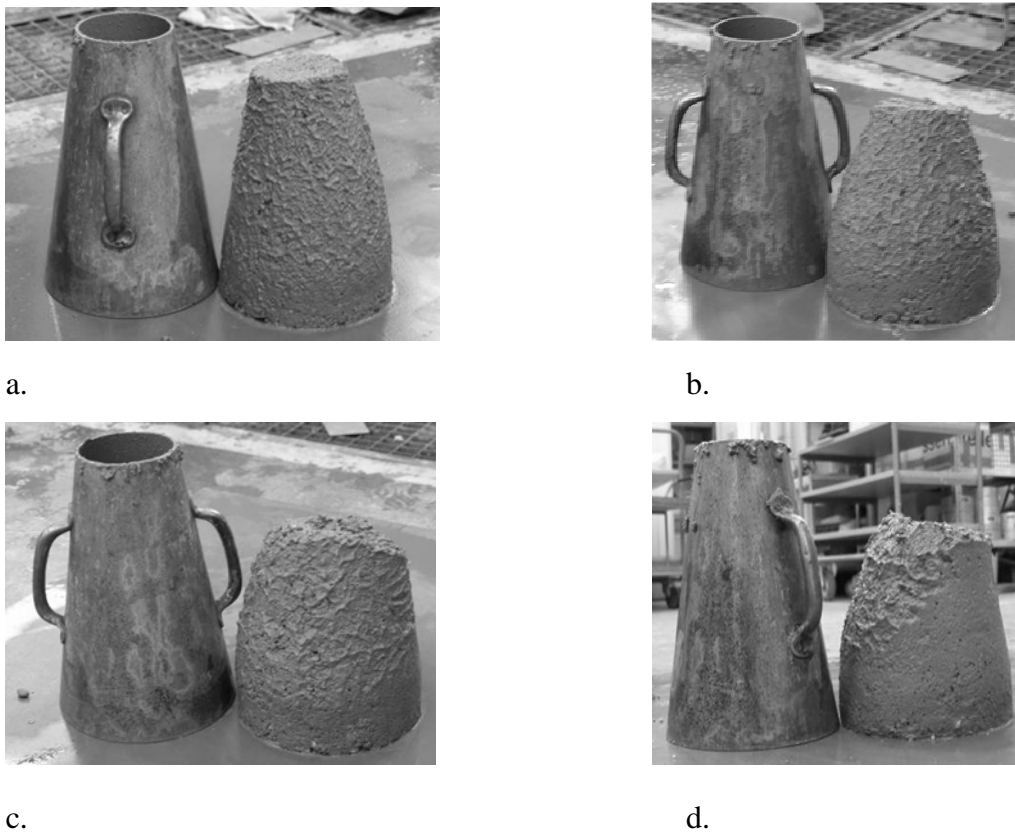


Figure 3.1: Examples of the deformed concrete samples and model of deformation after slump tests for mixes OC1 (a), OC2 (b), OC3 (c) and OC4 (d)

The new state of equilibrium is defined by the new stress distribution and, accordingly, the new geometry (shown schematically in Figures 3.1 and 3.2). The new geometry is characterised by an unyielding region (h_0) and yielding region (h_1). It should be noted that the plane which lies between the yielding and unyielding regions is not always parallel to the bottom surface.

3 Experimental investigation of fresh concrete rheology (Macrolevel)

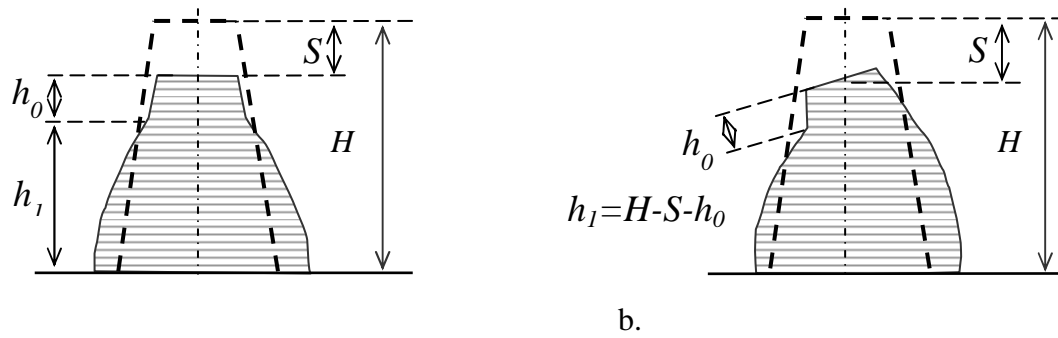


Figure 3.2: Possible geometry of fresh concrete probes after slump test and measured quantities S , h_0 and h_1 : a) without and b) with inclination (shown schematically)

Often the deformed concrete probes exhibit some inclination. In this case the height of unyielding region should be measured on the side surface of the probe and the height of yielding region should be calculated as shown in Figure 3.2.

The experimental values of slump S , h_0 and h_1 are given in Table 3.3.

Table 3.3: Results of the slump test tests

Concrete type	OC1	OC2	OC3	OC4
w/c (free water)	0.55	0.60	0.65	0.61
Slump S , mm	45	75	90	100
h_0 , mm	130	90	80	70
h_1 , mm	125	135	130	130

The results of the slump test show that increasing w/c significantly influenced the rheological behaviour of fresh ordinary concrete: ordinary concretes with higher w/c have higher slump S and smaller height of the unyielding region h_0 .

3.2.3 Slump flow test

The slump flow enables the assessment of the flowability and the flow rate of SCC in the absence of obstructions. It is based on the slump test described in EN 12350 part 2 (ASTM C143/C143M) [33, 4]. The result is an indication of the SCC's filling ability, which is proportional to the yield stress of the fresh concrete. The flowing time of concrete until 50 cm spread is reached (time T_{50}) is a measure of the speed of flow and, hence, the viscosity of the SCC.

A computer-controlled table with photovoltaic sensors was developed and assembled at the Institute of Construction Materials of the TU Dresden in order to investigate the process of spreading of the fresh concrete. It should be noted that for correct work of the photovoltaic sensors a well lit room is required. Sensors were located at the table in four radial directions. The distance between opposite lines is 200 mm (equal to the bottom radius of slump cone [33, 4]). The length of each line was 400 mm (80 sensors with 5 mm distance between neighbouring sensors). The material of the top surface of the computer-controlled table was transparent Plexiglas. The computer-controlled table developed allows for measuring the spread from 200 to 1000 mm. The information, such as the position of the sensors and time of sensor triggering, was transmitted to the personal computer.

Figure 3.3 shows the photo of the measuring apparatus and typical results of measurements for a SCC. The different markers in the diagram represent the different directions on the table.

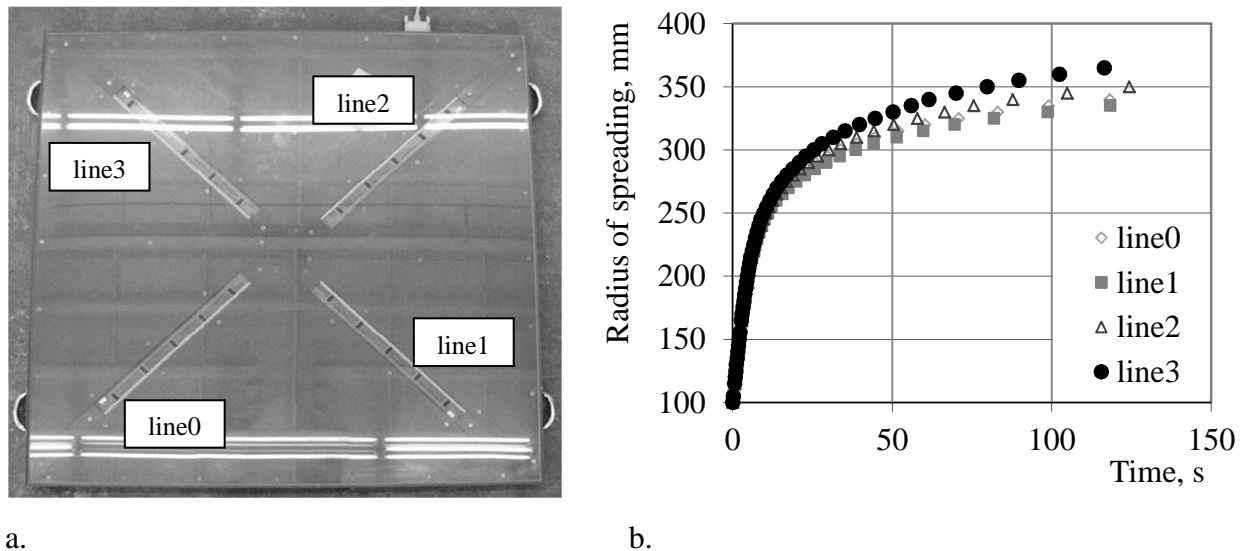


Figure 3.3: Measuring apparatus for slump flow test (a), typical results of measurements (b)

In order to insure the lifting of the cone at a controlled velocity, an electro-mechanical lifting device was used, which allows lifting of the cone with a specified constant velocity up to a specified height. With this device the maximal velocity of lifting is limited to 500 mm/min. The maximal height of the lifting was not more than 300 mm, the height of the Abram's cone [4].

The height of slump cone lifting plays a significant role in the slump flow test. First of all, the slump cone should not obstruct the concrete flow: the height of the cone lifting should be higher than the height of the flowing concrete. The height of the concrete flow depends on the yield stress and viscosity of the fresh concrete. For the fresh concretes investigated the height of concrete flow is not greater than 50 mm. If the cone is quickly lifted higher than the concrete inside it, then the concrete will have high potential energy, which is transformed into kinetic energy as the concrete starts flowing. The magnitude of the kinetic energy depends on many factors, first of all on density of the fresh concrete and height of the cone's lifting. Further, this "transformed energy" will be passed to the flowing fresh concrete; slump and slump flow can be very sensitive to this effect. Therefore, in order to minimize the influence of the height of the cone lifting on the results of tests, it was assumed that the height of cone lifting should be within an interval between 50 and 75 mm.

Measurement starts when lifting of the slump cone starts. The cone obstructs the concrete flow until it reaches the aforementioned height. Therefore, the cone-lifting velocity can also influence the results of the slump flow test. The maximal velocity of the cone lifting using the electro-mechanical lifting-device is smaller than the lifting of the slump cone by hand. Therefore, in slump tests the maximal lifting velocity 500 mm/min ($8\frac{1}{3}$ mm/s) of the electro-mechanical lifting device was used.

Different practitioners prefer either the normal orientation, i.e., where the bottom radius of the cone, which is in contact with table for measurement, is greater than the top radius, or the inverted orientation, i.e., inside out, of the Abram's cone. Due to the fluid nature of SCC, one must hold the cone down very firmly when it is in the normal orientation to prevent the concrete from leaking out of the bottom during filling. This is not the case with the inverted orientation and, therefore, a single person can more easily complete the test. The concern has been raised that the energy acting on the

3 Experimental investigation of fresh concrete rheology (Macrolevel)

SCC as well as the friction between the cone and the concrete will be different for the two orientations. Indeed tests with both orientations of the slump cone were performed in order to evaluate this issue.

The state of the surface of the table for measurements has a pronounced influence on the results. The surface can be either dry or wetted. Wetted surface means that directly before tests the table was wiped using damp cloth. Tests with a wet surface with inverted orientation of the cone were performed in order to estimate the influence of wetting the surface on the results.

The results of measurements for normal orientation of the slump cone are presented in Figure 3.4. The surface of the table was dry.

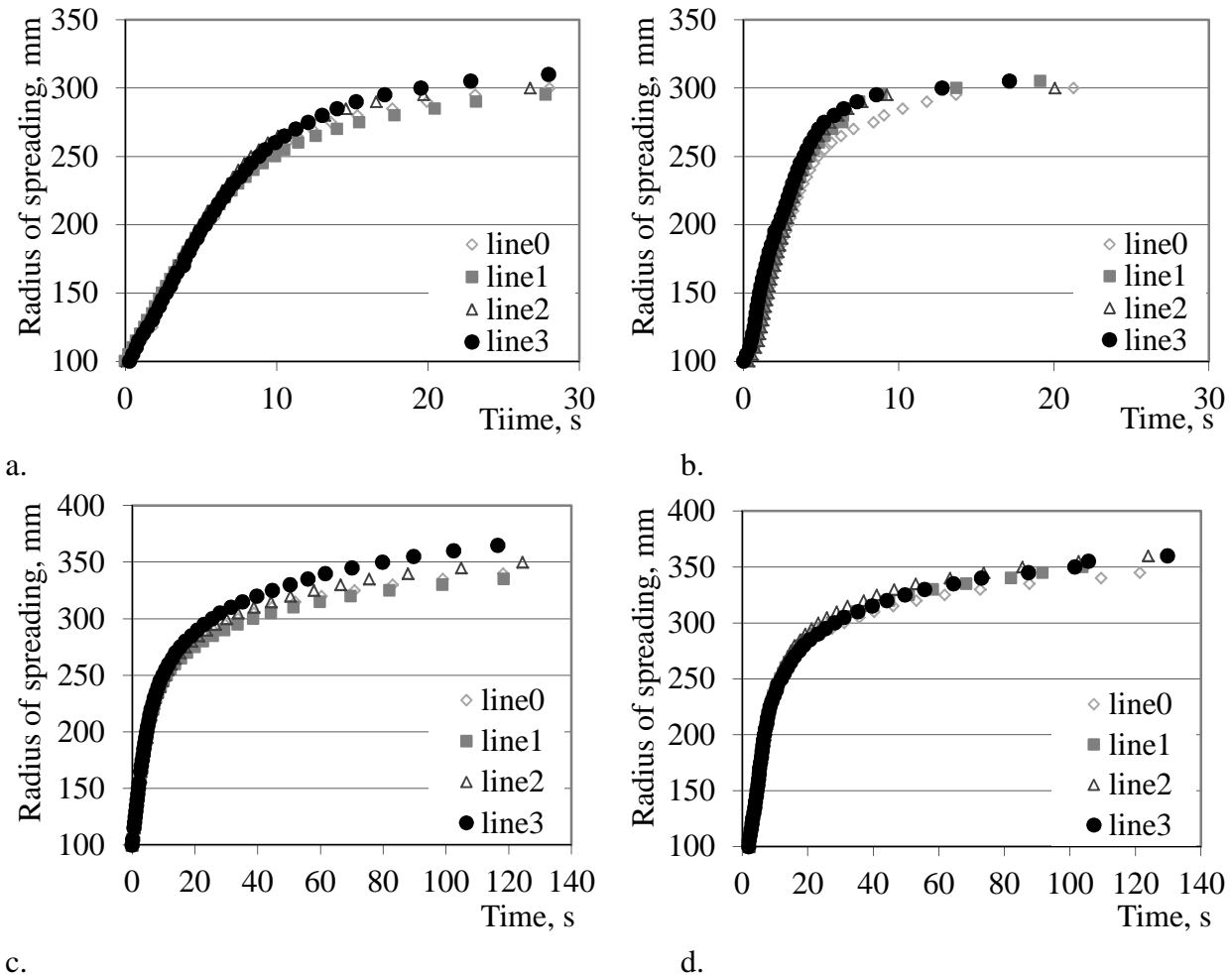


Figure 3.4: Slump flow test results with a) SCC, b) SCLC, c) UHPC1 and d) UHPC2

The results of the tests using the inverted cone orientation with wet and dry surface of the slump flow table are presented in Appendix C. The results of all slump flow tests are summarized in Table 3.4.

Table 3.4: Summarized results of the slump flow tests

Slump cone orientation / condition of the surface	SCC (2.361 kg/dm ³)		UHPC1 (2.353 kg/dm ³)		UHPC2 (2.495 kg/dm ³)		SCLC (1.758 kg/m ³)	
	Slump flow, mm	T_{50} , s	Slump flow, mm	T_{50} , s	Slump flow, mm	T_{50} , s	Slump flow, mm	T_{50} , s
Normal/dry	610	10	722	10.5	715	9.5	605	4
Inverted/dry	615	16	715	15	722	11	690	7.5
Inverted/wet	720	10.5	805	10.5	790	9	870	5

The discussion of the influence of the tests setup on the results of measurements is presented further in Section 3.4 after analysis using the analytical approach; see Section 3.3.

3.2.4 L-Box test

The L-box test is used to assess the passing ability of SCC through tight openings, including spaces between reinforcing bars and other obstructions, without segregation or blocking [32]. The principle of the L-Box test is presented in Section 2.4.2.2.

Pictures of the L-box test for SCC, UHPC1 and SCLC are presented in Figure 3.5. The results of all L-Box tests are summarized in Table 3.5.

Table 3.5: Summarized results of the L-Box tests

Type of concrete	h_1 , mm	h_2 , mm	h_2/h_1	T_{200} , s	T_{400} , s
SCC	90	66	0.74	3	7
UHPC1	85	81	0.95	3	8
SCLC	80	50	0.625	8	16

It may be supposed that the concrete with a worse passing ability, i.e., a lower volume of the fresh concrete passes from the vertical to the horizontal part of the L-box through the gaps, can point to a higher yield stress.

These results of the L-Box test will be used for verification of the results of modelling.

3 Experimental investigation of fresh concrete rheology (Macrolevel)



Figure 3.5: Images from L-box tests with a) SCC, b) UHPC1 and c) SCLC

3.3 Analytical approach for evaluation of results of a slump flow test

The slump test is well established as a method for quality control of fresh concrete. It has been made clear that the slump and slump flow values of fresh concrete increase with decreasing of the yield stress value and that the yield stress value can be estimated approximately from the slump value. On the other hand, the plastic viscosity of fresh concrete, the other constant of Bingham's model, is a parameter related to flow velocity and is, accordingly, rather more difficult in its estimation from the slump value [40].

Analysis of the slump test starts from the internal stress distribution of the material inside of the slump cone before lifting the cone. The variation of the stress along the height is of particular interest from the bottom surface, where the stress is at a maximum, to the top, free surface, where it is zero. So, it could be supposed that the internal stress is equal to the yield stress of the material at some height. The material lower then this height must be deformed in order to reduce the internal stress to the magnitude of yield stress after cone lifting. The material higher than this height must remain without any deformation because the internal stresses are smaller than the yield stress. Thus, the maximum internal stress at the end of the test will be equal or smaller than the yield stress of the material.

The analytical modelling of the slump test is a very important part of the whole approach. The analysis of the internal stresses in numerical modelling is based on the theoretical basis of the analytical approach for the slump test. The analytical approach should eventually provide a link between dimensionless analyses of the slump test and parameters of the numerical model, such as contact bond and the yield stress parameter; this is treated in more detail in Chapter 5.

Therefore, the formulations from analytical approach will be implemented into the program code for analysing the internal stress distribution and calculating the parameters of numerical model according to a specified yield stress value.

3.3.1 Estimation of the yield stress value

The slump test has the obvious advantage of its simplicity, its main drawback being the need for an empirical or semi-empirical calibration curve to convert the observed height change in the sample to a yield stress value. From published experimental works on the slump test [90, 108] it is not clear that there is a single, well defined calibration curve that is valid for a wide range of yield stresses. For the calibration curve based on an *ad hoc* model of the slump test, Pashias *et al.* [90] obtained an algebraic expression which, they concluded, was adequate for the range of materials investigated. Schowalter and Christensen [108] analysed the slump test for truncated cone samples. As with Pashias *et al.* [91], their results also indicate that it is necessary to adopt a more systematic approach to the modelling of the slump test.

The slump models are not empirical and provide a material-independent, unique relationship between yield stress and slump height. The first analysis was made by Murata [83], followed by Christensen [17], who corrected a simple integration error made by Murata. Rajani and Morgenstern [95] and Schowalter and Christensen [108] have investigated the conical test still further.

3.3.1.1 Analysis of deformation due to dead weight for ordinary concretes

The only stress acting on the material is assumed to be a vertical stress associated with the material's own weight. Therefore, the pressure in the material at some height below the top surface can be expressed as the weight of material above position z .

Using the assumption of the original Murata model [83], the vertical stress p_z acting on any horizontal layer at the distance z in a slump cone is Eq. 3.1:

$$p_z = \frac{W_z}{\pi \cdot r_z^2} \quad (3.1)$$

where W_z is the weight of the material from height z to the top of the slump cone; r_z is the radius of the cone at height z .

The weight W_z has been calculated as product of the sample density, volume, and the acceleration due to gravity; see Eq. 3.2:

$$W_z = \rho \cdot g \cdot V_z \quad (3.2)$$

where ρ is the unit mass of the concrete; g is the acceleration due to gravity; V_z is the total volume of the cone at any position of cross section to the top.

The volume V_z has been calculated using Eq. 3.3:

$$V_z = \frac{1}{3} \pi \cdot (H - z) \cdot \left[\frac{r_z^3 - r_t^3}{r_z - r_t} \right] \quad (3.3)$$

where r_z is the radius of the cone at height z ; r_t is the top radius of the cone; H is the total height of the cone.

3 Experimental investigation of fresh concrete rheology (Macrolevel)

Combining Eqs. 3.1, 3.2 and 3.3 gives Eq. 3.4:

$$p_z = \frac{\rho \cdot g}{3} \cdot \frac{(H-z)}{r_z^2} \cdot \left[\frac{r_z^3 - r_t^3}{r_z - r_t} \right] \quad (3.4)$$

This can be reduced as follows; see Eq.3.5:

$$p_z = \frac{\rho \cdot g}{3} \cdot \frac{(H-z)}{r_z^2} \cdot (r_z^2 + r_z \cdot r_t + r_t^2) \quad (3.5)$$

Assuming the Tresca criterion, the maximum shear stress acting on a plane is equal to half the applied pressure see Eq. 3.6:

$$\tau_z = \frac{1}{k} \cdot \frac{p_z}{2} \quad (3.6)$$

where k is a coefficient related to inertia; it is reasonable to assume $k=1$ since the slump cone is deformed only slowly.

Thus, the maximum shear stress can be expressed as in Eq. 3.7:

$$\tau_z = \frac{\rho \cdot g}{6} \cdot \frac{(H-z)}{r_z^2} \cdot (r_z^2 + r_z \cdot r_t + r_t^2) \quad (3.7)$$

Dimensionless shear stress is the normalized shear stress by height of the slump cone and material density (see Eq. 3.8):

$$\tau_z = \frac{\tau_z}{\rho \cdot g \cdot H} = \frac{1}{6 \cdot H} \cdot \frac{(H-z)}{r_z^2} \cdot (r_z^2 + r_z \cdot r_t + r_t^2) \quad (3.8)$$

The schematic diagram for the cone slump tests are presented in Figure 3.6. The figure displays the important variables and the stress distributions prior to lifting of the cone. The stress is at its maximum at the bottom of the cone due to the weight of sample; the stress value is zero at the top of the sample.

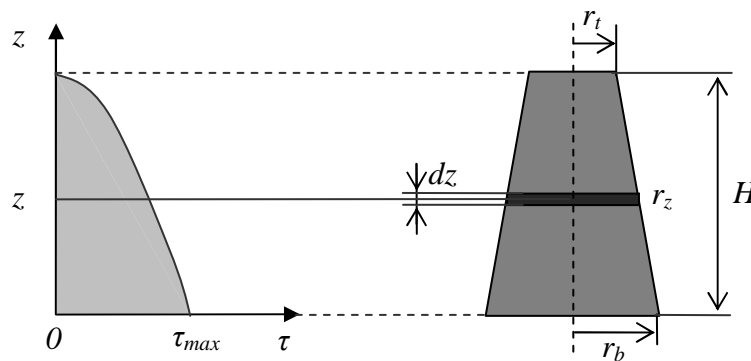


Figure 3.6: The stress distribution before slump cone lifting [108]

It is assumed that removal of the slump cone does not deform the material in any way. The initial undeformed material is therefore assumed to be either a perfect truncated cone. Practically speaking, this will only be achieved for perfect slip at the inner surface of the slump cone.

3.3 Analytical approach for evaluation of results of a slump flow test

At some point along the height of the undeformed cylinder, the material experiences a stress that is larger than the yield stress (τ_y) and the material flows (slumps) until the stress is reduced to the yield stress. In the material above the yielding region, the vertical stress does not exceed the yield stress and the region remains unyielding.

In the process of deformation, it is assumed that the interface layer between the yielding and unyielding material is a horizontal surface that moves down as the material beneath it flows. Therefore, the final height consists of an unyielded region (h_0) and a yielded region (h_1). Schematically it is shown in Figure 3.7.

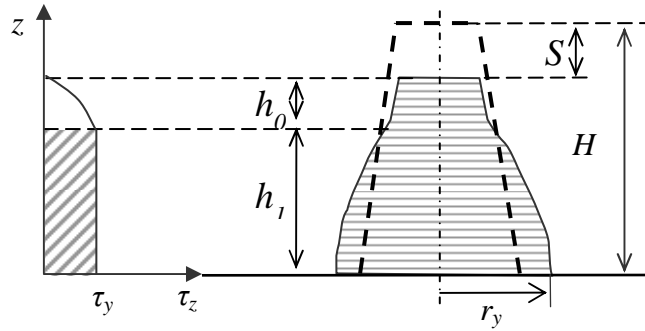


Figure 3.7: The stress distribution and final “Slump” of a material after the cone is lifted [108]

It is assumed that during deformation all horizontal sections remain horizontal, and slumping is due only to radial flow. Therefore, the yielding region (h_1) can be divided into elements of thickness dz and radius r_z , which reduce to thickness dz_1 and radius r_{z1} after slumping.

Assuming the material is incompressible; the volume of layer dz will be the same both before and after the slump cone is lifted (see Figure 3.8). Thus, the volume can be expressed as Eq. 3.9:

$$dz \cdot (\pi \cdot r_z^2) = dz_1 \cdot (\pi \cdot r_{z1}^2) \quad (3.9)$$

where dz and dz_1 are the height of a layer initially at distance z before and after the slump cone is lifted, respectively.



Figure 3.8: Change in layer of thickness dz : a) before and b) after lifting the cone

Eq. 3.9 can be reduced to Eq. 3.10:

$$dz_1 = dz \left(\frac{r_z}{r_{z1}} \right)^2 \quad (3.10)$$

3 Experimental investigation of fresh concrete rheology (Macrolevel)

The deformed section of the slumped material, shown in Figure 3.7, can be expressed as the sum of all elements dz_1 . Mathematically, this produces the integral; see Eq. 3.11:

$$h_1 = \int_0^{H-h_0} dz_1 = \int_0^{H-h_0} \left(\frac{r_z}{r_{z1}} \right)^2 dz \quad (3.11)$$

It is assumed that there is no flow between layers of the material and the material is incompressible. Thus, the cross sectional area of a layer in region h_1 will increase until the applied shear stress is equal to the yield stress.

Eq. 3.9 can then be expressed as follows; see Eqs. 3.12-3.14:

$$\tau_z \cdot (\pi \cdot r_z^2) = \tau_{z1} \cdot (\pi \cdot r_{z1}^2) = \tau_y \cdot (\pi \cdot r_{z1}^2) \quad (3.12)$$

$$\tau_z \cdot (\pi \cdot r_z^2) = \tau_y \cdot (\pi \cdot r_{z1}^2) \quad (3.13)$$

and

$$\frac{r_z^2}{r_{z1}^2} = \frac{\tau_y}{\tau_z} \quad (3.14)$$

Substituting Eq. 3.14 into Eq. 3.11 gives Eq. 3.15.

$$h_1 = \int_0^{H-h_0} dz_1 = \int_0^{H-h_0} \left(\frac{\tau_y}{\tau_z} \right)^2 dz \quad (3.15)$$

After integration h_1 will be as given in Eq. 3.16:

$$h_1 = 2 \cdot \tau_y \cdot H \cdot \ln \left(\frac{(r_t \cdot H)^3 - (r_b \cdot H)^3}{(r_t \cdot H)^3 - (r_t \cdot H + h_0 \cdot (r_b - r_t))^3} \right) \quad (3.16)$$

Referring to Figure 3.2, slump is the difference between the initial height at the top of the cone and the height of the material at rest after the cone is lifted. This can be expressed as Eq. 3.17:

$$S = H - (h_0 + h_1) \quad (3.17)$$

Normalizing slump to the height of the cone H yields an equation for dimensionless slump; see Eq. 3.18.

$$S' = \left(\frac{S}{H} \right) = 1 - \left(\frac{h_0 + h_1}{H} \right) \quad (3.18)$$

The height h_0 corresponds to the level ($z = H - h_0$) of the slump cone before lifting. The value of the height h_0 can be measured directly by experiment. The yield stress τ_y can be calculated using Eq. 3.8 with ($z = H - h_0$) and r_z correspondingly at this level; see Eq. 3.19.

$$\tau_y = \frac{\rho \cdot g}{6} \cdot \frac{(h_0)}{r_z^2} \cdot (r_z^2 + r_z \cdot r_t + r_t^2) \quad (3.19)$$

The dimensionless yield stress can be expressed in terms of h_0 and r_z , as in Eq. 3.20.

$$\tau_y' = \frac{\tau_y}{\rho \cdot g \cdot H} = \frac{1}{6H} \cdot \frac{(h_0)}{r_z^2} \cdot (r_z^2 + r_z \cdot r_t + r_t^2) \quad (3.20)$$

3.3 Analytical approach for evaluation of results of a slump flow test

The units are dimensionless for both slump and yield stress, normalised by the height of the slump cone and material density.

The radius of the bottom surface of the undeformed part can be calculated from its height by Eq. 3.21:

$$r_z = \frac{h_0 \cdot (r_b - r_t)}{H} + r_t \quad (3.21)$$

For Abrams cone ($r_b=100$ mm, $r_t=50$ mm, $H=300$ mm) Eq. 3.21 has the following form:

$$r_z = \frac{300 + h_0}{6}$$

Accordingly, yield stress for Abrams cone can be calculated by Eq. 3.22:

$$\tau_y = \frac{\rho \cdot g}{6} \cdot \left(\frac{(h_0 + 300)^3 - 300^3}{(h_0 + 300)^2} \right) \quad (3.22)$$

Dimensionless yield stress for Abrams cone is as expressed in Eq. 3.23:

$$\tau_y = \frac{1}{6H} \cdot \left(\frac{(h_0 + 300)^3 - 300^3}{(h_0 + 300)^2} \right) \quad (3.23)$$

where h_0 is the height of undeformed part in mm.

Measurement of the height h_0 can be more complicated if the “undeformed” part has some inclination (see Figure 3.9).



Figure 3.9: *The slump test of an ordinary concrete mixture. In this experiment the part of slump cone without deformation is observed; the undeformed part of the concrete has some inclination*

In this case, the height of the undeformed part can be associated with the length l_0 of the side surface of the undeformed part. This length can be measured more easily than the height h_0 ; only the measuring scale is needed for measuring, as shown in Figure 3.10.

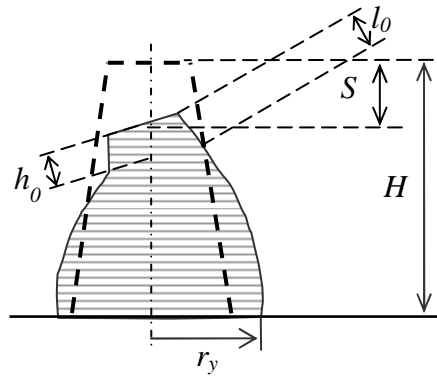


Figure 3.10: The slumped concrete and the measurable values

So, the height h_0 can be calculated from measured length l_0 using Eq. 3.24:

$$h_0 = \frac{l_0 \cdot H}{\sqrt{(r_b - r_t)^2 + H^2}} \quad (3.24)$$

3.3.1.2 Analysis of deformation due to dead weight for highly flowable concretes

SCC has a considerably smaller yield stress value in comparison with ordinary concrete. Therefore, the part of the slumped material which theoretically should not be deformed undergoes plastic deformation, shown schematically in Figure 3.11.

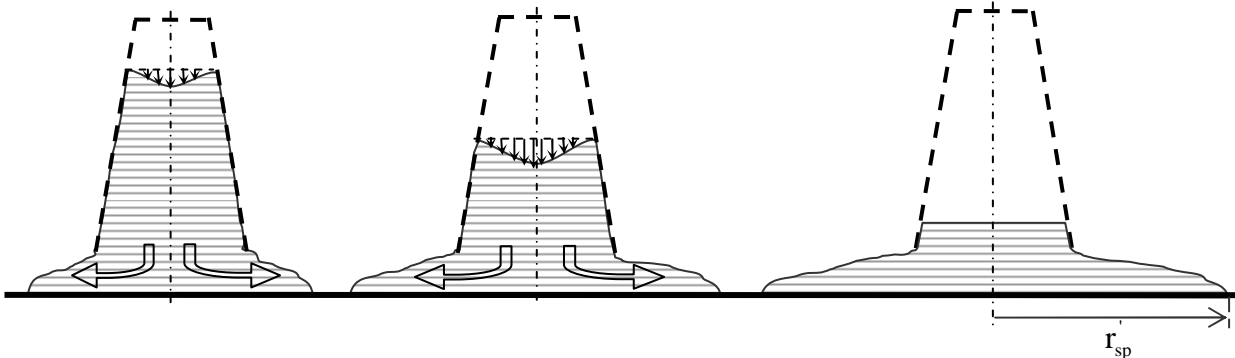


Figure 3.11: Deformation due to dead weight for highly flowable concretes

Before lifting the cone the maximum shear stress τ_{max} , calculated by Eq. 3.7 with $z=0$ and $r_z=r_b$, is at the bottom surface. When the cone is lifted, the flowing concrete moves toward the new state of equilibrium with a new geometry. It is assumed that the slump flow is influenced primarily by the yield stress value of concrete. The new geometry corresponds to the new stress distribution as shown schematically in Figure 3.12. The final height consists of deformed (h_1) and “undeformed” (h_0) parts.

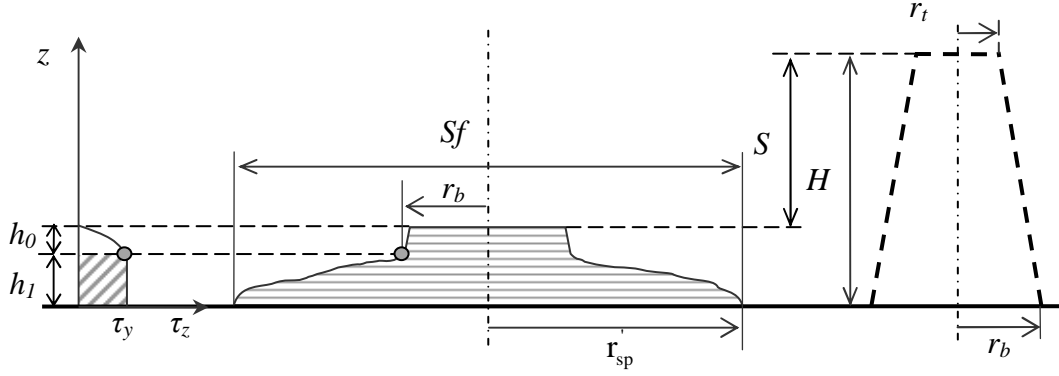


Figure 3.12: Final shape of SCC after lifting of the cone and the corresponding shear stress distribution

The deformation continues as long as the maximal shear stress is greater than the yield stress of the concrete. Therefore, the maximal shear stress after deformation is equal to yield stress.

Thus, Eq. 3.14 can be rewritten for the bottom layer ($z=0$) in following form:

$$\tau_y = \frac{r_b^2}{r_{sp}^2} \cdot \tau_{\max} \quad (3.25)$$

where r_{sp} is the radius of spreading (see Figure 3.13).

Substituting Eq. 3.7 into Eq. 3.25 gives (see Eq. 3.26):

$$\tau_y = \frac{\rho \cdot g \cdot H}{6 \cdot r_{sp}^2} \cdot (r_b^2 + r_b \cdot r_t + r_t^2) \quad (3.26)$$

For the Abrams cone, where $r_t=50$ mm, $r_b=100$ mm, $H=300$ mm, Eq. 3.26 can be simplified to the following equation, Eq.3.27:

$$\tau_y = \rho g \frac{0.875}{r_{sp}^2} = 3.5 \rho g \frac{1}{Sf^2} \quad (3.27)$$

where Sf is slump flow value and r_{sp} is the corresponding radius ($Sf/2$) in mm, while ρ is concrete density in kg/m^3 and g is acceleration of gravity (9.8067 m/s^2).

A similar dependence was obtained for the Abrams cone by Kurokawa *et al.* [69]. Some difference in the coefficients before the term $1/Sf^2$ results from a different assumption in calculating the initial stress distribution. The proposed model is based on the consideration of the stress distribution over the height of the material and an assumption that the material with non-zero yield stress value must have some undeformed part at the top; in this region stress does not exceed the yield stress and the concrete remains undeformed. The concrete volume associated with this undeformed part does not take part in the spreading process. In contrast, the Kurokawa model is based on the assumption that the entire volume of the concrete takes part in the spreading process. The difference in predicted values of yield stress from both formulas are nearly identical for most SCC, since the volume of the undeformed part, if such exists, is very small. Therefore, Eq. 3.27 seems to give a more general description of the relation between slump flow value and yield stress.

3.3.2 Estimation of the plastic viscosity

A large number of the studies surveyed, including theoretical analysis [83, 119] and numerical analysis [122], were about slump flow testing. However, the traditional slump flow test does not evaluate plastic viscosity. For this purpose, different apparatuses and methods have been developed. For instance, the so-called 4C-Rheometer has been developed in Denmark, combining the traditional slump flow test with digital video analysis to obtain the slump flow versus time curve, from which yield stress and plastic viscosity can be determined [1, 128]. The flow curve is subsequently compared to a database of simulated flow curves from which yield stress and plastic viscosity can be determined. Hence, the 4C-Rheometer obtains the flow curves just for one direction of the flow, some measuring errors are inevitable.

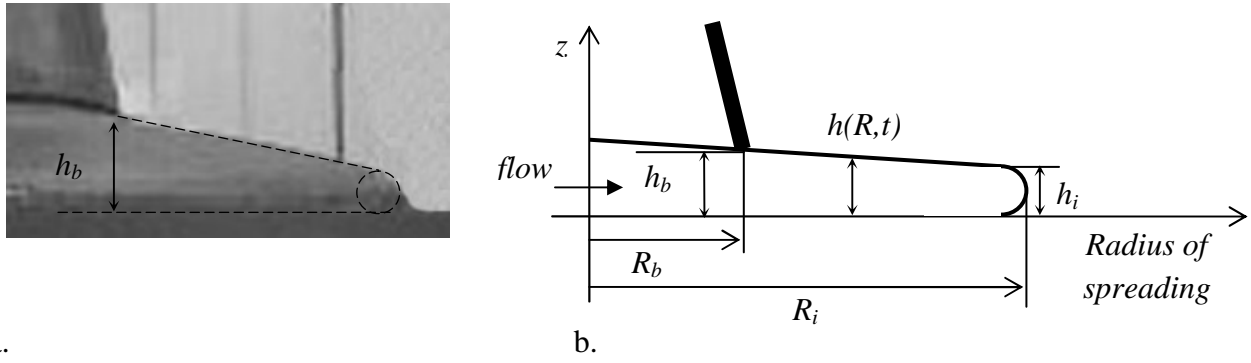
Innovative measuring apparatuses for slump flow test allows obtaining slump flow versus time curves for four radial directions of flow, from which averaged values of the plastic viscosity and yield stress are estimated using an own analytical approach. This section presents the concept of evaluation of plastic viscosity using the slump flow test results.

3.3.2.1 Analysis of the spreading process

Figure 3.13 shows schematically the cross-section of the flowing concrete in radial direction. Analysis of the slump flow vs. time curves, which were presented in Figure 3.4 and were measured using a computer-controlled table, makes possible the calculation of the flow rate of fresh concrete. The flow rate can be calculated for the cylindrical surface located between bottom surface of the truncated cone and surface of the slump flow table, shown schematically in Figure 3.13b. To do this a volume V_i of the concrete ring between the initial radius ($R_b=100$ mm) and the current value of slump flow radius $R_i(t)$ has to be calculated using Eq. 3.28. The volume V_i represents the amount of fresh concrete which passed through the abovementioned cylindrical surface when the slump flow value reaches the radius R_i .

$$V_i = \frac{1}{3} \cdot \pi \cdot R_i^2(t) \cdot (2 \cdot h_b - h_i) - \pi \cdot R_b^2 \cdot h_b \quad (3.28)$$

where h_b is the current height at the fixed radius R_b (displayed on the lifting-device) and h_i is the height at the slump flow radius R_i ; see Figure 3.13. It is assumed that h_i depends on the yield stress of the fresh concrete. Therefore, it might be supposed that a change in this thickness during the test is minor. The laboratory tests with highly flowable concretes indeed confirm this. Thus the thickness h_i can be measured at the end of the test.



a. **Figure 3.13:** Geometry of the SCC flow domain during lifting of the cone (a), and simplified geometrical representation of the SCC flow profile (b)

Observations of the spreading behaviour of SCC indicate that the height h_b does not change significantly up to a spreading radius of approximately 250 mm. Figure 3.14 illustrates this phenomenon: very nearly the same height h_b can be observed for spreading radii between 150 mm and 250 mm.

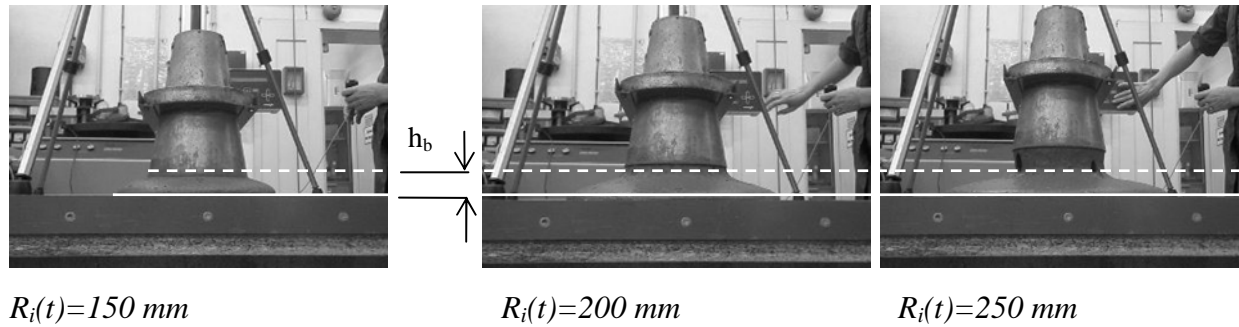


Figure 3.14: Three snapshots of a slump flow test on SCC; the height h_b does not change significantly at these stages of concrete spreading

The flow rate Q can be calculated using Eq. 3.29:

$$Q = \frac{\Delta V}{\Delta t} = \frac{V_{i+1} - V_i}{\Delta t} = \frac{\pi \cdot (2 \cdot h_b - h_i) \cdot (R_i^2(t + \Delta t) - R_i^2(t))}{3 \cdot \Delta t} \quad (3.29)$$

where V_i is the volume of the part of concrete cake between R_b and R_i ; V_{i+1} is the volume of the part of concrete cake between R_b and R_{i+1} ; Δt is the time difference between marks R_i and R_{i+1} .

Figure 3.15 shows the development of the flow rate Q , calculated using Eq. 3.29, with increasing radius of spreading R for two types of SCC, one light-weight concrete (SCLC) and another ultra-high performance concrete (UHPC1).

3 Experimental investigation of fresh concrete rheology (Macrolevel)

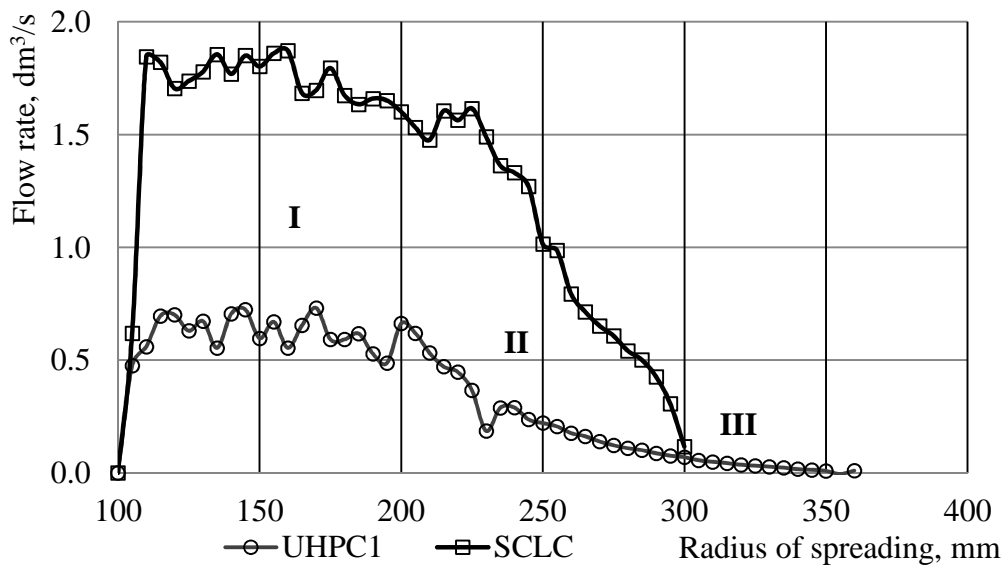


Figure 3.15: Development of the flow rate with increasing radius of spreading for UHPC1 and SCLC

The diagram can be subdivided into three parts. In the first part (I), at the beginning of the experiment, the flow rate changes very little. This holds true up to a spreading radius of 200 mm approximately. At this stage there is still concrete inside the cone, which plays the role of flow source. The characteristic of the second part (II) is that all the concrete has left the cone completely and spreads further due to its own weight, without any inflow, i.e., no more concrete flows from the cone. At this stage a quasi-linear decrease of flow rate can be observed, i.e., in inverse proportion to the radius of spreading. The spreading slows down. The third part (III) is characterized by very small flow rates. The acting shear stresses are close to the yield stress. Furthermore, the role of friction at the concrete/plate interface cannot be neglected at this stage. The nearly constant values of the flow rate during the first stage of spreading seem to be most reliable for assessing concrete viscosity.

The fresh concrete flows out from the slump cone through an imaginary cylindrical surface between the bottom surface of the slump cone and the base plate. The height of this cylindrical surface is equal to zero at the beginning of the test and increases until height h_b during lifting of the slump cone. The flow rate of the concrete is also equal to zero at the beginning of the test and increases rapidly when the lifting of the cone starts. Thus, it might be supposed that the flow rate in Figure 3.16 corresponds to the amount of the fresh concrete which flows out through the above mentioned cylindrical surface. This assumption is schematically presented in Figure 3.16.

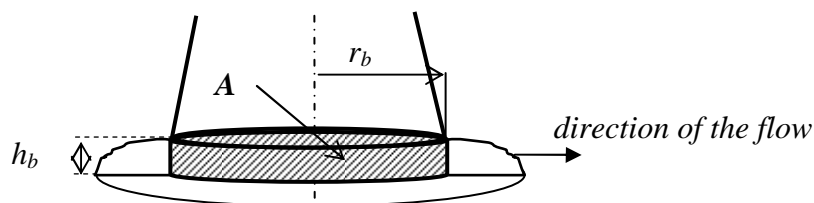


Figure 3.16: Schematic representation of the imaginary cylindrical surface between bottom surface of the slump cone and base plate

The section area A can be calculated using Eq. 3.30:

$$A = 2 \cdot \pi \cdot r_b \cdot h_b \quad (3.30)$$

The results of tests show that change in the velocity of flow is small at the beginning of the slump flow test: slump flow showed almost linear dependence with time inside the slump flow interval between 100 mm and 200 mm; see Figure 3.4. The change in thickness h_b is also very small (see Figure 3.14). Taking into account the abovementioned observation, the velocity v of the top surface of the flow can be calculated from the flow rate Q using Eq. 3.31:

$$v = Q/A \quad (3.31)$$

Assuming that the velocity at the concrete-to-plate surface is zero and the velocity gradient over the height of the flow is linear, the shear rate $\dot{\gamma}$ can be calculated using Eq. 3.32:

$$\dot{\gamma} = \frac{v}{h_b} = \frac{Q}{A \cdot h_b} = \frac{Q}{2 \cdot \pi \cdot r_b \cdot h_b^2} \quad (3.32)$$

It should be noted that there is no principal difference between normal and inverted orientations of the slump cone. The section area will be two times smaller in the case of inverted orientation because $r_b=50$ mm at the other end of the truncated cone.

3.3.2.2 Finding the velocity profile

Velocity profile is an important characteristic of the flow; the speed of the flow v is a function of depth z (shown schematically in Figure 3.17a). The velocity profile is needed in order to calculate the dynamic viscosity of the flow; see Eq. 2.2 in Section 2.2).

It is assumed that all the streamlines point in the same direction, the flow is wide and of uniform depth, and the depth is much smaller than the width. This assumption is needed to calculate the total flow rate, which can be presented as the sum of the flow contribution from the different depths. This will be an integral looking like shown in the illustration in Figure 3.17b.

Hydrostatic pressure certainly varies with depth. A thin layer of the flow lying between height z and $z + \Delta z$, as shown in Figure 3.17b, can be mentally separated from its surroundings, and Newton's Laws can be applied: it is not moving, so, it must be that its weight has to be balanced by the sum of the pressure forces it experienced from the remainder of the current surrounding it. In fact, its weight is indeed balanced by the difference between the pressure underneath and that on top [15].

However, in reality, this layer is moving, but at a constant speed, so the total force on it will still be zero.

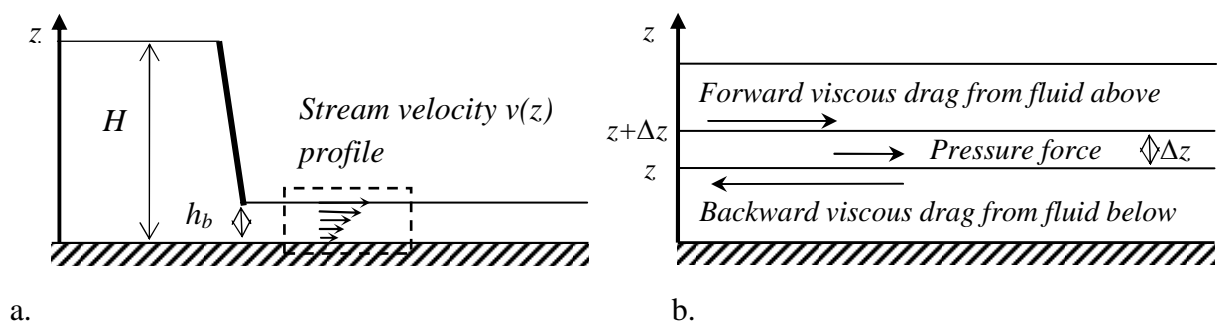


Figure 3.17: Stream velocity $v(z)$ at different depths (a) and the thin layer of the flow (b)[15]

3 Experimental investigation of fresh concrete rheology (Macrolevel)

Obviously for the forces to balance the backward drag on the thin layer from the slower moving current beneath has to be stronger than the forward drag from the faster current above; so the rate of change of speed with height above the flow bed decreases with an increase in the height above the bed.

The pressure force per unit width across a section of the layer is proportional to hydrostatic pressure ($\rho \cdot g \cdot H$). For thin layer Δz the pressure force is equal to $(\rho \cdot g \cdot (H-z) \cdot \Delta z)$.

For the viscous drag forces, a unit of surface area, square millimetre, in the layer experiences two viscous forces, one from the slower current below, equal to $(\eta \cdot dv(z)/dz)$, tending to slow it down, one from the faster current above it, $(\eta \cdot dv(z + \Delta z)/dz)$, tending to speed it up [15].

The pressure force must balance out the difference between the two viscous forces, see Eq. 3.33:

$$\rho \cdot g \cdot (H - z) \cdot \Delta z + \eta \cdot \frac{d}{dz} v(z + \Delta z) - \eta \cdot \frac{d}{dz} v(z) = 0 \quad (3.33)$$

Dividing Eq. 3.33 throughout by η and by Δz and taking the limit $\Delta z \rightarrow 0$ we find the differential Eq. 3.34:

$$\frac{d^2 v(z)}{dz^2} = - \frac{\rho \cdot g \cdot (H-z)}{\eta} \quad (3.34)$$

The solution of this equation is (see Eq. 3.35):

$$v(z) = - \frac{\rho \cdot g}{2 \cdot \eta} \cdot \left(\frac{z^3}{3} - H \cdot z^2 \right) + C \cdot z + D \quad (3.35)$$

where C and D are constants of integration.

Considering that the velocity $v(z)$ is zero at the bottom of the flow, $z = 0$, the constant D must be zero and therefore can be dropped immediately.

The constant C can be determined by examination of velocity profile near the flow surface, the balance of forces equation for the top layer is given by Eq. 3.36 below:

$$\rho \cdot g \cdot (H - z) \cdot \Delta z - \eta \cdot \frac{d}{dz} v(z) = 0 \quad (3.36)$$

The term $(\rho \cdot g \cdot (H - z) \cdot \Delta z)$ goes to zero in the limit of extreme thinness ($\Delta z \rightarrow 0$), so the other term must go to zero as well. Since η is constant, this means $\frac{d}{dz} v(z) = 0$ at the surface $z=h$.

So the velocity profile function $v(z)$ has zero slope at the flow surface, see Eq. 3.37:

$$v(z) = - \frac{\rho \cdot g}{2 \cdot \eta} \cdot \left(\frac{z^3}{3} - H \cdot z^2 \right) + C \cdot z \quad (3.37)$$

Now the arbitrary integration constant C can be calculated; see Eqs. 3.38-3.39:

$$\frac{dv(z)}{dz} = - \frac{\rho \cdot g}{\eta} \cdot \left(\frac{z^2}{2} - H \cdot z \right) + C \quad (3.38)$$

$$\text{and } \frac{d}{dz} v(z = h) = 0 \text{ gives } C = \frac{\rho \cdot g}{\eta} \cdot \left(\frac{h^2}{2} - H \cdot h \right) \quad (3.39)$$

Substituting this value for C into the equation for $v(z)$, the final expression for the velocity profile is the following; see Eq. 3.40:

$$v(z) = \frac{\rho \cdot g}{2 \cdot \eta} \cdot \left(H \cdot z^2 - \frac{z^3}{3} \right) + \frac{\rho \cdot g}{\eta} \cdot \left(\frac{h^2}{2} - H \cdot h \right) \cdot z \quad (3.40)$$

Knowing the velocity profile $v(z)$, one can calculate the total flow rate. The flow contribution from a single layer of thickness Δz at height z is $(v(z) \cdot \Delta z)$. The total flow is the sum over all layers. In the limit of many infinitely thin layers the sum becomes an integral, and the total flow rate is expressed in Eq. 3.41:

$$Q = L \cdot \int_0^{h_b} v(z) dz = L \cdot \frac{\rho \cdot g}{2 \cdot \eta} \cdot \int_0^{h_b} z \cdot (2 \cdot h - z) dz = L \cdot \frac{\rho \cdot g}{\eta} \cdot \left(\frac{H \cdot h_b^3}{3} - \frac{5 \cdot h_b^4}{24} \right) \quad (3.41)$$

where L is the circumference of the bottom surface of the slump cone, according to the orientation of the slump cone, in meters ($L = 2 \cdot \pi \cdot r_b$).

Therefore the viscosity can be calculated from the known value of the flow rate using Eq. 3.42:

$$\eta = L \cdot \frac{\rho \cdot g}{Q} \cdot \left(\frac{H \cdot h_b^3}{3} - \frac{5 \cdot h_b^4}{24} \right) \quad (3.42)$$

3.3.2.3 Transition from the dynamic to the plastic viscosity

Plastic viscosity is a measure of the internal resistance to fluid flow according to Bingham's rheological model, expressed as the tangential shear stress in excess of the yield stress divided by the resulting rate of shear. In contrast to the plastic viscosity, the dynamic viscosity is a measure of the frictional resistance of a fluid as calculated using Newton's law.

The plastic viscosity can be calculated from the known values of the yield stress, dynamic viscosity, and the corresponding shear rate. The principal scheme for such calculation is presented in Figure 3.18.

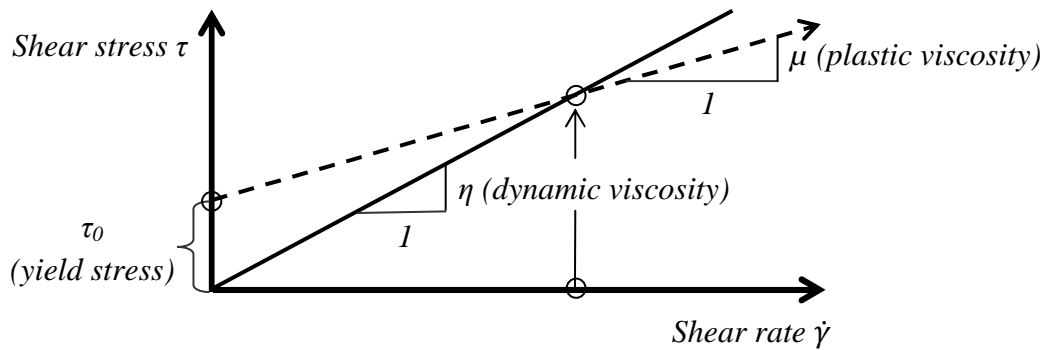


Figure 3.18: Sketch for the calculation of plastic viscosity

The plastic viscosity can be calculated using the Bingham equation, Eq. 2.7, and is represented in the following equation; see Eq. 3.43:

$$\mu = \frac{\tau - \tau_0}{\dot{\gamma}} = \frac{\tau}{\dot{\gamma}} - \frac{\tau_0}{\dot{\gamma}} = \eta - \frac{\tau_0}{\dot{\gamma}} \quad (3.43)$$

where τ is the shear stress applied to the material, $\dot{\gamma}$ is the shear strain rate, τ_0 is the yield stress and η is the dynamic viscosity.

3 Experimental investigation of fresh concrete rheology (Macrolevel)

By introducing Eq. 3.32 into Eq. 3.43 the final equation for plastic viscosity is shown to have the following form; see Eq. 3.44:

$$\mu = \eta - \frac{2 \cdot \tau_0 \cdot \pi \cdot r_b \cdot h_b^2}{Q} \quad (3.44)$$

where yield stress value τ_0 calculated by Eq. 3.26, flow rate Q by Eq. 3.29, dynamic viscosity η by Eq. 3.42. All expressions mentioned above are used for experimental evaluation of the Bingham rheological constants in corresponding tests which are presented in the next section.

3.4 Analysis and discussion of the experimental results using analytical approach

The influences of the slump flow test setups on the experimental results are discussed here. The results of the tests are processed using the analytical approach presented above.

3.4.1 Influence of the cone orientation

The first parameter of the slump flow test setup is the orientation of the slump cone: normal or inverted. While the remainder of the input parameters are or are held constant, the tests with different orientation of the slump cone were performed to evaluate this influence. Two series of tests are presented in Figure 3.19. The surface of the table for slump flow test is dry; the velocity of the cone lifting was 500 mm/min; height of the cone lifting was about 50 mm.

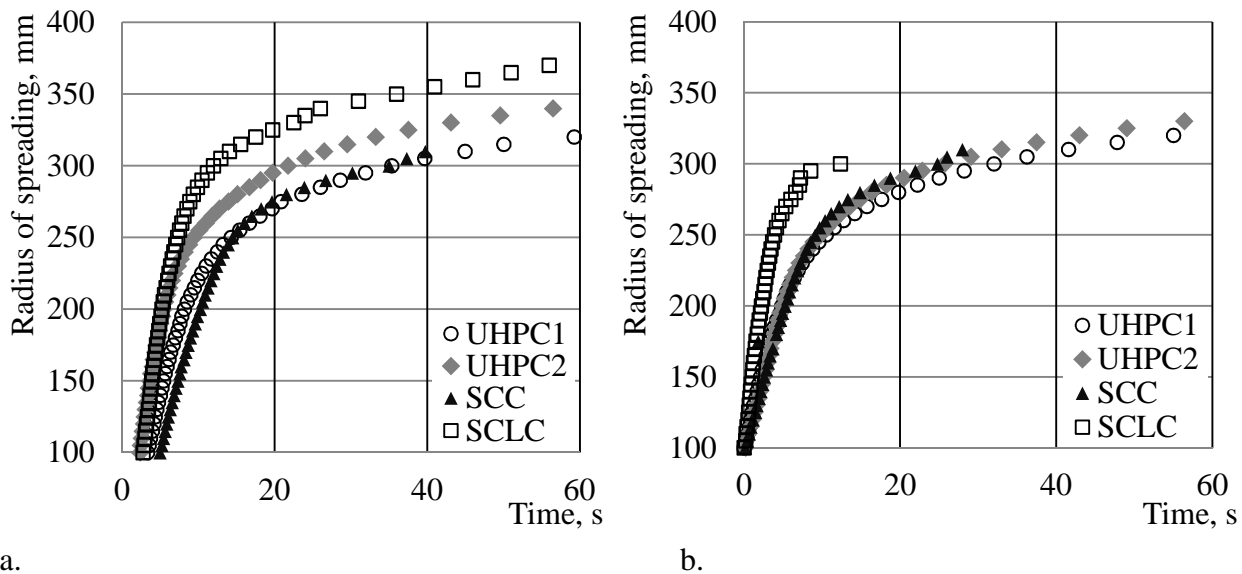


Figure 3.19: Development of radius of spreading in time with: a) inverted cone orientation; b) normal cone orientation

It should be noted that UHPC1 and UHPC2 continued the flow after 60 seconds from the beginning of the test.

The results of the slump flow tests with inverted and normal orientation of the cone show small differences in the slump flow for the concretes investigated, except for SCLC; see Table 3.4 and Figure 3.19. In the case of the inverted orientation of the slump cone the slump flow was much higher (about 20%). It may be supposed that low viscosity and smaller density of the SCLC play a

3.4 Analysis and discussion of the experimental results using analytical approach

certain part in the flowing process. The spreading process depends on the duration of the concrete outflow from the cone: this effect is more pronounced for concretes with low viscosity and small density because such concretes are more fluid. In the case of inverted orientation of the slump cone, the bottom radius of the slump cone is twice as small as is the case with normal orientation of the cone. Therefore, the fresh concrete needs more time to flow out of the slump cone.

This difference was observed in the radius-interval of 100 to 200 mm, presented in Figure 3.20. In the case of the inverted orientation of the cone, the concrete started flowing from a 50 mm radius. Hence, some time is needed in order to reach the first sensors (100 mm radius). This time also depends on the respective rheological properties of the concretes; see Figure 3.20a. In the case of normal orientation of the slump cone, the concrete started flowing from a 100 mm radius. Thus there is no delay between the beginning of cone lifting and the triggering of the first sensors; see Figure 3.20b. In addition, the difference between orientations of the cone is in the area of the imaginary cylindrical surface; see Figure 3.16. For normal orientation of the slump cone the area is two times as large as it is for the inverted cone. The concretes need more time to flow out of the cone in the case of its inverted orientation.

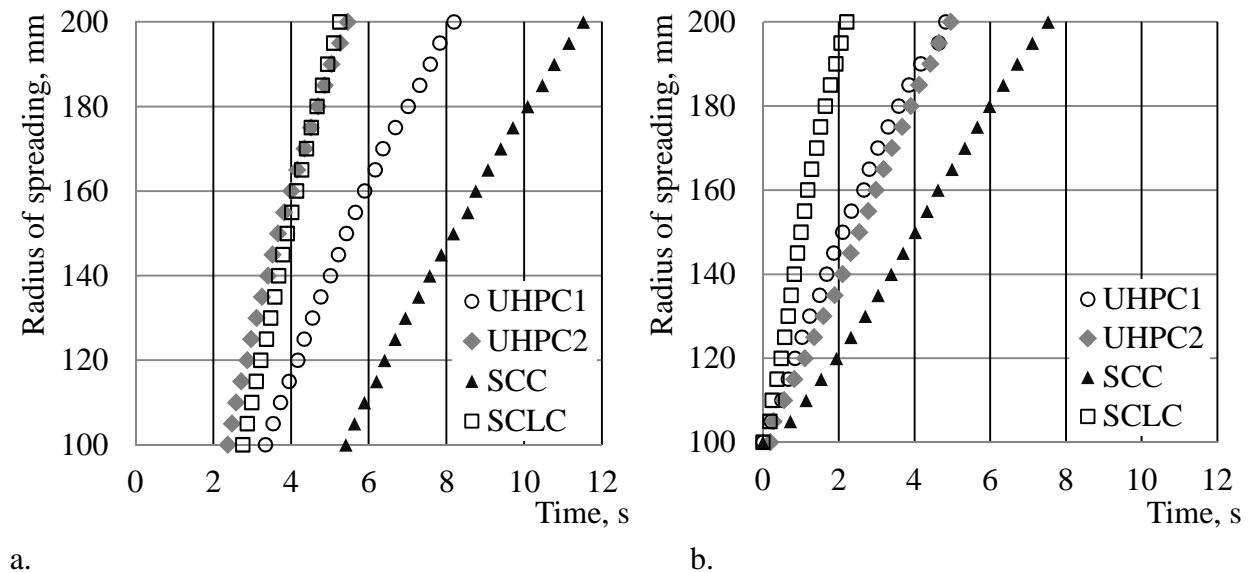


Figure 3.20: Development of radius of spreading in time in the radius interval of 100 to 200 mm in the slump flow tests with: a) inverted cone orientation; b) normal cone orientation

In comparing Figures 3.20a and 3.20b the lines for the same concretes look more or less parallel. This means that it may be supposed that the velocity of the spreading is also more or less same for the concretes under investigation. Thus there is no difference in the velocity of the spreading in the radius interval of 100 to 200 mm between two setups for concretes under investigation. However, it should be noted that even at the same spreading velocity and, consequently, measured flow rate, the values of dynamic viscosity will be different. This difference will be by a factor 2 in the case when fresh concrete has the same flow rate in both tests. For further details about results of calculation of the viscosities see Section 3.4.5.

3.4.2 Influence of the cone lifting velocity and height of lifting

The next factors to discuss are the input parameters of the electro-mechanical lifting device.

3 Experimental investigation of fresh concrete rheology (Macrolevel)

The cone lifting device has a limitation on the maximal lifting velocity of 500 mm per minute ($8\frac{1}{3}$ mm per second). The maximal velocity of the cone lifting using the cone lifting device is smaller than lifting of the cone with hand by more than 5 times. However, the advantages of the cone lifting device are quite evident: perfect repeatability, i.e., the velocity and height of the lifting, the stable position of the cone after lifting up to the specified height, no vibration and changing of the height, uniaxial lifting of the cone, and neither rotation nor horizontal shifting of the slump cone.

The influence of cone-lifting velocity was investigated by comparison of the results of tests with maximal (500 mm/min) and half of maximal (250 mm/min) velocity of the electro-mechanical lifting device. The results of these tests showed that decreasing the cone lifting velocity by two times does not influence the final slump flow. However, it should be noted that in the case of the smaller velocity concrete flowed significantly more slowly than in tests using the maximum lifting velocity. Therefore, the fresh concrete flows out with smaller velocity at the beginning of the test. From this the following conclusion can be drawn: velocity of the cone lifting should be high enough not to limit the outflow.

The importance of the height of cone lifting was presented in Section 3.2.3. The most important parameters which should be taken into consideration in estimating the optimal height of the slump cone lifting are following: maximal height of the flowing concrete, whereas some additional testing is required in the radius interval of 100 to 200 mm; maximum aggregate size – the height should be at least three times higher than the maximum size of aggregates (in order to avoid blocking). Thus the optimal height of cone lifting for the concretes under investigation is 50 mm. The cone prevents the concretes' flowing out at smaller heights, and lifting of the cone higher than 50 mm, up to 75 mm, has no significant influence on the results of tests. The slump cone has very little influence on the flow behaviour of the fresh concrete in the case when the cone is lifted higher than the flowing concrete. This effect can be seen in the video from the side of the slump cone. The snapshots from this video are presented in Figure 3.15.

3.4.3 Influence of table wetness on slump flow measurement

In order to investigate the influence of moisture on the surface of the slump flow table, a series of slump flow tests with inverted cone orientation have been compared; velocity of the cone lifting is 500 mm/min; height of the cone lifting is about 50 mm. Corresponding series of the test are presented in Figure 3.21. The “wet” surface means the presence of a water layer on the top surface, but no drops or moisture collection regions. This amount of water is enough to decrease the friction between flowing fresh concrete and slump flow table. Lower friction could produce a different flow regime. The fresh concrete starts sliding on the “wet” surface. This leads to considerably higher slump flow on the wet surface. The slump flow comes up to 750 mm and even higher (see Figure 3.21). For instance, the lowest slump flow on the dry slump flow table has the SCC with a slump flow about 615 mm. However in the test with wet surface of the slump flow table the slump flow was about 720 mm, which is comparable with results for UHPC. It should be noted that the UHPC1 and UHPC2 continue flowing after 60 seconds from the beginning of the test.

3.4 Analysis and discussion of the experimental results using analytical approach

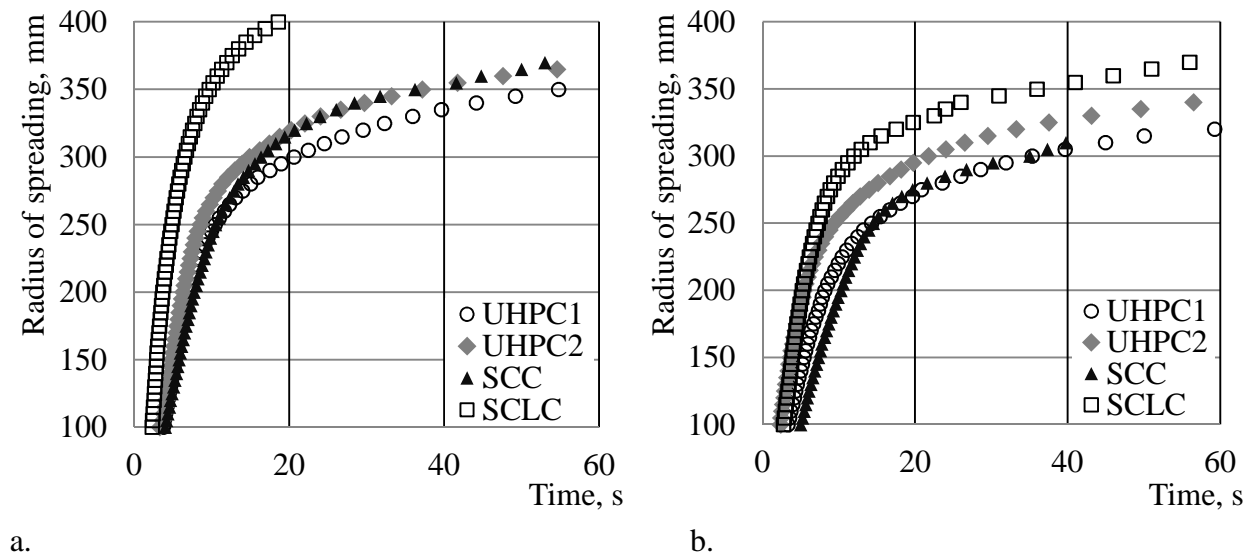


Figure 3.21: Development of radius of spreading in time with inverted cone orientation: a) wet surface of the slump flow table, b) dry surface of the slump flow table

The largest differences were observed in the radius interval of 100 to 200 mm presented in Figure 3.22. An inclination of the line in Figure 3.22 characterised the flowing process in the radius interval of 100 to 200 mm. Smaller angle with positive direction of the “Time” axis means a lower flow velocity and vice versa. The lines for the same concretes in the case of the “dry” surface of the table have considerably smaller inclination, as shown in Figure 3.22b comparing with tests on the “wet” surface; see Figure 3.22a.

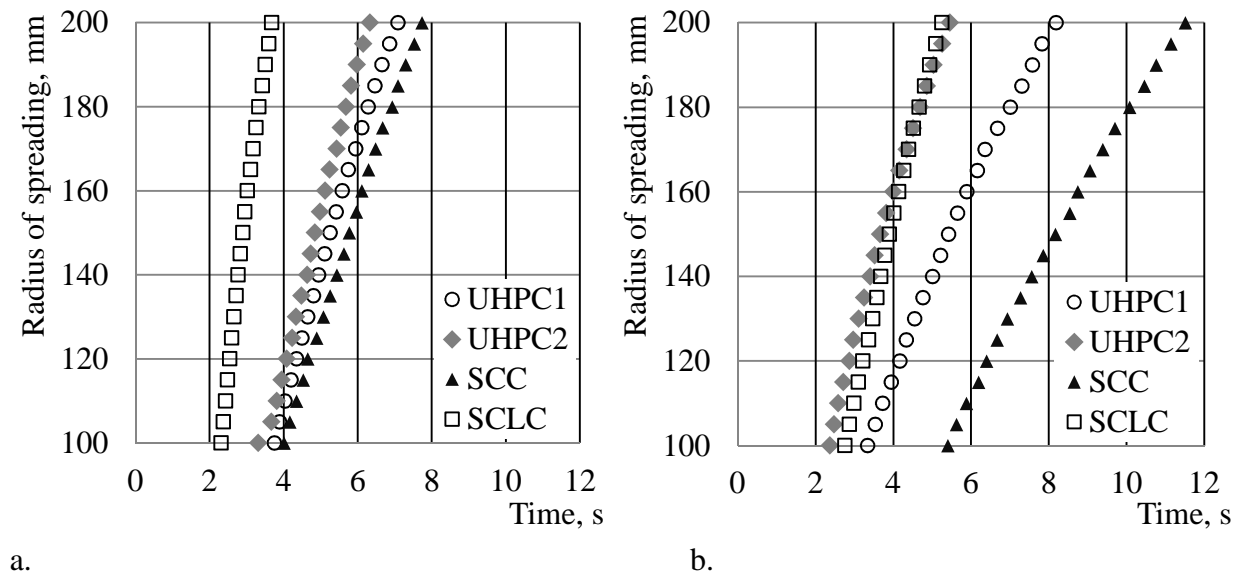


Figure 3.22: Development of radius of spreading in time in the radius interval of 100 to 200 mm with inverted cone orientation: a) wet surface of the slump flow table, b) dry surface of the slump flow table

Comparison of the tests with “wet” and “dry” surfaces of the slump flow table shows a limitation of the slump flow test: the surface of the slump flow test has to be always in the same condition: only in this case can the results of the tests be adequate and comparable with other results. It should be noted that the condition of the surface (“wet” or “dry”) is not an input parameter for analytical

3 Experimental investigation of fresh concrete rheology (Macrolevel)

solution for estimating of the viscosity of fresh concrete. Moreover, it is assumed that there is no slip between layers, including the bottom layer, which is in a contact with table. Therefore, the tests with a “dry” table provide a better data basis for estimating the viscosity.

3.4.4 Calculation of the yield stress

The yield stress value characterizes the stiffness of the fresh concrete. In the slump tests with ordinary concretes, the concrete with the higher value of yield stress has the smaller slump value.

The mix OC1 has the smallest slump value, i.e., the greatest height of the undeformed part and the smallest height of deformed concrete (see Figure 3.1). Therefore, this fresh concrete mix must have the highest yield stress in comparison to the rest. It should be noted that the new geometry of the fresh concrete after deformation is the reverse of that predicted analytically; see Figure 3.7. In contrast to the analytical model, where the bottom radius of the deformed part should increase during the deformation, the radius of the bottom surface in tests remains unchanged. This can be explained as the result of high friction between the fresh concrete and the surface of the slump table. Thus, the bottom surface of the concrete sample does not slide on the table surface. As the cone is lifted, the fresh concrete sample deforms and assumes its new shape. The new shape forms when the concrete loses contact with the slump cone, similar to the extrusion process. Hence, the new shape of the deformed fresh concrete sample looks like part of an ellipsoid. In contrast to the deformed part, the undeformed part loses the contact with slump cone at the beginning of the test already and remains in the shape of the truncated cone geometry. However, the shape of the “undeformed” part also has changed: the bottom base has a radius equal to the radius of the bottom area of the slump cone (100 mm). Consequently the new shape of the undeformed part is truncated cone with bottom radius 100 mm, top radius 50 mm and height h_0 .

The mix OC2 has a greater amount of water and, accordingly, a higher w/c. In the slump test this mix showed higher slump values, which indicates a smaller yield stress value. The shapes of deformed and undeformed parts are similar to those of the mix OC1. In contrast to the mix OC1, the undeformed part of this mix is inclined. It may be supposed that the undeformed part does not lose contact with the slump cone and starts sliding on its inner surface; the specific trail of sliding presents itself on the side surface of the sample; see Figure 3.1. Therefore, the new geometry of the undeformed part can be characterized as a truncated cone with an inclination. The bottom area of this truncated cone has a radius of about 100 mm and a top radius of 50 mm.

The mix OC3 contained the highest amount of water and has the highest w/c ratio among the normal concretes investigated without superplasticizer. This mix shows a higher slump in comparison to the mixes OC1 and OC2; thus, it has the smallest yield stress. The shape of the sample after deformation for this mix is similar to the mixes OC1 and OC2. It should be noted that further increases in w/c led to bleeding.

The mix OC4 has a w/c ratio equal to that of the mix OC2, and contains superplasticizer. Thus the mix OC4 shows the highest slump and, as a consequence, the smallest yield stress.

The corresponding values of the yield stress calculated according to Eq. 3.24 are presented in Table 3.6.

Table 3.6: *Calculated yield stress values for ordinary concretes*

Mix	OC1	OC2	OC3	OC4
Yield stress, Pa	1070	815	725	650

The results presented in Table 3.6 confirm that the model presented above for estimating the yield stress of ordinary concrete (see section 3.3.1.1) represents the effect of the concrete composition on the yield stress correctly. The abovementioned analytical solution is later implemented in the PFC for adequate representation of the yield stress in dimensionless form in numerical modelling. It is worth mentioning that the internal stress distribution inside the fresh concrete specimen is the same for ordinary and self-compacting concretes; see Figure 3.6. This being so, the same analytical methodology may be used for SCC.

SCCs have much smaller yield stresses in comparison to ordinary concrete. Therefore, the deformation process of fresh concrete sample of SCC occurs in a different way. As a rule the slump for a SCC is higher than 200 mm, the concrete sample deforming completely. Thus, the main indicator of yield stress in SCC is slump flow value.

The experimental investigations of fresh self-compacting concretes show that UHPC1 and UHPC2 have the highest slump flows of more than 700 mm; see Table 3.7. The SCLC shows 600 and 690 mm slump flow for normal and inverted cone orientation, respectively. The last fresh concrete sample is normal-weight, self-compacting concrete, which has slump flow 610 mm for normal cone orientation and 615 mm for the inverted. Therefore, UHPC1 and UHPC2 have smaller yield stress values than SCLC, which in turn has a smaller yield stress value than SCC. The corresponding values of the yield stress, calculated according to Eq. 3.27, are presented in Table 3.7.

Table 3.7: *Calculated yield stress values for flowable concretes*

Concrete	SCC		UHPC1		UHPC2		SCLC	
	Norm.	Inv.	Norm.	Inv.	Norm.	Inv.	Norm.	Inv.
Slump flow, mm	610	615	722	715	715	722	600	690
Yield stress, Pa	217.9	214.4	155.0	158.1	167.6	164.4	167.7	126.8

It was found that there is no significant difference in the yield stress for different orientations of the slump cone (normal or inverted). An exception is lightweight concretes with extremely low viscosity, such as SCLC; it was shown in Section 3.4.1 that orientation of the cone has great influence on the results of the slump flow test with such concrete.

3.4.5 Calculation of plastic viscosity

The plastic viscosity of fresh concretes can be estimated by analysing their flow behaviour. It is almost a truism that materials with higher viscosity flow more slowly than materials with low viscosity. Time T_{50} is used in the slump flow test as a qualitative estimation of the viscosity of the fresh concrete, whereas the analytical solution is used as a quantitative estimation. The concrete with higher viscosity have the higher time T_{50} . Table 3.8 summarizes the results of the slump flow tests of the highly fluid concretes under investigation. The flow rate values were calculated as average values of all points in the radius interval 100 to 200 mm; see Figures 3.21 and 3.23 for

3 Experimental investigation of fresh concrete rheology (Macrolevel)

normal and inverted orientation of the cone, respectively. The dynamic and plastic viscosities were calculated according to Eq. 3.42 and Eq. 3.44, respectively.

Table 3.8: Estimation of the plastic viscosity from the results of the slump flow tests for highly fluid concretes

Concrete	SCC		UHPC1		UHPC2		SCLC	
	Norm.	Inv.	Norm.	Inv.	Norm.	Inv.	Norm.	Inv.
Cone orientation								
Time T_{50} , s	10	16	10.5	15	9.5	11	4	7.5
Flow rate, $10^3 \text{ mm}^3/\text{s}$	537	558	654	641	628	899	1697	1270
Height h_b , mm	50.7	50.7	50.2	50.3	50.7	50.6	50	50.3
Viscosity, Pa·s	31.6	15.2	25.1	12.9	28.5	9.9	7.2	4.9
Plastic viscosity, Pa·s	23.4	13.3	20.4	11.7	23.2	9.0	5.2	4.4

The most viscous concrete is SCC; UHPC1 and UHPC2 have lower viscosities; the least viscous is SCLC. In the case of the tests with normal cone orientation the bottom surface of the cone has a radius 100 mm. Thus, the spreading starts from the radius of 100 mm. In the case of inverted cone orientation, the bottom radius of the cone is 50 mm and concrete starts spreading from this position. The calculated values of the flow rate for normal and inverted orientation of the slump cone can be very close, as examples, SCC and UHPC1; see Table 3.8. In other words the flow behaviour of these concretes is similar in the measured radius interval (100 to 200 mm). It should be noted here that the cross-sectional area of the flow is important for calculation of the viscosities and this area is two times higher for normal orientation of the cone; see Eq. 3.30. Thus the calculated viscosities for the tests with inverted orientation of the cone will be two times smaller at the same flow rate for the case of normal orientation of the cone; see Table 3.8. In the case of UHPC2 the flow rate for the inverted cone is higher than for normal orientation of the cone and vice versa for the tests with SCLC.

It is logical that concretes with smaller viscosity have a higher spreading velocity. The results of the spreading measurements with normal cone orientation are presented in Figure 3.23. The average values of the radius of spreading and flow velocity are presented in Figure 3.23.

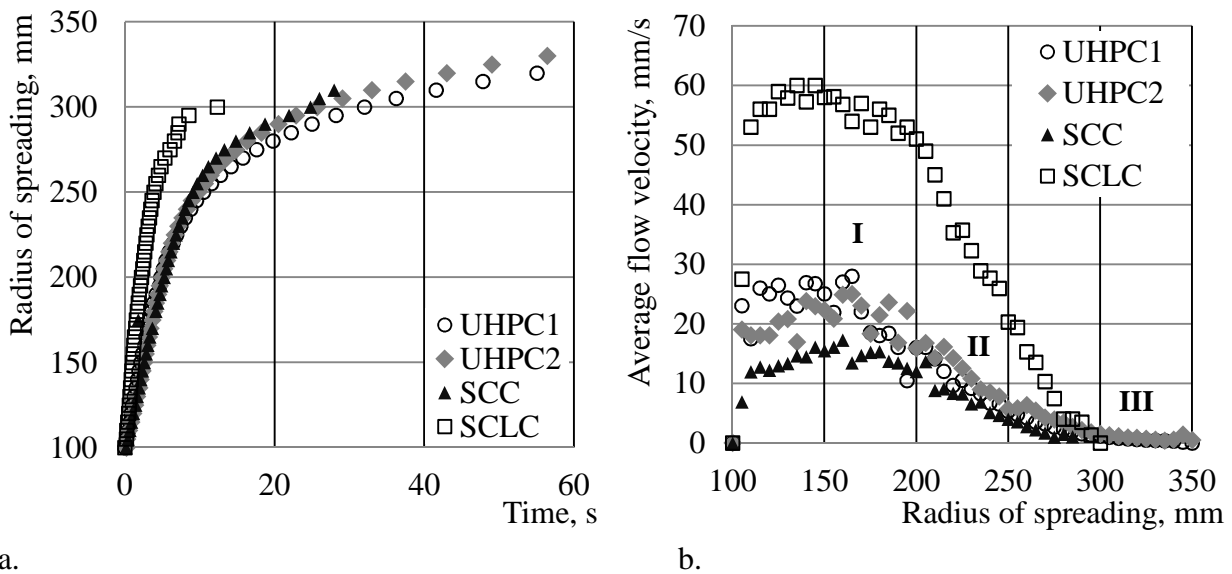


Figure 3.23: Results of spreading measurements with normal cone orientation: a) development of spread radius over time; b) average flow velocity for flowable concretes under investigation

The shapes of the curves for average flow velocity consist of 3 parts, as shown in Figure 3.15; see also Figure 3.23b. Some spread of the data points in Figure 3.23b results from the somewhat different flow velocities in various directions of flow; see Figure 3.4. The experimental points of different concretes are located very close to each other at the beginning of the test in the spread-radius interval from 100 to 200 mm, as shown in Figure 3.24a. Figure 3.24b presents the calculated flow rates in the given interval.

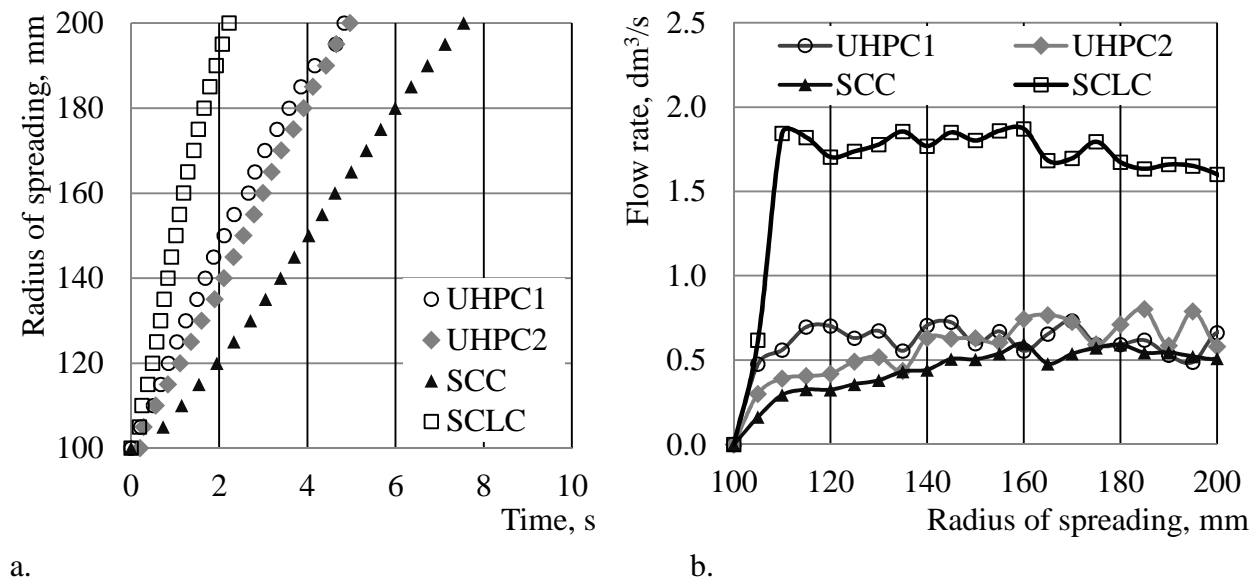


Figure 3.24: Results of the spreading measurement with normal cone orientation: a) development of spread radius over time in the radius interval of 100 to 200 mm; b) flow rate for flowable concretes under investigation.

The measured time-spreading relationships in the radius interval of 100 to 200 mm are nearly linear with various inclinations with respect to the horizontal axis, depending of the concrete type. The

3 Experimental investigation of fresh concrete rheology (Macrolevel)

angle of this inclination corresponded to the velocity of the flow ($v = \Delta R / \Delta t$, where ΔR is distance between neighbouring sensors (5 mm); Δt is time difference between triggering of these sensors).

It should be noted that there is no significant difference between normal and inverted orientation of the cone. The time-spreading relationships in the radius interval of 100 to 200 mm have the same inclination, though shifted with respect to time; for more detail see Section 3.4.1.

3.5 Summary

The investigation of the rheological behaviour on the macrolevel of observation as presented in this chapter was aimed at getting the input data for numerical modelling and for verification of the material model. Three common tests in estimating the rheological behaviour of the fresh concretes were presented and the influence of the setups of the tests on their results critically discussed.

The experimental investigation was performed with the simple test methods for fresh concrete, i.e., slump and slump flow tests as well as the L-Box test. The following concrete types were chosen for experimental investigation: ordinary concrete (OC), self-compacting light-weight concrete (SCLC), ultra-high performance concrete (UHPC) and normal-weight self-compacting concrete (SCC). These concretes had obviously different rheological properties.

First, the fresh concretes were investigated using a slump test for ordinary concretes and a slump flow test for flowable concretes. Automatic measuring apparatus developed at the TU Dresden for slump flow tests was used. The data was evaluated applying a newly proposed analytical approach for estimation of the Bingham rheological parameters. The measuring apparatus allowed the obtaining of the slump flow versus time curves for four radial directions of flow, from which averaged values of the plastic viscosity and yield stress were determined.

The influence of the setups of tests on the results of slump flow test was presented and critically discussed. It was shown that not just the rheological behaviour of the investigated material but also parameters such as orientation of the slump cone, lifting velocity and height of lifting of the slump cone, moisture state of the table surface on slump flow measurements can have great influence on the results of tests.

The results of the slump flow tests with inverted and normal orientation of the cone showed very small differences in the slump flow for the concretes under investigation. Moreover, there is no difference in the velocity of spreading in the radius interval of 100 to 200 mm among the concretes under investigation. However, it is important to note that even at the same spreading velocity and, as a result, measured flow rate, calculated values of dynamic viscosities will be two times smaller in the case of inverted orientation of the slump cone. The reason for this is the different area of the imaginary cylindrical surface, shown in Figure 3.16, needed for calculation of the shear rate and dynamic viscosity. This area is two times larger in the case of the normal orientation of the slump cone, i.e., the larger section of the slump cone is in contact with the slump flow table.

It was shown that decreasing the cone lifting velocity by two times (from 500 to 250 mm/min) did not influence final slump flow. But the height of cone lifting plays indeed a significant role in the slump flow test. It was found that the optimal height of the cone lifting for the highly flowable concretes under investigation is 50 mm.

Moisture on the surface of the slump flow table has a pronounced effect on the results of the slump flow tests. In the case of a “wet” surface, an effect of the viscosity on the flowing process is superimposed with effect of sliding of fresh concrete on the surface with low friction. Therefore, the “true” viscosity of the fresh concrete can only be estimated using tests with a dry table surface for slump flow testing, assuming that there is no sliding in the case of “dry” surface.

The analytical approach for the slump test is a very important part of further modelling. Analysis of the internal stresses in numerical modelling is based on the theoretical basis of analytical approach for slump test. The analytical approach provides a link between dimensionless analyses of the slump test and parameters in the numerical model such as contact bond and yield stress parameter. Therefore, the formulations from analytical approach will be implemented into the program code for analysing of the internal stress distribution, calculation of the parameters of numerical model according to the specified yield stress value, see Chapter 5.3.1.3.

Key positions of the analytical solution are the following:

- ✓ Yield stress is determined as a function of the cone geometry and the final slump.
- ✓ The dynamic viscosity of fresh concrete is determined as a function of flow rate and spread time.

It was shown that the analytical solutions presented for estimating the Bingham rheological parameters are adequate and can be used for numerical modelling. Analytical solutions will be implemented into the PFC for adequate representation of the yield stress in dimensionless form in numerical modelling.

3 Experimental investigation of fresh concrete rheology (Macrolevel)

CHAPTER 4

INTERACTION BETWEEN DISCRETE PARTICLES – EXPERIMENTAL INVESTIGATION ON THE MESOLEVEL

4.1 Introduction

This chapter presents an investigation whose objective is development of a material model for adequate simulation of the rheological behaviour of fresh concrete using the Discrete Element Method (DEM). The methodology for investigation of interaction between neighbouring particles with some amount of viscoelastic material between them is explained. The experimental investigations were performed with various materials: polymer solutions in water, i.e., material with time-independent rheological behaviour, and two types of fresh mortar with time-dependent rheological properties. The characteristic material behaviour of various loading regimes is presented and critically discussed. Based on experimentally obtained force-displacement relationships, a material model for the interaction of neighbouring solid particles was developed. This model can be introduced directly into numerical codes based on the Distinct Element Method.

4.2 Discretisation of meso-structure of fresh concrete

Concrete is a very complex composite with a highly heterogeneous structure at various length scales ranging from nanometers to millimeters. The latter is also referred to as the meso-level of observation. At this level the meso-structure of concrete consists of aggregates, cement paste or fine mortar, air inclusions, and, in some cases, fibres. When the DEM is applied to simulate the behaviour of fresh concrete, the usual approach is to make the aggregate particles discrete, primarily the coarse particles, as solid spheres or clumps of several overlapping spheres, depending on the shape of the aggregates. The fine mortar filling the space between the aggregates is regarded as a fluid phase. A huge number of modelled particles would be needed to make fine mortar appropriately discrete! So, in order to limit the number of particles needed for simulation, this phase is not represented in a discrete manner, but rather by defining the interaction between neighbouring particles according to the rheological properties of a fluid. Therefore, the quality of the model depends both on making the aggregates, and, if needed, the fibres appropriately discrete as particles and on applying the correct description of the force-displacement relationships among these particles.

The choice of particle sizes and quantities to model the aggregates can follow the particle size distribution given by the grading curve; see, for example, [45, 111]. In many cases, a simple presentation of aggregates by monosize spheres of representative diameter might be sufficient [89, 92, 68, 45, 77].

Only the basic elements available in the programme should be used in making the meso-structure discrete in modelling: particles (spheres for 3D and discs for 2D) and walls, for which different

4 Experimental investigation on the mesolevel

shapes are possible. Walls are used to represent the boundary conditions in the numerical model, and particles with different sizes and different behaviours are used to discretise the fresh concrete meso-structure. Figure 4.1 presents a virtual vertical cross-section of the slump cone with fresh concrete and an example of the discretisation of the meso-structure using discrete elements. Here, the vertical cross-section of the slump cone means the imaginary removing of fresh concrete from one side of the vertical cross-section plane; see Figure 4.1a. The aggregates which have their center of mass in another half-space are assumed to remain intact. In Figure 4.1 an image of the concrete surface after the slump flow test was used to visualize concrete heterogeneity. One section of the cross-section is zoomed, Figure 4.1b; an example of the discretisation of meso-structure is superimposed on the zoomed image; see Figure 4.1c.

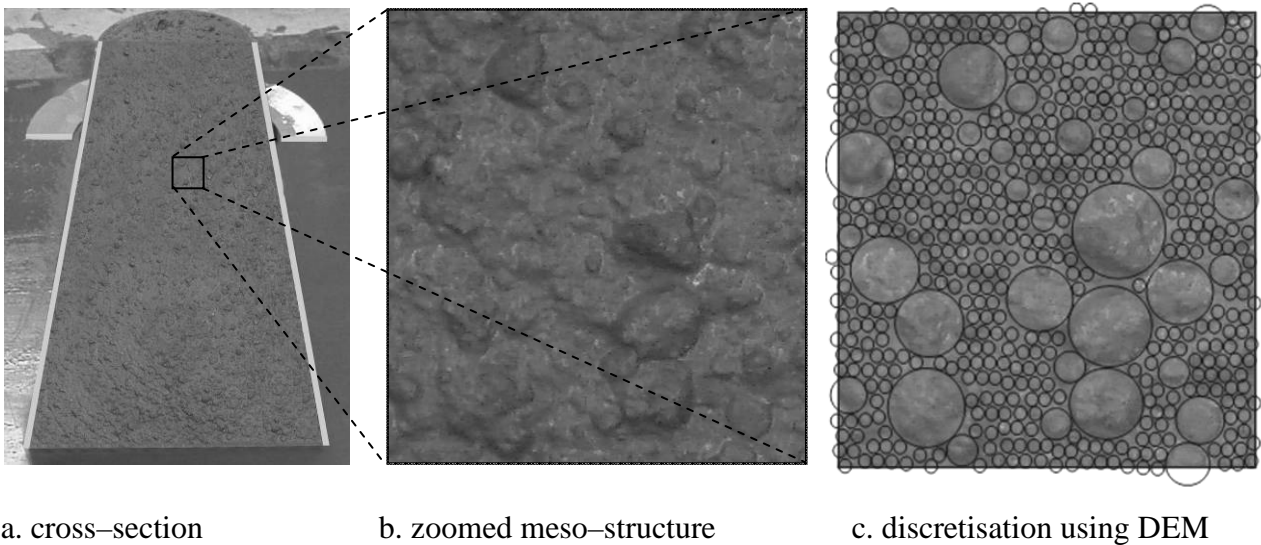


Figure 4.1: *Cross-section of the slump flow cone with fresh concrete and an example of the discretisation of the meso-structure of fresh concrete using discrete spheres*

The volume of the slump flow cone is approximately 5.5 dm^3 . The larger spherical particles represent the coarse aggregates and smaller particles represent sand grains covered with mortar.

Figure 4.2 shows schematic representative discretisation of the meso-structure of fresh concrete and the possible modes of contacts between neighbouring entities. Since the entities are bonded by the viscoelastic material located among them, forces and moments can be transferred from one entity to another also in the case when the surfaces of entities have no points of contact.

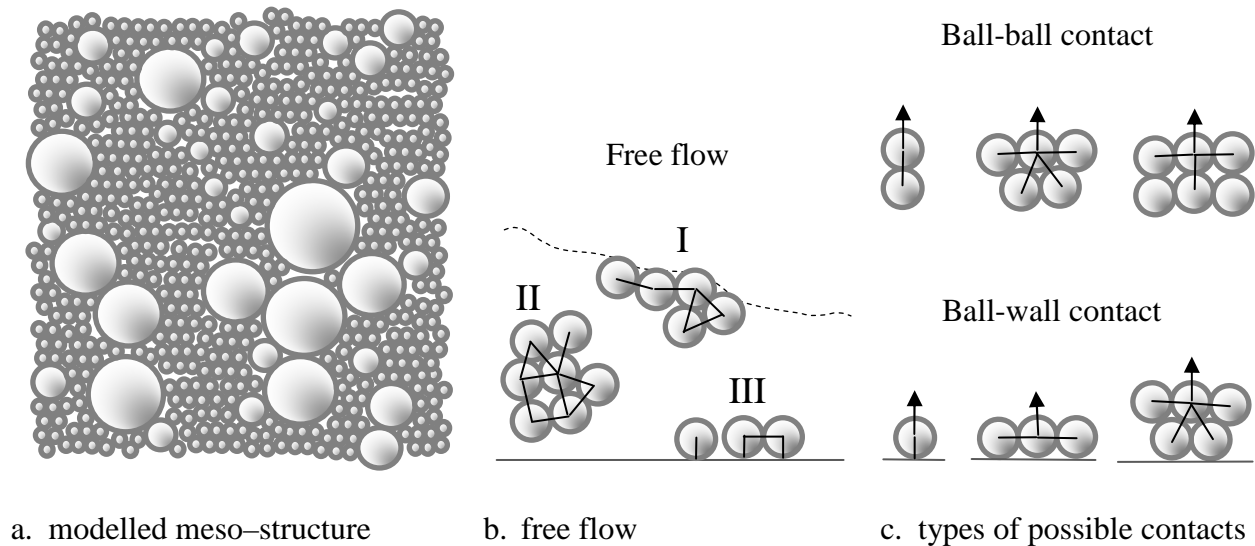


Figure 4.2: *Modelled meso-structure of fresh concrete and possible locations of the particles in a free flowing fresh concrete*

Figures 4.2b and 4.2c present two main types of contacts used in the DEM: particle–particle and particle–wall contacts. It is assumed that at one instant of simulation only one contact can exist between two neighbouring particles while all bonds between the considered particle and individual neighbouring particles which are in contact with it are simultaneously active. It goes without saying that a wall element can have multiple simultaneous interactions with particles. The number of contacts of a particle with its neighbours is limited by the coordination number, which depends on the sizes of the neighbouring particles. The maximal coordination number is possible inside the modelled material, where each particle is surrounded by other particles on every quarter; see II in Figure 4.2b. If the particle is located on a free surface or is in contact with a wall, then the coordinate number is smaller; see I and III in Figure 4.2b. Each contact bond has its individual properties. By taking it into account the experimental investigation should be carried out in such a manner that each representative contact interaction is isolated from other interactions. Possible locations of particles for investigation are sketched in Figure 4.2c.

It should be noted that in free flow the entities move relative to the center of coordinates of each other. The interaction between neighbouring entities implies the motion of one entity relative to the second entity on the understanding that both entities are connected by means of the contact bond.

4.3 Viscoelastic materials used in the investigation

Two cement–based materials with different rheological behaviour were used in this study: a fine mortar for self–compacting concrete (further referred to as SCC) and a fine–grain, ultra–high performance concrete (UHPC). Their compositions are given in Table 4.1. Since it is well known that the rheological behaviour of fresh concrete is highly thixotropic and time–dependent, aqueous solutions of the polymer Carbopol [93] were tested first to exclude such effects. Carbopol solutions were chosen as reference materials because they exhibit a rheological behaviour according to the Bingham model and do not change their properties over time. Similar solutions have been successfully used as the matrix in model concretes by some other researchers as well [13, 86].

4 Experimental investigation on the mesolevel

The rheological behaviour of all materials under investigation was measured using a HAAKE MARS III rheometer equipped with a special measuring cell for approximately 500 ml of material [58]. The observed average shear stress–shear rate curves are shown in Figure 4.3. The courses of the curves confirm that all these materials can be well approximated by the Bingham model with plastic viscosity η and the yield stress τ_0 .

The fresh concrete is sheared at a high rate before the rheological test. Then, the shear rate is decreased gradually and the stress is measured. The relationship between the stress and shear rate is plotted and the intercept at zero–shear rate is the yield stress, while the slope is the plastic viscosity. Only the linear part of the diagram can be used for determination of the Bingham parameters. The corresponding Bingham parameters were obtained as shown in Figure 4.3 in following shear rate intervals, depending on the type of material:

1. Carbopol 0.3% and 0.5% – from 2 to 10 rot/min;
2. SCC – from 2 to 10 rot/min;
3. UHPC – from 2 to 6 rot/min.

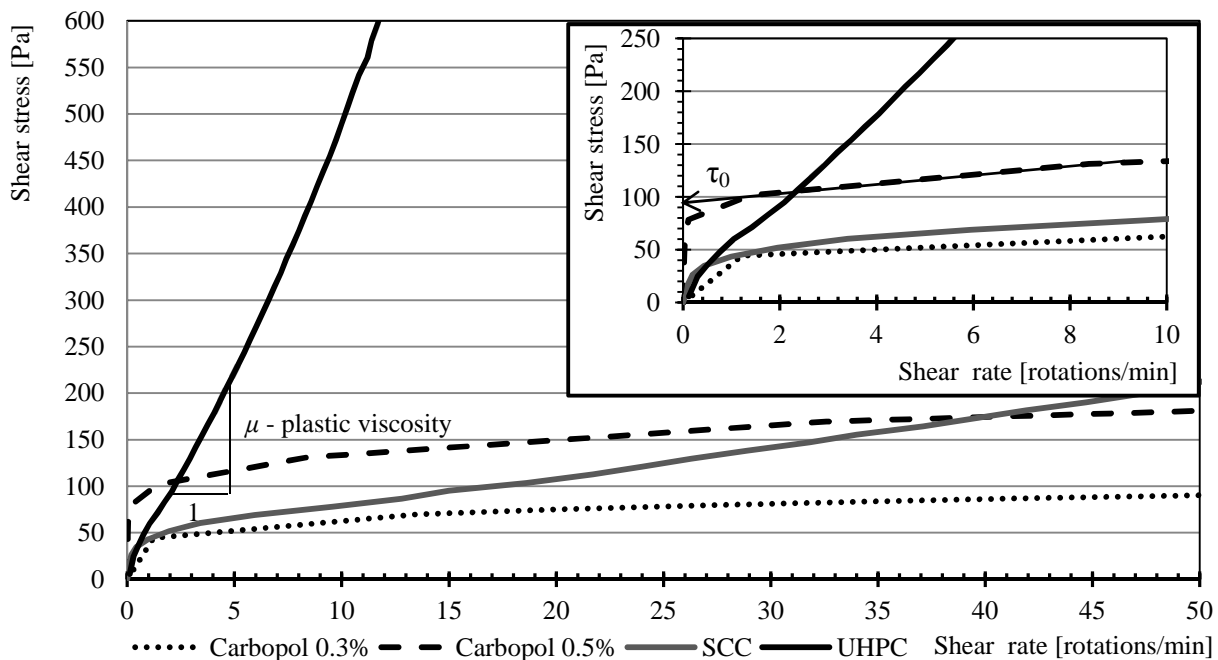


Figure 4.3: Average shear stress–shear rate curves for the materials under investigation

A comparison of the curves shows that UHPC has the highest plastic viscosity, followed by SCC mortar, and then by Carbopol solutions; also see Table 4.1. For the Carbopol solutions the plastic viscosity increases slightly with the polymer content; here two concentrations of 0.3% and 0.5% by mass were considered. The clearly highest yield stress was obtained for the 0.5% Carbopol solution; the lowest was measured for UHPC, cf. Table 4.1. Obviously the increase in the concentration of the polymer in the solution had a much more pronounced effect on the yield stress than on the plastic viscosity. It should be noted here that the derived yield stress values according to the Bingham model do not describe the behaviour of the materials under investigation very well due to the pronounced nonlinearity of the measured curves at low shear rates.

Table 4.1: *Rheological properties of materials under investigation according to Bingham model*

	SCC	UHPC1	Carbopol 0.3%	Carbopol 0.5%
Viscosity, Pa·s	23.4	155	4.9	6.5
Yield stress, Pa	50	5	42	96

Furthermore, it should be noted that the rheometer measures the shear stress–shear rate curve in a wide range of shear rates in contrast to the slump flow test; see Figure 4.3. The slump flow test is a one–point test delivering a yield stress on the basis of concrete deformability at some not well defined, relatively low shear rate in the test; see Section 2.4.2. This might be one of the possible explanations for the difference in the yield stress values obtained from the slump flow test and the rheometer measurements for the same mix.

The rheological measurements on the UHPC1 showed that this concrete had an extremely low yield stress in the chosen interval of shear rates. However, the slump flow of the UHPC1 was not extremely high. In addition, the plastic viscosity of the UHPC1 was measured using the rheometer at several times higher than the viscosity obtained from the slump flow test, although the times T_{50} are the same for UHPC1 and SCC; see Table 3.8. Thus, the plastic viscosity also has to be approximately the same.

It can be concluded that the data obtained from the rheometer measurements differ from the data obtained from the slump flow tests but does not contradict them. It is safe to say that the UHPC1 has a lower yield stress and a higher plastic viscosity in comparison with SCC or SCC mortar, which was important to confirm using rheological measurements.

4.4 Interaction between neighbouring entities with viscoelastic material between them

Viscoelastic material among entities acts as a vehicle for forces and moments between the entities. Moreover, the viscoelastic material takes part in the process of deformation; i.e., the shape of the viscoelastic material changes during deformation. The force which arises out of this deformation is a contact bond force. The magnitude of the contact bond force depends on the behaviour of the viscoelastic material, here fine mortar, the amount of viscoelastic material which should be deformed, and deformation rate, etc.

Interaction between neighbouring entities implies that one of the entities moves relative to the second and each of their motions influences the other. The number of such interactions depends on the number of neighbouring entities. The information on all interactions determines the resulting force, which provides direction and velocity of the motion of the entity under investigation. It is assumed that the behaviour of the investigated entity depends only on the motion of the neighbouring entities. However, other adjoining, not neighbouring, entities have contact bonds with neighbouring entities, and they may therefore indirectly influence the behaviour of the entity under investigation.

Two modes of interaction are possible: tension and compression. Tension implies that neighbouring entities have no direct contact with each other. The forces and moments pass from one entity to another due to the viscoelastic material between them. Compressive force is possible in the tension

4 *Experimental investigation on the mesolevel*

mode but this compressive force arises due to compression of the viscoelastic material and cannot be higher than the yield stress of the material. When the entity's surfaces are in direct contact, compressive forces are transferred directly from one entity to the other. It goes without saying that the stiffness of the solid components of fresh concrete aggregates is much higher than the stiffness of fine mortar.

It is reasonable to assume that viscoelastic material (fine mortar) is homogeneous. Then the main parameters of the contact bond are the rheological behaviour of the viscoelastic material and the area of the cross-section of the viscoelastic material in the zone of deformation. The area of the cross-section depends on the shape of the viscoelastic body, which changes with changing of the distance between entities. The smaller entity determines the thickness of the contact bond. In the case of monotonic tension the viscoelastic material is stretched in the direction of motion. The thickness of the contact bond decreases with increasing distance between the entities and vice versa. At some specified distance between entities the thickness of the contact bond decreases to zero and the contact bond fails.

The main characteristic of this interaction is shown using a force-displacement diagram, which represents changes of the state of the contact bond. Therefore, the parameters which should be measured are the displacement of one entity relative to the second entity in the specified time interval and the corresponding force of the contact bond. This displacement can be resolved into its normal and shear components with respect to the contact plane. The pure normal component of the displacement is defined such that the particles move along the line which connects the centers of the particles in the case of particle-particle contact and along the perpendicular dropped from the center of the particle on the wall for the case of particle-wall contact. The pure shear component of the displacement is defined as the rotation of one particle around another in the case of particle-particle contact and sliding, no rolling, of the particle along the wall in the case of particle-wall contact; the distance between particles or particle and wall remains unchanged. It is assumed that pure shear displacement can be infinite because some viscoelastic material always remains between entities independent of their tangential motion. Thus the contact bond cannot be broken in this mode, while pure normal displacement is finite and can lead to complete separation of the particles.

Both components of the motion, normal and shear, can be investigated separately. However, the equipment needed to investigate pure shear motion is much more complicated than the equipment for investigation of purely normal motion. Development of such equipment is a very complicated task requiring extensive resources. Hence, in this study only the pure normal motion is investigated, while the behaviour of the contact bond by pure shear motion will be predicted using theoretical knowledge in combination with the results of investigation of normal motion. The equipment for the investigation of pure normal motion and the methodology of measurements are presented in the following section.

4.5 Experimental equipment

The measuring equipment used in this investigation consists of a "Zwick Z 1445" universal electrical-mechanical machine with a load cell of max. 10 N, to which a transparent equipped ball made of glass was rigidly attached, and a personal computer for the test control and for recording of data; see Figure 4.4. The data of the cross-head movement and the load cell were transmitted to the

personal computer at a rate of 100 Hz. One point in the force–displacement diagram corresponds to a measurement during one time interval.

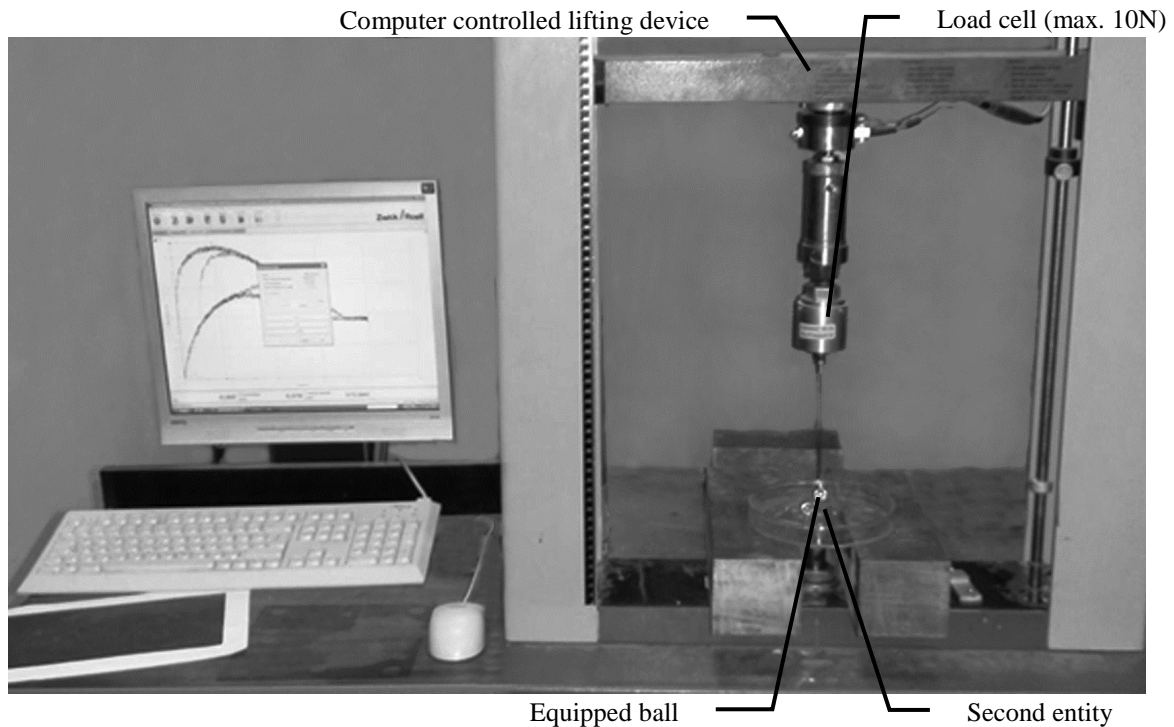


Figure 4.4: *The equipment used for measurement of the interaction of two entities with a layer of viscoelastic material in between*

The given ball of diameter 10 mm was moved with the cross–head of the testing machine; the second entity was either a glass surface or another particle made of glass. The position of the second entity was always fixed. The load cell was zeroed before the entities were brought into contact. The displacement measurement was zeroed when the two entities came into direct contact with each other. The experiments were performed with various displacement rates ranging from 10 mm/min to 200 mm/min.

4.6 Arrangement of solid spheres and viscoelastic material and measurement procedure

The test setups chosen for this investigation covered all possible types of the contact bond, as presented in Figure 4.2c. The force–displacement behaviour of the contact bond is investigated for various amounts of the viscoelastic material between entities and for different regimes of the entities' motion.

The methodology of the measurements is based on published work on adhesion and liquid bridge forces [51, 53, 54]. In the investigations cited, the particles are arranged vertically and viscoelastic material is placed between them. The amount of viscoelastic material depends on the size of the particles. Changes in the shape of the liquid bridge are considered theoretically and presented in [145, 12]. The lower particle is fixed and vertical motion of the upper particle is monitored. It is assumed that the effect of gravity in this case is negligible [16, 51, 132]. The results of the investigation are presented in the form of the force–displacement diagrams. While the

4 Experimental investigation on the mesolevel

investigations cited considered only monotonic tensile loading, the current experimental work included stops for the motion as well as backward motion.

The first type of contact under investigation is the contact “single ball – viscoelastic material – wall”. In this experiment the viscoelastic material covers the surface of the test glass, which represents a wall element. Three different thicknesses of the layer were used; they corresponded to 25%, 50% and 100% of the ball diameter, with the ball, hereinafter called the equipped ball, representing a spherical discrete element in the DEM simulation, or aggregate in real concrete; cf. Figure 4.5.

In the experiment the equipped ball moves down until it comes into contact with the bottom surface of the test glass (point contact) and deforms the viscoelastic material through what we consider to be uniaxial compression. The contact force increases in proportion to the depth of penetration of the equipped ball into the layer of viscoelastic material. Direct contact between equipped ball and wall is the initial position of the equipped ball in the series of experiments with “single ball – viscoelastic material – wall” contact.

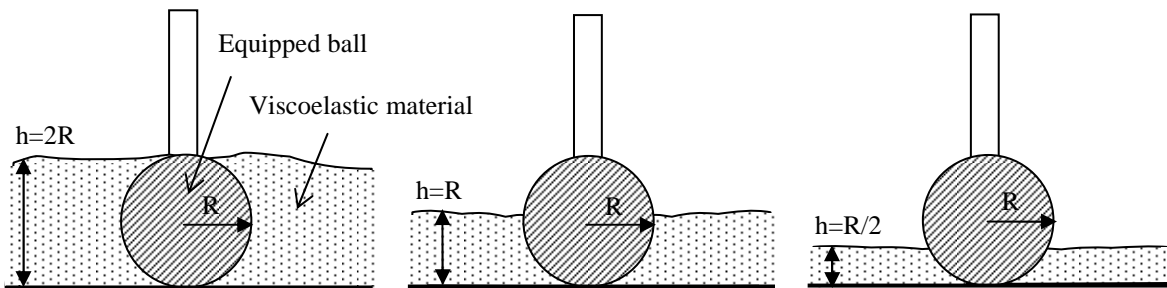


Figure 4.5: Initial positions of the equipped ball and different thicknesses of layers of viscoelastic material for the experiment “single ball – viscoelastic material – wall” (the covering layer is related to the diameter of the ball, from left to right: 100%, 50% and 25%)

The initial thicknesses of the covering layer and corresponding coverings of the equipped ball for experiments with “ball–wall” contact are presented in Table 4.2.

Table 4.2: Covering of the equipped ball in the experiments with “ball–wall” contact and various thickness of covering layer; see Figure 4.5

Thickness of the covering layer, mm	Initial thickness of the contact bond, mm	Covering of the equipped ball, %
10	10	100%
5	5	50%
2.5	2.5	25%

In the case of the investigation of the contact “single ball – viscoelastic material – single ball” the viscoelastic material is located between two balls. The second ball is glued to the surface of the test glass. The initial position of the equipped ball is direct contact with the second ball. The center of the second ball is located on the axis of motion of the equipped ball. Initially the top of the second ball is covered with some viscoelastic material. In the next step the equipped ball is brought into

4.6 Arrangement of solid spheres and viscoelastic material and measurement procedure

contact with the second ball and the excess of viscoelastic material is removed from the zone of contact.

The amount of the material between the equipped ball and the second ball depends on the size of the second ball. In this investigation second balls with diameters 10, 8, 4 and 2 mm were used, while the diameter of the equipped ball was always 10 mm. The initial position of the balls and initial shape of the viscoelastic material between them are schematically presented in Figure 4.6. It is assumed that the side surface of the viscoelastic material has the shape of a cylinder with the diameter d equal to the diameter of the second ball; see Figure 4.6.

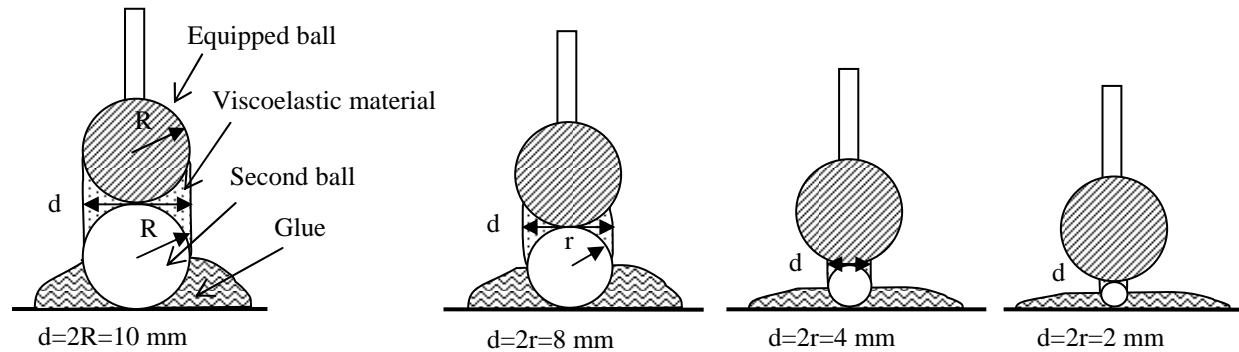


Figure 4.6: Initial positions of the equipped ball and thicknesses of the viscoelastic material for the test “single ball – viscoelastic material – single ball” with balls of different sizes

Initial conditions for tests “single ball – viscoelastic material – single ball” are summarized in Table 4.3.

Table 4.3: Initial thickness of the contact surface and corresponding covering of the equipped ball for various sizes of the second ball in the tests “single ball – viscoelastic material – single ball”, cf. Figure 4.6

Diameter of the second ball, mm	Initial thickness of the contact, mm	Covering of the equipped ball, %
10	10	50%
8	8	20%
4	4	4.17%
2	2	1.01%

The covering of the second ball is always 50%, but the covering of the equipped ball is different depending on the size of the second ball. For a 50% covering of the ball with 8 mm in diameter the covering of the equipped ball is 20%. For the balls of 4 mm and 2 mm diameter the covering of the equipped ball is about 4.2% and only 1%, respectively.

The arrangement described in the previous paragraph represents contact between two neighbouring balls only. In concrete, however, each particle has numerous contacts simultaneously to other particles. Figure 4.7 schematically presents a ball which is surrounded by other balls of various sizes and possible direction of the motion of this ball for investigation of the contact bond behaviour. The spaces between particles are filled by viscoelastic material. For investigation of the

4 Experimental investigation on the mesolevel

contact bond behaviour some particles should be removed in order to have free access to the ball under consideration and the possibility to measure the contact force. Thus the adjoining balls, i.e. the centers of the balls, should be located in a half-space and the plane which divides the space into two half-spaces should pass through the center of the selected ball. The direction of motion is perpendicular to this plane as it is shown in Figure 4.7. In this case covering of the ball is approximately 50% of its surface.

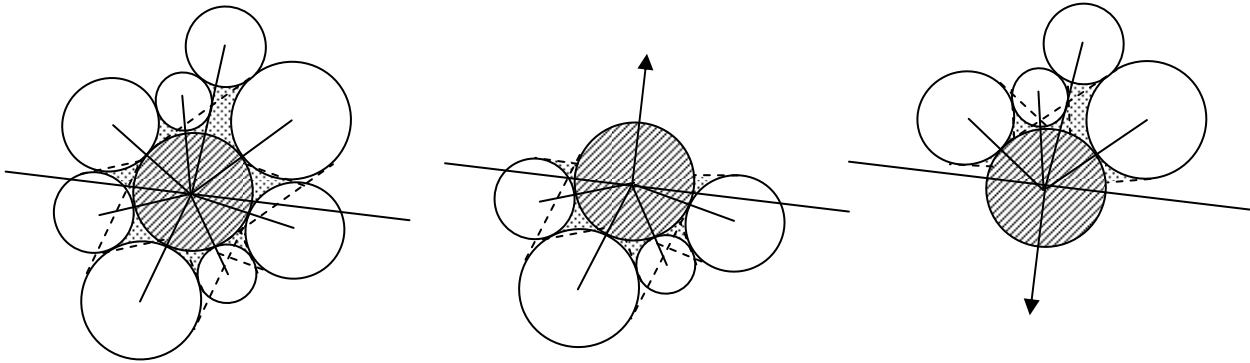


Figure 4.7: Representation of the ball, which is surrounded by other balls of various sizes (left) and possible directions of the motion of this ball for investigation of contact bond behaviour (middle and right)

In order to fill all voids between the selected ball and those adjoining, the covering of the adjoining balls also should be about 50%, see the dashed lines in Figure 4.7. It should be noted that Figure 4.7 is two-dimensional (2D). Thus, it takes 3 or 4 balls, here circles, of approximately the same size as the ball under consideration. In the three-dimensional (3D) case the number of the balls in contact increases up to a coordination number of 9.

For experiments with the system “single ball – viscoelastic material – adjoining balls” the surrounding balls were located around or below the equipped ball. Surrounding balls were glued to the surface of the test glass. The initial position of the equipped ball is in direct contact with surrounding balls, schematically presented in Figure 4.8. The main condition of the test “single ball – viscoelastic material – adjoining balls” is that each adjoining ball is in direct contact with the equipped ball while the tops of the surrounding balls are covered with viscoelastic material. Further, the equipped ball is brought in contact and the excess of viscoelastic material is removed from the zone of contact. The covering of the equipped ball is 50% in all tests with adjoining balls in order to be comparable with other tests.

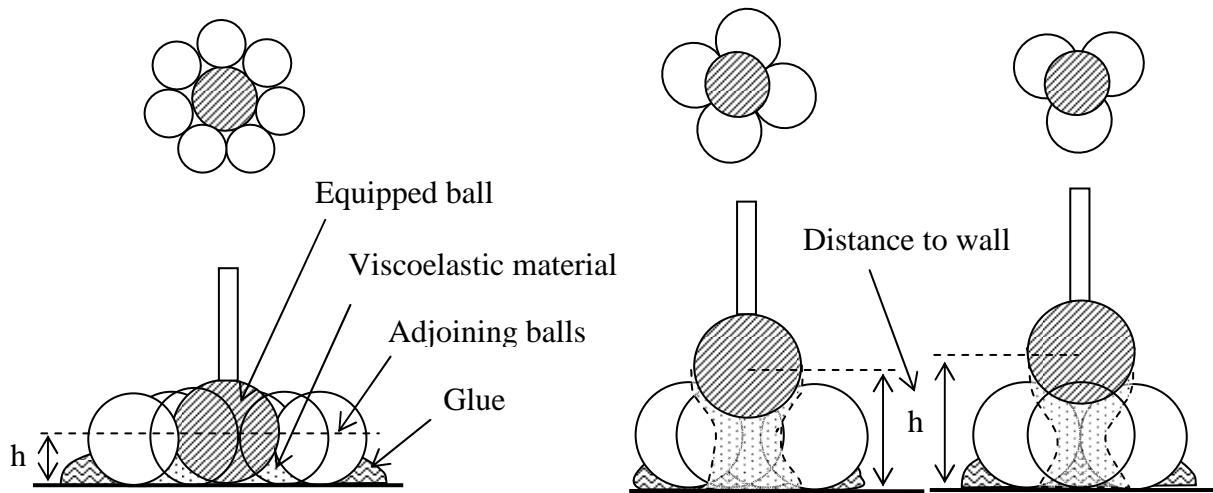


Figure 4.8: The initial position of the equipped ball in the tests “single ball – viscoelastic material – adjoining balls” with 7, 4 and 3 adjoining balls. Covering of the equipped ball is 50%

Initial conditions for tests are summarized in Table 4.4.

Table 4.4: Initial thickness of the contact and corresponding covering of the equipped ball for various arrangements of the adjoining balls (cf. Figure 4.8)

Number of adjoining balls	Initial thickness of the contact, mm	Covering of the equipped ball, %
7	10	50%
4	10	50%
3	10	50%

It should be noted that an increase in the number of adjoining balls leads to an increase of the void space between adjoining balls, which can be characterised by the radius of an inscribed circle between the adjoining balls: a larger radius of the inscribed circle implies a larger void between the adjoining balls. The distance h between equipped ball and wall, as in Figure 4.8, depends on radius of inscribed circle. The minimal distance h is equal to the radius of the equipped ball; the radius of the inscribed circle is maximal in this case and also equal to the radius of the equipped ball. Only 6 adjoining balls (each 10 mm in diameter) can be placed around the equipped ball in the case of the maximal radius of the inscribed circle. However, the balls have to cling close each other. Such an arrangement of the adjoining balls is possible only in theory, zero gaps between balls. In reality the adjoining balls hamper the motion of the equipped ball. The gaps between balls have to be increased. It is possible using 7 adjoining balls, each 8 mm in diameter.

The parameter which varies in the tests “single ball – viscoelastic material – adjoining balls” is the amount of material which has to be deformed, proportional to the volume of void between adjoining balls. Thus the largest amount of the viscoelastic material is seen in the case of 7 adjoining balls, smaller in the case of 4 balls and smallest in the case of 3 balls.

In addition it should be noted that the difference between tests with 3 or 4 adjoining balls and 7 adjoining balls is the manner of deformation. A free surface of the viscoelastic material deforms in

4 Experimental investigation on the mesolevel

the case of 3 or 4 adjoining balls deforms; there is no need to extract additional material from the void between balls. However, in the case of 7 adjoining balls, extraction of the viscoelastic material from the voids between adjoining balls and wall is obligatory. An area of the cross-section of the voids between adjoining balls and wall plays a great role here. For more details see Section 4.9 for a discussion of the results of tests “single ball – viscoelastic material – adjoining balls”.

Three types of motion of the equipped ball were used in this study:

- increasing the distance between entities monotonically from the initial position until complete separation (when bridging by the viscoelastic material fails);
- decreasing the distance between two entities after their previous complete separation; and
- moving the equipped ball with stops and further continuation of the motion in opposite direction.

The measured quantities and a typical force–displacement diagram are schematically presented in Figure 4.9.

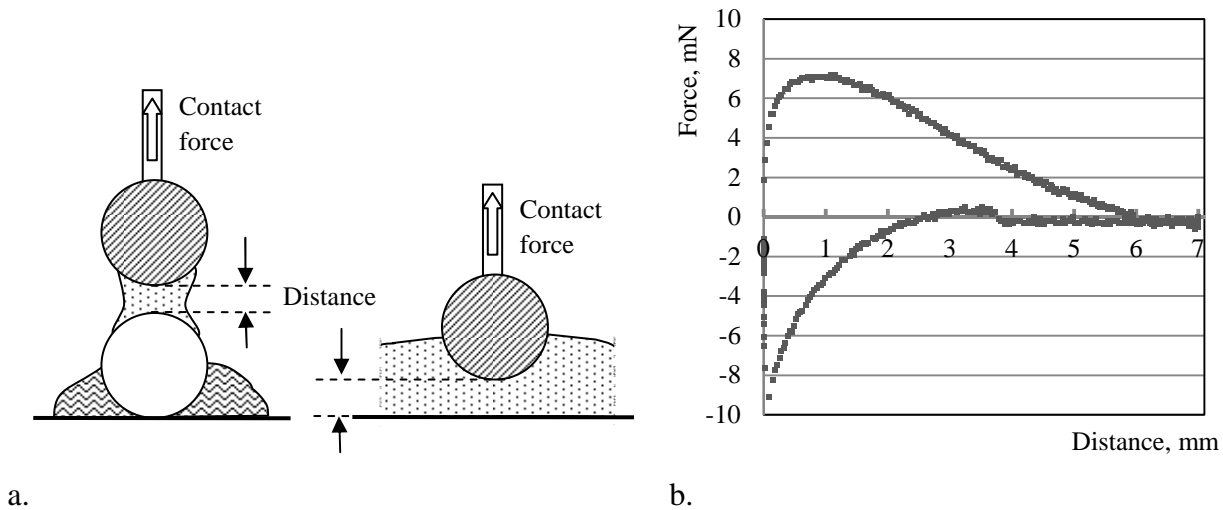


Figure 4.9: a) measured quantities and b) a typical force–displacement diagram obtained from the test with an equipped ball

The initial position of the equipped ball is always in direct contact with second entity (ball, wall or adjoining balls) – “zero” gap. Therefore, the “positive” distance means some gap between entities, represented as a displacement of the moving block with the equipped ball attached rigidly to the moving block, or lifting device for the case when both entities are on the axis of motion; see Figure 4.9. The measured distance in the tests with the system “single ball – viscoelastic material – adjoining balls” presents the displacement of the equipped ball from the initial position, which depends on the arrangement of the adjoining balls; see Figure 4.8.

4.7 Evaluating the force–displacement diagrams

Figure 4.10 presents typical force–displacement diagrams of the ball–ball experiments performed in the monotonic regime (Figure 4.10a) and with stops (Figure 4.10b). The characteristic points are highlighted; characteristic forces and distances between entities are given. In the monotonic regime,

the first point gives the initial force at the beginning of the experiment at a distance equal to zero; the second point shows the maximum tensile force at some distance between the entities; and the last point corresponds to zero force at the distance at which the entities separate completely, i.e., bond failure. After complete loss of contact the equipped ball is moved in the reverse direction back to the initial position; a new contact is created at a distance smaller than the distance of the contact loss. This distance depends on the thicknesses of the viscoelastic material between the balls. At the very beginning of the new contact the contact force is zero. With distance decreasing between the entities the cross–section of the contact increases. The viscoelastic material in the path of equipped ball is gradually squeezed out of the gap between the balls, while the contact, compression force steadily increases. After the equipped ball reaches its initial position in contact with the second ball, the viscous component of the force gradually vanishes due to continuing viscous deformation of the material between the balls until the initial elastic compressive force is reached after some time.

The contact force acting between entities can be always resolved into elastic and viscous components. This characteristic behaviour can best be demonstrated in experiments with stops, as shown in Figure 4.10b. After each stop in the ball movement, the viscous component vanishes, while the elastic component remains. However, when the equipped ball starts moving again, the viscous component of the force appears again, so that the force–displacement curve comes back to its original shape as measured in the monotonic regime (experiments without stops). The characteristic points coincide in both experiments (with and without stops).

The principal difference between ball–ball and ball–wall contacts is the amount of the material which is deformed when the equipped ball starts to move. Since it is larger in the case of ball–wall contact in comparison with ball–ball contact, the contact force changes less pronouncedly with increasing distance. As a result, the force–displacement diagrams of the experiments with ball–wall setup are “stretched” in the direction of longer distances. Furthermore, larger initial thickness of the contact results in higher maximum force values.

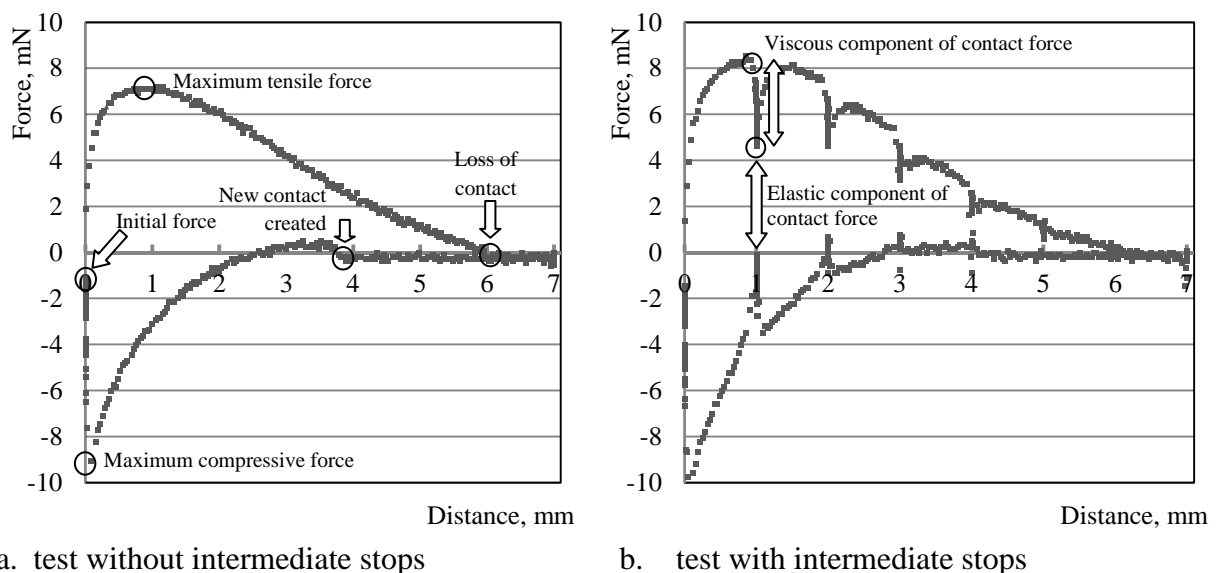


Figure 4.10: Typical force–displacement diagrams from ball–ball experiments with highlighted characteristic points: a) monotonic separation of the balls and monotonic restoration of direct ball–ball contact; b) measurements with a number of intermediate stops

4.8 Testing programme

The first series of tests was performed on Carbopol solutions with concentrations of 0.3% and 0.5%. Other parameters under investigation were the type of contact (“ball–ball”, “ball–wall”), covering of the equipped ball, displacement rate, and direction of motion (with or without changes).

In particular the following ball–wall tests were carried out:

- tests with different coverings of the equipped ball (100%, 50% and 25%);
- tests with various displacement rates (10, 20, 50, 100 and 200 mm/min);
- tests with stops and various displacement rates (10, 20, 50, 100 and 200 mm/min);
- series of tests with one change of the direction of motion (10 and 50 mm/min);
- series of tests with multiple changes of the direction of motion (10 and 50 mm/min).

The ball–ball tests included:

- tests with different sizes of the second ball (10, 8, 4 and 2 mm in diameter);
- tests with various displacement rates (10, 20, 50, 100 and 200 mm/min);
- tests with stops and various displacement rates (10, 20, 50, 100 and 200 mm/min);
- series of tests with one change of the direction of motion (10 and 50 mm/min);
- series of tests with multiple changes of the direction of motion (10 and 50 mm/min);
- series of tests with several balls (7, 4 and 3 balls) with stops and with different displacement rates (10 and 50 mm/min).

Analyses of the test results of Carbopol solutions, SCC mortar and UHPC were performed. Since the rheological behaviour of cement–based materials in the fresh state is time–dependent, particular care was taken in recording the time during the experiments. The time measurement started when the material was extracted from the mixer for the first time. In addition it should be noted that the rheological properties of fresh concrete or mortar change quickly on the exposed surface than is the case deep inside the probe, i.e., stiffening due to water evaporation. From this perspective it could be expected that only the ball–wall test would provide meaningful and reproducible results. In the case of ball–ball tests the ratio of free surface to material volume is less advantageous, which causes a rapid stiffening of the material. Moreover, the process of covering the balls with an even layer of mortar also takes some time, which strongly affects the results. Therefore, only ball–wall experiments on cement–based materials are presented here. The programmes of the tests with SCC mortar and UHPC were similar to the programmes of the “ball–wall” tests on Carbopol solutions.

4.9 Results and discussions of the tests with Carbopol solutions

The experiments with Carbopol solutions were performed with two concentrations of polymer: 0.3% and 0.5% by mass. Further parameters under investigation were velocity of the equipped ball and the covering of the equipped ball. Both types of testing regimes, monotonic and that with stops, were applied.

Figure 4.11a shows the effect of the concentration of the Carbopol on the force–displacement diagram in the ball–ball experiments with stops performed, and with the equipped ball 50% covered. In general, the increase in the polymer content causes a considerable increase in the elastic component of contact force, while the effect on the viscous component of the contact force is less pronounced. This result agrees well with the results of rheological measurements, cf. Section 4.3,

where the polymer concentration influenced the yield stress, here responsible for the elastic component, to a much higher extent than the plastic viscosity, i.e., viscous component.

In the ball–wall experiments with the same testing parameters, similar results were obtained. Due to higher amounts of polymer between equipped ball and wall in comparison to the ball–ball test, the peak of the tensile force was higher and shifted slightly in the direction of the higher distances. The increase in the distance values on separation of the contact was, however, relatively small. Furthermore, it should be noted that in the case of ball–wall contact, where there is a higher amount of Carbopol solution between the entities, the effect of the polymer concentration was more pronounced than in the ball–ball tests.

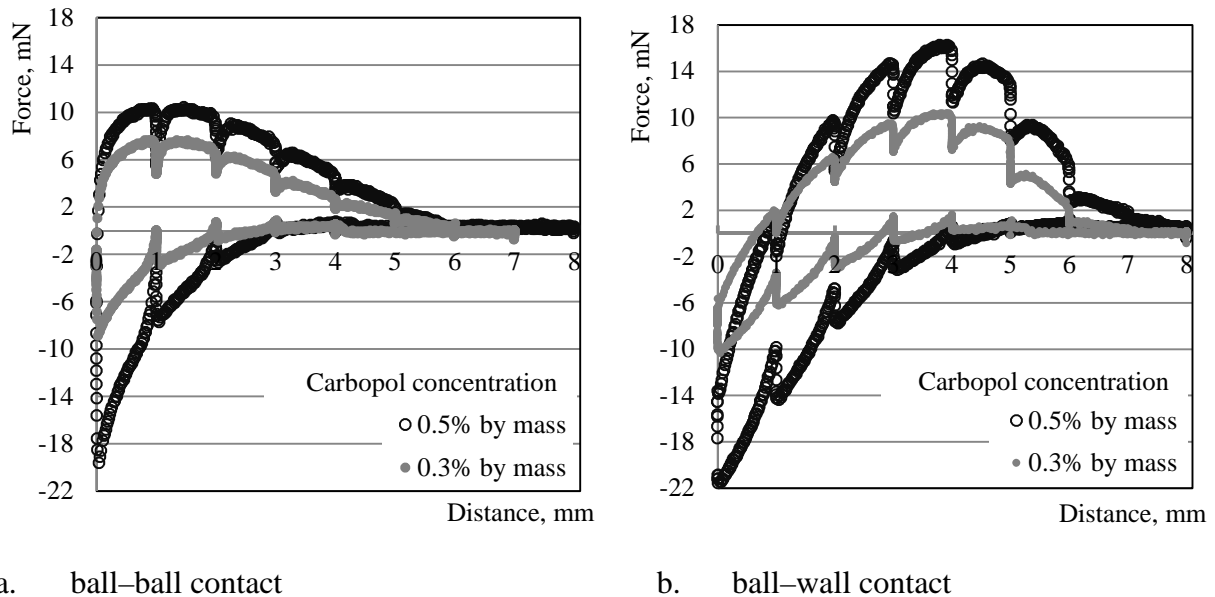
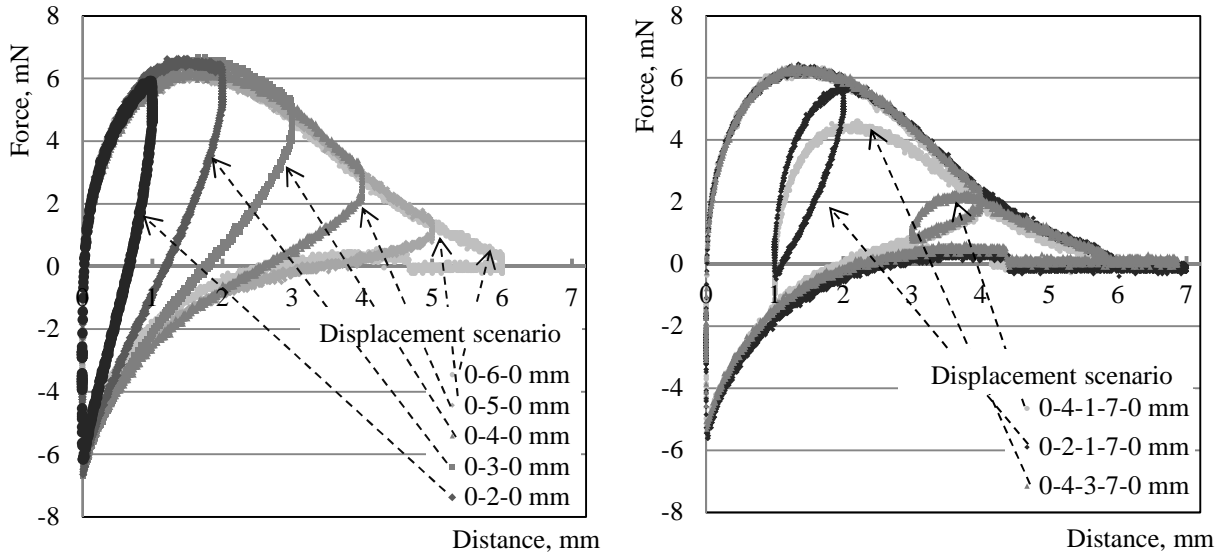


Figure 4.11: Force–displacement diagrams for a) ball–ball contact and b) ball–wall contact obtained for two different Carbopol concentrations. The covering of the equipped ball was 50%; the velocity of the equipped ball was 50 mm/min

In addition to the testing regime with movement of the equipped ball in one direction until the complete separation of the entities and eventually the movement of the ball in the reverse direction, shown in Figure 4.11, further regimes were applied to cover possible scenarios for movement of two neighbouring entities. In the first one, monotonic tension was interrupted by stops at increasing distances between the entities and followed by returning the equipped ball to its initial position. It can be clearly seen that after the “reloading” the course of the curve remains unaltered; see Figure 4.12a. Figure 4.12b shows responses of the system for three other, more complex testing regimes. The legend gives the sequences of distances at which the equipped ball started or stopped moving or changed the direction of movement. For instance, the sequence 0–4–1–7–0 means that the motion started from the initial position and continued until the distance between both balls reached 4 mm; then the equipped ball moved backward until the distance between the entities was 1 mm; after second stop the equipped ball changed the direction of motion again and moved to a distance of 7 mm. Finally, the zero at the end means that the equipped ball returned to its initial position after reaching the distance of 7 mm. Similar to the results presented in Figure 4.12a, the loops end at the envelope curve, which is identical to the curve obtained in the purely monotonic testing regime. The only case when it was not exactly like this was the earlier mentioned scenario 0–4–1–7–0. Here,

4 Experimental investigation on the mesolevel

after relatively large tensile deformation, a partial “unloading” occurred, which was immediately followed by another stretching of the Carbopol solution between the balls. Obviously in this particular case the solution could not “recover”, i.e., gain the initial shape during the very brief stop at the distance of 1 mm. Thus, the force–displacement curve in the “reloading” regime was slightly below the envelope curve.



a. single change in the direction of motion b. multiple changes in the direction of motion

Figure 4.12: Results of the ball–ball tests performed with 0.3% Carbopol solution in various movement regimes of the equipped ball; 50% covering of the equipped ball; the displacement rate of 50 mm/min

The experiments with changing directions of movement after each stop not only showed that testing in the monotonic regime provides an envelope curve for experiments with changing motion directions of the equipped ball but also proved the good precision and stability of the measurements. Similarly consistent results showing the same tendencies were also obtained in tests with the polymer concentration of 0.5% as well as for various displacements rates and coverings of the equipped ball.

Figure 4.13 presents the results of the tests performed with various displacement rates of the equipped ball and stops after every 1 mm of displacement. With increasing displacement rate the forces at given distances between the entities increase while the characteristic distances, i.e., at reaching maximum force or on losing contact, do not change. Both in ball–ball and ball–wall tests the elastic component of the force, force value after a stop, remains nearly unchanged while the viscous part of the force, difference in force before and after a stop, depends strongly on the displacement rate. To demonstrate this more clearly, the calculated values of the elastic and viscous components of the force are presented in Figure 4.14. Figure 4.14 also shows that the points presented for the tension and compression regimes can be fairly connected by bilinear curves. Moreover, the points at the same distance for the viscous component of the force are located symmetrically with respect to the “Distance” axis. These facts will be used in the following section for the development of the material model. Please note that some scatter in the values of the elastic component of the force results from minute inaccuracies in the measurements.

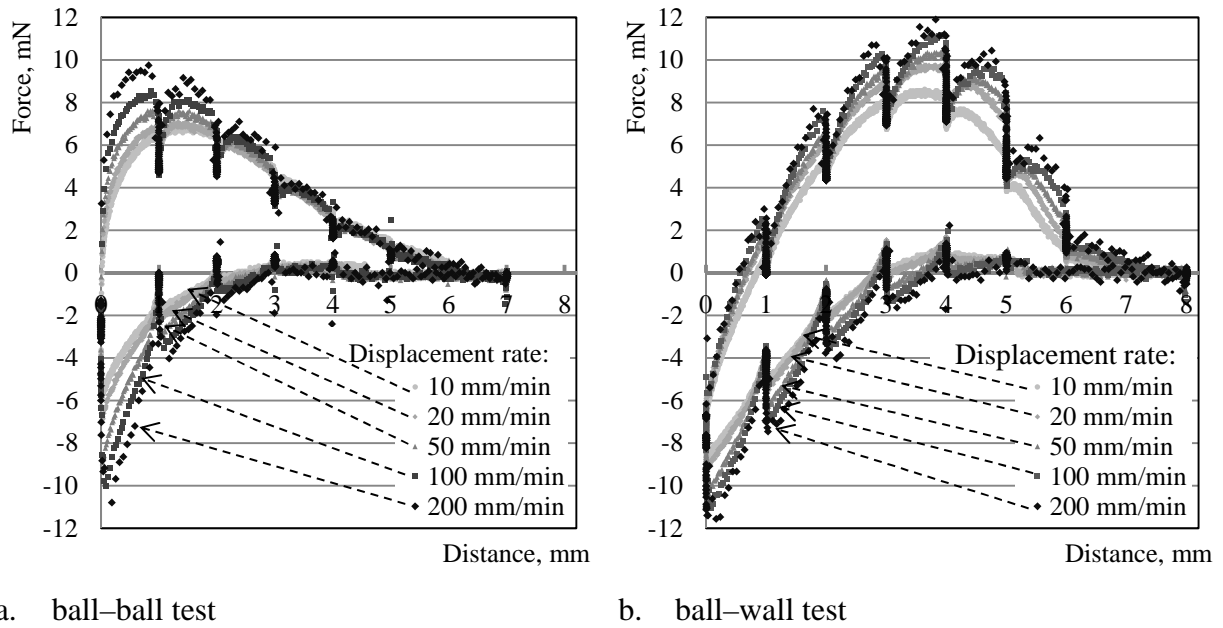


Figure 4.13: Effect of the displacement rate of the equipped ball on the force–distance diagram in a) ball–ball and b) ball–wall tests; 0.3% Carbopol solution, 50% covering of the equipped ball

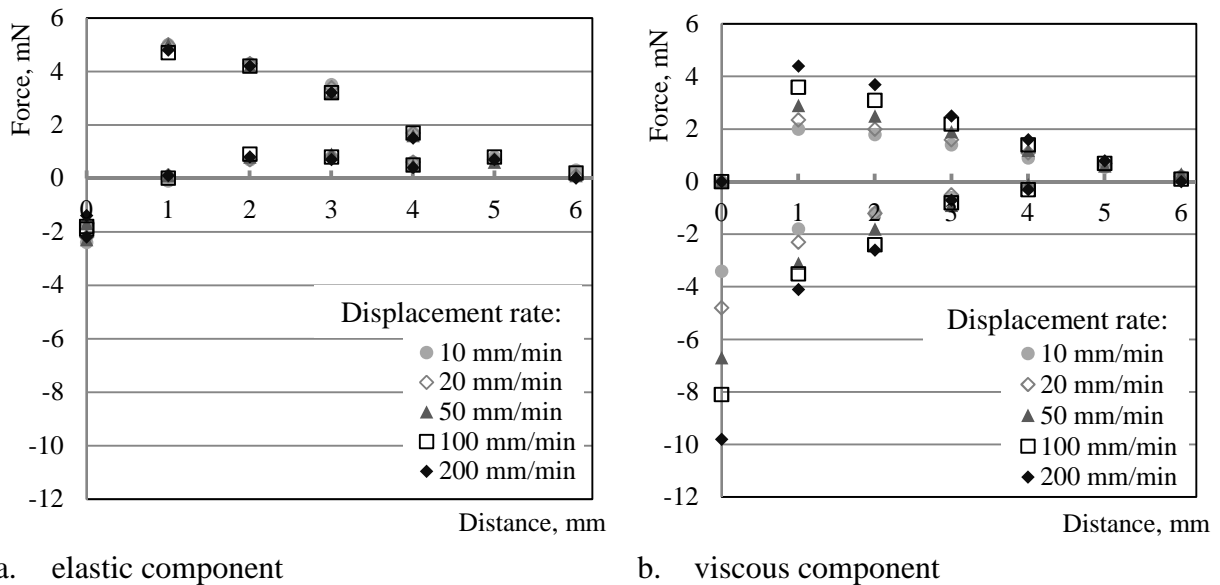


Figure 4.14: Calculated values of a) elastic and b) viscous components of the contact force for the ball–ball tests; 0.3% Carbopol solution, 50% covering of the balls

The findings from the experiments with various initial thicknesses of the contact in ball–ball tests as defined by the diameter of the second, smaller ball; cf. Figure 4.6 and in ball–wall tests as defined by the immersion depth of the equipped ball, cf. Figure 4.5, are presented in Figure 4.15. A smaller thickness of the layer between two entities means that less Carbopol solution is involved in the deformation process, which results in lower maximum tensile and compressive forces as well as in smaller distances of complete separation of the entities. Furthermore, the peak tensile forces are attained at lower distances. The characteristic values for forces and distances obtained from ball–ball and ball–wall tests are summarised in Tables 4.5 and 4.6.

4 Experimental investigation on the mesolevel

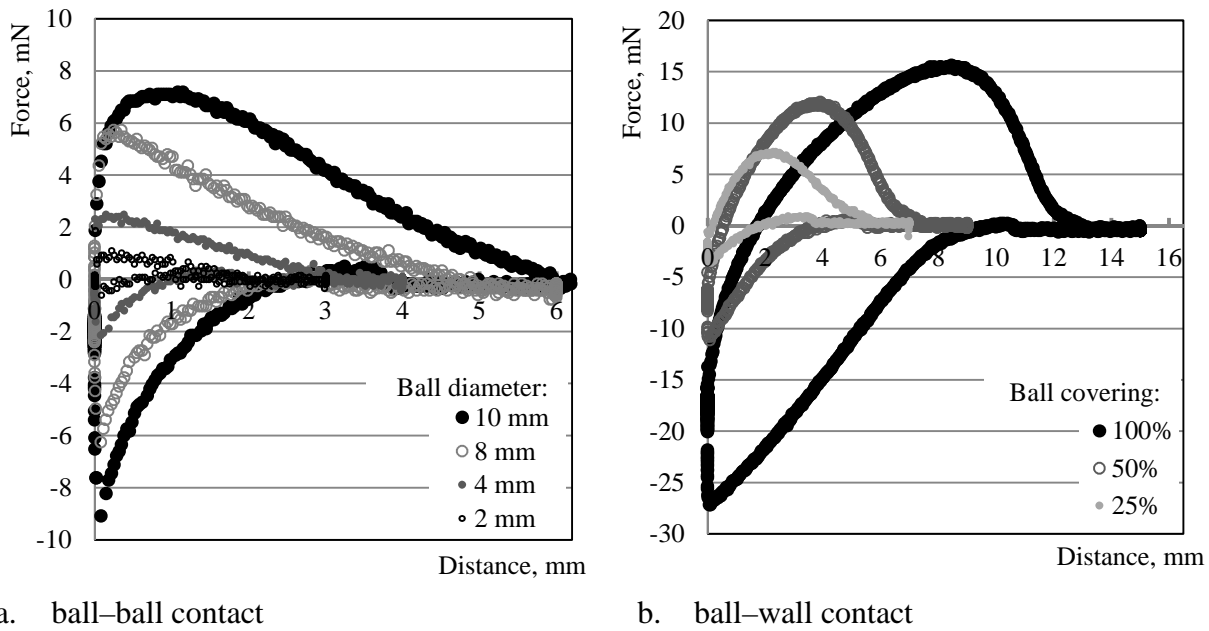


Figure 4.15: Effect of a) the size of the second ball in the ball-ball tests and b) the covering of the equipped ball in ball-wall tests on the force-displacement diagram; 0.3% Carbopol solution, a displacement rate of 100 mm/min

Table 4.5: Characteristic values obtained from the ball-ball tests with different sizes of the second ball

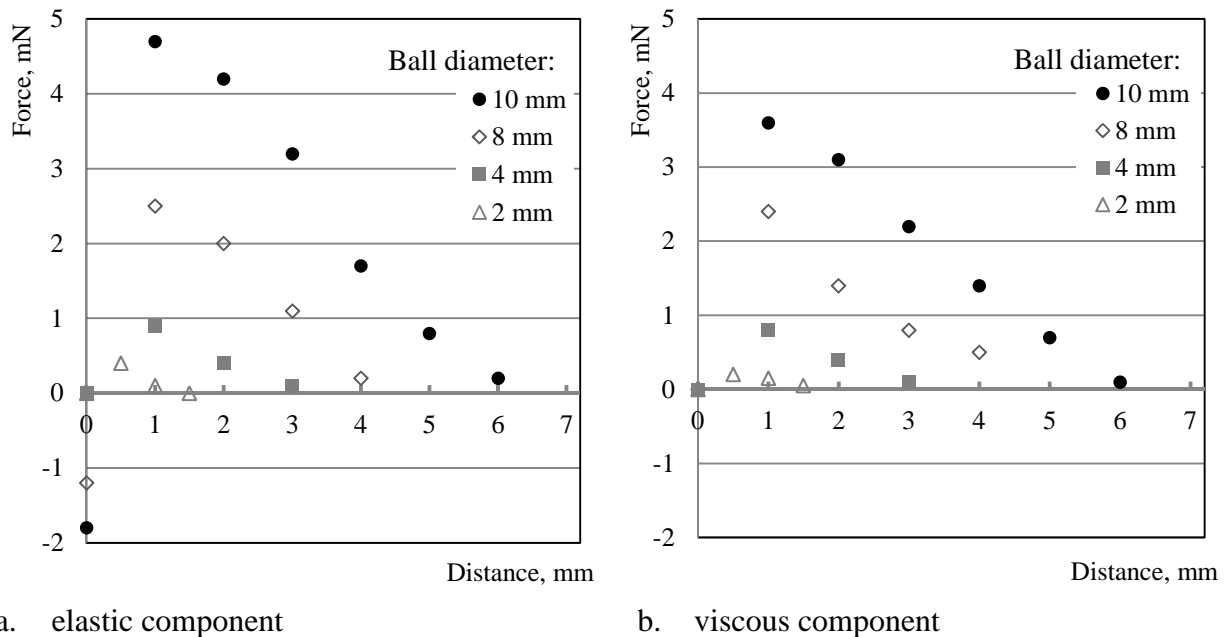
Diameter of the second ball	Covering of the equipped ball	Initial thickness of the contact	Maximum tensile force	Distance at the maximum tensile force	Distance of contact loss	Maximum force in compression
[mm]	[%]	[mm]	[mN]	[mm]	[mm]	[mN]
10	50%	10	7.1	1	6	-9
8	20%	8	5.5	0.3	4.6	-6
4	4.17%	4	2.3	0.2	3.2	-2.2
2	1.01%	2	1	0.2	2	-1

Table 4.6: Characteristic values obtained from the ball-wall tests with different covering of the equipped ball

Covering of the equipped ball	Initial thickness of the contact	Maximum tensile force	Distance at the maximum tensile force	Distance of contact loss	Maximum force in compression
[%]	[mm]	[mN]	[mm]	[mm]	[mN]
100%	~	15	9	13	-27
50%	10	12	4	7	-11
25%	5	7	2	6	-5

Both elastic and viscous components of the contact force are proportional to the initial thickness of the contact layer. Figure 4.16 shows these components for the ball-ball tests as presented in Figure

4.15a. The force–distance diagrams for components of the contact force look very similar. In both cases same effect of ball diameter was observed. In addition, the force decreases quasi linearly after reaching the maximum value. These facts will be used for developing of the material model.



a. elastic component

b. viscous component

Figure 4.16: Calculated values of a) elastic and b) viscous components of the contact force obtained from the ball–ball tests with various sizes of the second ball; 0.3% Carbopol solution, the displacement rate of 100 mm/min

The results presented above were obtained from experiments with 0.3% Carbopol solution as the material between entities. Further tests with 0.5% Carbopol solution showed the same tendencies and therefore are not presented here; see Appendixes D and E.

Figure 4.17 presents the results of the tests with multiple adjoining balls. A higher number of balls means a larger radius of the inscribed circle between them and the equipped ball. Therefore the initial position of the equipped ball is shifting down: the height of the initial position of the equipped ball towards the test glass decreases while the total amount of Carbopol solution between the balls increases. When the radius of the inscribed circle between adjoining balls reaches the radius of the equipped ball then the equipped ball will have a direct contact with the test glass – the covering of the equipped ball will be maximal at this position; cf. Figure 4.8. In this case both types of contact, ball–balls and ball–wall, work in parallel and supplement each other.

While in the tests with a single contact the material between the entities deforms only at its free surface, in the case of multiple contacts the polymer must be extracted from the gaps between balls in order to compensate the vacuum which arises when the equipped ball starts moving; cf. Figure 4.8.

4 Experimental investigation on the mesolevel

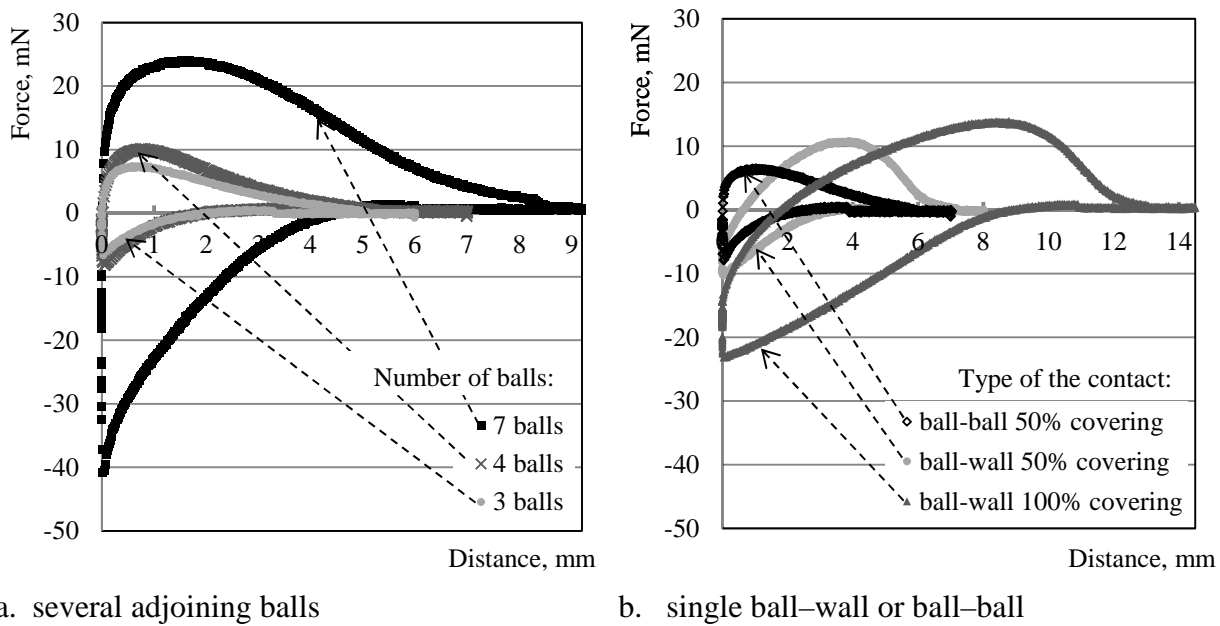


Figure 4.17: Force–displacement diagrams for a) tests with several adjoining balls and b) tests with single ball–ball or ball–wall contacts; the Carbopol concentration is 0.3 %; the velocity of the lifting of the equipped ball is 50 mm/min

Figure 4.17 shows that force–displacement diagrams of the tests with several balls have shapes similar to the diagrams for contact of just two balls, however, the characteristic forces increase with an increasing number of adjoining balls. The main reason for this increase is the higher amount of Carbopol solution between the entities involved and also the need to extract some viscoelastic material from the voids between adjoining balls. The maximum tensile force was observed in the tests with 7 adjoining balls. This force was approximately 4 and 2 times higher than the corresponding values obtained for single ball–ball contact and ball–wall contact tests, respectively; see Figure 4.17.

The amount of polymer between the equipped ball and adjoining balls follows the number of adjoining balls but is not directly proportional. Each additional ball will add some additional amount of polymer to the contact. However, the amount of additional polymer can be different because of overlapping of the contact zones for neighbouring balls; cf. Figure 4.7. Thus, every new added ball will add a relatively lower amount of polymer to the contact bond than did the previous ball and a higher amount than the next ball. The size of the adjoining balls is also an important factor due to the different volumes of the voids between balls. It is significant to note that all effects which were observed in the tests with single contacts also seem to be valid in the tests with multiple contacts; see Appendixes D and E.

In summarising the results of the ball–ball and ball–wall tests on two different Carbopol solutions, it can be stated that they both showed very similar behaviour. Since rheological behaviour of Carbopol is similar to cement mortar described by Bingham model, it can be assumed that similar phenomena should be observed in the ball–wall experiments on mortars, certainly by taking the time–dependent rheological behaviour of the cementitious materials into account.

4.10 Results and discussion of the tests with mortar for fresh SCC and UHPC

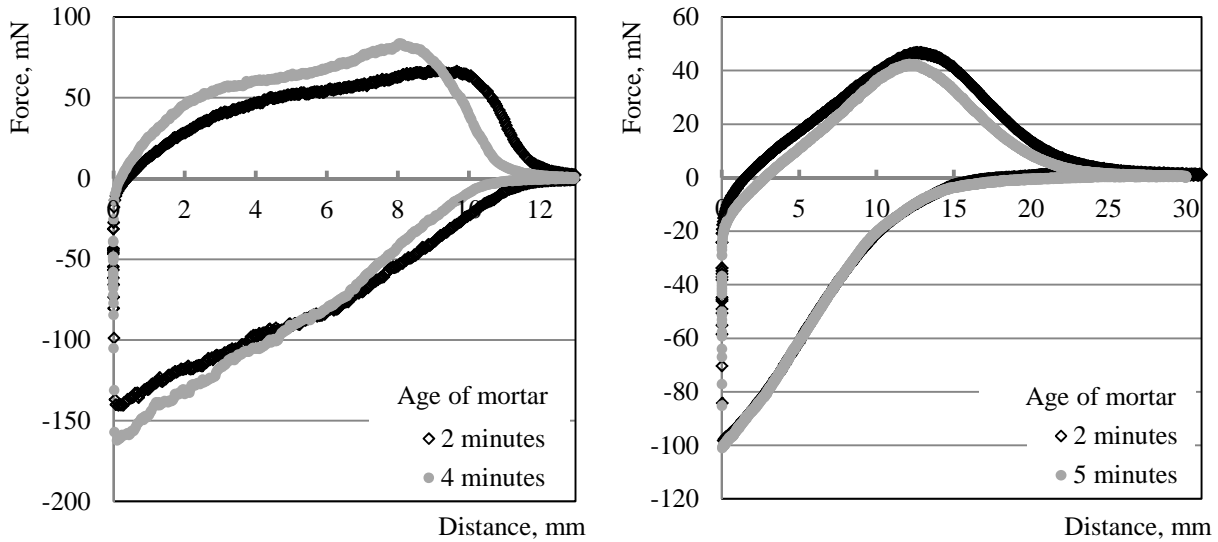
Since the rheological behaviour of cement-based materials in the fresh state is time-dependent, particular care was taken to record the time during the experiments. The time measurement was started when extraction of the material from the mixer began. After retrieving some material from the mixer for the series of tests the remaining part continued to be mixed at a very low speed. In addition, it should be noted that the rheological properties of fresh concrete or mortar change much faster at the free surface than within the mass of the sample, reminding of the effect of stiffening due to water evaporation. From this perspective, it could be expected that only ball-wall tests would provide meaningful and reproducible results. In the case of ball-ball tests the ratio of free surface to material volume is much less advantageous, which causes a rapid stiffening of the material. Moreover, the process of covering the balls with an even layer of mortar also takes some time, which strongly affects the results. Therefore, only ball-wall experiments are presented here. For further evaluation it was assumed that the difference between ball-wall and ball-ball contacts is similar to the corresponding difference measured in the tests with Caropol solutions.

In addition, it should be noted that it is difficult to control the covering of the equipped ball in case of mortars. Mortars are not transparent and have much stronger adhesive behaviour. Therefore, the covering of the equipped ball can be different in the same series of experiments ($\pm 10\%$). It is one of the reasons for the poor repeatability of the experiments with mortars. An additional parameter which influenced the repeatability of the experiments with mortars was the time dependence of the rheological behaviour. Therefore, before analyzing the main series of experiments, the influence of time dependence of rheological behaviour of mortars on the results of measurements is presented and discussed. This knowledge is needed for proper interpretation of the test results.

4.10.1 Investigation of time-dependence of rheological behaviour

The influence of the time-dependent rheological behaviour of the mortars was investigated using the following methodology: experiments with the same setup were carried out with specified time intervals. Short time intervals of 1 to 3 minutes were used for investigation of the short-term effects in order to show possible differences between consecutive tests. Longer time intervals of about 10 minutes were used for capturing the “long-term” effects.

Figure 4.18 shows that even a little difference in the age of the mortar may result in a measurable, but minimal influence on the results of consecutive tests. In the case of mortar for SCC, in Figure 4.18a, with a slightly higher age the maximum force is increased by approximately 15%, and the corresponding distance is also approximately 15% lower. However, the tests with UHPC did not show such an effect, as in Figure 4.18b; the consecutive force-displacement diagrams measured in a time interval of two minutes almost coincided. The difference in the time-dependent behaviour of SCC mortar and UHPC may have resulted from the different types and content of superplasticizer used for the mixtures. The addition of superplasticizer to the UHPC was considerably higher, which might have caused more stable rheological behaviour of mortar in the first few minutes after mixing.



a. fine mortar for SCC

b. UHPC

Figure 4.18: The force–displacement diagrams of the experiments with ball–wall contact with fine mortars for SCC and UHPC of different ages; the covering of the equipped ball is 100%; the displacement rate is 100 mm/min

The experimental findings related to longer intervals between individual measurements are given in Figure 4.19. In these tests the age effect was found to be very pronounced. In the case of SCC mortar both the maximum tensile force and maximum distance (just before separation) increased by approximately 2.5 times when the results obtained at the age of 12 minutes are compared with the results for an age of three minutes; see Figure 4.19a. In the case of UHPC the increase in the maximum distance in time was less pronounced, but the relative increases in the maximum tensile and maximum compressive forces were similar to those measured for SCC mortar. Similar effects were obtained in the experiments with other coverings of the equipped ball and with other displacement rates than shown in Figure 4.19.

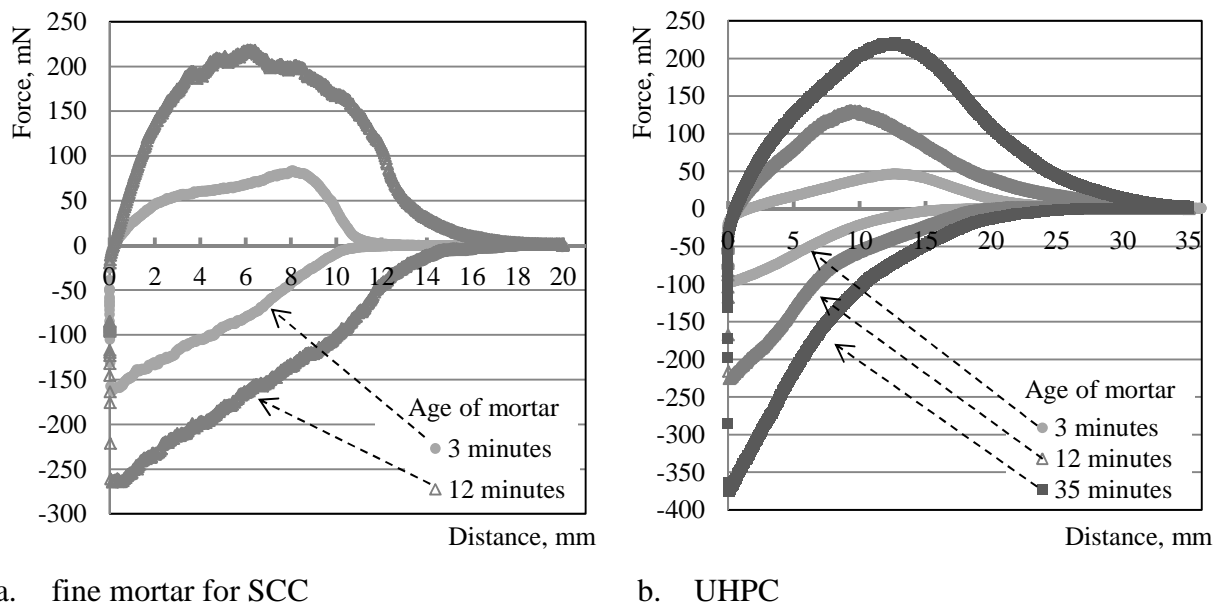


Figure 4.19: The force–displacement diagrams of the experiments with ball–wall contact with fine mortars for SCC and UHPC of different ages; the covering of the equipped ball is 100%; the displacement rate is 100 mm/min

4.10.2 Discussion of the results of the tests with mortars with ball–wall contact

The curves of the ball–wall experiments with 100% and 50% covering of the equipped ball by SCC mortar and UHPC are presented in Figures 4.20 and 4.21. The displacement rates of the equipped ball were 50, 100 and 200 mm/min; the age of the fine mortar at the beginning of each testing cycle is given in brackets.

The curves measured with UHPC (Figure 4.21) are stretched in the direction of larger distances, i.e., higher distances of maximum tensile force, contact bond loss and creation of new contact, in comparison with the curves obtained in the tests with SCC mortar (Figure 4.20). This can be traced back to the higher viscosity of UHPC: the amount of the material deformed by the motion of the equipped ball is larger and the separation occurs later. In addition, no major effect of the displacement rate was observed in the tests with SCC mortar. Since the viscosity of this material is not high, the effect was probably diminished by the counteracting effect of increasing stiffening of the material with time; cf. Figure 4.18a. The tests with lower strain rates were performed at a later time, even if the time difference was rather small. However, in the tests with UHPC the effect of the displacement rate was pronounced; that can be explained by taking the viscosity of the UHPC into account, 6 times higher than the viscosity of the fine mortar for SCC, cf. Table 4.1.

In tests with 100% covering of the equipped ball the characteristic forces are smaller than those in tests with 50% covering, in contrast to corresponding tests with polymers where characteristic forces are higher for the tests with higher covering; see Figure 4.15. This can be explained at least partly by the higher age of the materials in the second series of the tests with 50% covering, begin 4 minutes later; cf. Figure 4.19 and corresponding discussion in Section 4.10.1. However, a more significant reason might be the fact that in the tests with smaller covering the ratio of surface to volume of the material is higher. Therefore, an increase in stiffness due to water loss might be more pronounced.

4 Experimental investigation on the mesolevel

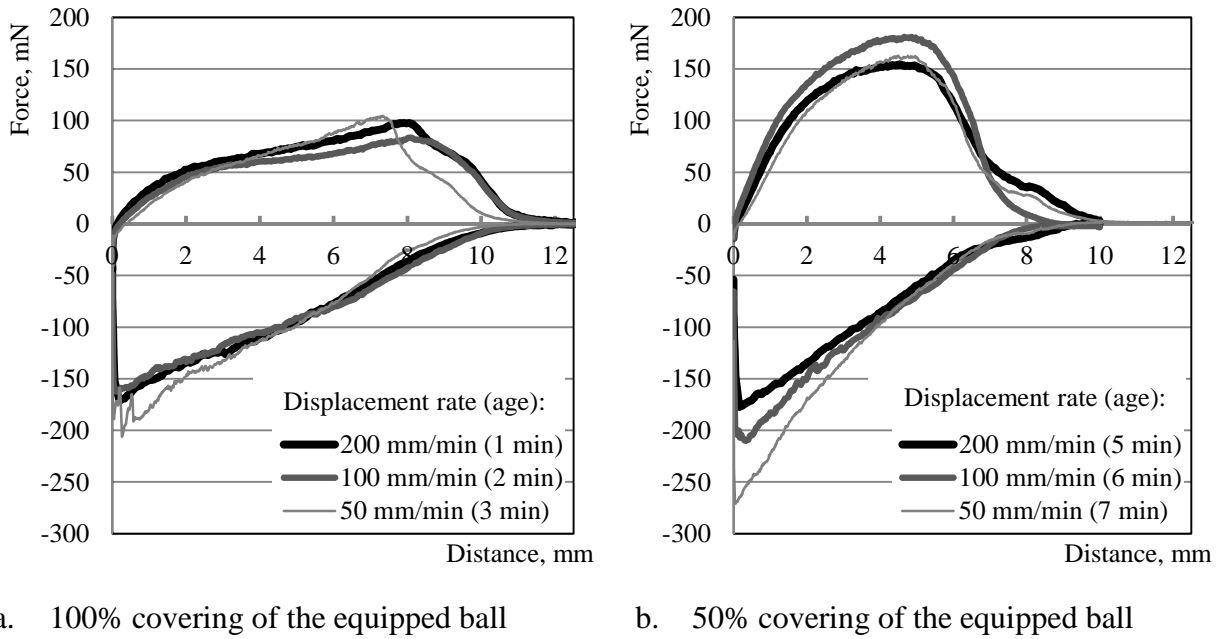


Figure 4.20: Force–displacement curves obtained from ball–wall tests on SCC mortar with a) 100% and b) 50% covering of the equipped ball, and three different displacement rates

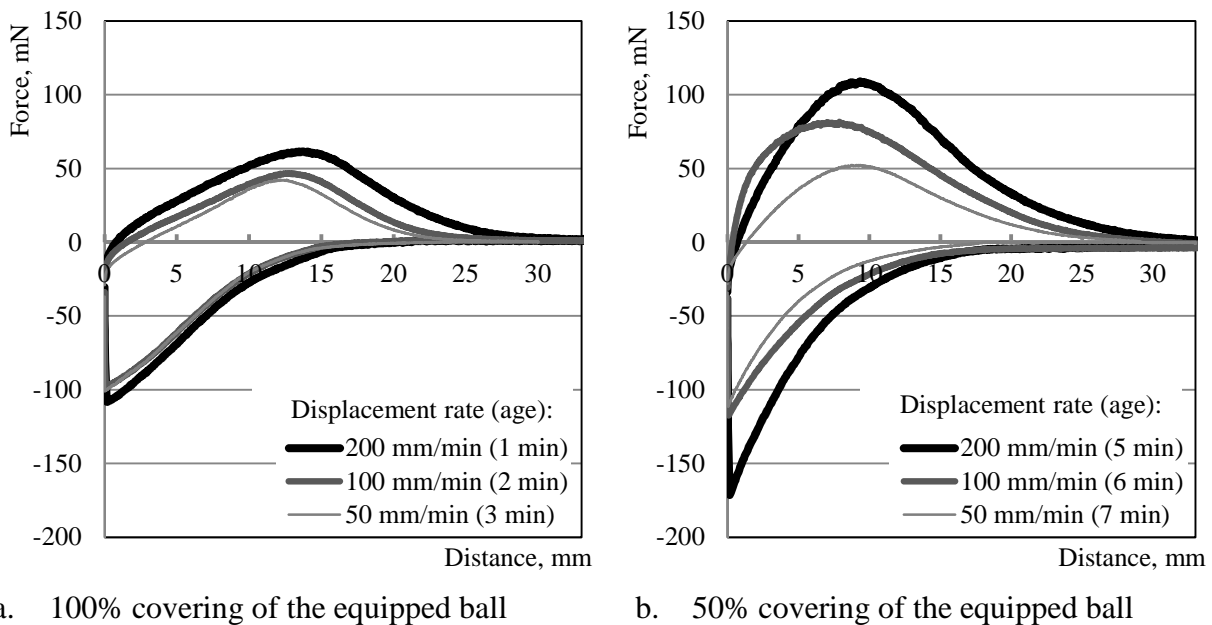
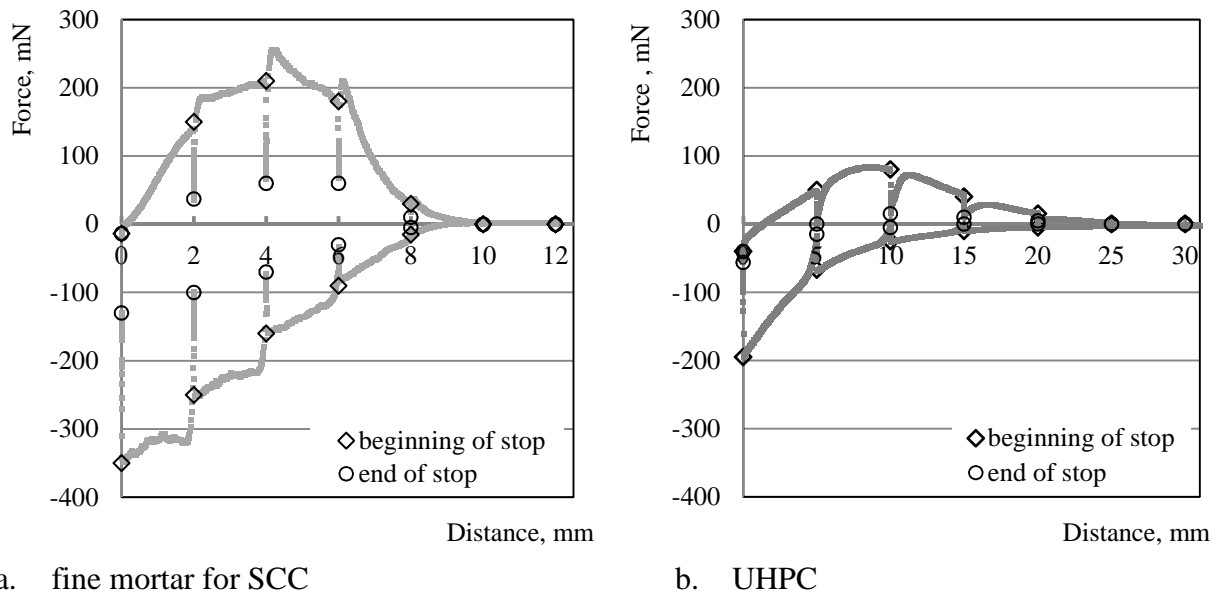


Figure 4.21: Force–displacement curves obtained from ball–wall tests on UHPC with a) 100% and b) 50% covering of the equipped ball, and three different displacement rates

Figure 4.22 shows the results of the ball–wall tests with 50% covering of the equipped ball and with stops every 2 mm for the fine mortar of SCC and every 5 mm for UHPC. The duration of each pause was two seconds. During these pauses the viscous component of the force decreased to zero very rapidly, so that it can be assumed that at the end of each pause only the elastic component of the force was active. The displacement rate of the equipped ball was 50 mm/min. For these tests material was used from the same mix as referred to in Figures 4.20 and 4.21. It remained in the mixer and was mixed with a very low intensity. The age of both SCC mortar and UHPC at the

beginning of testing was 11 minutes. The envelope curves for these tests generally correspond to the force–distance relations obtained from the monotonic tests; cf. Figures 4.20 and 4.21.



a. fine mortar for SCC

b. UHPC

Figure 4.22: Force–displacement diagrams obtained for a) SCC and b) UHPC from ball–wall tests; 50% covering of the equipped ball, a displacement rate of 50 mm/min

However, a closer look at Figure 4.22a discloses unexpected behaviour of the SCC mortar when reloaded after the intermediate stops. The force increases very rapidly with increasing distance and reaches higher values than the contact force before the stop. This response is in contrast to the behaviour of UHPC (Figure 4.22b) or Carbopol solution (Figure 4.13) in the experiments with stops: both these materials show a smooth increase in force with increasing distance, gradually approaching the reference curve as obtained from the test without stops. The reason for such specific behaviour of SCC mortar is yet to be clarified.

From the data presented in Figure 4.22 the components of the contact force for each intermediate stop were calculated; see Figure 4.23. While for both materials the viscous components are clearly larger than the elastic ones, the proportions of the components are different. In the case of UHPC the ratios of the viscous force component to the elastic component are considerably higher than the corresponding ratios for SCC mortar. This can be traced back to the results of the rheometer measurements of both materials: UHPC showed a lower yield stress, which correlates here with the elastic component, than SCC mortar, but a higher viscosity, which is “responsible” for the viscous force component. Furthermore, it can be seen that the elastic and viscous force components, when considered separately, follow the general course of the corresponding force–displacement relation to a great extent. Also the maxima of the tensile viscous and elastic components are attained at nearly same distance between the entities. Further tests with 100% and 50% covering of the equipped ball showed the same tendencies and therefore are not presented here; see Appendixes F and G.

4 Experimental investigation on the mesolevel

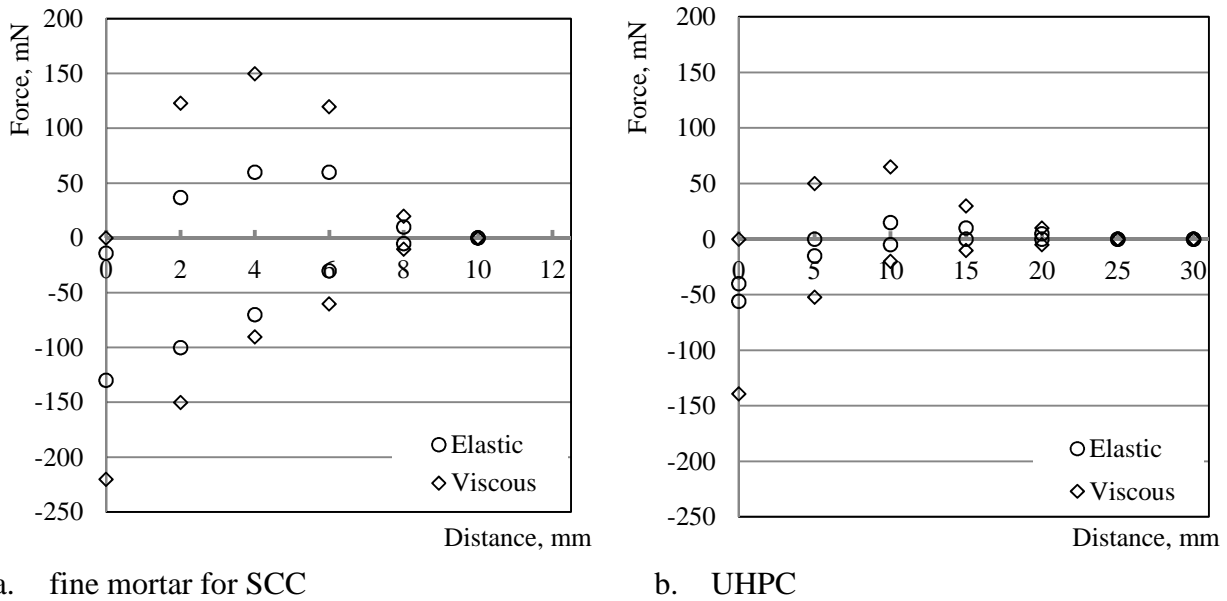


Figure 4.23: Elastic and viscous force components measured in ball–wall tests with stops for a) fine mortar of SCC and b) UHPC; 50% covering of the ball, a displacement rate of 50 mm/min

Finally, experiments with changes in the direction of motion of the equipped ball were performed; see Figure 4.24. The general behaviour is similar to that observed in the corresponding tests with Carbopol solutions. It can be concluded that the force–displacement curve obtained in the monotonic regime can serve as a good approximation for the envelope curve for more complex loading regimes for SCC mortar and UHPC.

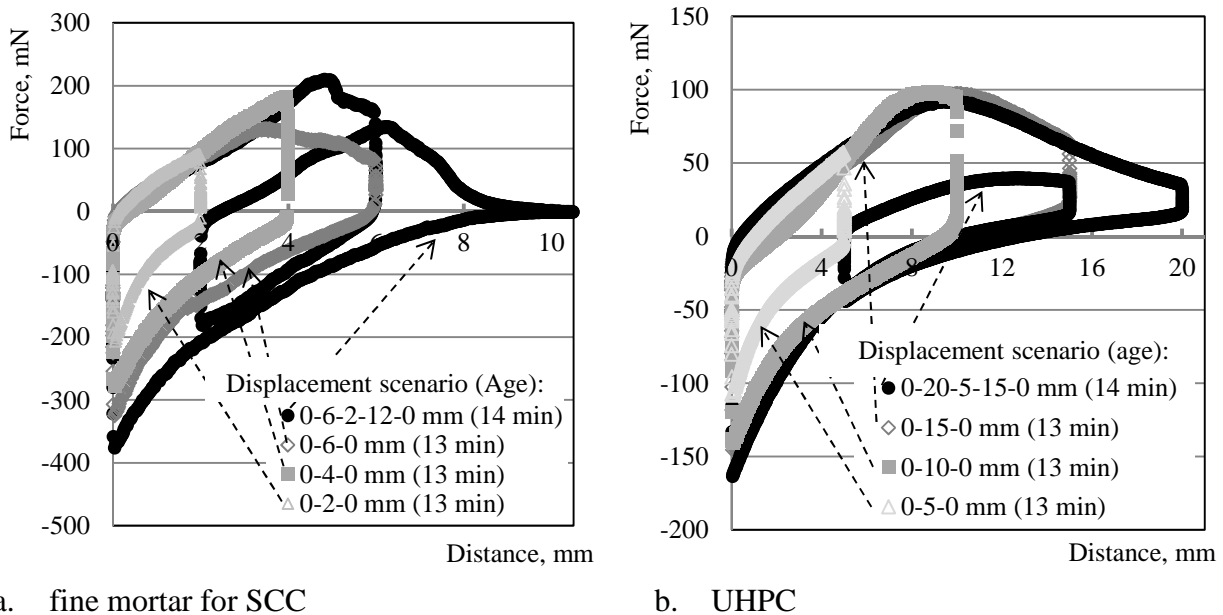


Figure 4.24: Results of the ball–wall tests performed with SCC mortar in various movement regimes of the equipped ball; 50% covering of the equipped ball; displacement rate of 50 mm/min; mortar age of 13 to 14 minutes

By summarizing the results of the ball–wall experiments with SCC mortar and UHPC and by comparing them to the corresponding results obtained with Carbopol solutions, it can be concluded that the viscoelastic behaviour of the cementitious materials and Carbopol solutions is almost

similar. Still further, it may be supposed that for the case of a “virtual” ball–ball contact with fresh cement–based material between the balls also there would be a pronounced similarity with the force–displacement curves obtained for the polymer solutions. Thus it might be assumed that the difference between diagrams obtained from ball–wall and ball–ball experiments as observed in the tests with polymer solutions can be transferred to SCC mortar or UHPC so that a corresponding force–displacement curve for the ball–ball contact model can be estimated. Such an estimation is indeed essential for deriving constitutive relationships for the DEM of fresh concrete based on an experimental basis; as explained above, an accurate ball–ball experiment with cement–based material is scarcely possible to perform.

In looking at the results of the tests performed with Carbopol solutions covering 50% of the equipped ball, the force–displacement diagram for the ball–ball contact should have slightly smaller maximum tensile and compressive forces. The maximum tensile force would be reached at a considerably smaller distance between the entities and the distance of the contact loss would be smaller as well. Examples of a reference force–displacement diagram for the ball–wall contact and of an estimated diagram for the ball–ball contact are presented in Figure 4.25. The estimated force–displacement diagram for ball–ball contact looked like a compacted force–displacement diagram for ball–wall contact. In addition, it might be supposed that the influence of the size of the second particle will also be the same.

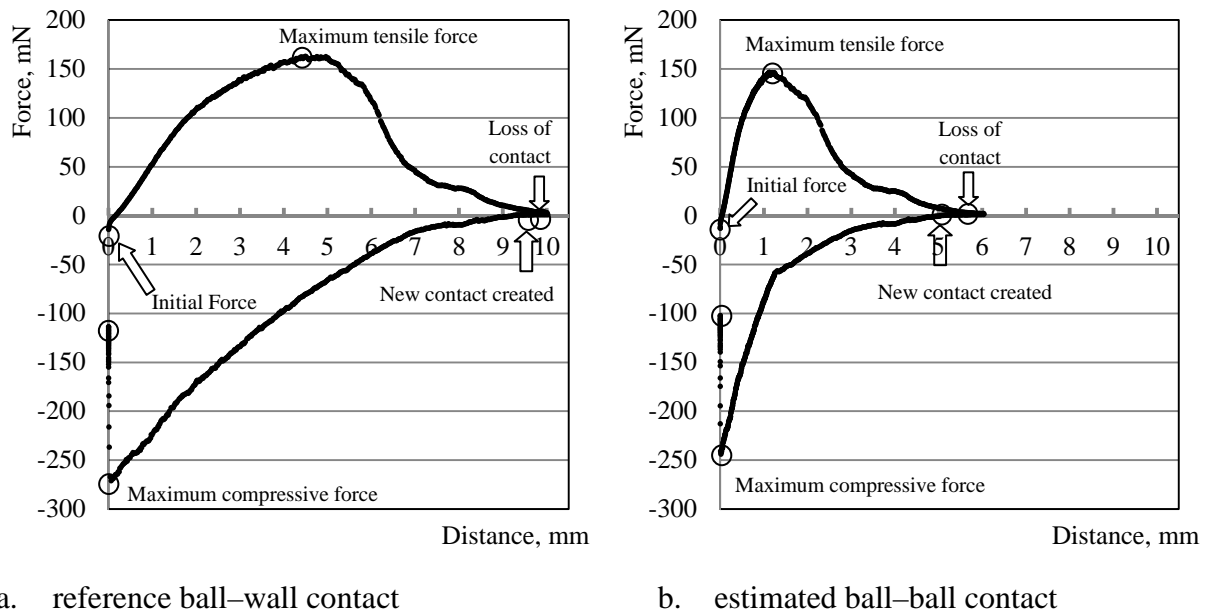


Figure 4.25: a) Reference force–displacement diagram for ball–wall contact and b) estimated relationship for ball–ball contact for SCC mortar; 50% covering of the equipped ball; a displacement rate of 50 mm/min

4.11 Material model for interaction between entities in DEM

The following statements and assumptions can be made by summarizing the experimental findings with objective of developing material model for distinct element analysis:

1. The investigated materials (Carbopol solutions, SCC mortar and UHPC) exhibit rheological behaviour which, to a good extent, can be described by the Bingham model.

4 Experimental investigation on the mesolevel

2. The contact force acting between the entities can always be resolved into elastic and viscous components. These components should be considered separately and independently. The viscous component is highly time dependent, the time dependency increasing with increasing plastic viscosity of virtual viscoelastic material between distinct elements. The elastic component correlates primarily with the yield stress of the virtual material between elements and the amount of this virtual material (analogous to the covering of the equipped ball in experiments).
3. Force–displacement diagrams for interaction between distinct elements should possess – as observed in the corresponding experiments – similar shapes for various viscoelastic virtual matrices between them. However, the characteristic points of the diagrams have magnitudes which depend on specific rheological properties of a particular matrix and its quantity (depending on the size and shape of the neighbouring entities).
4. Simplified graphical representation of the force–displacement relations by using bi- or trilinear force–displacement curves for monotonic tensile and compressive loading is adequate.
5. The force–displacement curves for monotonic tensile and compressive loading can serve as envelope curves for more complex loading regimes, i.e., loading with stops or reversals of direction of movement.

According to the experimental results the elastic and viscous components of the contact force should be considered separately. Thus the material model should contain two force–displacement relations which, when superimposed, describe the complete contact behaviour of two neighbouring entities. The material models for the components of the contact force can be implemented into the commercial DEM programmes by means of user–defined contact models or used in programming one’s own DEM packages.

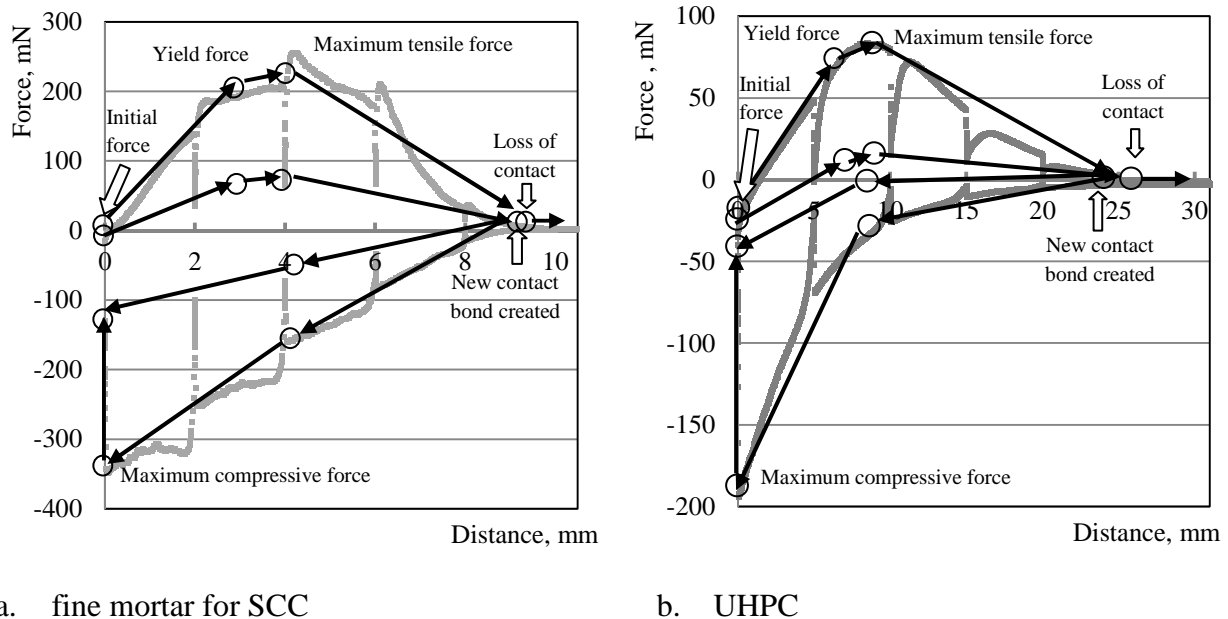
A methodology of developing the user–defined contact model consists of the following steps:

1. Analysis of experimentally obtained force–displacement relations.
2. Development of the graphical form for the eventual mathematical formulation of the force–displacement relationship, taking limitations of the available DEM code into account.
3. Development of the mathematical formulation for the user–defined contact model.
4. Implementation of the mathematical formulation into the DEM code.
5. Verification of the user–defined contact model by comparing the numerical prediction with experimental or analytical results for a particular set of experiments.

Steps 1 and 2 are presented in the current section; steps 3, 4 and 5 are presented in Chapter 5.

Figure 4.26 presents force–displacement diagrams as obtained from ball–wall tests performed with stops on UHPC and SCC mortar. The characteristic points of these curves are highlighted and connected by straight lines. The arrows show whether an increase or decrease in the distance between two neighbouring entities is considered. These characteristic points and connecting lines, arrows, are a graphic representation of the material model for the interaction between two entities. The force–displacement diagrams and corresponding graphical representations can be divided into two regions by distance: Region I, in which the contact force increases from the “Initial force” up to the “Maximum tensile force”, and Region II, in which the contact force decreases from the “Maximum tensile force” until “Loss of contact”. Moreover, the force–displacement curve of the backward motion also changes its inclination at the border between Regions I and II. Such change was pronounced for UHPC, but less pronounced in the tests with SCC mortar; see Figure 4.26.

The ascending curve in Region I is divided into two parts: the contact force increasing until some point (the so-called “Yield force”); then the curve changing inclination and increase of the contact force continuing until “Maximum tensile force”. This latter point has a particular importance for the modelling of the ball–ball contact.



a. fine mortar for SCC

b. UHPC

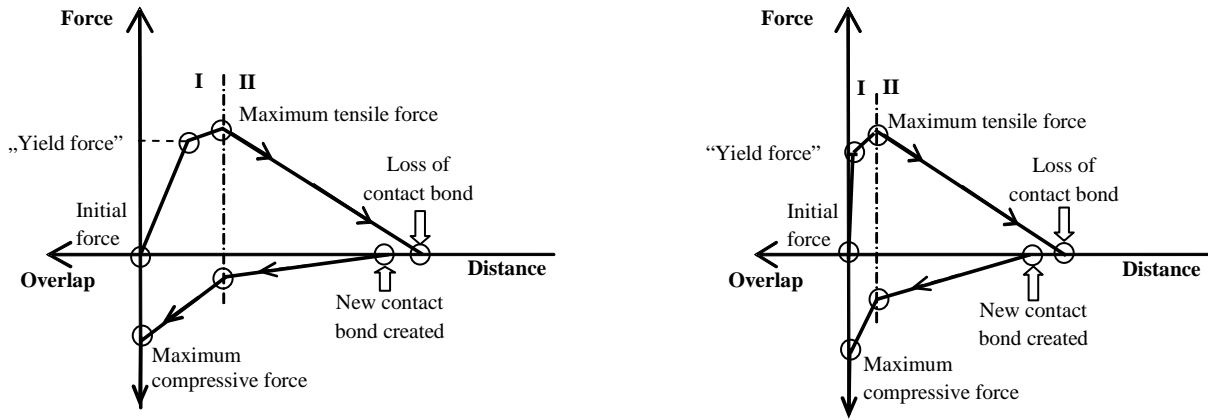
Figure 4.26: Force–displacement diagrams obtained from ball–wall tests with stops on a) SCC mortar and b) UHPC with highlighted characteristic points and connected arrows as a graphical representation of the material model for interactions between two neighbouring entities in discrete element analysis

Figure 4.27 presents a generalized model of the reference ball–wall contact and estimated material model of the ball–ball contact. Regions I and II are marked on the diagrams as (I) and (II) respectively. In the case of the ball–ball contact, the contact force increases rapidly from the “Initial force” until the “Yield force” is reached as observed in corresponding tests with Carbopol solutions. The left part of the force–displacement diagram represents the case when two entities come into direct contact. Here, further motion in the backward direction means squeezing the solid bodies, which are much stiffer than the viscoelastic material.

On the basis of the results obtained in the tests with stops, cf. Figures 4.14, 4.16 and 4.23, material models for the individual components of the contact force were derived as shown in Figure 4.28. The elastic component of the contact force for a given material is velocity–independent and depends only on the thickness of the contact bond. In contrast, the viscous component of the contact force depends on both the displacement rate and the thickness of the contact bond. The dashed lines in Figure 4.28 show how the viscous component changes with increasing displacement rate in comparison to the reference displacement rate (solid line).

Generalized material models for components of the contact force for ball–ball contact will have a similar shape; however, the length of Region I will be smaller (the diagram will look as if pressed towards the “Force” axis).

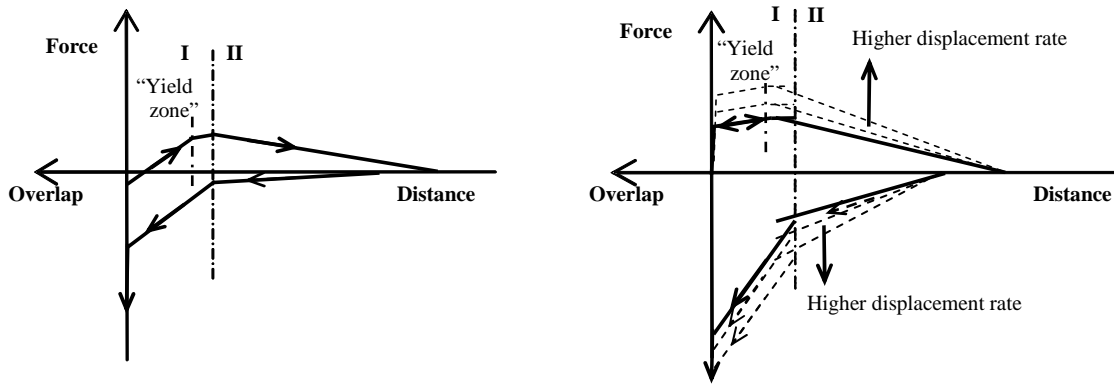
4 Experimental investigation on the mesolevel



a. reference ball–wall contact

b. estimated ball–ball contact

Figure 4.27: Generalized material model of the interaction between discrete entities with some viscoelastic material between them



a. elastic component of the force

b. viscous component of the force

Figure 4.28: Generalized material models for components of the contact force for ball–wall contact

The lines representing the behaviour of the elastic component of the contact force in the tension and compression regimes are parallel in Region I and converge to the horizontal axis in Region II. The convergence of the lines to the horizontal axis in Region II results from the changing of the thickness of the contact bond. The thickness decreases with increasing distance between entities and vice versa. It may be assumed that the thickness of the contact bond is changed equally by forward and backward directions of the motion. The distances which correspond to loss of the contact bond and creation of the new contact bond do not coincide because of relaxation of the viscoelastic material after the loss of the contact. Thus the new contact bond is created at a shorter distance between the entities. The lines representing the viscous component of the force in the tension and compression regimes are not parallel in Region I; however, in Region II they make equal angles with the “Distance” axis.

The history of the deformation has an important role. After each stop the viscous component of the force vanishes, and it is assumed that the residual force corresponds to the elastic component of the force. However, the magnitude of the elastic component of the contact force depends on the regime of deformation. The regime of deformation means the state of the viscoelastic material: tension or compression. In the case when the direction of the motion remains unchanged after stopping, the

regime of deformation of the contact bond also remains unchanged. However, if the direction of motion is reversed after stopping, then the regime of the deformation is also changed. For instance, if initially it was tension then after changing the direction of the motion the current regime of deformation is compression. The thickness of the contact bond remains unchanged but the elastic force which represented the yield stress in reverse direction of the motion prevents the motion. Supposing that the yield stress of the material has the same magnitude independent of the direction of motion and depends just by thickness of the contact bond, then the true value of the yield stress is equal to the average value of the elastic forces in tension and compression for corresponding distances between entities. This effect is presented schematically in Figure 4.29.

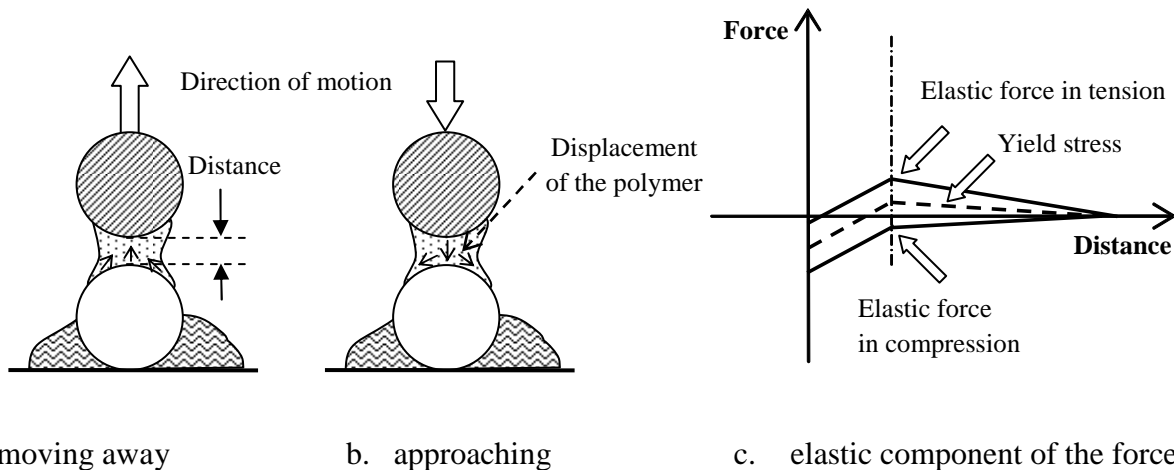


Figure 4.29: Schematic view of the regimes of deformation by a) moving away and b) approaching of the equipped ball and c) influence of the regimes of deformation on the elastic component of the contact force

Thus the material model for elastic component of the contact force consists of two curves which represent the regimes of deformation: tension and compression for the contact bond.

4.12 Summary and conclusions

The investigations presented here aimed to develop a material model of the rheological behaviour of fresh concrete using the DEM. In particular, the interaction between neighbouring spherical entities representing aggregates with a virtual layer of fine mortar between them should be experimentally studied and described.

Four viscoelastic materials were investigated: two Carbopol water solutions and two cement-based materials (a fined-grained UHPC and a mortar for SCC). First, the materials were characterised using a HAAKE MARS rheometer and the Bingham model. Carbopol solutions proved to be adequate substances to be used as mortar-like references with time-independent rheological properties. As the next step, tests were performed to measure force-distance relations for two balls, or a ball and a wall, with some viscoelastic material in between. In the tests with Carbopol solutions the effects of various parameters such as the yield stress of the material, i.e., different concentration of Carbopol; type of contact, ball-ball or ball-wall, amount of viscoelastic material between entities, covering of the equipped ball; and deformation rate were investigated. Tests with the monotonic regime of the ball motion in tension and subsequent compression provided an overall response of the system, while the tests with intermediate stops gave information about

4 Experimental investigation on the mesolevel

velocity-independent elastic and velocity-dependent viscous components of the measured force. Sets of characteristic forces and corresponding distances were derived from the experimental data.

In ball-wall tests performed on UHPC and SCC mortar a generally similar behaviour was measured as in corresponding tests on Carbopol solutions. However, as expected, a pronounced time dependence of the material response was observed for cement-based materials. While thixotropy certainly plays a role, the major cause of this effect might be the stiffening of fine mortar due to water loss at the mortar surface. Furthermore, it was shown that the magnitudes of elastic and viscous components of the contact force measured in ball-wall tests correlate well with the rheological constants obtained from the rheometer tests: UHPC has a much higher viscosity than SCC mortar. So, the viscous component of the contact force for UHPC is also much higher; SCC mortar has a higher yield stress and therefore higher values of the elastic component of the contact force.

Finally, the results of the tests were summarized and a generalized material model for the interaction among discrete elements with some viscoelastic material between them was proposed. It was shown that this material model can be resolved into two models, which represent the viscous and elastic components of the contact force. The exact mathematical description of the developed model and the explanation of its implementation in a DEM code including its verification by comparison of predictions of numerical simulations with experimental results are presented in the next chapter.

CHAPTER 5

MATERIAL MODEL AND NUMERICAL SIMULATIONS

5.1 Introduction

In this chapter the material model developed based on the results of the mesolevel tests is implemented into DEM programme Itasca Particle Flow Code (Itasca PFC 3D) and verified. Section 5.2 presents Itasca PFC 3D as a basis programme which used in this investigation; see Section 4. Herein the limitations of the PFC are critically discussed and the steps of the developing of user-defined contact model (UDM) are presented. Furthermore, some important procedures for making discrete the mesostructure of fresh concrete and controlling of the numerical modelling are described and discussed.

Section 5.3 treats numerical modelling using the UDM and the set of procedures presented in Section 5.2. It includes parameter study for UDM and a calibration of the UDM using the Slump flow test as well as verifications of the UDM using other test methods for fresh concrete (e.g. L-Box tests, LCPC-Box test).

Finally, the results are summarized in Section 5.4.

5.2 Numerical model

The numerical model for DEM includes the modelling of the material as a collection of discrete particles, defining the mode of interaction between the neighbouring particles, setting boundary conditions and external forces and assigning a solution algorithm. The result of the interaction of numerous particles represents the behaviour of the material on the macrolevel of observation.

5.2.1 The Particle Flow Code Itasca

The Particle Method is a variation of the Discrete Element Method, which allows for the modelling of movement (translation and rotation) including the separation and automatic contact detection of particles [59]. In this work ITASCA PFC 2D and PFC 3D, was used as a basic programme.

5.2.1.1 Basic concepts of the method

The model is comprised of discrete particles that move independently of each other and interact only at contacts or interfaces between the particles. In contrast to a more general DEM, only two basic elements are used in the particle method: circular particles with a unit thickness (2D simulations) or spherical particles (3D simulations) and walls. The circular or spherical particles, depending on the number of chosen dimensions, can be used to make concrete or mortar discrete with round-shaped coarse aggregates. In order to make aggregates with an irregular shape or fibres discrete, a number of particles can be rigidly connected/clumped to provide the necessary geometries.

The particles are treated as rigid bodies. The interaction of the particles is treated as a dynamic process attaining equilibrium whenever the internal forces are balanced. The contacts occur over a vanishingly small area, i.e., at a point. Newton’s laws of motion provide the fundamental relationship between particle motion and the forces causing that motion.

The calculations performed in the DEM alternate between the application of Newton’s second law to the particles and a force–displacement law at the contacts. Newton’s second law is used to determine the motion of each particle arising from the contact and the forces acting upon it, while the force–displacement law is used to update the contact forces arising from the relative motion at each contact. The dynamic behaviour is numerically represented by a timestepping algorithm in which it is assumed that the velocities and accelerations are constant within each timestep. The solution scheme is identical to that used by the explicit finite–difference method for continuum analysis. The DEM is based upon the idea that the timestep chosen may be so small that, during a single timestep, disturbances cannot propagate further from any particle than its immediate neighbours. Then, at a given time, the forces acting on any particle are determined exclusively by its interaction with the particles with which it is in contact. Since the speed at which a disturbance can propagate is a function of the physical properties of the discrete system, the timestep must be chosen to satisfy the above constraint. The use of an explicit, as opposed to implicit, numerical scheme makes it possible to simulate the nonlinear interaction of a large number of particles without excessive memory requirements or the need for an iterative procedure [59].

The force–displacement law is then applied to each contact to update the contact forces based on the relative motion between the two entities at the contact and the contact constitutive model, cf. Figure 5.1. Next, the law of motion is applied to each particle to update its velocity and position based on the resultant force and moment arising from the contact forces and any force acting on the particle. The wall positions are updated based on the specified wall velocities. Newton’s second law is not applied to walls, since the wall motion is specified by the user.

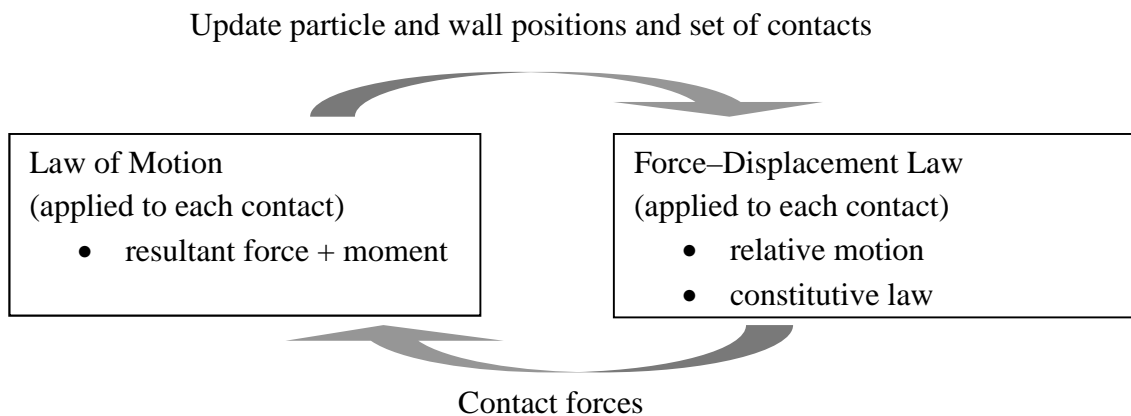


Figure 5.1: Calculation cycle within DEM calculation [59]

5.2.1.2 Characteristics of the elements

The basic elements of the PFC (particles and walls) have a set of characteristics which describes the physical properties, i.e., geometry and material properties, of the elements and should be defined before modelling of the elements. Names and short description of these characteristics are presented in Table 5.1.

Table 5.1: Characteristics of the elements in the PFC

Element	Name	Description
Particle	Radius	Characterises the initial size of the particle.
	Position	Gives the coordinates of the center of the mass.
	Density	Characterises the initial density of the particle.
	Stiffness	Characterises the rigidity of the particles in compression (for linear contact model).
	Coefficient of friction	Gives the coefficient of friction between two neighbouring particles.
Wall	Shape	There are two kinds of walls: standard walls and general walls. General walls differ from standard walls (planar) only in their geometric shape (cylinder, disk, ring, sphere or spiral).
	Size	The position and orientation of the standard wall depend on list of vertices. The vertices must form a planar, convex polygonal surface. The number of parameters for general walls depends on shape of the wall. For instance two points and radius are required for a general cylinder wall.
	Active side	Only one side of a standard wall is considered to be active, whereas both sides of a general wall are active. The order of the vertices defines the active side of the wall; they must be given counterclockwise as seen from the active side.
	Stiffness	Characterises the rigidity of the particles in compression (for the linear contact model).
	Coefficient of friction	Gives the coefficient of friction between a wall and a particle.

The characteristics presented in Table 5.1 are needed to generate particles and create wall elements. The modes of interaction between such elements are presented in the following section.

5.2.1.3 The force–displacement law

The force–displacement law relates the relative displacement between two entities at a contact to the contact force acting on the entities. The contact force arises from contact occurring at a point for both ball–ball and ball–wall contacts. For ball–ball contact, an additional force and moment arising from the deformation of some interface material, represented by a parallel bond, can also act on each particle.

The force–displacement law operates on contact and can be described in terms of a contact point, $x_i^{[C]}$, lying on a contact plane that is defined by a unit normal vector, n_i . The contact point is within the interpenetration volume of the two entities. For ball–ball contact, the normal vector is directed along the line between ball centers; for ball–wall contact, the normal vector is directed along the line defining the shortest distance between the ball center and the wall. The contact force is dissected into a normal component acting in the direction of the normal vector, and a shear component acting in the contact plane. The force–displacement law relates these two components of

force to the corresponding components of the relative displacement via the normal and shear stiffness at the point of contact [59].

The force–displacement law is described for both ball–ball and ball–wall contacts. For ball–ball contact, the relevant equations are presented for the case of two spherical particles, labelled A and B in Figure 5.2a. For ball–wall contact, the relevant equations are presented for the case of a spherical particle and a wall, labelled b and w , respectively, in Figure 5.2b. In both cases, U^n denotes overlap.

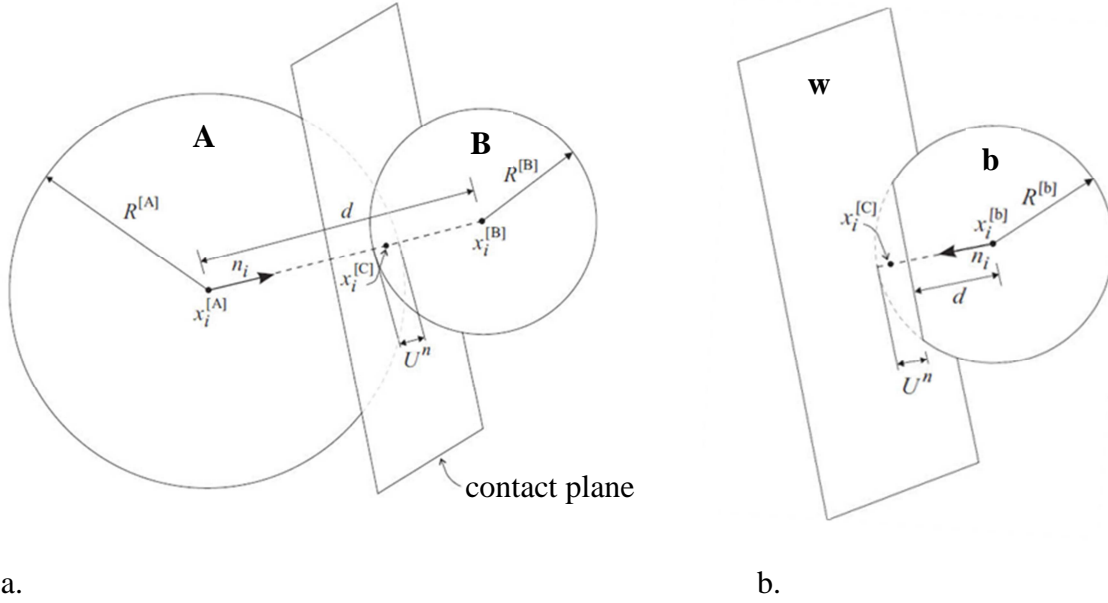


Figure 5.2: Notation used to describe a) ball–ball and b) ball–wall contacts [59]

For ball–ball contact, the unit normal, n_i , that defines the contact plane is given by Eq. 5.1:

$$n_i = \frac{x_i^{[B]} - x_i^{[A]}}{d} \quad (\text{ball–ball contact}) \quad (5.1)$$

where $x_i^{[A]}$ and $x_i^{[B]}$ are the position vectors of the centers of balls A and B, and d is the distance between the ball centers; see Eq. 5.2.

$$d = |x_i^{[B]} - x_i^{[A]}| = \sqrt{(x_i^{[B]} - x_i^{[A]}) \cdot (x_i^{[B]} - x_i^{[A]})} \quad (\text{ball–ball contact}) \quad (5.2)$$

For ball–wall contact, n_i is directed along the line defining the shortest distance, d , between the ball center and the wall.

The overlap U^n , defined to be the relative contact displacement in the normal direction, is given by Eq. 5.3:

$$U^n = \begin{cases} R^{[A]} + R^{[B]} - d & (\text{ball–ball contact}) \\ R^{[B]} - d & (\text{ball–wall contact}) \end{cases} \quad (5.3)$$

where $R^{[A,B]}$ are the radii of the balls.

The location of the contact point is given by Eq. 5.4:

$$x_i^{[C]} = \begin{cases} x_i^{[A]} + \left(R^{[A]} - \frac{1}{2}U^n\right) n_i & (\text{ball–ball contact}) \\ x_i^{[b]} + \left(R^{[b]} - \frac{1}{2}U^n\right) n_i & (\text{ball–wall contact}) \end{cases} \quad (5.4)$$

The contact force vector F_i , which represents the action of particle A on particle B for particle–particle contact and represents the action of the particle on the wall for particle–wall contact, can be resolved into normal and shear components with respect to the contact plane as shown in Eq. 5.5:

$$F_i = F_i^n + F_i^s \quad (5.5)$$

where F_i^n and F_i^s denote the normal and shear component vectors, respectively.

The normal contact force vector and shear contact force are calculated by Eq. 5.6:

$$F_i^n = K^n \cdot U^n \cdot n_i \quad (5.6)$$

$$F_i^s = F_i^{s-old} + \Delta F_i^s$$

where K^n is the normal stiffness [force/displacement] at the contact; F_i^{s-old} and ΔF_i^s are the old value of the shear force vector and shear elastic force increment, respectively.

The shear contact force is computed in an incremental fashion. When the contact is formed, the total shear contact force is initialised at zero. Each subsequent relative shear–displacement increment results in an increment of elastic shear force that is added to the current value. The shear elastic force increment can be calculated by Eq. 5.7:

$$\Delta F_i^s = -k^s \cdot \Delta U_i^s \quad (5.7)$$

where k_s is the shear stiffnesses [force/displacement] at the contact.

It should be noted that the normal stiffness, K^n , is a secant modulus in that it relates *total* displacement and force. The shear stiffness, k_s , on the other hand, is a tangent modulus in that it relates *incremental* displacement and force. An uppercase K is hereinafter used to denote a secant modulus, and a lowercase k is used to denote a tangent modulus. The values of K^n and k_s are determined by the current contact stiffness model.

5.2.1.4 Law of Motion

The motion of a single rigid particle is determined by the resultant force and moment vectors acting upon it and can be described in terms of the translational motion of a point in the particle and the rotational motion of the particle. The translational motion of the center of mass is described in terms of its position, x_i , velocity, \dot{x}_i , and acceleration, \ddot{x}_i ; the rotational motion of the particle is described in terms of its angular velocity, ω_i , and angular acceleration, $\dot{\omega}_1$. The equations of motion can be expressed as two vector equations: one relates the resultant force to the translational motion; and the other relates the resultant moment to the rotational motion.

The equation for translational motion can be written in the vector form as in Eq. 5.8:

$$F_i = m \cdot (\ddot{x}_i - g_i) \quad (5.8)$$

where F_i is the resultant force, the sum of all externally applied forces acting on the particle; m is the total mass of the particle; and g_i is the body force acceleration vector, e.g., gravity loading.

5 Material model and numerical simulations

The equation for rotational motion can be written in the vector form; see Eq. 5.9:

$$M_i = \dot{H}_i \quad (5.9)$$

where M_i is the resultant moment acting on the particle, and \dot{H}_i is the angular momentum of the particle. This relation is referred to a local coordinate system that is attached to the particle at its center of mass. If this local system is oriented such that it lies along the principal axes of inertia of the particle, then Eq. 5.9 reduces to Euler's equation of motion; see Eq. 5.10:

$$\begin{aligned} M_1 &= I_1 \cdot \dot{\omega}_1 + (I_3 - I_2) \cdot \omega_3 \cdot \omega_2 \\ M_2 &= I_2 \cdot \dot{\omega}_2 + (I_1 - I_3) \cdot \omega_1 \cdot \omega_3 \\ M_3 &= I_3 \cdot \dot{\omega}_3 + (I_2 - I_1) \cdot \omega_2 \cdot \omega_1 \end{aligned} \quad (5.10)$$

where I_1 , I_2 , and I_3 are the principal moments of inertia of the particle; $\dot{\omega}_1$, $\dot{\omega}_2$, and $\dot{\omega}_3$ are the angular accelerations about the principal axes; and M_1 , M_2 , and M_3 are the components of the resultant moment referred to the principal axes.

For a spherical particle of radius R , whose mass is distributed uniformly throughout its volume, the center of mass coincides with the sphere center. Any local-axis system attached to the center of mass is a principal-axis system, and the three principal moments of inertia are equal to one another. Thus, for a spherical particle, Eq. 5.10 can be simplified and referred to the global-axis system as shown in Eq. 5.11:

$$M_i = I \cdot \dot{\omega}_i = \left(\frac{2}{5} \cdot m \cdot R^2 \right) \cdot \dot{\omega}_i \quad (5.11)$$

The equations of motion, given by Eqs. 5.8 and 5.9, are integrated using a centered finite difference procedure involving a timestep of Δt . The quantities \dot{x}_i and ω_i are computed at the mid-intervals of $(t \pm n \cdot \Delta t / 2)$, while the quantities x_i , \ddot{x}_i , $\dot{\omega}_1$, F_i and M_i are computed at the primary intervals of $(t \pm n \cdot \Delta t)$. The following expressions describe the translational and rotational accelerations at time t in terms of the velocity values at mid-intervals. The accelerations can be calculated as shown in Eq. 5.12:

$$\begin{aligned} \ddot{x}_i^{(t)} &= \frac{1}{\Delta t} \cdot \left(\dot{x}_i^{(t+\frac{\Delta t}{2})} - \dot{x}_i^{(t-\frac{\Delta t}{2})} \right) \\ \dot{\omega}_i^{(t)} &= \frac{1}{\Delta t} \cdot \left(\omega_i^{(t+\frac{\Delta t}{2})} - \omega_i^{(t-\frac{\Delta t}{2})} \right) \end{aligned} \quad (5.12)$$

Inserting these expressions into Eqs. 5.8 and 5.11, and solving for the velocities at time $(t \pm \Delta t / 2)$, results in Eq. 5.13:

$$\begin{aligned} \dot{x}_i^{(t+\frac{\Delta t}{2})} &= \dot{x}_i^{(t-\frac{\Delta t}{2})} + \left(\frac{F_i^{(t)}}{m} + g_i \right) \cdot \Delta t \\ \omega_i^{(t+\frac{\Delta t}{2})} &= \omega_i^{(t-\frac{\Delta t}{2})} + \left(\frac{M_i^{(t)}}{I} \right) \cdot \Delta t \end{aligned} \quad (5.13)$$

Finally, the velocities in Eq. 5.13 are used to update the position of the particle center as Eq. 5.14:

$$x_i^{(t+\Delta t)} = x_i^{(t)} + \dot{x}_i^{(t+\frac{\Delta t}{2})} \cdot \Delta t \quad (5.14)$$

The calculation cycle for the law of motion can be summarized as follows. Given the values of $\dot{x}_i^{(t-\frac{\Delta t}{2})}$, $\omega_i^{(t-\frac{\Delta t}{2})}$, $x_i^{(t)}$, $F_i^{(t)}$ and $M_i^{(t)}$, Eq. 5.13 is used to obtain $\dot{x}_i^{(t+\frac{\Delta t}{2})}$ and $\omega_i^{(t+\frac{\Delta t}{2})}$. Further, Eq. 5.14 is used to obtain $x_i^{(t+\Delta t)}$. The values of $F_i^{(t+\Delta t)}$ and $M_i^{(t+\Delta t)}$, to be used in the next calculation cycle, are obtained by using force–displacement law.

The equations of motion are integrated using a centered finite–difference scheme expressed by Eqs. 5.12 and 5.13. The computed solution produced by these equations will remain stable only if the timestep does not exceed a critical timestep related to the minimum eigenperiod of the total system. However, global eigenvalue analyses are impractical to apply to the large and constantly changing systems typically encountered in simulation. Therefore, a simplified procedure is implemented to estimate the critical timestep at the start of each cycle.

The critical timestep can be expressed as Eq. 5.15:

$$t_{crit} \begin{cases} \sqrt{m/k^{tran}} \\ \sqrt{I/k^{rot}} \end{cases} \quad (5.15)$$

where k^{tran} and k^{rot} are the translational and rotational stiffness, respectively; m is a mass of the particles, and I is the moment of inertia of the particle. In terms of the contact model the k^{tran} and k^{rot} corresponded to the K^n and k_s (normal and shear stiffnesses at the contact), respectively.

The system modelled in PFC is a collection of discrete bodies (particles and clumps) and springs. Each body may have a different mass, and each spring may have a different stiffness. A critical timestep is found for each body by applying Eq. 5.15 separately to each degree of freedom, and assuming that the degrees of freedom are uncoupled. The stiffnesses are estimated by summing the contribution from all contacts, using only the diagonal terms of the contact stiffness matrix. The final critical timestep is taken to be the minimum of all critical time–steps computed for all degrees of freedom of all bodies [59].

5.2.1.5 Modelling of the contact bond

PFC allows particles to be bonded together at contacts. The two standard bonding behaviours are embodied in contact bonds and parallel bonds. Both bonds can be envisioned as a kind of glue joining the two particles. The contact–bond glue is of a vanishingly small size that acts only at the contact point, while the parallel–bond glue is of a finite size that acts over either a circular or rectangular cross–section lying between the particles, see Figure 5.3. The contact bond can transmit only force, while the parallel bond can transmit both force and moment.

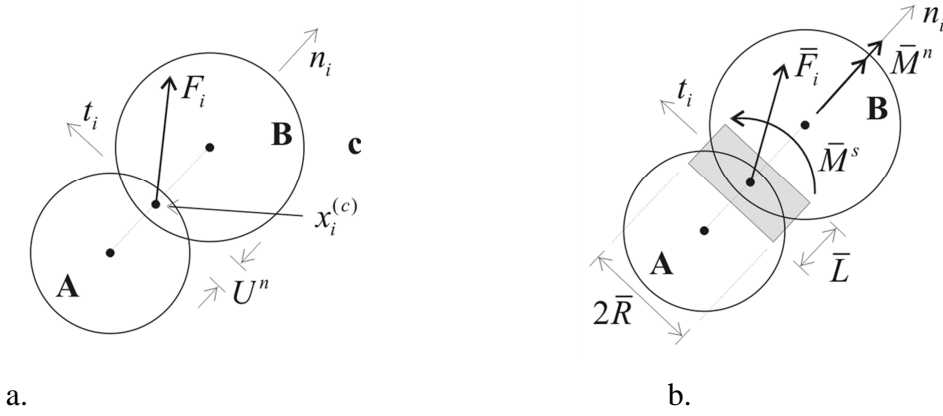


Figure 5.3: Notation used to describe a) contact bond and b) parallel bond [59]

Both types of bonds may be active at the same time. However, the presence of a contact bond supersedes the slip behaviour. If a bond is once formed at a contact between two particles, then that contact continues to exist until the bond is broken. Particles may be bonded only to one another; a particle may not be bonded to a wall. As the default condition, particles are not bonded.

A contact bond can be envisioned as a pair of elastic springs (or a point of glue) with constant normal and shear stiffnesses acting at the contact point. These two springs have specified shear and tensile normal strengths, see Figure 5.4. The existence of a contact bond precludes the possibility of slip. Instead, the magnitude of the shear contact force is limited by the shear contact bond strength. Contact bonds also allow tensile forces to develop at a contact. In this case, the contact bond acts to bind the balls together. The magnitude of the tensile normal contact force is limited by the normal contact bond strength.

The contact stiffness is defined by the normal and shear stiffnesses (k^n and k^s) of the two contacting entities (ball-to-ball or ball-to-wall). The contact bond stiffnesses for the linear contact model are computed assuming that the stiffnesses of the two contacting entities act in series. The contact bond normal secant stiffness is given by Eq. 5.16

$$K^n = \frac{k_n^{[A]} \cdot k_n^{[B]}}{k_n^{[A]} + k_n^{[B]}} \quad (5.16)$$

and the contact bond shear tangent stiffness is given by Eq. 5.17:

$$K^s = \frac{k_s^{[A]} \cdot k_s^{[B]}}{k_s^{[A]} + k_s^{[B]}} \quad (5.17)$$

where the superscripts [A] and [B] denote the two entities in contact.

For the linear model, the normal secant stiffness, k^n , is equal to the normal tangent stiffness since in Eq. 5.18:

$$k^n \equiv \frac{dF^n}{dU^n} = \frac{d(K^n U^n)}{dU^n} = K^n \quad (5.18)$$

where K_n is given by Eq. 5.16.

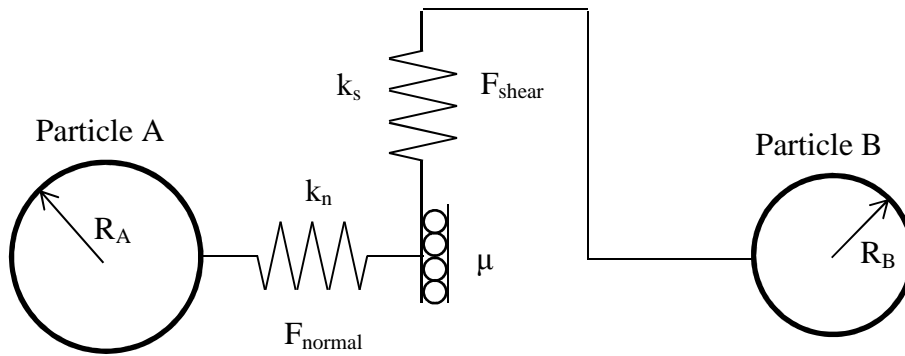


Figure 5.4: Notation used to describe the scheme of interaction [59]

A contact bond is defined by the following two parameters: normal contact bond strength, F_c^n (force); and shear contact bond strength, F_c^s (force). If the magnitude of the tensile normal contact force equals or exceeds the normal contact bond strength, the bond breaks, and both the normal and shear contact forces are set to zero. If the magnitude of the shear contact force equals or exceeds the shear contact bond strength, the bond breaks, but the contact forces are not altered, provided that the shear force does not exceed the friction limit, and provided that the normal force is compressive.

The force–displacement behaviour relating the normal and shear components of contact force and relative displacement for particle contact occurring at a point is shown in Figure 5.5. At any given time, either the contact–bond or the slip behaviour is active. In this figure, F^n is the normal contact force, where: $F^n > 0$ indicates tension; U^n is the relative normal displacement, where $U^n > 0$ indicates overlap; F^s is the magnitude of the total shear contact force; and U^s is the magnitude of the total shear displacement measured relative to the location of the contact point when the contact bond was formed. Note that an additional force *and moment* may also be acting, as well as the force shown in Figure 5.5, if a parallel bond is present.

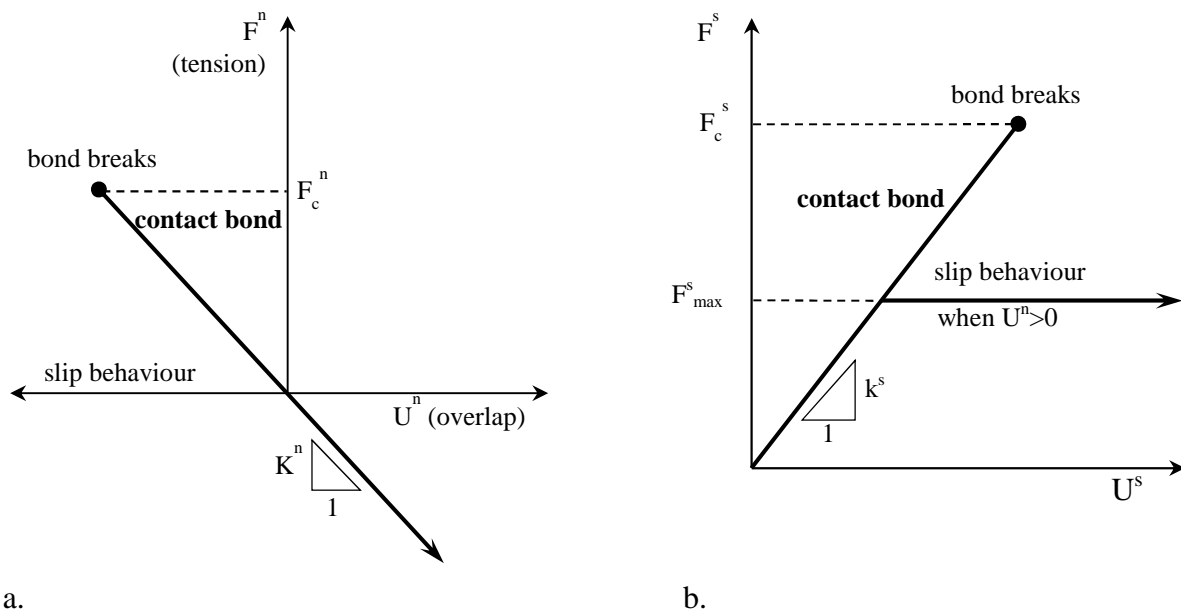


Figure 5.5: Force–displacement behaviours for contact occurring at a point for a) normal and b) shear components of the contact force [59]

Slip behaviour means that the system can start motion in a shear direction, i.e., motion in a viscous medium. Slip behaviour is given by defining a relationship between shear and normal force such that the two contacting entities may slip relative to one another. Slip behaviour is always active unless a contact bond is present, in which case the contact–bond behaviour supersedes the slip behaviour.

Slip behaviour is defined by the friction coefficient at the contact μ [dimensionless], where μ is taken to be the minimum friction coefficient of the two contacting entities. The contact is checked for slip conditions by calculating the maximum allowable shear contact force; see Eq. 5.19:

$$F_{max}^s = \mu \cdot |F_i^n| \tag{5.19}$$

If $|F_i^s| > F_{max}^s$, then slip is allowed to occur during the next calculation cycle by setting the magnitude of F_i^s equal to F_i^{max} via Eq. 5.20:

$$F_i^s \leftarrow F_i^s (F_{max}^s / |F_i^s|) \tag{5.20}$$

5.2.1.6 Dissipating the kinetic energy

Energy supplied to the particle system is dissipated through frictional sliding. However, frictional sliding may not be active in a given model or, even if active, may not be sufficient to arrive at a steady–state solution in a reasonable number of cycles. Local damping and viscous damping are available to dissipate kinetic energy. Local damping acts on each ball, while viscous damping acts at each contact. Local damping applies a damping force of magnitude proportional to the unbalanced force to each ball. Viscous damping adds normal and shear dashpots at each contact. These dashpots act in parallel with the existing contact model, and provide forces that are proportional to the relative velocity difference between the two contacting entities (ball–ball or ball–wall). The interaction scheme with damping is presented in Figure 5.6.

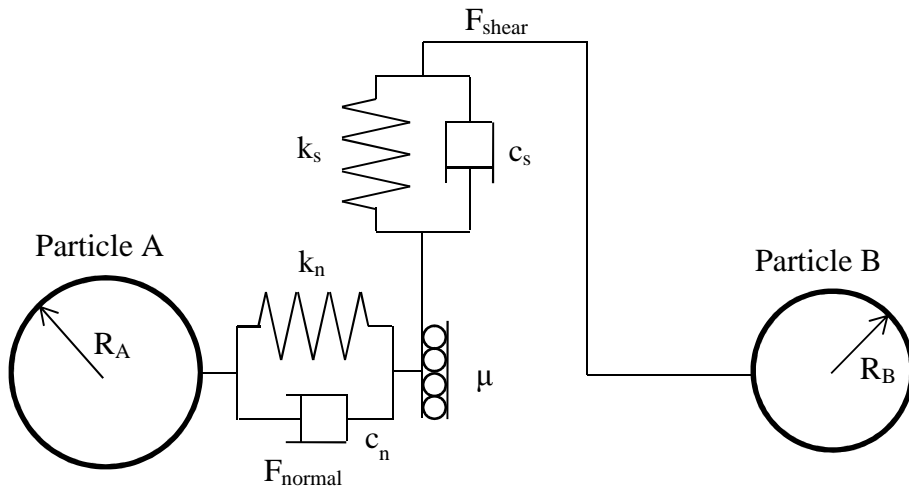


Figure 5.6: Notation used to describe the scheme of interaction with damping [59]

For compact assemblies, local damping, using the default parameter setting, is the most appropriate form to establish equilibrium and to conduct quasi–static deformation simulations.

In the case of local damping a damping–force term is added to the equations of motion, given by Eqs. 5.8 and 5.11, such that the damped equations of motion can be written as Eq. 5.21.

$$F_{(i)} + F_{(i)}^d = M_{(i)} \cdot A_{(i)}; \quad i=1 \dots 6$$

$$M_{(i)} \cdot A_{(i)} = \begin{cases} m \ddot{x}_{(i)}, & \text{for } i=1 \dots 3 \\ I \dot{\omega}_{(i-3)}, & \text{for } i=4 \dots 6 \end{cases} \quad (5.21)$$

where, $F_{(i)}$, $M_{(i)}$ and $A_{(i)}$ are the generalized force, mass and accelerating components; $F_{(i)}$ includes the contribution from the gravity force and $F_{(i)}^d$ is the damping force; see Eq. 5.22:

$$F_{(i)}^d = -\alpha \cdot |F_{(i)}| \text{sign}(v_{(i)}); \quad i=1 \dots 6$$

$$v_{(i)} = \begin{cases} \dot{x}_{(i)}, & \text{for } i=1 \dots 3 \\ \omega_{(i-3)}, & \text{for } i=4 \dots 6 \end{cases} \quad (5.22)$$

where, $v_{(i)}$ is generalized velocity; α is non-dimensional damping constant.

Thus only accelerating motion is damped.

In the case of viscous damping the dashpots act in parallel with the existing contact model as well as with the bonding model. A damping force is added to the contact force, of which the normal and shear components are given by Eq. 5.23:

$$D_{n,s} = c_{n,s} |V_{(n,s)}| \quad (5.23)$$

where $c_{n,s}$ is the damping constant, $V_{(n,s)}$ is the relative velocity at the contact, and the damping force acts to oppose motion. The subscripts n and s refer to one of the components of the contact force (n – normal, s – shear).

The damping constant is not specified directly; instead, the critical damping ratio $\beta_{n,s}$ is specified, and the damping constant satisfies via Eq. 5.24:

$$c_{n,s} = \beta_{n,s} c_{n,s}^{crit} \quad (5.24)$$

where $c_{n,s}^{crit}$ is the critical damping constant which is given by Eq. 5.25:

$$c_{n,s}^{crit} = 2 m \omega_{n,s} = 2 \sqrt{m k_{n,s}} \quad (5.25)$$

where, $\omega_{n,s}$ is the natural frequency of the un-damped system, $k_{n,s}$ is the contact tangent stiffness, and m is the effective system mass. In the case of ball-wall contact, m is taken as the ball mass; in the case of ball-ball contact, m is given by Eq. 5.26:

$$m = \frac{m_1 m_2}{m_1 + m_2} \quad (5.26)$$

where, m_1 and m_2 are masses of ball 1 and ball 2, respectively.

5.2.1.7 User-defined contact model

Initially the PFC was developed for modelling in the field of geomechanics. The standard code library contains only the very simple contact, slip and bond models which were developed for solid materials exhibiting elastic or viscoelastic mechanical behaviour. The functionalities of the standard contact models are limited by the foreseen modelling of solid materials. For modelling of the rheological behaviour of fluid materials, the standard contact models are inadequate.

For such cases the PFC provides a feature which allows user to write his or her own contact model, so-called user-defined contact model, which can represent the contact behaviour of the material model more accurately than the standard contact model.

5.2.2 Developing of the material model for numerical simulation

The material model for numerical simulation is a mathematical model which can be implemented into Itasca PFC. The material model consists of two components: the model for the normal component of contact force and the model for the tangential component of the contact force. Each component of the material model for numerical simulation includes a rheological model of the interaction between neighboring entities and the mathematical description of the rheological model, i.e., the force-displacement relationship in mathematical form.

It is assumed that the Bingham rheological model can be used for representation of the rheological behaviour of fresh concrete on macrolevel of investigation. The Bingham rheological model is based on the definition of yield stress and plastic viscosity. Thus, it is assumed that the concept of yield stress and plastic viscosity should also be presented on the mesolevel of investigation. However, for correct representation of the behaviour at the mesolevel of investigation the classical Bingham rheological model needs some modification.

The classical Bingham model represents the rheological response of the viscoelastic materials to shear motion. Motion in the normal direction is not considered in the classical Bingham model. So, the classical Bingham rheological model must be modified in order to consider the rheological behaviour for the normal direction of motion. The rheological model and mathematical descriptions for modified normal and tangential directions of motion are presented in the previous chapters.

5.2.2.1 Normal direction

As stated above, motion in the normal direction is not described by the Bingham model. Therefore, the rheological behaviour of the motion in normal direction needs defining in this chapter.

Motion in the normal direction means that the entities move only along the line which connects their centers of mass, in the case of ball-ball contact, or the perpendicular dropped from the center of the ball on to the wall plane in the case of ball-wall contact. It is shown schematically in Figure 5.7.

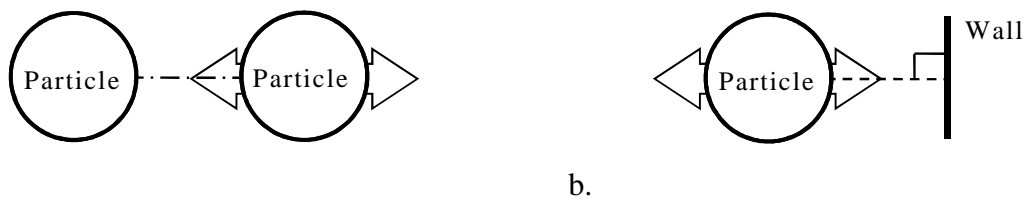


Figure 5.7: Motion of the entities in the pure normal direction for a) particle-particle and b) particle-wall contacts

The representation of yield stress is based on the definition of the phenomenon of yield stress. The yield stress means that the internal structure of the material remains unchanged when the stress produced by applied forces is lower than the yield stress of the material. The representation of the plastic viscosity is also based on the definition of the phenomenon of plastic viscosity. The effect of plastic viscosity with Bingham arises when yield stress is attained and the system starts moving.

The viscous force either hinders or prevents this movement. Thus, the direction of the viscous force is opposite to the direction of the total force.

The total force measured experimentally consists of two components: viscous and elastic, which work simultaneously; see Section 4.11. Therefore, the rheological model of an interaction in the normal direction consists of basic rheological elements: an ideal dashpot and an ideal spring connected in parallel. The interaction model also includes the element “contact” positioned in series with the basic rheological elements. The ideal spring represents the effect of an elastic interaction between entities, including an effect of yield stress, and the dashpot represents the effect of inelastic interaction, the effect of viscosity. The element “contact” defines the mode of the material model, the yield zone or viscoelastic zone of interaction between entities, and the state of the contact bond, i.e., broken or unbroken. The stiffness of the spring depends on the mode of the material model. Moreover, the element “contact” enables the definition of the strength of the contact bond, simulation of the loss of an existing contact/interaction when particles separate by a certain predefined distance, and the formation of a new interaction.

The material model in the normal direction is presented schematically in Figure 5.8.

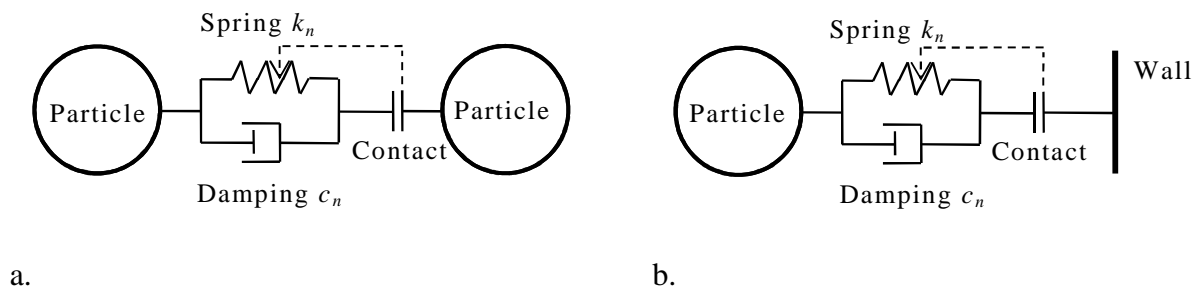


Figure 5.8: The rheological model of particle–particle interaction in the normal direction for a) particle–particle and b) particle–wall contacts

Figure 5.9 shows schematically two types of the force–displacement relationships as introduced for the contact elements in the normal direction.

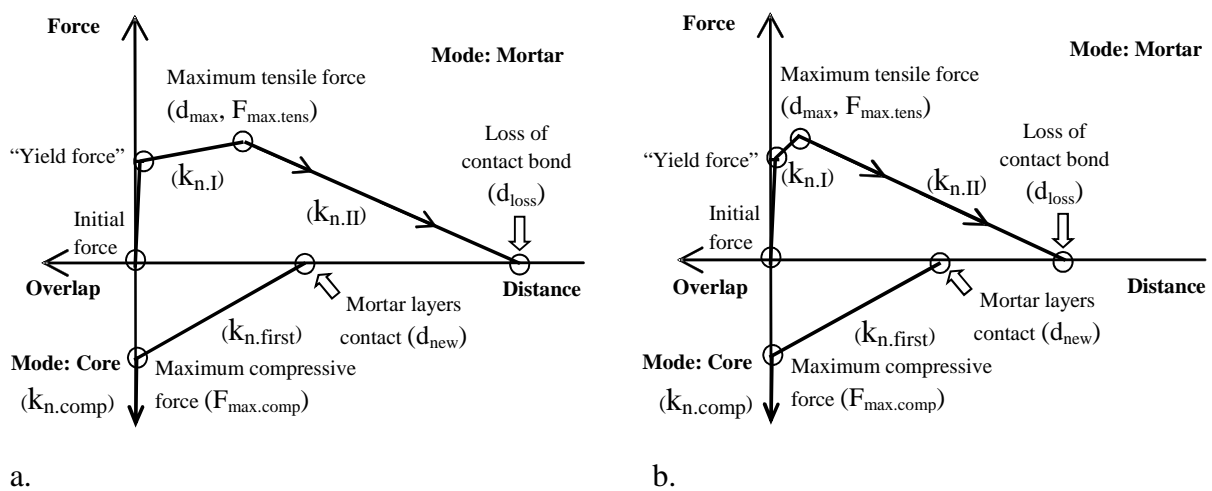


Figure 5.9: The force–displacement relations for contact elements in the normal direction for a) particle–wall and b) particle–particle contacts

It is assumed that all particles are covered with a layer of fine mortar. Therefore, when two particles approach each other the mortar layers come into contact first. In approaching further the distance between cores decreases until there is direct contact of the cores. The stiffness of the mortar layer is much less than the stiffness of the cores. Therefore it is assumed that the fine mortar layer deforms as a linear function of force and displacement; see the line segment between “Mortar layer contact” and “Maximum compressive force”. For more details about the layer of fine mortar see Section 5.2.4.5.

Thus, the force–displacement relation consists of two modes: Core and Mortar. “Core” mode means that two entities are in direct contact; “Mortar” mode means that entities have no direct contact; however forces and moments are transmitting from one entity to another by means of viscoelastic material between them. The angle of inclination to the “Force” axis depends on the stiffness of the spring (which depends on mode of “contact” element). The force–displacement relationship can be divided into four parts, from initial approaching to direct contact of cores based on significant change of inclination.

The first part is a compression mode when two entities are in direct contact. It is assumed that the particles and walls are solid and thus the compression force increases rapidly with increasing overlapping, i.e., the angle to the abscissa is approximately 90 degrees. The second part from left to right is the yielding zone. In this part both the entities are separated by some distance. Taking into account the definition of the yield stress, the inclination of this part of force–displacement relation to the displacement axis should also be about 90 degrees. The third part is called hardening: the total force increases in this region until “Maximum tensile force” is reached. The fourth part starts when the total force starts to decrease after reaching “Maximum tensile force”. The total force decreases to zero and contact fails. The stiffness of the spring changes depending on the mode of interaction.

It is worthy of note that the force–displacement relations presented in Figure 5.9 correspond to the experiments with a given velocity of movement. For another velocity the viscous component of the force will be different because this component of the force is velocity–dependent. The shape of force–displacement relations and all distance characteristics of the force–displacement relations remain unchanged; only the force characteristics vary; see Figures 4.13 and 4.27. The diagram stretches or shrinks along the axis of “Force” similar to the experiments with different velocities.

5.2.2.2 Tangential direction

Taking into account the complexity of the required equipment the force–displacement relation for shear direction was not investigated experimentally. Pure shear displacement means rotation of one particle around another in the case of ball–ball contact and sliding, no rolling, of the particle on the surface of wall in the case of ball–wall contacts; distance between particles or particle and wall remains unchanged. The pure shear motion is presented schematically in Figure 5.10.

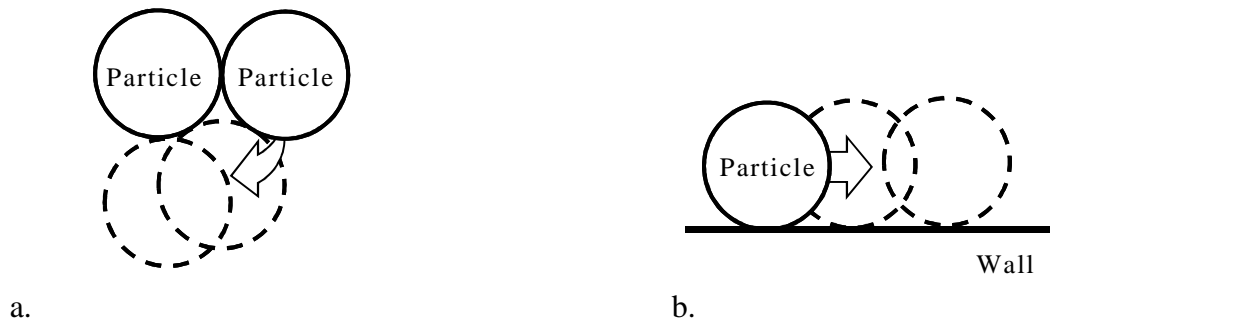


Figure 5.10: Motion of the entities in pure shear direction for a) particle–particle and b) particle–wall contacts

The Bingham rheological model is a model of the motion in the shear direction and which consists of two basic rheological elements: dashpot and friction elements connected in parallel. The dashpot represents the viscosity and the friction element represents the yield stress. The material model in the shear direction is presented schematically in Figure 5.11.

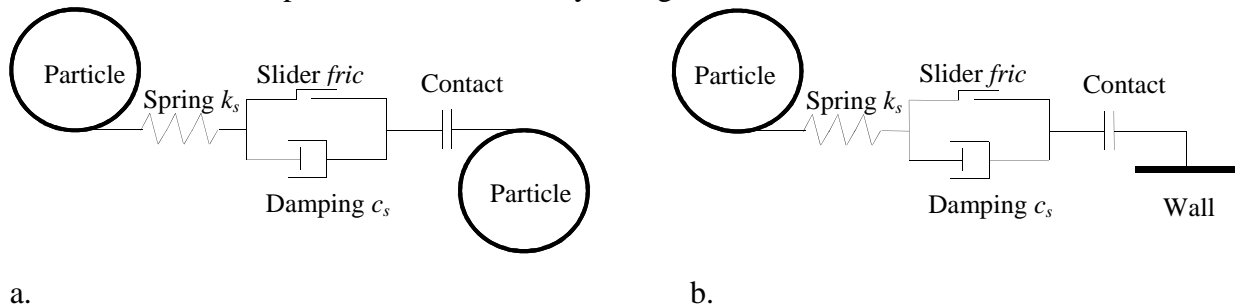


Figure 5.11: The rheological model of interaction in shear direction for a) particle–particle and b) particle–wall contacts

The interaction model also includes the element “contact” in series with the basic rheological elements. The element “contact” represents the state of the contact bond, i.e., broken or unbroken, and the mode of the material model, i.e., contact between cores or mortar layers. Taking into account the results of the investigation of the FDL in the normal direction (see Section 4.11) it is safe to say that:

- ✓ the force–displacement relation for shear direction should also have a part which represents the yield stress behaviour of the contact bond;
- ✓ the resulting force of the shear motion consists of two components: elastic and viscous; the elastic component of the contact force is velocity–independent and depends on thickness of the contact bond in normal direction. The elastic component of the contact force by pure shear displacement is constant; the viscous component of the contact force is velocity–dependent and proportional to the velocity of shear motion.

In addition it should be noted that shear displacement is relative; shear force is independent of the direction of shear motion. Therefore, pure shear motion can be infinite. This means that the contact bond cannot be broken by pure shear motion, taking into account that particles are surrounded by a fluid phase. The characteristic of the shear motion is shear displacement in the corresponding timestep, in contrast to the distance between entities in the case of normal direction.

Figure 5.12 shows schematically the predicted force–displacement relation for the “contact” element in the shear direction.

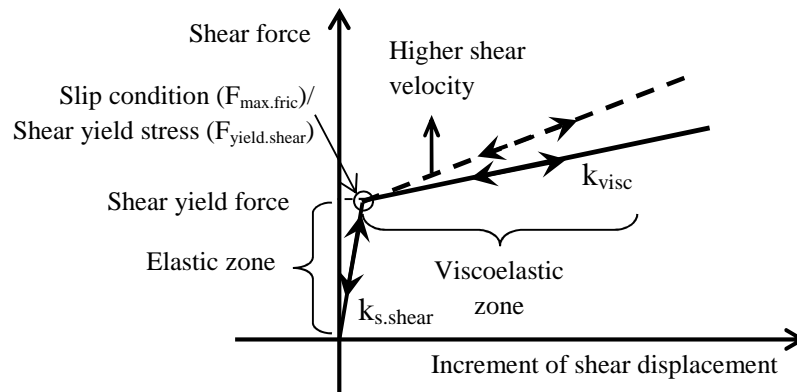


Figure 5.12: Predicted force–displacement relation for contact elements (shear direction)

The force–displacement relation for shear direction includes two modes: Core and Mortar, as does the force–displacement relation for the normal direction. The difference between the modes consists in their different coefficients of friction, the friction between cores by direct contact and the internal friction in the mortar layer. The angle of inclination of the linear parts of the force–displacement relation to the horizontal axis is related to the stiffness of the spring in shear direction; see Figure 5.11. The force–displacement relation contact can be divided into two parts according to the noticeable change in its inclination. The first part is a “Elastic zone” of small deformation, which represents the yield stress behaviour in the direction of shear. It is assumed that the deformation is very small; therefore, the shear force increases rapidly, angle to the abscissa is slightly less than 90 degrees. The “Slip condition/Shear yield stress” means the beginning of the motion in the shear direction. The difference between “Slip condition”, similar to the standard contact model – see Section 5.2.1.5, and “Shear yield stress” is in calculation of the maximum shear force, similar to the standard contact model for “Slip condition” or user–defined value for “Shear yield stress”; see Section 5.2.1.5. The motion in the shear direction corresponds to the second part of the force–displacement relation – “Viscoelastic zone”. The angle of inclination to the abscissa in the “Viscoelastic zone” depends on the coefficient of viscosity in the shear direction (see Figure 5.11). According to Newton’s Law for viscosity, it is assumed that the viscous component of the force is in direct proportion to the velocity of the shear motion and also proportional to the thickness of the contact, the amount of material between particles, as well as the viscous component of the contact force for the normal direction of motion.

It is significant to note that the frictional force is nonzero only for the case of approaching, because the nature of friction always implies some compression force in the normal direction. In the case of “moving away” the normal component of the force has a tension mode; the frictional force must be zero. Therefore, the shear force is equal to the viscous component of the shear force taking into account the “Shear yield force”, which depends on the coefficient of friction for a given normal force.

5.2.3 Implementation of the contact model into PFC programme

The above-described material models for numerical simulation in the normal and shear directions were written in mathematical form and implemented into Itasca PFC using a user-developed C++ code option.

This option allows user to write his or her own code in C++ language and then create a private PFC executable file from which the code can be run. In order to add user-written C++ functions, a private PFC executable file was created using the binary libraries supplied [59], and new object files were compiled. The compiled binary libraries include the complete information about the material model in both directions (normal and shear) which can be applied to all or selected groups of contacts. The contact bond model applies to each pair of contacting entities individually with individual set of contact bond characteristics. The use of the user-defined contact model allows from the core of the PFC the reading of information such as positions and sizes of the particles and the calculating of the parameters which are necessary for the user-defined contact model: distance between particles and mode of contact, i.e., compression or tension, relative displacements between particles, and their velocities. The contact bond characteristics can be specified by the user for each contact bond separately, taking into account the types of the particles, i.e., aggregates, steel fibres etc., and their sizes. All this initial information is processed using the binary library and returns new initial parameters for the next cycle in compliance with user-written contact model.

5.2.3.1 Description of the parameters of contact model

Each linear part on the force–displacement diagram in the normal or shear directions has its own characteristics. By analogy with experimental force–displacement diagrams, these characteristics can be divided into two groups: characteristic distances and characteristic forces. Each part of the force–displacement diagram has a different inclination to the displacement axis. The magnitude of this inclination is in direct proportion to the coefficient of stiffness of the spring; the position of the spring in the material model is presented in Figures 5.8 and 5.11 for the shear and normal directions, respectively. With increasing distance between entities the contact force changes linearly in accordance with the actual stiffness until another pair of characteristic values is reached, e.g., when the magnitude of the maximum force and the corresponding distance between entities is achieved, the force–displacement curve changes its inclination at this point, which implies that other coefficients of stiffness are applicable.

The set of parameters of the contact model in normal direction depends on mode of the interaction: “Core” or “Mortar”. The “Mortar” mode consists of two regimes – “First contact” and “Mortar layer”, according to Figure 5.9. The “First contact” in “Mortar” mode means that the entities comes into contact; the characteristics of this regime are the following: distance at which the new contact has to be created (d_{new}) for the first time, the maximum compressive force ($F_{max.comp}$), and the stiffness coefficient for the mortar layer ($k_{n.first}$). It is noteworthy that the stiffness coefficient for the mortar layer is not an input parameter for the contact model; its magnitude is calculated as a ratio of $F_{max.comp}$ to d_{new} . The regime “First contact” moves into the regime “Compression” (“Core” mode) in the case of approaching, or the contact can be broken at the distance where the new contact bond was created in case of the particle’s moving away. The condition of transition from the “First contact” regime to the “Core” mode is a specified overlap between particles which corresponds to the end of the mortar layers’ interaction and the beginning of the core interaction. Higher overlap

implies contacts among the cores; therefore, the “Core” mode always means compression. The major characteristic of the “Core” mode is the stiffness coefficient ($k_{n.comp}$), which is much higher than the corresponding stiffness coefficient for the mortar layer. The “Mortar” mode activates when the overlap between entities is smaller than the condition for the “Core” mode. The “Mortar” mode has the following characteristics: the coefficient of stiffness for the mortar layer before maximum tensile force ($k_{n.I}$), maximum tensile force ($F_{max.tens}$) and distance of the maximum tensile force (d_{max}), coefficient of stiffness for mortar layer after maximum tensile force ($k_{n.II}$) and distance to loss of contact bond, coefficients of yield stress (k_{yield}) and plastic viscosity (k_{visc}). The stiffness coefficients are not input parameters; their magnitudes are calculated from the known values of characteristic distances and forces. The “Mortar layer” regime includes two types of motion: approaching and moving away, decrease and increase of the distance between entities, respectively. Approaching always means compressive normal force and moving away – tensile normal force. Change of the type of motion means change of the direction of the force vectors for the elastic and viscous components of the contact force according to the results of the tests; see Section 4.9. The contact bond is considered broken when the current motion is “moving away” and the contact force is equal to zero.

Parameters of the contact model for normal direction are summarized in Table 5.2.

Table 5.2: Parameters of the contact model in normal direction

Mode	Regime	Name	Input parameter	Description
Core	Compression	$k_{n.comp}$	Yes	Coefficient of stiffness in compression
Mortar	First contact	d_{new}	Yes	Distance where new contact bond created
		$F_{max.comp}$	Yes	Maximum compressive force
		$k_{n.first}$	No	Coefficient of stiffness by first contact of mortar layers before “core” contact
	Mortar layer	$k_{n.I}$	No	Coefficient of stiffness for mortar layer before maximum tensile force (force increases)
		$F_{max.tens}$	Yes	Maximum tensile force
		d_{max}	Yes	Distance of the maximum tensile force
		$k_{n.II}$	No	Coefficient of stiffness for mortar layer after maximum tensile force (force decreases)
		d_{loss}	Yes	Distance to loss of contact bond
		k_{visc}	Yes	Coefficient of plastic viscosity
		k_{yield}	Yes	Coefficient of yield stress

The modes of the contact model are the same for normal and shear directions. However, transition between modes is possible only in the normal direction. Thus, the parameters of the contact model in shear direction for “Mortar” mode are the following: coefficients of static ($fric_{stat.mortar}$) and dynamic ($fric_{dyn.mortar}$) friction for the mortar layer, maximum friction force ($F_{max.fric}$) or shear yield force ($F_{yield.shear}$), and coefficient of plastic viscosity (k_{visc}). The parameters of the “Core” mode are as follows: coefficient of shear stiffness in compression, the same value used for “Mortar” mode,

coefficients of static ($fric_{stat.core}$) and dynamic ($fric_{dyn.core}$) friction for mortar layer, maximum friction force ($F_{max.fric}$). It should be noted that the maximum friction force depends on compressive normal force. The “Shear yield force” is the input parameter which represents yield stress behaviour in the case when yield force has to be higher than the friction force.

Parameters of the contact model for shear direction are summarized in Table 5.3.

Table 5.3: *Parameters of the contact model in the shear direction*

Mode	Regime	Name	Input parameter	Description
Core	Compression	$k_{s.shear}$	Yes	Coefficient of stiffness in compression
		$fric_{stat.core}$	Yes	Coefficient of static friction for cores
		$fric_{dyn.core}$	Yes	Coefficient of dynamic friction for cores
		$F_{max.fric}$	No	Maximum friction force (sliding regime)
Mortar	Compression/ Tension	$fric_{stat.mortar}$	Yes	Coefficient of static friction for mortar
		$fric_{dyn.mortar}$	Yes	Coefficient of dynamic friction for mortar
		$F_{max.fric}$	No	Maximum friction force (sliding regime)
		$F_{yield.shear}$	Yes	Shear yield force
		k_{visc}	Yes	Coefficient of plastic viscosity

5.2.3.2 Limitations of the contact model

The user-defined contact model represents the rheological model of interaction between two entities. It has some limitations, which are related to the features of the numerical simulation of the flow of discrete particles. The main limitation is the time needed for simulation. Accordingly, the duration of numerical simulation is in direct correspondence with the complexity of the contact model, the number of particles, and the number of the contacts. The timesteps in the numerical simulation are in direct correspondence to the square root of the weight of the particles and in inverse proportion to the square root of the stiffness of entities; see Eq. 5.15. Therefore, in a particle system including particles with different parameters, i.e., sizes, densities and stiffnesses, the applied timestep is equal to the minimum time step needed for stable numerical modelling. Thus, the numerical simulation passes more quickly by using relatively soft particles of larger size.

One of the limitations here is the number of particles in one simulation and the grading of these particles. As an example, for simulation of the slump flow test with the Abrams cone, of volume about 5.5 liters, the required number of the uni-sized particles with a diameter 1 mm is about 10^6 . The numerical simulation of the slump flow test with such a number of particles has a duration of more than a month on an ordinary modern desktop computer. A more or less appropriate time for numerical simulation is one week. Experience has shown that the number of particles should not be higher than 150.000 and the diameter of the smallest particles not below 2 mm. In addition the stiffness of the particles in compression cannot be infinite because of the cycling timestep. More details on composition of the “virtual concrete” are presented in the next section.

5.2.4 Additional tools for the “Virtual concrete laboratory”

The additional tools for the “Virtual concrete laboratory” consist of a set of procedures which create the geometry of the equipment; generate the particles with given grading; generate the fibres and coarse aggregates, consisting of particle clumps; and control and save the important aspects in the simulation which are related to the experiments such as the shape of the concrete specimen. Furthermore, these data are needed for analysing the intermediate and final states of the specimens with respect to stresses, fibres and coarse aggregates, distribution, and orientation. The procedures should deliver the characteristic features as observed in real experiments plus provide additional information which cannot be obtained from the test directly.

By applying the Particle Method, it is possible to simulate the effect of concrete composition on its rheological behaviour by defining the components of the concrete meso-structure, i.e., coarse sand, aggregates and fibres, discretely as shown in Figure 5.13. Spherical particles were used to make the concrete mesostructure discrete while walls were utilized for simulating the boundaries. If more complex geometries are to be simulated – like fibres or non-spherical aggregates, a number of particles can be rigidly interconnected providing necessary geometries. These complex assemblies are termed as clumps in PFC.

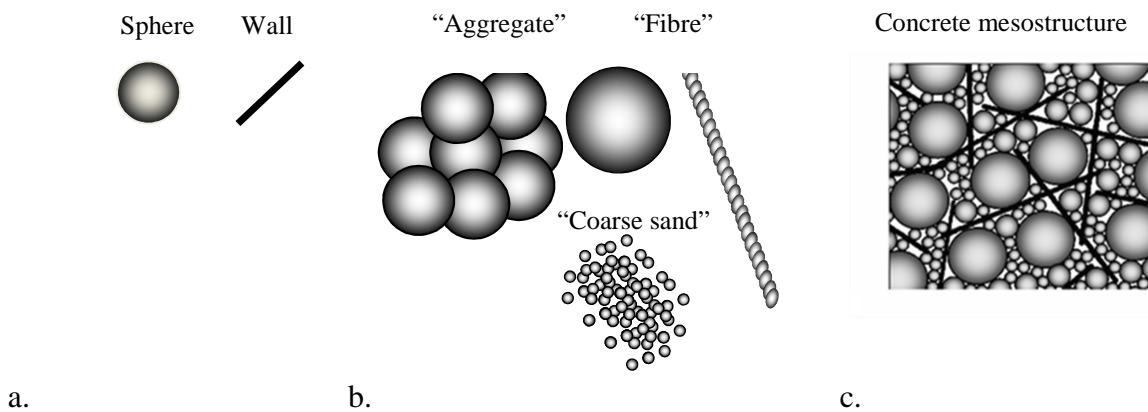


Figure 5.13 Schematic view of: a) basic model elements, b) computed constituents of concrete and c) discretisation of fibre-reinforced concrete

5.2.4.1 Modelling of the equipment and boundary conditions

The first step is modelling the geometry of the equipment, moulds, etc. For instance, for modelling the slump flow test the following equipment and accessories should be represented: the slump flow cone and slump flow table, the mixer or hopper where the components of the fresh concrete are generated, and the accessories which connect the mixer/hopper with the slump cone and allows filling of the cone with virtual concrete. These elements should be modelled before generation of concrete components.

All parts of the equipment can be modelled using wall elements in PFC. The behaviour of the walls depends on the following parameters: normal stiffness, shear stiffness, and coefficient of friction. The wall elements cannot interact with each other; they interact only with particles. The stiffness of the contact between balls and wall, all of which may have different stiffnesses, can be calculated using Eqs. 5.7 and 5.8.

5.2.4.2 Procedure for generation of particles representing fresh concrete

When generating the particles which represent the components of the fresh concrete the limitation of the PFC must be taken into consideration. The goal of this procedure is to produce a compacted mix of “numerical concrete” in an appropriate volume which is needed for numerical simulation.

The following factors should be taken into consideration:

1. required volume of “numerical concrete”;
2. shape of the components of the mix (aggregates and fibres);
3. particle size distribution and spatial distribution of the components.

The amounts of the components for fresh concrete depend on the composition of the concrete and the required volume of the material. After that the components can be mixed. There are many different mixers and procedures for mixing, but the goal of the mixing procedure is uniform spatial distribution of the components of fresh concrete over a given volume. Thus, in most cases, it is not important how the mixing process was simulated, while the final space distribution of the components of fresh concrete after mixing is always essential.

Before running the procedure for generating the particles, the real composition of the fresh concrete should be recalculated in terms of composition for numerical concrete, taking into account the cutoff level for grading of the particles. The cutoff level is defined as the minimum size of particles which should be used in the simulation. An example of this recalculation for a slump flow test with the Abrams cone (5.5 liter) is presented in Table 5.4.

Table 5.4: *An example of the composition of concrete and estimated number of particles for a slump flow test*

	Components	Amount in m ³ concrete [kg]	Amount in 5.5 l. [kg]	Number of particles
Fine mortar	Cement type II 42.5	472	2.596	–
	Fly ash	45	0.2475	–
	Water	216	1.188	–
	Superplasticizer	6.36	0.035	–
	Sand <2 mm	595	3.2725	>1000000
Aggregates	Sand 2–4 mm	102	0.561	114578
	Gravel 4–8 mm	153	0.8415	21483
	Gravel 8–16 mm	886	4.873	15091

The cutoff line of the level 2 mm in diameter, bold line in Table 5.4 was selected taking into account available computer resources. The limiting factor is computational time, which increases in correspondence with the number of particles in the numerical simulation. Moreover, the size and weight of the smallest particle have a strong influence on the duration of modelling via timestep; see Section 5.2.1.4. The available computer resources allow using approximately 150,000 particles in one simulation; the computational time for the slump flow test modelling is about 6 days (136 hours). Computational time for the composition presented above is about 13 days (312 hours), the number of particles is about 220,000; see Table 5.4. The components which cannot be made

discrete, i.e., are of size smaller than the cutoff level, will be considered as a medium (paste or mortar) among the discretised components. However, the volume of this “medium” is often higher than the total volume of the voids among the discretised components. Therefore, the volume of the discretised components after compacting will be smaller than the required volume for modelling. The algorithm for compensating this volume is presented in Section 5.2.4.4.

The number of particles is directly proportional to the amount of material. Moreover, the number of particles depends on the grading of the particles. For instance, the sand presented in Table 5.4 includes about 70% of the weight of sand particles smaller than 2 mm (about 17.5% 2–4 mm and 12.5% 2–4 mm). Thus, just 30% of the weight of sand can be modelled. In addition it is assumed that the particle size distribution in every interval is similar to the Gaussian distribution. The number of particles for each component is estimated according to the assumption mentioned above.

The input parameters for procedure for generation of the particles are following:

1. density, i.e., specific weight, of the component;
2. weight of the component – see Table 5.4 “Amount in 5.5 l.”;
3. minimum and maximum particle size of the component, i.e., grading;
4. parameters of the region where the particles must be generated.

The volume of the component is calculated from known values of density and weight. The particles are generated in such a manner that the volume of the particles is equal to the volume of component. The density of the particles corresponds to the real density of the component. Therefore, the weights of the components, as presented in Table 5.4, and the corresponding proportions between components of the fresh concrete in numerical modelling corresponded to the real composition of fresh concrete.

In addition it should be noted that the generating procedure distributes the particles uniformly in the specified region. However, new generated particles should not have any overlap with particles already generated. Otherwise there will be a very high compressive force, core–core contact, at the beginning of the modelling. In order to avoid this limitation the component with the largest particles is generated first, then the component with smaller particles is generated. The component with the smallest particles is generated at the end of the procedure.

It is worth noting that the volume of the region for the generating procedure has to be higher than the required volume of the material, as a minimum by two times. Otherwise the generating procedure cannot find enough storage capacity to operate, which in turn leads to an endless search for space, thus bringing the generation process to a halt.

5.2.4.3 Procedure for generating of non–spherical aggregates and fibres

In contrast to the procedure for generation of the particles of fresh concrete, where all particles are single spherical or circular entities, the procedure for generation of the non–spherical aggregates and fibres delivers components of the concrete which are more complex. This procedure is also supposed to make the spatial distribution of the specified type of fibres or aggregates uniform in the given volume. In addition the procedure controls the number and volume of generated fibres/aggregates. Figure 5.14 gives an example of fibres and irregularly shaped aggregates as implemented into the PFC. Each parameter of the fibres and aggregates such as dimensions,

thickness, and number of balls in each fibre or aggregate can be individually modified either manually or automatically.

In the case of fibres, their number can be calculated from their known weight and the weight of a single fibre. Moreover, all fibres can have similar shape; therefore a template can be used. A template of fibre means specified positions and sizes of the balls composing the fibre, i.e., fibre with and without hooks etc. The template can be modified manually or automatically if several types of fibre are required. The coarse aggregates are generated by analogy with fibres. In the case of regular shaped aggregates; the number of aggregates can be calculated from known volume of the component and volume of single aggregate. However, it is much more complicated task in case of irregularly shaped aggregates because a procedure for calculating of the volume of each new generated aggregate is required. The final volume of generated aggregates has to be equal to the required volume of the corresponding components of fresh concrete.



Figure 5.14: Schematic view of already developed and implemented into PFC a) fibres and b) coarse aggregates

The input parameters for procedure for generating fibres and non-spherical aggregates are following:

1. density (specific weight) of the component (aggregates) or weight of single fibre;
2. entire weight of the component;
3. parameters of the template or parameters for automatic generation of the fibres or non-spherical aggregates;
4. parameters of the region where the fibres or non-spherical aggregates must be generated.

Thus, all fibres or aggregates can have same or different shapes and dimensions. Further, the dimensions and shapes of aggregates should follow the required grading curve.

5.2.4.4 Compensating of the volume of components which cannot be made discrete

The components of the fresh concrete are divided into two groups: fine mortar and solid components; see also Table 5.4. The solid components are distributed more or less uniformly in the volume of the fresh concrete under consideration, and fine mortar is placed between solid components. However, fluid components of the concrete (water, superplasticizer) and fine solid components below the cut-off-line cannot be modelled using DEM discretisation; see Section 5.2.4.2. Therefore, the volume of fine mortar must be compensated by increasing the total volume of the solid components.

There are two manners of such compensation:

1. proportional increase of the number of solid particles in each group;
2. proportional increase of the size of solid particles in each group.

The first way has one essential drawback: the proportion between components remains unchanged but the number of particles and corresponding volume concentrations increase. However, the quantity of some special component should remain unchanged. For instance, increasing the number of fibres results in increasing of the volume concentration of the fibres in the numerical simulation, which in turn means another rheological behaviour of the fresh concrete. Thus this approach is not applicable to the simulation of the fibre-reinforced concrete. Naturally by increasing the number of particles the time needed for modelling increases.

The second way of compensation is simultaneous increase of the size of all particles. In this case the proportion between components and number of the special components, to wit: fibres, remains unchanged. Therefore, it can be argued that in such manner all particles are covered by a layer of fine mortar, which corresponds to the situation in the real concrete mix. The advantage of the second way is that the number of particles remains unchanged. This approach is more universal in comparison to the first one and can be used for any kind of modelling.

Increasing the diameter of the particles can be organized in two different ways. The diameter of the particles can be increased by the same value for all particles or the diameters of each particle can be multiplied by the same coefficient. In the first case the thickness of the covering layer is the same for all particles. In the second case the thickness of the covering layer depends on the initial diameter of the particle: the larger the size the thicker the covering layer. It is assumed that the fine mortar has uniform rheological behaviour. Therefore it may be supposed that the thickness of the covering layer depends on its rheological behaviour only. Taking into account these assumptions the thickness of the covering layer has to be the same for all particles irrespective of their size.

The aforementioned factors influencing the thickness of covering layer are the volume of fine mortar, which is not supposed to be modelled directly depending on the cutoff level, and grading of the particles. This thickness can be calculated more or less accurately before generating the particles by taking into account that the packing density is about 60% for random packing of monosize spherical particles [94]. It has been shown empirically in corresponding simulations after compacting the particles that the packing density is about 60–65% for random packing of not monosize spherical particles taking into consideration the minimum particle size, specified by the cutoff level at 2 mm, and the maximum particle size of 16 mm. The calculated volume of the total space between particles can be compared with volume of the mortar in real concrete under consideration of the cutoff level. The thickness of the covering layer depends on the difference between these two volumes.

The calculated thickness of the covering layer is considered in the corresponding user-written procedure.

The input parameters for this procedure are following:

1. existing generated particles, needed for calculation of the total volume of particles without voids among them;
2. total volume which has to be filled with particles, e.g. 5.5 l in the case of the slump flow test with the Abrams cone;

3. packing density, default value is 0.6;
4. maximum difference between volumes of the material which have to be modelled and the volume of the material after compensation, needed for iterative method.

The procedure calculates the total volume of particles which are already generated and estimates the volume after compacting, taking into consideration given packing density. The volume after compacting is compared with the required volume of the material. The iterative method is used in order to find the optimal thickness of the covering layer, taking into consideration the maximum difference between the required volume of the material and the volume of the material after compensation with an eye to the given packing density. The procedure for compensating can be run one more time after compacting with the optimized packing density if the volume of modelled material is different to required volume. It is significant to note that this procedure has to be run first before compacting in order to avoid a high compressive state of the particle systems after increasing the size of the particles. The second run of the procedure increases the size of the particles much less than in the first run and can be used for fine tuning the particle system in the already compacted state.

5.2.4.5 Layer of fine mortar for material model

In the previous section an approach for compensating the fine mortar volume, which cannot be made discrete using the PFC, was presented. The covering layer is incompressible in the case of the need for volume compensation. However, the material model includes a layer of fine mortar which is compressible; see Section 5.2.2.1. This layer represents the layer of fine mortar between entities which transmits the moments and forces from one entity to another without direct contact between the entities. In addition this layer is needed for well-timed contact detection in numerical modelling, the first contact between layers of fine mortar, as shown schematically in Figure 5.9.

Thus, the layer of fine mortar for the contact model means that the size of the particles has to be increased once more, but this increase has no significant influence on the total volume of the material – compressible layer. It is assumed that the yield stress behaviour of fine mortar is the main parameter influencing the thickness of the layer; it follows by definition of the yield stress and by analogy with the height of the undeformed part of the specimen in Section 3.3.1.1. Thus the fine mortar with higher yield stress provides a higher thickness of the covering layer; the results of the experiments with Carbopol solutions with different amount of Carbopol powder confirm this; see Section 4.9.

It is assumed that the thickness of the fine mortar layer in numerical modelling corresponds to the distance of the contact detection in the experiments with interaction between discrete particles with some viscoelastic material between them; see Figure 4.10. Thus, in the case of contact of monosize particles the thickness of covering layer is equal to the half the distance of new contact detection; reference contact is the best coincidence with experiments. In the case of contact of non-monosize particles the total distance of contact detection will be smaller in comparison with contact with monosize particles of larger size, but higher in comparison to the contact with monosize particles with smaller size; this is not fully consistent with experiments, but the tendency is right. For comparison with results of the tests see Figure 4.15 and Table 4.5. It is assumed that the small difference in the distance of the contact detection might not influence the results of modelling. In fact, the results of the modelling confirm this.

The stiffness of the fine mortar layer depends on its yield stress behaviour. This stiffness is much less than the stiffness of cores. Taking into account an analytical solution for stress distribution before and after lifting of the slump cone, all contacts “under” the yield stress level have to be compressed due to gravity force until the “cores” make contact while the contacts “upper” yield stress level will have contacts between the mortar layers; see Section 3.3.1.1 and Figure 3.7. The stiffness of the fine mortar layer gives rise to this effect. Two parameters are needed for estimation of this stiffness: distance of the contact detection and maximum compressive force (see Figure 5.9). Both parameters are input parameters for the material model. However, the maximum compressive force in numerical modelling is dimensionless as is maximum tensile force. Therefore the maximum compressive force is estimated only after estimation of the maximum tensile force, or contact bond strength; more details about link between yield stress of the material and contact bond strength can be seen in Section 5.3.1.3.

The user-written procedure modifies the size of particles for the fine mortar layer after fine tuning the volume-use procedure for compensation; see the previous section. This procedure is the first part of the initialization of the user-defined contact model – in preparation for applying the user-defined contact model. The second part is applying the user-defined contact model to all existing contacts; newly detected contacts are updated automatically.

Input parameters for the procedure for adding the fine mortar layer are the following:

1. generated and compacted particles with added compensating layer;
2. magnitude of the distance of contact detection for reference pair of particles.

It is known from the test results that the distance of the contact detection is proportional to the size of smaller particle. It is assumed that this proportionality is linear, which is very close to reality; see Figure 4.15 for comparison. Thus, the thickness of the fine mortar layer can be calculated from the known distance of contact detection for the reference ball, tests with ball-ball contact using the 10 mm ball.

5.2.4.6 Procedures for time-controlling function

Extensive time-control procedures are needed for evaluation of the results of modelling. For instance, a user-written procedure connects the time function of the numerical simulation with other model parameters such as slump flow or velocity of spreading. Use of this procedure allows visualization of the development of the slump flow test over time by analogy with the computer-controlled table for slump flow test in the experiments. This procedure was implemented by the author into the PFC because the code has no standard function which could provide the required information. The velocity of spreading corresponds to velocities of the particles which are located on the forward position of the flow front. However, these particles on the flow front are not always the same during the flowing process, but there are new particles coming into this position and leaving it again to give space to other particles. The time-controlling procedure scans all particles in order to find the particles which are located on the forward position of the flow front and saves the information of their locations and corresponding time of scanning. In the next step the secondary data are calculated: distance between particles and center of the slump cone, the current slump flow, and the spreading. An example of the output data is data-set on the kinetics of the spreading of concrete specimen with markers of the specified times and distances, e.g., time T_{50} .

In addition, by means of the time–controlling procedure the changes in the shape of the concrete specimen during simulation can be traced and the information about specified regions of the flow can be collected by calculating the height and velocity profile of the flow.

5.2.4.7 Procedure for obtaining the shape of the simulated concrete specimen

The details of the shape of the simulated concrete specimen are needed for comparing the results of the numerical simulation with the predictions of analytical model and/or with corresponding experimental results. The shape of the profile in numerical simulation requires a height–spreading diagram. However, since the modelled concrete consists of discrete particles, all particles in the specified region must be scanned in order to find the particle with highest height coordinate. To achieve this, the entire free surface, simulation domain, of the simulated concrete is divided into sectors, and each sector is scanned in search of particles with maximal height coordinates for their positions related to the direction of the flow. After identifying and marking all balls which are highest in their corresponding sectors, the information about their positions and height can be saved in a data file. In the next step a cross–section of interest is chosen and the shape of the profile corresponding to this cross–section is built.

Since the procedure for obtaining the shape of the simulated concrete can be used at any time during simulation, changes in the shape can be monitored as a dynamic process.

5.3 Numerical simulations

The results of the verification of the material model are presented here. The slump flow test was selected as the reference test for parameter study and calibration of the contact model. In order to assess the predictive ability of the numerical simulation, two other tests were chosen to validate the model further while the model parameters were held constant. These two tests are L–Box and LCPC–Box tests.

Each numerical simulation includes the following steps:

1. creating the geometry of the equipment and defining the boundary conditions;
2. generating the particle, mixing, compacting and relaxation of the specimen;
3. starting the numerical simulation;
4. controlling the numerical simulation, collection and processing of information during simulation;
5. analysing the results of numerical simulation; comparing the results of the simulation with corresponding results of laboratorial experiments and/or analytical model.

5.3.1 Parameter study and calibration of the UDM using the slump flow test

In the following parameter study concrete was simulated using particles of only one size at a time. In this way the effects of various model parameters should be more recognizable. Such a numerical model with monosize particles can be interpreted as a multitude of round, or spherical, aggregate grains of some “average”, representative size. Each particle is considered to be uniformly covered with a layer of cement paste or fine mortar. It should be mentioned here that the assumption of a single particle size has clear advantages with regard to the prospective practical application of the

numerical approach presented, since making a concrete discrete in this way is simple and the corresponding calculations are very fast.

The parameters of the contact model can be subdivided into two categories. The first category relates to the properties of individual particles such as the size, density and stiffness of the “core”. Furthermore, the choice of 2– or 3–dimensional discretisation results in two different shapes of particles, i.e., disks or spheres, respectively. The second category includes all parameters which define the interaction between the particles. These parameters are the stiffness of the contact bond, the coefficients of friction, and the viscosity as well as the shape of the force–displacement relation in the normal direction. The force–displacement relation determines the strength of contact bond and the value of the “yield force”, among others.

The sequence of the parameters as presented in the following chapters results from the logical succession of the choices to be made. To begin with, an appropriate particle size must be chosen. In doing this naturally the maximum aggregate size of concrete should be considered as well as the geometrical data of the boundaries; e.g., the size and shape of the formwork. Since no special consideration of particular concrete compositions was a goal of this study, the limits for the choice of the particle sizes were provided by the geometry of the “virtual testing equipment” used, i.e., the Abram’s cone.

The density of the particles provides the definitive value for the calculation of particle actions due to gravity. In the case of the slump–flow test as simulated in this investigation, gravity is the only operating force in the system. The density equal to 2.3 kg/dm³ was assigned to all the particles in the parameter study performed by simulating ordinary and normal–weight concrete as a homogenous mass.

Since the particles are considered to be rigid bodies in the calculation, their stiffness is infinite, both in the compression and tension modes. The finite stiffness of the virtual concrete results from the definition of elastic properties for the interaction between the particles. In doing this, concrete was considered as a nearly incompressible material; this means that the particles under compression would have only a minimal overlap.

The parameters of the second category, i.e., those defining the interaction among the particles, are important to the simulation of concretes with different rheological properties. The aim of the parameter study is to identify quantitatively the effects of the individual parameters and, further, to develop an algorithm based on observed effects for the purposeful choice of their combinations in order to represent the behaviour of a particular fresh concrete accurately.

The set of parameters used for the reference numerical simulation in the parameter study is presented in Tables 5.5 and 5.6.

Table 5.5: *Set of parameters used in parameter study – particle category*

Particle parameters	Symbol	Value	Unit/Dimension
Radius	–	2.5	L
Density	–	2.3e-3	M L ⁻³
Stiffness of the core	–	1.0e3	M T ⁻²

Table 5.6: Set of parameters used in parameter study – interaction category

Mode	Regime	Symbol	Value	Unit/Dimension
Core	Compression	$k_{n.comp}$	1.0e3	$M T^{-2}$
		$k_{s.shear}$	1.0e1	$M T^{-2}$
		$fric_{stat.core}$	0.85	dimensionless
		$fric_{dyn.core}$	0.65	dimensionless
Mortar	First contact (tension/compression)	d_{new}	2e0	L
		$F_{max.comp}$	2e0	$M L T^{-2}$
	Mortar layer (tension/compression)	d_{max}	0.2	L
		$F_{max.tens}$	2e0	$M L T^{-2}$
		d_{loss}	3.2	L
		k_{visc}	1.0e1	dimensionless
		k_{yield}	1.0e1	dimensionless
		$fric_{stat.mortar}$	0.85	dimensionless
		$fric_{dyn.mortar}$	0.65	dimensionless
		$F_{yield.shear}$	1.0e0	$M L T^{-2}$

The slump test was simulated several times as part of this parameter study. Key data, i.e., slump value, slump–flow diameter for concretes with a soft consistency, and the time of spreading, were determined similar to practical tests. This study should help to establish links between the model parameters and the experimentally obtained key values.

5.3.1.1 Effect of the characteristic distances

The values of the characteristic distances in the force–displacement relation as provided by the experiments are related to the viscous behaviour of the material under investigation. It was noted in Section 4.10.2 that the force–displacement curves measured for UHPC are stretched in the direction of larger distances in comparison with the curves obtained in the tests with SCC mortar. Moreover, the distance of the loss of contact bond in the tests with UHPC is several times larger than the diameter of the equipped ball.

The results of the numerical simulations with different characteristic distances have shown that the characteristic distances exert more significant influence on computational time than on the final results of modelling. The reference characteristic distances were equal to the measured characteristic distances in the tests with early age SCC mortar; see Table 5.6. It is noteworthy that the characteristic distances were increased/decreased proportionally according to the size of the particles; the contact bond between non–uniformly sized particles depends on the size of the smaller particles, similar to the experiments. The key data for comparison were final slump flow and computational time. The slump flow is very much closer to the reference simulation in the case of smaller characteristic distances, by a factor of 2, than the reference. A further decrease of the characteristic distances, by factor 10, leads to the vanishing of the mortar layer. However, it has very little influence on the results of testing because most of the contacts are in the “Compression”

regime in the “Core” mode. The contact bonds in the “Mortar” mode can be found only in the region of active deformation and have very little influence on the results of modelling.

The parameters which change significantly are computational time and time of simulation. Time of simulation is related to the coefficient of viscosity (k_{visc}) – more detail is found in Section 5.3.1.4; smaller characteristic distances mean a much smaller possibility for the viscous component of the contact force to influence the interaction between entities: the contact bond model becomes more elastic than viscoelastic. The computational time also decreases by a factor of two with a reduction of the characteristic distances by a factor of 10. The inverse is also true in the case of increase of characteristic distances. Doubling the characteristic distances significantly increases the number of the contact bonds in numerical simulation because of the doubled “distance to loss of contact bond”. New contact bonds are created while the “initial” contact bonds are not broken. However, the final slump flow changes are found to be negligible because most of the contacts are in “Compression” regime in “Core” mode, while the computational time and the time of simulation increase by several times. It is significant to note that the increase in “distance to loss of contact bond” is still smaller than the diameter of the particle increased by factor two. However, further increase of the characteristic distances leads to the situation when the “distance to loss of contact bond” becomes greater than the size of contacting particles. For example, a third particle can be placed between the two bonded particles without breaking their contact bond; the number of contact bonds in this case increases dramatically. Numerical modelling of the particle system with such distance characteristics becomes very difficult because of the much longer computational time. It may be supposed that further increase of the characteristic distances can influence the final slump flow, i.e., a small decrease in slump flow, because the contact bond keeps particles together for longer distances.

In addition it is worth noting that in all simulations with different characteristic distances the same set of characteristic forces was used. It goes without saying that an increase in the characteristic forces leads to an increase of the effects of characteristic distances. More details about characteristic forces are presented in next section.

5.3.1.2 Effect of the characteristic forces

The characteristic forces are the “maximum tensile force”, $F_{max.tens}$, i.e. contact bond strength, and “maximum compressive force”, $F_{max.comp}$. It is assumed that the magnitudes of these characteristics are the same as both of them are related to the rheological behaviour of the mortar layer between entities. This assumption is in good agreement with results of tests obtained with Carbopol solutions; see Section 4.9. In the case fresh concretes the “maximum compressive force” is a bit higher than the “maximum tensile force”; this can be explained by some stiffening of the fresh concrete during the test.

The value of the bond strength *bond* ($F_{max.tens}$) in the contact model is the determining factor in the interaction between neighbouring particles. When the tensile force reaches this value, the force–displacement relation shifts to the softening regime and, as a rule, contact will be lost gradually; see Figure 5.9. Hence, it is not surprising that this parameter has a dramatic effect on the results of simulations, cf. Figure 5.15. By modifying the value *bond* by a factor of 100, the calculated response of the numerical concrete changes from a kind of “self-compacting concrete”, with a slump-flow of 60 cm, to “stiff ordinary concrete”, with no slump-flow. Considering such a

pronounced effect as well as the physical meaning of the parameter *bond*, this parameter seems appropriate to determine the type of virtual concrete. The set of parameters used in the reference numerical simulation is presented in Tables 5.5 and 5.6.

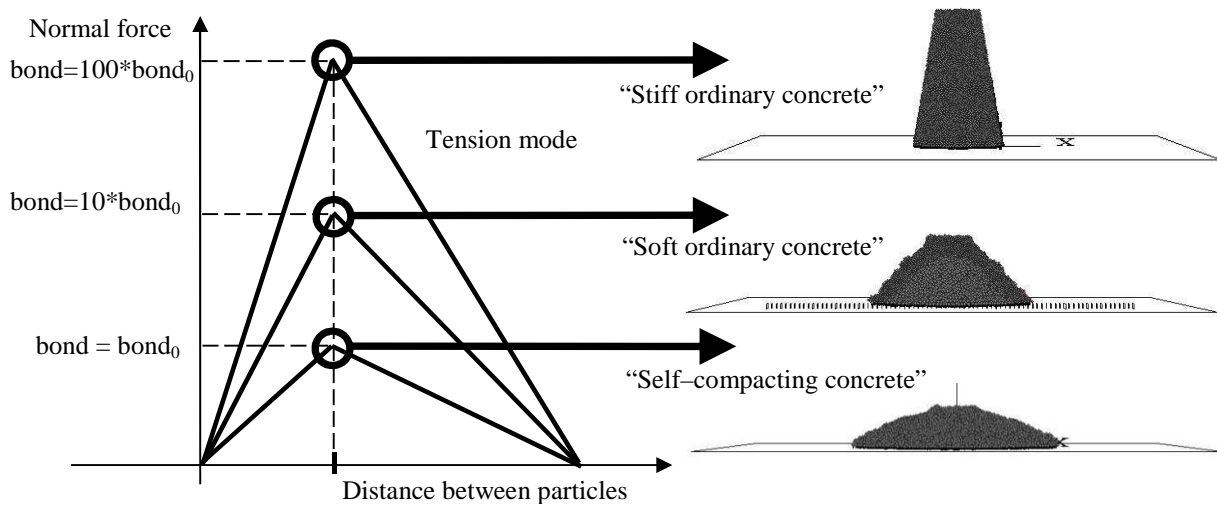


Figure 5.15: Effect of bond strength “*bond*” in the contact model on the final shape of the concrete “cake” in the simulated slump test

The “maximum compressive force” represents the compressive behaviour of the mortar layer. There is little or no influence of $F_{max.comp}$ on the final slump flow. The nature of $F_{max.comp}$ dictates that the particles in “undeformed” part of the concrete specimen can have a bit smaller overlap than the particles in “deformed” part.

5.3.1.3 Link between contact bond strength in the simulation and yield stress of the fresh concrete in the experiment

The parameters of the DEM-based model are not rheological constants and cannot be obtained directly from the experiment. That being said, a link between the yield stress of fresh concrete and the parameters of the DEM-based model is required. This section describes the derivation of yield stress by adjusting the bond strength parameter ($F_{max.tens}$) of the DEM model in such a way that the numerical prediction corresponds to the prediction provided by the analytical solution obtained for a given yield stress. For this, an analytical prediction of stress-distribution at the beginning of the slump flow test is used as reference for the corresponding numerical analysis (see Section 3.3.1.1).

Before cone lifting, all particles are pressed by the weight of other particles and the reaction of the boundaries, i.e., the cone walls cf. Figure 5.16. The pressure induced by the particles’ weight is balanced by the reaction of the cone. Lifting the cone disturbs this balance, and the concrete specimen changes its shape under the action of gravitation until another state of equilibrium is attained. This is the case when gravity is balanced by internal forces of the material, primarily by the yield stress.

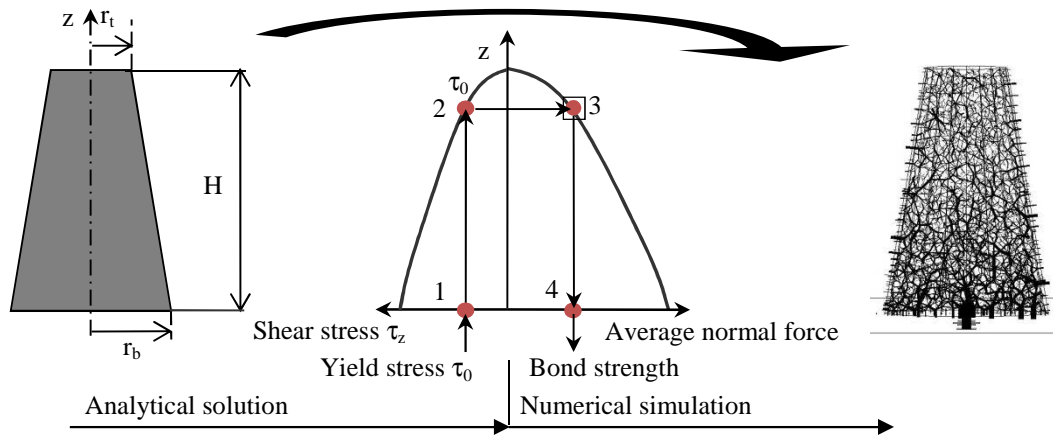


Figure 5.16: Algorithm of bond strength determination

As shown in Section 5.2.2.1, the interaction of the two neighbouring particles in the normal direction is described by an ideal spring, a dashpot, and a specific contact element. In a compressive regime the deformation of the spring is proportional to the magnitude of the compressive force; some elastic energy is accumulated due to this deformation. This elastic energy is released at the beginning of cone lifting. At some moment the energy of compression is completely released as energy of tension. In the case of an ideal spring and without considering damping effects, the energy of the compressed spring will be equal to the energy of the spring under tension. If there is a damping force, the maximum energy decreases cycle by cycle to zero; the first cycle features maximum amplitude. Therefore the magnitude of the compressive force is used as an indicator of maximum tensile force in the numerical modelling.

The contact behaviour of particles only was sketched in Sections 5.2.2.1 and 5.2.2.2. However, each particle has as a rule contact to more than one neighbouring particle. Furthermore, the deformation occurs under the weight of the upper particles' wedging into the space among the neighbouring particles positioned below.

Generally it can be stated that the system of particles representing concrete is being plastically deformed when the tensile forces acting at the mesolevel become higher than the contact bond strength. This basic concept was used first in developing the algorithm which should provide a link between the yield stress of concrete according to the Bingham model and the bond strength parameter of the particle model.

Figure 5.16 shows this algorithm schematically. In the first step, the given input parameter “yield stress τ_0 ” is introduced into Eq. 3.22, cf. Chapter 3. The solution of the equation, Step 2, provides the height z of the horizontal concrete layer in the cone, as measured from the bottom of the cone, at which the shear stress level is equal to the given yield stress. One value of the yield stress τ_0 corresponds to only one particular height z . Subsequently, the numerical simulation is performed for a chosen basic set of model parameters, i.e., particle size, size distribution, and particle stiffness. The distribution of the normal compressive forces over the height of the cone is then calculated. The average force values for different heights, when connected to each other, form a curve which has in general a shape similar to that of the analytically derived stress distribution. In more detail, a special numerical procedure enables the scanning of existing contacts between particles and the sorting of these contacts according to their height in the cone into chosen height intervals

(0 – 5 mm, 5 –10 mm, , 295 – 300 mm from the bottom). Further, an average normal stress value is calculated for each height interval. As explained above, the compressive force calculated for each particular height in the cone corresponds to a tensile force which instantaneously develops in the material model at this height level when the cone is lifted. The force acting at the level on which the yield stress is attained according to the analytical formula, Step 3, is of interest. The average interaction force between the particles at this height must be equal to their bond strength in order to simulate the effect of the yield stress and the beginning of plastic deformation; in this manner the required bond strength is derived, Step 4.

5.3.1.4 Effect of internal friction and viscosity

The effect of the parameter $fric$, which represents the yield stress of concrete in the direction of shear and is manifested in the rheological model by the friction element “slider”, is demonstrated in Figure 5.1. The viscosity as a parameter of the model based on the DEM is dimensionless. The link between yield stress [Pa] and contact bond strength makes it possible to estimate the magnitude of the viscous parameter in the contact model. For that the value of the Bingham plastic viscosity, k_{visc} in [Pa·s], multiplies with the “yield stress – to – contact bond strength” ratio. As a result an adopted value of plastic viscosity for given proportion [Pa] – [Contact bond force] can be obtained.

The parameter $fric$ can neither be predicted analytically nor measured experimentally, in contrast to the *bond strength* parameter. Therefore it is reasonable to use the former parameter for the fine calibration of the material model.

An increase of the $fric$ value by a factor of 10 leads to a decrease of the calculated slump–flow diameter by 7 cm. Remarkably, a further increase in $fric$ by a factor of 10 or 100 results again in a decrease in the slump–flow diameter by 7 and 14 cm, respectively. The set of parameters used for reference numerical simulation is presented in Tables 5.5 and 5.6.

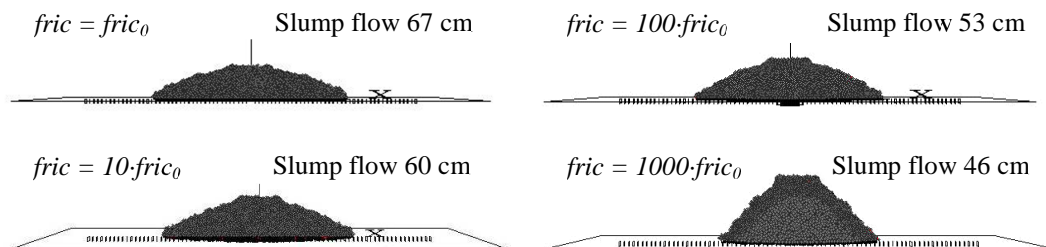


Figure 5.17: Influence of the friction parameter $fric$

When the particles start to move, the dashpot parameter k_{visc} representing the viscosity of the material comes into action. It was found that the parameter k_{visc} influences the time of calculation only. The shape of the virtual concrete “cake” at the end of the simulation was the same, independent of this parameter. An increase of the value k_{visc} by a factor of three, when simulating “self–compacting concrete”, caused a nearly proportional increase of the programme calculation time from 48 seconds to 167 seconds.

5.3.1.5 Effect of particle size

The use of small particle sizes is limited by long calculation times resulting from the great number of the particles per unit volume; the maximum size of the characteristic aggregate should, however,

5 Material model and numerical simulations

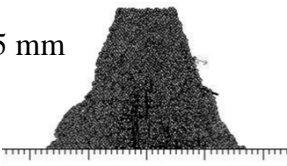
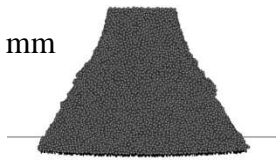
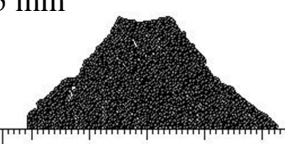
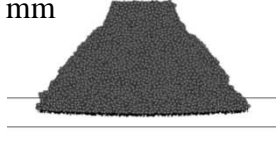

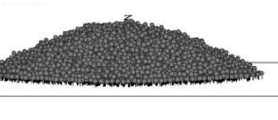
be smaller than the maximum aggregate size of the concrete under consideration. Table 5.7 shows the results of the 2D and 3D simulations of the slump test using particle sizes with a radius of 2.5 mm, 3.5 mm and 5 mm, respectively, while all the other parameters of the model mentioned in the section before remained unchanged. The set of parameters used for reference numerical simulation is presented in Tables 5.5 and 5.6.

A change in particle size evidently leads to an alteration of the mechanical interaction between particles and, as a result, to a pronounced effect on the rheological behaviour of the simulated concrete. Larger particle sizes correspond to higher values of the slump and the slump–flow diameter.

This effect can be traced back to the fact that larger particles are heavier, i.e., the force of gravity acting on each large particle is higher in comparison with small particles. Since all the parameters describing the interaction between particles remain unchanged, the balance between the force acting and the resistance to the movement changes in favour of higher displacements. This means that with increasing particle size the parameters of the particle interaction should be adjusted in order to obtain the same simulation result in terms of slump and slump–flow values.

It should be noted that the use of particles with a radius of 1.25 mm, not presented in Table 5.7, did not show a pronounced change in the simulation results in comparison to the calculation in which a radius of 2.5 mm was used. Hence, the effect of particle size fades with increasingly smaller particle sizes.

Table 5.7: *Effect of particle size on the results of the simulated slump test*

2D simulation		3D simulation	
Particle radius and the image of the “concrete cake” at the end of simulation	Calculation data	Calculation data	Particle radius and the image of the “concrete cake” at the end of simulation
2.5 mm 	Number of particles: 3254 Slump: 12 cm Slump–flow: 37 cm	Number of particles: 51551 Slump: 12 cm Slump–flow: 35 cm	2.5 mm 
3.5 mm 	Number of particles: 1546 Slump: 13 cm Slump–flow: 41 cm	Number of particles: 18512 Slump: 13 cm Slump–flow: 37 cm	3.5 mm 
5 mm 	Number of particles: 624 Slump: 20 cm Slump–flow: 50 cm	Number of particles: 6491 Slump: 20 cm Slump–flow: 50 cm	5 mm 

A comparison of the calculated images of the “concrete cake” at the end of simulation as described in Table 5.7 shows that the dimension of modelling does not significantly affect the results obtained. This is good news since a two-dimensional analysis is easier and faster and, thus, would be the first choice if the accuracy of the numerical simulation is comparable to that of the three-dimensional analysis.

5.3.1.6 Compensating for particle size effect

The choice of particle size may significantly influence calculation results if all other model parameters remain unchanged. This results from the hyperbolic increase in the mass of individual particles with increasing particle diameter. So, if the interactive forces between the particles remain unchanged, the higher gravitational force tends to destroy “weak” contacts, and the “material consistency” appears to be softer. Figure 5.18 illustrates this in the example of SCC; here gravity is the only operating force in the system. While virtual SCC with a particle radius of 2.5 mm showed a slump flow value of 58 cm, simulation with larger particles, of radius 5 mm, provided a slump flow value of 70 cm. Furthermore, when gravity is greater than the contact bond strength, the contact bond cannot keep the particles together, and the concrete starts to crumble. Separation of some particles from the rest of the “cake” can be observed in this case. The set of parameters used for reference numerical simulation is presented in Tables 5.5 and 5.6.

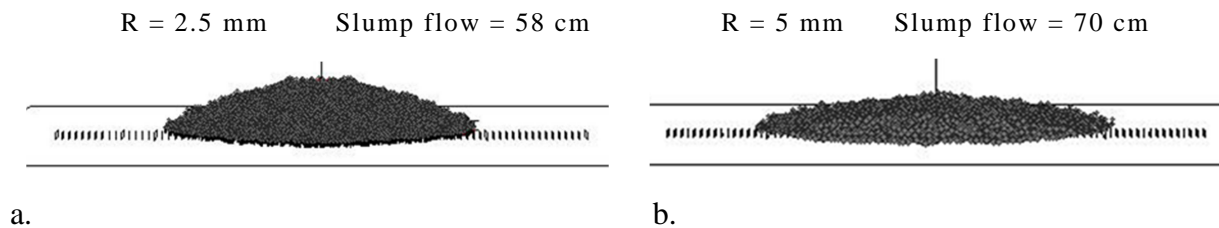


Figure 5.18: Final shapes of concrete “cakes” as obtained from numerical simulation using particles with radius of a) 2.5 mm and b) 5 mm, while other model parameters remained unchanged

In order to compensate the effect of particle size, i.e. to obtain same flow behaviour independent of the radii of the spheres, the maximum interaction forces between particles of virtual concrete should be proportional to the particle mass. The particle mass is calculated using Eq. 5.27.

$$m = \frac{4}{3} \rho \pi R^3 \quad (5.27)$$

where R is the radius of particle, ρ is the density of the particle.

The correction coefficient k to compensate for the particle size effect of the same density ρ can then be obtained from Eq. 5.28.

$$k = \frac{m_i}{m_0} = \frac{\rho V_i}{\rho V_0} = \frac{\frac{4}{3} \pi R_i^3}{\frac{4}{3} \pi R_0^3} = \left(\frac{R_i}{R_0} \right)^3 \quad (5.28)$$

where m_i , V_i , and R_i are the mass, volume and radius of particles with the size different from the reference radius R_0 , while m_0 and V_0 are the values for the reference particle size R_0 .

5 Material model and numerical simulations

Numerical analyses of the slump–flow tests were repeated for assumed ($R_0 = 2.5$) mm and ($R_i = 5$) mm, i.e., using the correction factor k as given by Eq. 5.28. A smaller particle size was used as reference here, since it was in accordance with the experimental data from the slump flow test for reference SCC. The relatively small slump flow value is below those which are usually associated with SCC. However, the choice of this SCC was appropriate for the use as the experimental reference.

Figure 5.19 shows the shapes of the final state of the spreading “cakes” for both particle sizes. The difference in the slump–flow diameter was only 2 cm in this case (58 cm for $R_0 = 2.5$ mm and 60 for $R_i = 5$ mm). However, the concrete “cake” from the simulation in which larger particles were used appears still shallower. This can probably be traced back to the fact that Eq. 5.28, which is based on the assumption of a static equilibrium, does not consider some inertial forces acting during the simulation of the slump–flow test.

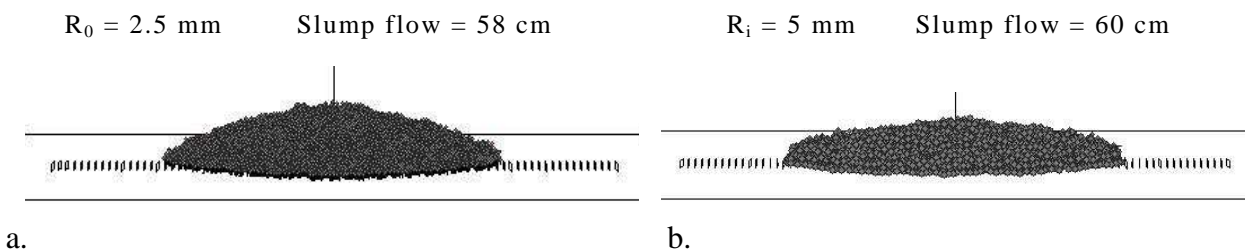


Figure 5.19: Final shapes of concrete “cakes” as obtained from numerical simulation using particles with radius of a) 2.5 mm and b) 5 mm, the size effect was compensated using coefficient k

Simulating concrete using monosize particles is a fast and efficient procedure which can be used in a number of applications. However, while using this approach the meso–structure of concrete is represented in a very coarse manner, so that numerous phenomena might not be detectable in such a simulation. The segregation of larger aggregates or the effect of the aggregates grading curve on the rheological behaviour of fresh concrete are examples of such phenomena.

The simulations of the slump–flow test with SCC were repeated one more time using two different particle sizes, i.e., with the radii of 2.5 mm and 5 mm, simultaneously. Again the coefficient k was applied to compensate for the higher mass of larger particles. It should be noted that for the case where a small particle has contact with a larger one, the size of the smaller particle is crucial to the value used for coefficient k .

Figure 5.20 shows the result of the simulation. It appears that the calculated final shape of the concrete cake is located between the shapes obtained from the simulations using only small or only larger particles (cf. Figure 5.19). The slump–flow value was 60 cm, which again corresponds well to the values from simulations with monosize particles.

$$R_o = 2.5 \text{ mm (50 vol\%), } R_i = 5 \text{ mm (50 vol\%), Slump-flow} = 60 \text{ cm}$$

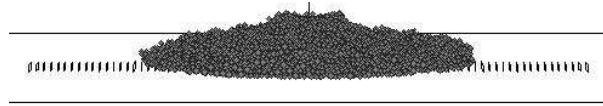


Figure 5.20: Final shape of concrete “cake” as obtained from a numerical simulation using a mix of two particle sizes and the compensating coefficient k

5.3.1.7 Choice of the initial model parameters and calibration of the numerical model

As noted above, the parameters of the contact model can be subdivided into two categories: the properties of individual particles and the parameters which define the interaction between the particles.

To begin with, an appropriate *particle size* or *grading* must be chosen. In doing this, naturally, the maximum aggregate size of concrete should be considered as well as the geometrical data of the boundaries, e.g., the size and shape of the formwork. The *density* of the particles provides the definitive value for the calculation of particle actions due to gravity. The density, equal to 2.3 kg/dm^3 , can be assigned to all particles which represent the modelled concrete, simulating ordinary, normal-weight concrete as a homogenous mass. The density of the particles of fibres corresponded to the real density of the material, 7.8 kg/dm^3 for steel fibres. The *initial stiffness* of the particles must provide the only a minimum overlap. The initial stiffness can be estimated from the calculated value of the compression force, which results from the chosen density of the particles in the simulation.

The parameters of the second category, i.e. those defining the interaction between the particles, are important to the simulation of concretes with different rheological properties. The bond strength *bond* ($F_{max.tens}$) should be chosen in the first step, since it is the main parameter for characterising the interaction of the neighbouring particles in the normal direction. The *bond* value must be set according to the type of concrete to be simulated, stiff ordinary concrete, SCC etc. However it should be noted that calculation of the contact bond value is possible only when the Abram’s cone is filled completely with particles of the modelled fresh concrete and the particle system is relaxed, i.e., the state of equilibrium has been reached. For the second step a characteristic distance for the material model should be chosen. The main criterion in choosing the characteristic distances is that the “distance to loss of contact bond” (d_{loss}) should not be higher than the diameter of the particles. An appropriate proportion between characteristic distances (d_{loss} , d_{max} and d_{new}) is presented in Table 5.6.

The fine-tuning of the model is performed by adjusting the parameters *fric* and k_{visc} , which are related to the rheological properties “yield stress” in the shear direction and “plastic viscosity” according to the Bingham model, respectively. Both parameters are secondary and must be used only for fine calibration of the material model. Initially both parameters have very low values: $fric=0.05$ and $k_{visc}=1$ in order to avoid their influence on the results of the reference simulation. The friction parameter *fric* can be calibrated on the final slump or slump flow diameter from the tests with the Abram’s cone. If the slump or slump flow diameter have smaller/higher value than analytically predicted value then the *fric* parameter have to be increased/decreased. The parameter

k_{visc} has an effect on the computation time only, which can be related to the spreading time in the slump flow test on flowable or self-compacting concrete.

5.3.2 Verification of the material model

The slump-flow test served as the basis for previous parameter studies as well as for the calibration of the model. The results of such calibration are presented in this section. Further, the set of parameters (calibrated using slump flow test) was used for numerical simulation of two other flow tests (L-Box and LCPC-Box test) for verification. The results of these numerical simulations are presented and compared with analytically predicted values.

5.3.2.1 Simulation of slump-flow test

In previous DEM simulations presented in the literature, a container, e.g., a cone was filled by “dropping” randomly generated particles into it. An acknowledged shortcoming of this procedure is the possible occurrence of large-scale gradients in the particle-packing density [112, 113].

In this study concrete was modelled by spherical particles of different sizes in such a way that a realistic grading curve of aggregates could be represented with good approximation. The particles were uniformly distributed in a given volume, which in this case was cylinder-shaped and placed over the cone eventually to be filled. A random function was used to set the initial position of the particles in the cylinder. Since the cylinder has a much larger volume than that needed to place all the particles generated, the overlapping of particles could be excluded. Eventually the force of gravity was applied to the particles so that they could fall from the cylinder into the cone and fill it. Gravitation also ensured the compacting of the particles in the cone. The number of generated particles was slightly higher, by approximately 5%, than the total volume of compacted particles needed to fill the cone. The superfluous particles were removed after achieving equilibrium in order to level the top surface of the cone. An evaluation of the positions of the particles at equilibrium showed that the distribution and packing density of the particles in the volume of the cone were uniform.

Table 5.8 provides an overview of the representative radii of the generated particles, the number of particles in each fraction, and the percentage of the fraction in the total volume of concrete. The total volume of each fraction and, hence, the corresponding number of particles resulted from the volume of Abram’s cone to be filled with virtual concrete. Aggregates were represented by three fractions 2/4, 4/8 and 8/16, while particle radius varied within the given representative values, e.g., R_i between 4 mm and 8 mm for the fraction 8/16. Aggregate grains with a radius of less than 1 mm were not considered in the simulation in order to limit the computation time, which is directly proportional to the number of particles, i.e., increasing with decreasing particle size.

Table 5.8: *Chosen particle size distribution representing grading curve of aggregates*

Aggregate fraction [mm]	Number of particles in the slump-flow test [-]	% of total volume of aggregates [%]
2/4	59617	24.2
4/8	10262	33.6
8/16	1557	42.2

In considering the contribution of the thin layer of cement paste or fine mortar covering each aggregate particle to the filling of the cone volume, the initial radius of each particle was increased by the thickness of covering layer, which has the same stiffness as the particles and very small overlap, which can be neglected. The thickness of the covering layer was calculated for a given gradient curve of aggregates, taking into account the volume of the components which cannot be modelled using DEM, i.e., constituents with a radius of less than 1 mm.

The maximum overlap of two neighbouring spheres depends on the maximum force in compression and the stiffness $k_{n.comp}$ of the particles under compression. The level of the compressive forces is determined by the density of the particles and by the geometry of the testing equipment modelled in the simulation, indeed the boundary conditions. The normal contact force is in direct proportion to the stiffness $k_{n.comp}$, while the timestep is in an inverse proportion. High values of normal stiffness yield a small degree of overlapping, but also to a corresponding increase the computational time due to the decrease in the length of the timesteps. However, the contact should act too “soft” in compression, since it would lead to a high degree of overlapping of particles when under compression and even to penetration of a particle through another particle or a wall element. The chosen value of the stiffness $k_{n.comp} = 10^3$ was a compromise based on these considerations. No pronounced large-scale gradients in particle packing occurred over the height of the cone due to differences in the compressive force in the upper and lower layers. The change in the packing density did not exceed 1%.

Table 5.9 gives also other model parameters as applied for all numerical simulations presented in this section. The meaning of the parameters in the normal direction is presented in Figure 5.9. The same approach is also valid for the tangential direction; in this case the parameters are marked with the index s .

Table 5.9: *Model parameters used in the simulations (n: normal direction, s: tangential direction)*

Mode	Regime	Symbol	Value	Unit/Dimension
Core	Compression	$k_{n.comp}$	1.0e3	$M T^{-2}$
		$k_{s.shear}$	1.0e1	$M T^{-2}$
		$fric_{stat.core}$	0.85	Dimensionless
		$fric_{dyn.core}$	0.65	Dimensionless
Mortar	First contact (tension/compression)	d_{new}	2e0	L
		$F_{max.comp}$	2e0	$M L T^{-2}$
	Mortar layer (tension/compression)	d_{max}	0.2	L
		$F_{max.tens}$	2e0	$M L T^{-2}$
		d_{loss}	3.2	L
		k_{visc}	1.0e1	Dimensionless
		k_{yield}	1.0e1	Dimensionless
		$fric_{stat.mortar}$	0.85	Dimensionless
		$fric_{dyn.mortar}$	0.65	Dimensionless
		$F_{yield.shear}$	1.0e0	$M L T^{-2}$

It should be noted that the values of stiffness under compression and under tension before the force reaches the yield stress are equal. This means that only small deformations occur until the forces reach the yield force. The values of the coefficients of friction corresponded to the values which were used for calibrating of the contact model (see Table 5.6).

The contact bond is characterised by two independent characteristics: bond strength in the normal direction $F_{max.tens}$ and bond strength in the shear direction $F_{yield.shear}$. The function of the parameter $F_{max.tens}$ is to represent the yield behaviour of fresh concrete. It was obtained using the procedure described in Section 5.3.1.3. The role of the bond strength in the shear direction is associated with slip behaviour in the shearing movement. The calculation of the shear force using the approach described in Section 5.3.1.3 is not possible because this procedure requires the equilibrium state of the specimen, i.e., no particle movement; forces acting on particles are balanced, while the shear force arises only when the particles move. Therefore, the value of $F_{yield.shear}$ has to be set conditionally. The choice is made on the basis of the experience from parameter studies. The value given in Table 5.9 was obtained from such parameter study as an optimum solution with regard to minimizing the time of numerical simulation.

Figure 5.21a illustrates the distribution of the particles in the cone at the beginning of the calculation and Figure 5.21b shows the contact forces acting between particles before cone lifting. The black coloured lines represent compressive forces; the thickness of these lines is proportional to the magnitude of the force. Figure 5.21c gives the distribution of the calculated contact forces over the height of the cone. Each point represents the height of a contact between two particles and the corresponding value of the contact force. The grey dashed line in the diagram connects the points corresponding to average of the maximum values of the contact force, i.e., averaged contact force for 10 points having highest values. This curve is smoothed for the sake of clearer presentation; in reality it cannot be smooth because concrete is simulated in a discrete manner when using DEM.

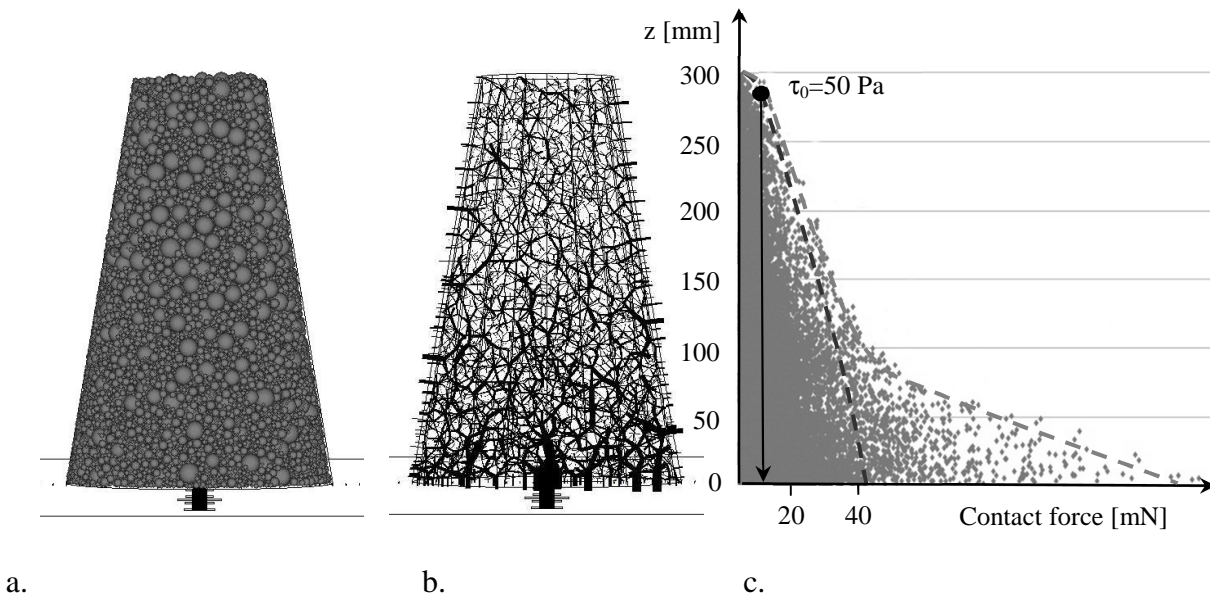


Figure 5.21: The initial state of the numerical simulation: a) concrete particles in the cone, b) normal contact forces, and c) contact force distribution

Furthermore, it should be noted that the upper two thirds of the force distribution curve have a shape which can be expected on the basis of the analytical solution, cf. Figure 5.16; the expected

shape of the curve is shown in Figure 5.21 as a black dashed line. The yield stress in this interval covers self-compacting and flowable concretes. The wide range of force values, especially in the lower third of the cone, originates primarily from the incomplete relaxation of the specimen. Equilibrium is not reached yet at this stage of the calculation; more calculation steps would bring the result nearer to the expected force distribution, which means, however, a considerable increase in the calculation time. For the selected reference material, a self-compacting concrete with a yield stress of 25 Pa, 50 Pa, or 100 Pa, continuing the calculation would not produce any improvement since the shape of the upper two thirds of the curves, i.e., the region corresponding to relatively low values of yield stress would not change.

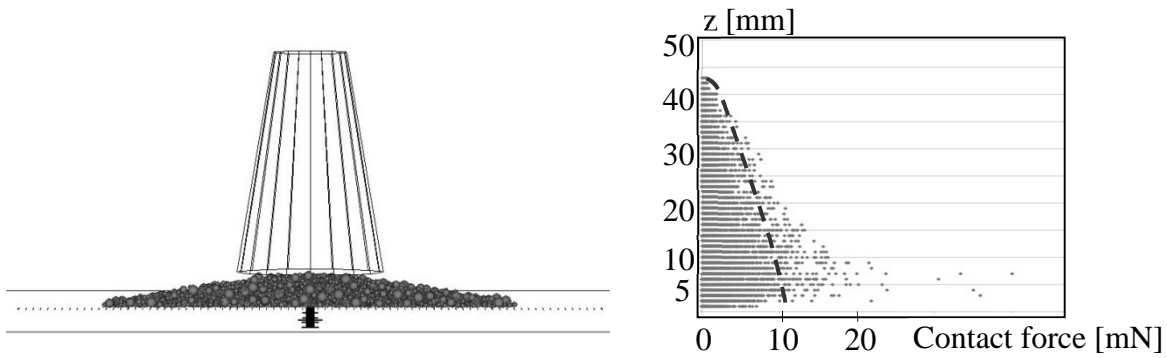
Following the procedure described in Section 5.3.1.3 the height z was calculated using Eq. 3.7 on the basis of the given yield stress $\tau_z = \tau_0$. Table 5.10 gives the calculated z -values for three chosen values of the yield stress. Using these z -values, the contact bond strength $F_{max.tens}$ for each of the given values of yield stress can be read from the calculated curve for the contact force distribution over the height of the cone. Figure 5.21c shows a reading procedure for the yield stress of 50 Pa; the corresponding $F_{max.tens}$ -value is 8 mN. The $F_{max.tens}$ -values for the yield stresses of 25 Pa and 100 Pa are 4.7 mN and 21 mN, respectively.

Table 5.10: Chosen yield stresses for SCC and corresponding values of the height z and the contact bond strength

Yield stress τ_0 [Pa]	Height z [mm]	Contact bond strength $F_{max.tens}$ [mN]
25	297.7	4.7
50	295.6	8
100	291.5	21

Note that up to this stage no simulation of the flowing process has been involved. Before starting the calculation of the flowing process the $F_{max.tens}$ -value is adjusted according to the yield stress of the simulated SCC, e.g., it is set to 8 mN for a yield stress of 50 Pa. When the cone is lifted, the virtual concrete begins to flow, the flowing process continuing until the tensile forces at work become lower than the bonding strength of the particles. Figure 5.22a shows the shape of the concrete “cake” in its final state, i.e., when no further flowing occurs. The corresponding distribution of the contact forces is shown in Figure 5.22b. Basically, the final force distribution has a similar form when compared to its initial state, but the height of the concrete cake is considerably smaller. The maximum forces in the bottom part of the cake are limited by the set bond strength of 8 mN. The points positioned to the right of the dashed line result from some inaccuracies in the simulation process; as described above the equilibrium of the entire system requires an increasing number of steps as the demand for accuracy increases. The slump-flow value obtained from the simulation was 600 mm. The analytical prediction using the formula by Roussel and Coussot [103] provides a value of 600 mm for the input yield stress of concrete equal to 50 Pa as well. For the yield stresses of 25 Pa and 100 Pa the numerical calculation yielded slump flow values of 535 mm and 705 mm, respectively. The corresponding analytically predicted values were 525 mm and 695 mm, respectively. This very good correspondence of numerical and analytical results can be regarded as an initial validation of the methodology developed to derive the DEM key parameter, bond strength. It should be noted that no additional fine-tuning of the contact model by the use of

fric parameter was required. That means that initial value of *fric* parameter fit well for the modelling of SCC.



a. b.
Figure 5.22: Results of a slump-flow test simulation for a concrete with a yield stress of 50 Pa; a) final shape of the concrete “cake”; b) contact force distribution over the height of the “cake”

In order to obtain the height profile of the virtual concrete “cake”, 8 directions at intervals of 45° were considered, cf. the black stripes in Figure 5.23. The measured height is the highest point in the profile. The average values, i.e., the average of the maximal heights in each direction in same radial interval, in radial direction are presented in Figure 5.24 for yield stresses of 25 Pa, 50 Pa and 100 Pa, respectively. As a comparison the analytical solutions by Roussel and Coussot [103] are given. For each yield stress the investigated shapes of the analytically and numerically predicted profiles are very similar.

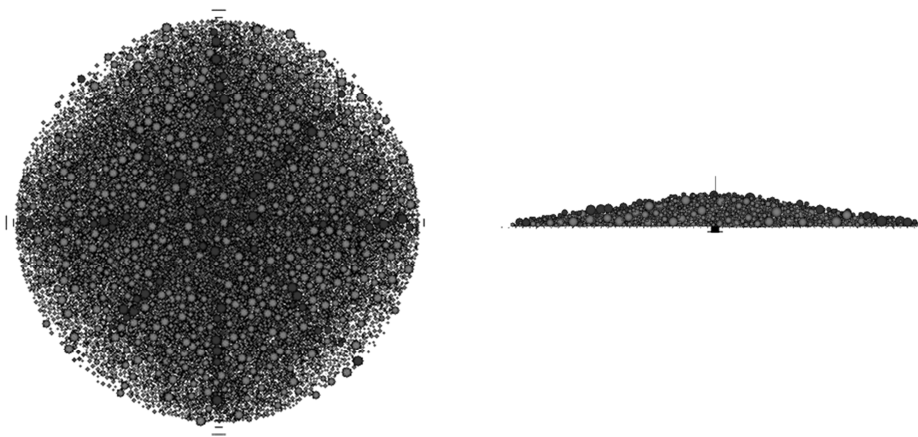


Figure 5.23: Final shape of the concrete “cake” in the slump-flow test

The measured height is the highest point in the profile. The average values, i.e., the average of the maximal heights in each direction in same radial interval, in the radial direction are presented in Figure 5.24. The analytical solution by Roussel and Coussot [103] is also given for comparison.

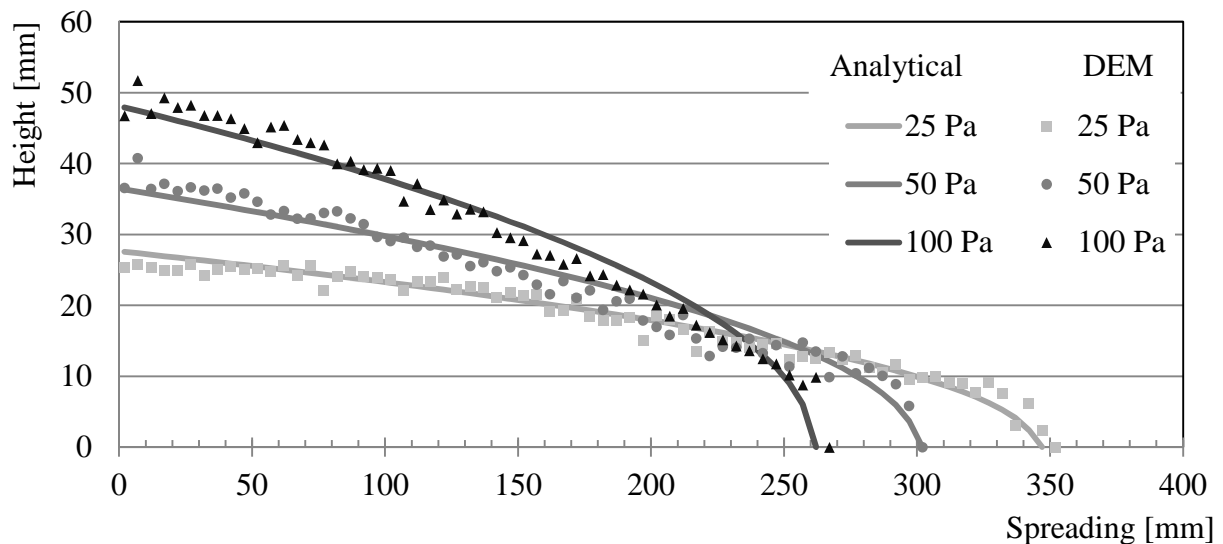


Figure 5.24: Results of the numerical and analytical predictions of the final shape of concrete “cake” in a slump–flow test for the yield stress of 50 Pa; analytical solution according to [103]

Concerning the comparison of the profiles as presented, it should be noted that the profiles from the numerical simulation were estimated using an interval of 5 mm. The last point in the height profile is always set to zero because no particles are registered for this radius. This also means that the given accuracy of the readings for spreading is 5 mm, which is below 2% of the calculated spreading radii. Note as well that the difference between the numerically calculated and analytically predicted slump flow values is below 2%, thus in the range of the accuracy of the readings. The heights generated by the numerical simulation show some statistical “noise” in comparison to the absolutely smooth curves provided by the analytical prediction. In some cases the vertical jumps between two adjacent points are about 2 or 3 mm. A jump occurs when, for example, a number of larger particles are present on the surface while measuring a slump radius and if no or only very few larger particles are present for the next measurement. Note that the largest differences in the height values for the numerically calculated and analytically predicted curves do not exceed 3 mm. Again, this is in the range of the accuracy of the procedure of reading the results of the numerical simulation.

Simulations were performed on a PC with an Intel Core 2 Quad CPU Q9550 of speed 2.83GHz and 4 GB RAM with a 64–Bit system using one processor core per simulation. The total calculation time of one slump–flow test was approximately 70 h.

5.3.2.2 Simulation of the LCPC–box test

In order to validate the quality of the developed link between the yield stress and the model parameter $F_{max.tens}$, another concrete flow test, the so–called LCPC–box test, was simulated using the same set of parameters used in simulating the slump–flow test. The LCPC–test was chosen because an analytical solution for the final shape of the concrete profile is available [31]. It represents the flow process of SCC in a channel. The width of the channel is 200 mm, the length is 1200 mm, and the volume of concrete is 6 litres.

Figure 5.25 shows the shape of simulated concrete at the end of the flowing process. For a yield stress of 50 Pa, the final length of the SCC spread was approximately 730 mm. The average height at the left wall was approximately 70 mm.

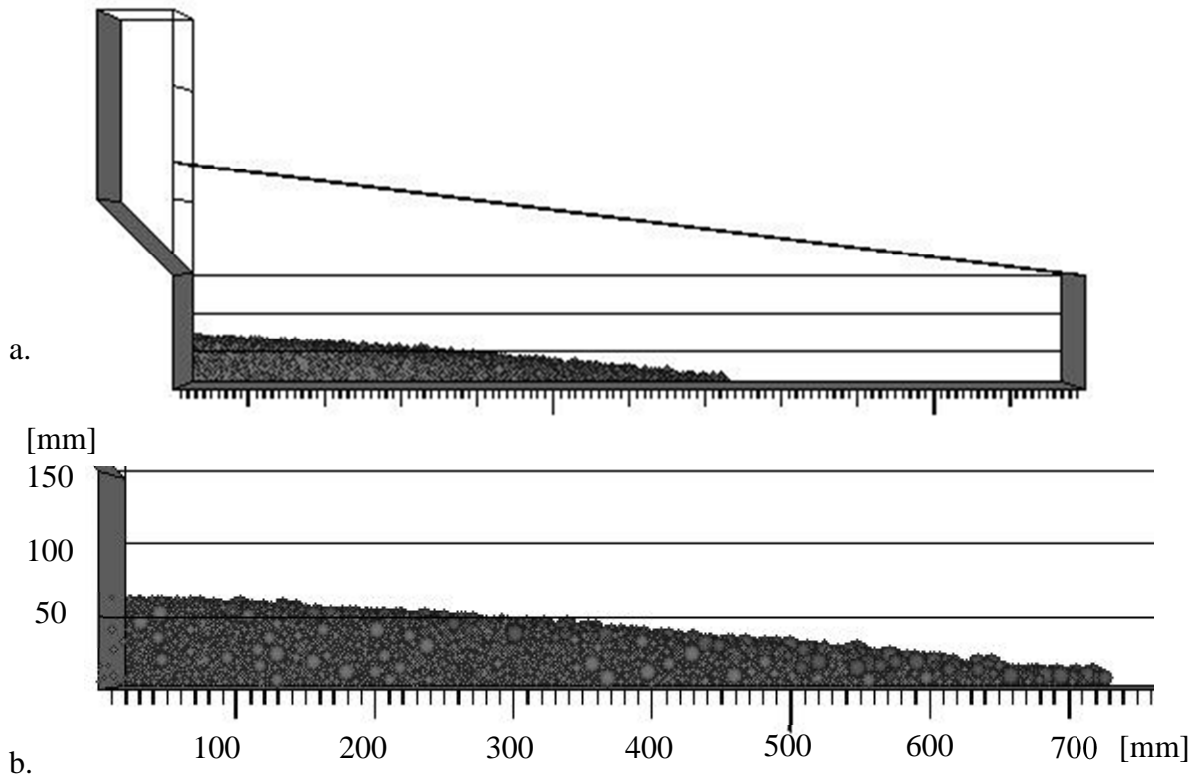


Figure 5.25: Final shape of concrete in the simulation of an LCPC-Box test for the yield stress of concrete equal to 50 Pa: a) general side view, b) detailed side view

Figure 5.26 shows the final SCC profiles (average heights) in the LCPC-box obtained for yield stresses of 25 Pa, 50 Pa and 100 Pa, respectively, using both the numerical simulation and the analytical formula [88, 102]. As in the case of the slump-flow test, the numerical and analytical results are in very good agreement. The difference between the results is within the range of the accuracy of the readings of the profiles arising from the numerical simulation.

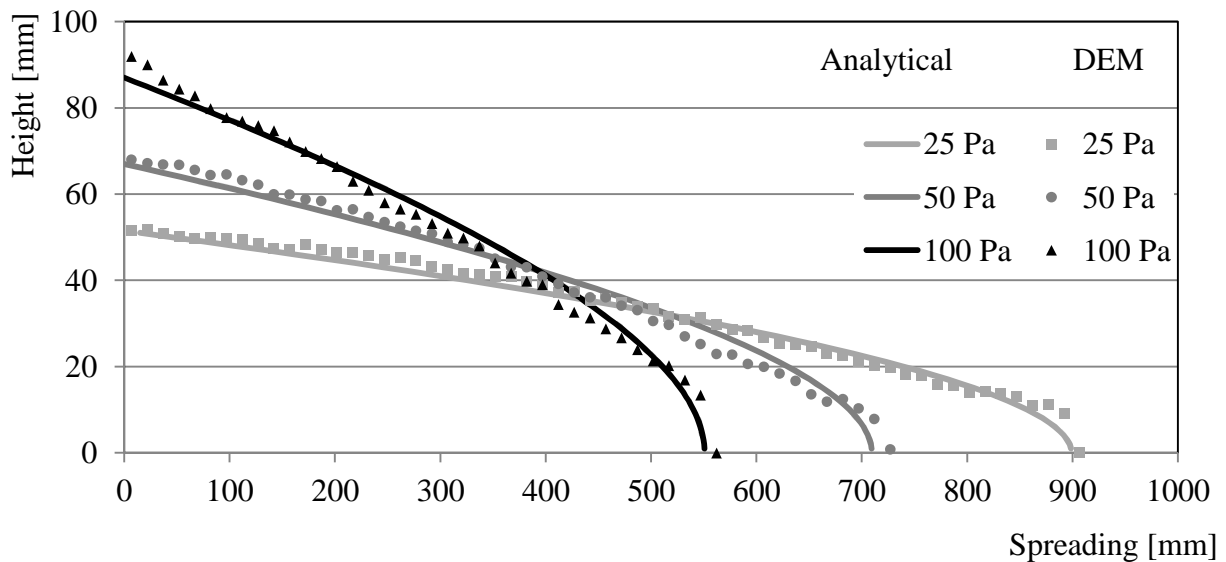


Figure 5.26: Results of the numerical and analytical predictions of the final shape (profile) of concrete spread in a LCPC–Box test for yield stress of 50 Pa; analytical solution according to [88, 102]

Simulations were performed on a PC with an Intel Core 2 Quad CPU Q9550 of speed 2.83GHz and 4 GB RAM with a 64–Bit system using one processor core per simulation. The total calculation time of one LCPC–box test was approximately 200 h.

5.3.2.3 Simulation of the L–box test

The L–Box is commonly used to assess the filling ability and passing ability of SCC. Figure 5.27 shows three snap–shots from the numerical simulation. They were captured when the flow front reached the 20 cm mark, the 40 cm mark, and the final state. The same figure presents the corresponding images from the L–Box test on SCC.

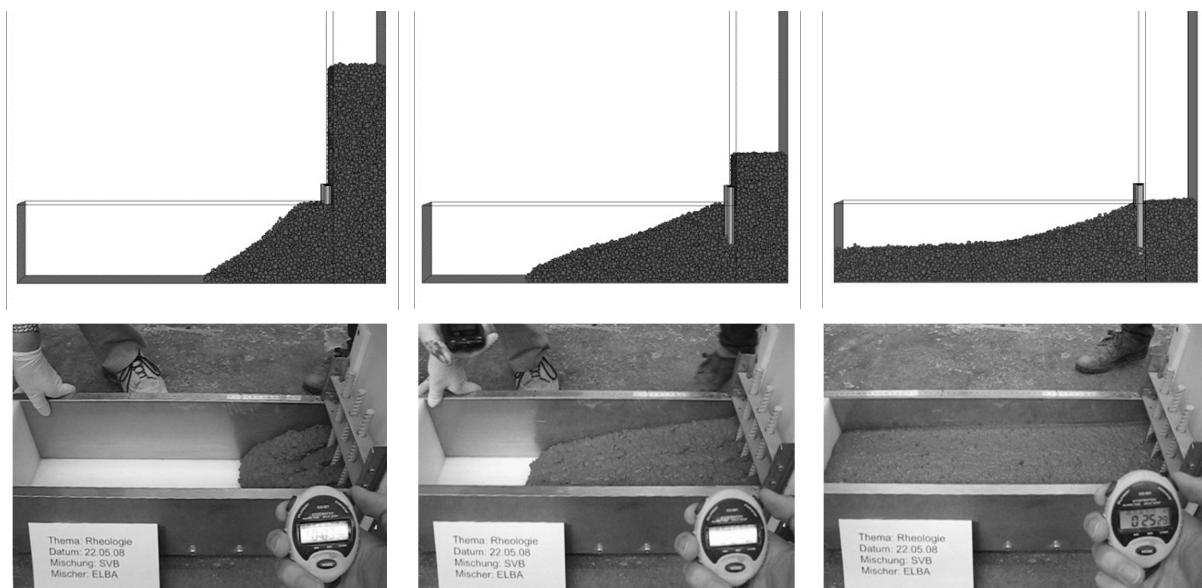


Figure 5.27: Results of the numerical simulation (above) and of the L–Box test (below) for three different time steps: when the flow front reaches the marks 20 cm, 40 cm, and the final state

The results of the simulation and experiments are in satisfactory agreement with regard to the shape of the concrete flow. Furthermore, the measured times in the experiment (when these defined states were reached) correspond well to the internal computation time of the DEM programme.

The total calculation time of one L–box test was approximately 200 h.

5.4 Summary and conclusions

The material model for the simulation of the rheological behaviour of fresh concrete was developed and implemented in the PFC. The material model developed consists of two contact models which treat the normal and tangential direction of particle movement and the corresponding normal and shear components of the force. Both models, in the normal and tangential directions, work simultaneously. The contact model for the normal direction was developed on the basis of the results of investigation on the mesolevel of observation. The contact model in shear direction was developed on the basis of standard model in shear direction taking into account the yield behaviour of the fresh concrete.

The parameters of the contact models can be subdivided into two categories. The first category relates to the properties of individual particles such as size, density and stiffness. The second category includes all parameters which define the interaction between the particles: characteristic distances and forces.

The set of user–written procedures needed for adequate modelling and data processing was developed and implemented in the PFC. This set of procedures includes following functions:

- creation of the geometry of the equipment;
- generation of the particles with given grading and control this grading until the end of simulation;
- generation of the fibres and coarse aggregates which consists of several particles;
- control and saving of the important aspects in the experiment which are connected to the time of the experiments such as spreading of the concrete in a time;
- analysis of the final state of fresh concrete specimen after simulation: internal stresses, distribution and orientation of the fibres;
- analysis of the shapes of fresh concrete specimen after simulation, etc.

Subsequently, a parameter study was performed in order to quantify the effects of individual parameters of the model on the results of the numerical simulation of the slump test with Abram's cone. The analysis of the results observed provided a basis for first considerations concerning an algorithm for the choice of the model parameters when concretes with various rheological properties are to be simulated.

It does indeed seem logical to start setting the parameters by choosing an appropriate particle size. In doing this, a representative size of the aggregates can serve as a reference measure. A particle size of between $1/3$ and $1/2$ of the maximum aggregate size can be recommended at this stage if particles of only one size are used.

Further, a procedure for counteracting the effect of particle size was developed and tested. On that account, slump–flow tests served as a reference for calibration. By using the proposed coefficient

the same workability could be obtained for simulated self-compacting concrete independent of the chosen particle size.

The characteristic distances should be chosen taking into account given appropriate particle size. The “distance to loss of contact bond” should not be greater than the diameter of the particle.

The characteristic forces should be chosen in the second step. The bond strength ($F_{max.tens}$) is the main parameter for characterising the interaction of the neighbouring particles. The ($F_{max.tens}$) value must be set according to the type of concrete to be simulated (stiff ordinary concrete, SCC etc.). An algorithm for deriving the bond strength parameter of the DEM model from a given value of yield stress according to the Bingham model was developed. The keystone of the algorithm was comparison of the analytically predicted stress distributions in the Abram’s cone filled with concrete and the corresponding force distribution obtained from corresponding numerical simulation by means of DEM, both calculations performed before cone lifting. The link between yield stress and contact bond strength makes it possible to estimate the magnitude of the viscous parameter (k_{visc}) in the contact model (“Pa·s” is transferred to “unit·s” according to the proportion which was derived for yield stress (Pa) and contact bond (unit)). Thus, real values of yield stress and plastic viscosity of the material under investigation can be translated into the material parameters.

The fine-tuning of the model can be performed by adjusting the parameters $fric$ and k_{visc} , which represents the yield stress and viscous behaviour of fresh concrete in the shear direction. The friction parameter $fric$ can be calibrated on the final slump or slump-flow diameter from the tests with the Abram’s cone. The parameter k_{visc} has an effect on the computation time only, which can be related to the spreading time in the slump-flow test on flowable or self-compacting concrete.

Finally, the quality of such estimation of parameters was validated by comparing the final shape of the concrete cake in the slump-flow test obtained from the numerical simulation, using the derived value of bond strength, and the corresponding prediction by analytical formula. It was found that the numerical simulation provided quantitatively accurate results. Further validation of the modelling approach was done by simulating the LCPC-box and L-box tests. This investigation dealt with analytical solution of a different test geometry and its corresponding numerical prediction. Similar to slump flow test, very good agreement of the numerical and analytical solutions was observed for LCPC-box test. Therefore, the proposed algorithm has been proven to be a sound procedure in linking the yield stress of the simulated concrete and the bond strength which are the main parameter of the suggested model.

CHAPTER 6

GENERAL CONCLUSIONS AND OUTLOOK

The overall aim of this thesis was to investigate how the rheological behavior of fresh concrete can be adequately simulated using the Discrete Element Method (DEM). With that in mind, the focus was on the development and implementation of a material model which would define the interaction between discrete elements in the DEM on the meso-level and would provide a sound description of the rheological properties of the fresh concrete on the macro-level of observation.

Fresh concrete is a composite material, and in terms of its rheology in the fresh state, it can be presented as a concentrated suspension consisting of solid particles (aggregates) dispersed in a viscous liquid (cement paste). The Particle Flow Code ITASCA was used in this investigation as a basic program, which enabled modelling the movement of discrete particles representing the aggregates. The interaction between individual particles in contact with one another depends to a great extent on the properties of fine mortar between aggregate particles and is described by corresponding constitutive relations.

The slump test was selected as a reference for calibration of the material model in the numerical simulation of yield stress from the slump test and was determined as a function of the cone geometry and the final slump. Additionally, an analytical solution for estimating plastic viscosity by analysing the spreading process in the slump test was developed. Further tests such as L-Box and LCPC-Box tests were selected as a basis for the verification of the material model developed.

The material model for the interaction between discrete elements was developed on the basis of experimental investigation of the interaction between discrete entities with some viscoelastic material between them. Four viscoelastic materials were investigated: two Carbopol water solutions, a fined-grained UHPC and a mortar for SCC. Carbopol solutions proved to be appropriate substances to be used as mortar-like references with time-independent rheological properties. Force–distance relations for two balls or an arrangement with a ball and a wall were performed. In the tests with Carbopol solutions effects of various parameters such as the yield stress of the material by varying the concentration of Carbopol; the type of contact, i.e., ball–ball or ball–wall; the amount of viscoelastic material between entities, i.e., covering of the equipped ball; and deformation rate were investigated. Tests with the monotonic regime of the ball motion in tension and, subsequently, compression described an overall response of the system, while the tests with intermediate stops gave information about velocity-independent elastic and velocity-dependent viscous components of the measured force.

In ball–wall tests performed on UHPC and SCC mortar generally similar behaviour was observed, as in the corresponding tests on Carbopol solutions. However, as expected, a pronounced time dependence of the material response was observed for cement-based materials. While thixotropy certainly plays a role, the major cause of this effect might be the stiffening of fine mortar due to water loss at the mortar surface. It was shown that the magnitudes of elastic

and viscous components of the contact force measured in tests correlated well with the rheological constants obtained from the rheometer tests: the elastic component of the contact force was proportional to the yield stress, while the viscous component of the contact force was proportional to the plastic viscosity. Sets of characteristic forces, such as maximum tensile and compressive forces, and corresponding distances, such as distance of the maximum tensile force, distance of the contact bond loss and distance of the creation of new contact bond, were derived from the experimental data.

Finally, the results of the tests were summarised and a generalised material model for the interaction between discrete elements with some viscoelastic material between them was proposed. It was shown that this material model can be resolved into two models, which represent the viscous and elastic components of the contact force.

The proposed material model was described mathematically and implemented in a DEM code. The material model in a DEM code was resolved into normal and shear components with respect to the contact plane. The material model derived from the experiments represented the contact model in normal direction. Its input parameters fall into two categories: the first relates to the individual particles and the second to the interaction between particles. The second category of the input parameters is based on the results of test on meso-level, characteristic distances and forces. The force-displacement relation for shear direction was not investigated experimentally, taking into account the complexity of the required equipment. Therefore, the contact model in the shear direction was developed on the basis of the standard contact model in the direction of shear, taking into account the yield behavior of the fresh concrete.

Furthermore, a parameter study was performed in order to quantify the effects of individual parameters of the model on the results of the numerical simulation of the slump test with Abram's cone. The analysis of the results obtained provided a basis for initial considerations concerning an algorithm for the choice of the model parameters, when concretes with various rheological properties must be simulated.

The quality of such parameter estimation was verified by comparing the final shape of the concrete cake in the slump-flow test obtained from the numerical simulation, with the derived value of the bond strength, and the corresponding prediction by analytical formula. Further validation of the modelling approach was done by simulating the LCPC-Box test. This investigation dealt with the analytical solution of a different test geometry and its corresponding numerical prediction. Similar to the slump flow test, very good agreement of the numerical and analytical solutions could be reported for the LCPC-Box test. Thus, the proposed algorithm has been proven to be a sound procedure to link the yield stress of the simulated concrete and the bond strength which are the main parameter of the suggested model.

The proposed modeling approach has a potential to be developed to a powerful tool in optimizing and developing new concrete technologies, especially in optimizing the composition, the grading of and the proportion among the components, of the fresh concrete to predict its rheological behavior, fibre distribution and orientation as well as other properties. Moreover, the material model as developed can be easily modified and improved for numerical modeling relating to de-airing process. Air bubbles can be presented in numerical modeling as compressed particles with low density, small contact bonds and the ability to merge. Time-dependent rheological behavior of the

fresh concrete can be modeled using additional calibration of the material model in relation to time although additional experiments are required. The use of fibre and crushed aggregates, rigid components of the fresh concrete with complex geometry, can be modeled using clump logic. As a reference a 3D model of the envelope surface filled with particles can be used; the spatial distribution of the clumps, position and orientation of any individual clump or group of clumps can be easily monitored during the whole modeling process.

BIBLIOGRAPHY

- [1] 4C-Rheometer, user's manual, Danish Technological Institute, 2008
- [2] ACI 116R-00. Cement and concrete terminology, 2005
- [3] ALDEA, C.-M.; SHAH, S.P.; KARR, A.: Permeability of cracked concrete. *Materials and Structures*, Vol. 32, 1999, pp. 370-376
- [4] ASTM C143/C143M-00. *Standard test method for slump of hydraulic-cement concrete*
- [5] BACKHAUSE, G.: *Deformationsgesetze*. Akademie-Verlag, Berlin, 1983
- [6] BANFILL, P.F.G.; BEAUPRE, D.; CHAPDELAIN, F.; DE LARRAD, F.; DOMONE, P.; NACHBAUR, L.; SEDRAN, T.; WALLEVIK, O.H.; WALLEVIK, J.: Comparison of concrete rheometers: international tests at LCPC (Nantes, France). In: FERRARIS, C.F.; BROWER, L.E. (Eds.): NISTIR 6819, September 2001
- [7] BARNES, H.A.; HUTTON, J.F.; WALTERS, K.: *An introduction to rheology*. Elsevier Science Publishing Company INC.; New York, 1989
- [8] BARTOS, P.J.M.: *Fresh concrete: properties and tests*. Elsevier Science Publishers, Amsterdam, 1992
- [9] BARTOS, P.J.M.; SONEBI, M.; TAMIMI, A.K. (Eds.): *Workability and rheology of fresh concrete: compendium of tests*. RILEM, France, 2002
- [10] BEAUPRÉ, D.: *Rheology of High Performance Shotcrete*. Doctoral Thesis, University of British Columbia (Canada), 1994
- [11] BEAUPRÉ, D.; MINDESS, S.: Rheology of fresh concrete: principles, measurements, and applications. In: SKALNY, J.; MINDESS, S. (Eds.): *Materials Science of Concrete*, American Ceramic Society, 1998, pp. 149-190
- [12] BHUSHAN, B.: Adhesion and stiction: mechanisms, measurement techniques, and methods for reduction. *Journal of Vacuum Science & Technology B*, Vol. 21(6), pp. 2262-2296
- [13] BOULEKBACHE, B.; HAMRAT, M.; CHEMROUK, M.; AMZIANE S.: Flowability of fibre-reinforced concrete and its effect on the mechanical properties of the material. *Construction and Building Materials*, 2010, Vol. 24, pp. 1664–1671
- [14] BRANDT, A.M.: *Cement-based composites: materials, mechanical properties and performance*. E&FN Spon., London, 1995, p. 470
- [15] CHANSON, H.: *Applied hydrodynamics: an introduction to ideal and real fluid flows*. CRC Press, Taylor & Francis Group, Leiden, Netherlands, 2009
- [16] CHEN, Y.; ZHAO, Y.; GAO, H.; ZHENG, J.: Liquid bridge force between two unequal-sized spheres or a sphere and a plane. *Particuology*, 2011, Vol. 9, pp. 374– 380
- [17] CHRISTENSEN, G.: *Modelling the flow of fresh concrete: the slump test*. Doctoral Thesis, Princeton University, 1991

- [18] CHU, H.; MACHIDA A.; SUZUKI, N.: Experimental investigation and DEM simulation of filling capacity of fresh concrete. *Transactions of the Japan Concrete Institute*, Vol. 16, 1996, pp. 9-14
- [19] COUSSOT, P.: Rheologie des Boues et Laves Torrentielles – Etudes de Dispersions et Suspensions Concentrees. L'Institut National Polytechnique de Grenoble, et Etudes du Cemagref, 1993
- [20] CUNDALL, P.A.: A computer model for simulating progressive large scale movements in blocky rock systems. International Symposium on Rock Fracture, Nancy, France, Proc. 2, 1971, pp. 129-136
- [21] CUNDALL, P.A.: Formulation of a three-dimensional Distinct Element Model-Part I: A scheme to detect and represent contacts in a system composed of many polyhedral blocks. *International Journal of Rock Mechanics and Mining Sciences & Geomechanics Abstracts*, Vol. 25(3), 1988, pp. 107-116
- [22] CUNDALL, P.A.; STRACK, O.D.L.: A discrete numerical model for granular assemblies. *Geotechnique*, Vol. 29(1), 1979, pp. 47-65
- [23] CUNDALL, P.A.; HART, D.H.: Numerical modelling of discontinua. *Engineering Computations*, Vol. 9(2) , 1992, pp.101-13
- [24] DAVIDSON, M.R.; KHAN, N.H.; YEOW, Y.L.: Collapse of a cylinder of Bingham fluid. In: Proceedings of international conference on Computational techniques and applications, Australian Mathematical Society, Canberra, 2000, pp. 499–517
- [25] DE LARRARD, F.; FERRARIS, C. F.: Rhéologie du béton frais remanié. II: relations entre composition et paramètres rhéologiques. Bulletin des Laboratoires des Ponts et Chaussées, Vol. 214, 1998, pp. 69-79
- [26] DE LARRARD, F.; SEDRAN, T.; HU, C.; SZITKA, R J.C.; JOLY, M.; DERKX, F.: Evolution of the workability of superplasticized concretes: assessment with BTRHEOM rheometer. In: BARTOS, P.J.M.; MARRS, D.L.; CLELAND, D.J. (Eds.): Proceedings of the International RILEM Conference on production methods and workability of concrete, RILEM Proceedings 32, Paisley, Scotland, 1996, pp. 377-388
- [27] DE LARRARD, F.; SZITKAR, J.-C.; HU, C.; JOLY, M.: Design of a rheometer for fluid concretes. RILEM workshop special concretes – workability and mixing, 1993, pp. 201-208
- [28] DETWILER, R.J.; MEHTA, P.K.: Chemical and physical effects of silica fume on the mechanical behavior of concrete. *Materials Journal*, Vol. 86(6), 1989, pp. 609-614
- [29] DOMONE, P.L.J.; XU YONGMO; BANFILL, P.F.G.: Developments of the Two-Point workability test for high-performance concrete. *Magazine of Concrete Research*, Vol. 51, 1999, pp. 181-190
- [30] DUFOUR, F.: *Developpements de la methode deselements finis avec des points d'integration lagrangiens: Application a la geomecanique*. Doctoral Thesis, Ecole Centrale de Nantes, 2002

- [31] DUFOUR, F.; PIJAUDIER-CABOT, G.: Numerical modeling of concrete flow: Homogeneous approach. *International Journal for Numerical and Analytical Methods in Geomechanics*, Vol. 29, 2005, pp. 395-416
- [32] EFNARC: Specification Guidelines for Self-Compacting Concrete. European Federation of Producers and Contractors of Specialist Products for Structures, 2001
- [33] EN12350. Testing fresh concrete. *European Committee for Standardization*, 2000
- [34] FERRARI, C.F.; BROWER, L.E.; BEAUPRE, D.; CHAPDELAIN, F.; DOMONE, P.; KOEHLER, E.; SHEN, L.; SONEBI, M.; STRUBLE, L.; TEPKE, D.; WALLEVIK, O.; WALLEVIK, J.: Comparison of Concrete Rheometers: International Tests at MB. In: FERRARIS, C.F.; BROWER, L.E.(Eds.), Cleveland, OH, 2004
- [35] FERRARIS, C.F.; MARTYS, N.: Relating fresh concrete viscosity measurement from different rheometers. *Journal of research of the national institute of standards and technology*, Vol. 108(3), 2003, pp. 229-234
- [36] FERRARIS, C. F.; DE LARRARD, F.; MARTYS, N.: Fresh concrete rheology: recent developments. In: MINDESS, S.; SKALNY, J. (Eds.): *Materials Science of Concrete VI*, The American Ceramic Society, Westerville, OH, 2001, pp. 215-241
- [37] FERRARIS, C.F.: Measurement of the rheological properties of high performance concrete: state of the art report. *Journal of research of the National Institute of Standards and Technology*, Vol. 104(5), 1999, pp. 461-478
- [38] FERRARIS, C.F.; BROWER, L.; OZYILDIRIM, C.; DACZKO, J.: Workability of Self-Compacting Concrete. In: Proceedings of international symposium on high performance concrete, Orlando, Florida, 2000, pp. 398-407
- [39] FERRARIS, C.F.; BROWER, L.E. (Eds.): Comparison of concrete rheometers: international tests at LCPC (Nantes, France) in October 2000. (NISTIR 6819), Gaithersburg, MD, *National Institute of Standards and Technology*, 2001
- [40] FERRARIS, C.F.; DE LARRARD, F.: Modified slump test to measure rheological parameters of fresh concrete. *Cement, Concrete and Aggregates*, Vol. 20(2), 1998, pp. 241-247
- [41] FINDLEY, W.; LAI, J.; ONARAN, K.: Creep and relaxation of nonlinear viscoelastic materials. North-Holland Publishing company, Amsterdam, 1976, pp. 51-10
- [42] FLATT, R.J., MARTYS, N.; BERGSTRÖM, L.: The rheology of cementitious materials. *Materials Research Bulletin*, Vol. 29 (5), 2004, pp. 314-318
- [43] FREDRICKSON, A.G.: Principles and applications of rheology. Prentice-Hall, New York, 1964
- [44] GRAM, A.; FARHANG, A.; SILFWERBRAND, J.: Computer-aided modelling and simulation of self-compacting concrete flow. In: Proceeding of 5th international RILEM Symposium on self-compacting concrete, RILEM publications SARL, Ghent, Belgium, Vol. 1, 2007, pp. 455-460
- [45] GRAM, A.; SILFWERBRAND, J.: Numerical simulation of fresh SCC flow: applications. *Materials and Structures*, Vol. 44, 2011, pp. 805-813

- [46] GRAU, P.; BERG, G.; GIESSMANN, E.-J.: Rheologische Untersuchungen fester Stoffe mit Dehnungsratenwechselfersuchen. *Technische Mechanik 4*, Vol. 3 , 1983, p. 54
- [47] HACKLEY, V. A.; FERRARIS, C. F.: Guide to rheological nomenclature: measurements in ceramic particulate systems. *NIST Special Publication 946*, February 2001
- [48] HACKLEY, V.; FERRARIS, C.F.: The use of nomenclature in dispersion science and technology. National Institute of Standards and Technology, Gaithersburg, MD, 2001
- [49] HART, R.; CUNDALL, P.A.; LEMOS, J.: Formulation of a three-dimensional distinct element model - part II. Mechanical calculations for motion and interaction of a system composed of many polyhedral blocks. *International Journal of Rock Mechanics and Mining Sciences & Geomechanics Abstracts*, Vol. 25(3),1988, pp. 117-125
- [50] HELMUTH, R.A.; HILLS, L.M.; WHITING, D.A.; BHATTACHARJA S.: Abnormal concrete performance in the presence of admixtures. *Portland Cement Association*, Skokie, IL, 1995
- [51] HERIS, S.Z.; HAMED MOSAVIAN, M. T.; WHITE, E. T.: Capillary holdup between vertical spheres. *Brazilian Journal of Chemical Engineering*, Vol. 26(4), 2009, pp. 695 – 704
- [52] HOOGERBRUGGE, P.J.; KOELMAN, J.M.V.A.: Simulating microscopic hydrodynamic phenomena with Dissipative Particle Dynamics. *Europhysics Letter*, Vol. 19(3), 1992, p. 155
- [53] HOORNAHAD, H.; KOENDERS, E.A.B.; VAN BREUGEL, K.: Capillary cohesion between two spherical glass particles. *Key Engineering Materials*, Vol. 417-418, 2010, pp. 449-452
- [54] HOORNAHAD, H.; KOENDERS, E.A.B.; VAN BREUGEL, K.: Towards a model for fresh granular-paste systems based on Discrete Element Method. *Key Engineering Materials*, 2011, Vol. 452-453, pp. 569-572
- [55] HU, C.: Rhéologie des bétons fluides. *Etudes et recherches des Laboratoires des Ponts et Chaussées*, Paris, France, 1995
- [56] HU, C.; DE LARRARD, F.; SEDRAN, T.; BONLAG, C.; BOSE, F.; DEFLORENNE, F.: Validation of BTRHEOM, the new rheometer for soft-to-fluid concrete. *Materials and Structures*, Vol. 29(194),1996, pp. 620-631
- [57] HU, C.; DE LARRARD, F.: The rheology of fresh high-performance concrete. *Cement and Concrete Research*, Vol. 26(2), 1996, pp. 283-294
- [58] Instruction Manual, HAAKE MARS III, Version 1.5
- [59] Itasca consulting group Inc: PFC 3D. ICG, Minneapolis, 2004
- [60] JUVAS, K.: Very dry precasting concrete. In: BARTOS, P.J.M. (Eds.): Proceedings of the international RILEM workshop on special concretes: workability and mixing, E&FN Spon., London, UK, 1994, pp. 153-168
- [61] KHAYAT, K.H.: Workability, testing and performance of Self-Consolidating Concrete. *Materials Journal*, Vol. 96(3), 1999, pp. 346-353
- [62] KITAOJI, H.; TANIGAWA, Y.; MORI, H.; KUROKAWA, Y.; URANO, S.: Flow simulation of fresh concrete cast into wall structure by Viscoplastic Divided Space Element Method. *Transitions of the Japan Concrete Institute*, Vol. 16, 1996, pp. 45-52

- [63] KODAKA, S.; TANIGAWA Y.; MORI H.; KUROKAWA Y.: Flow simulation of fresh concrete using dynamic visco-plastic suspension element method. In: *Proceedings of the Japan Concrete Institute*, Vol. 15(1), 1993, pp. 345–350
- [64] KOEHLER, E.; FOWLER, D.: Summary of concrete workability test methods. *Researcher report ICAR-105-1*, The university of Texas at Austin, 2003
- [65] KOELMAN, J.M.V.A.; HOOGERBRUGGE, P.J.: Dynamic simulation of hard-sphere suspension under steady shear. *Europhysics Letters*, Vol. 21(3), 1993, p. 363
- [66] KONIETZKY, H.: Numerical modeling in micromechanics via particle methods. In: *Proceedings of the 1st International PFC Symposium*, Balkema Publishers, Netherlands, 2002
- [67] KUCH, H.; SCHWABE, J-H.: Anwendung der Partikelsimulation auf Verarbeitungsprozesse von granularen Stoffen. In: Vortrag zur VDI-Tagung „Schwingungen in Verarbeitungsmaschinen“ vom 26.- 27.04.2005, Leonberg Tagungsband
- [68] KUCH, H.; PALZER, S.; SCHWABE, J.-H.: Anwendung der Simulation bei der Verarbeitung von Gemengen. In: F. A. Finger-Institut für Baustoffkunde (Eds.): *Tagungsbericht der 16. Internationalen Baustofftagung*, Ibausil, Weimar, Germany, 2006, Vol. 1, pp. 1321–1327
- [69] KUROKAWA, Y.; TANIGAWA, Y.; MORI H.; KOMURA, R.: A Study on the slump test and slump-flow test of fresh concrete. *Transactions of the Japan Concrete Institute*, Vol. 16, 1994, pp. 25-32
- [70] KUROKAWA, Y.; TANIGAWA, Y.; MORI H.; NISHINOSONO, Y.: Analytical study on effect of volume fraction of coarse aggregate on Bingham’s constants of fresh concrete. *Transactions of the Japan Concrete Institute*, Vol. 18, 1996, pp. 37-44
- [71] MACOSKO, C.W.: *Rheology: principles, measurements and applications*. Wiley-VCH Publishers, New York, 1994
- [72] MARTINIE, L.; ROUSSEL, N.: Simple tools for fibre orientation prediction in industrial practice. *Cement and Concrete Research*, Vol. 41, 2011, pp. 993-1000
- [73] MARTYS, N.; FERRARIS, C.H.: Simulation of SCC flow. In: *Proceedings of the 1st North American Conference on the design and use of Self-Consolidating Concrete*, Chicago, IL, 2002, pp. 27-30
- [74] MARTYS, N.S.: Study of a dissipative particle dynamics based approach for modeling suspensions. *Journal of Rheology*, Vol. 49 (2), 2005, pp. 401–424
- [75] MARTYS, N.S.; MOUNTAIN, R.D.: Velocity Verlet algorithm for Dissipative-Particle-Dynamics-Based model of suspensions. *Physical Review E*, Vol. 59(3), 1999, pp. 3733-3736
- [76] MECHTCHERINE, V.; HAIST, M.; STÄRK, L.; MÜLLER, H.S.: Optimization of the rheological and fracture mechanical properties of lightweight aggregate concrete. In: BRANDT, A.M.; LI, V.C.; MARSHALL, I.H. (Eds.): *Proceedings of the 7th International Symposium on Brittle Matrix Composites*, Woodhead Publishing Ltd, 2003, pp. 301-310
- [77] MECHTCHERINE, V.; SHYSHKO, S.: Self-compacting concrete simulation using Distinct Element Method. In: WALLEVIK, O.H.; KUBENS, S.; OESTERHELD, S. (Eds.): *Proceedings of*

- the 3rd International RILEM symposium on rheology of cement suspensions such as fresh concrete, *RILEM Publications SARL*, Reykjavik, Iceland, 2009, pp. 171–179
- [78] MEHTA, K.; MONTEIRO, P.: Concrete: microstructure, properties, and materials. McGraw Hill, New York, 2006
- [79] MEZGER, T.: The rheology handbook, Vincentz Network, Hannover, 2006
- [80] MORESI, L, DUFOUR, F, MÜHLHAUS, H-B.: A Lagrangian integration point finite element method for large deformation modeling of viscoelastic geomaterials. *Journal of Computational Physics*, Vol. 184(2), 2003, pp. 476–497
- [81] MORI, H.; TANIGAWA, Y.: Simulation methods for fluidity of fresh concrete. *Memoirs of the School of Engineering, Nagoya University*, Vol. 44, 1992, pp. 71-133
- [82] MORI, H.; TANIGAWA, Y.; WATANAWA, K.; UMEMOTO, M.: Flow analysis of fresh concrete using two phase model. *Journal of Structural and Construction Engineering*, Transactions of Architectural Institute of Japan, Vol. 427, 1991, pp. 11–21 (in Japanese)
- [83] MURATA, J.; Flow and deformation of fresh concrete. *Materials and Structures*, Vol. 17(2), 1984, pp. 117– 129
- [84] MURATA, J.; KIKUKAWA, H.: Viscosity equation for fresh concrete. *Materials Journal*, Vol. 89(3), 1992, pp. 230-237
- [85] NABETA, K.; et al.: Flow simulation of fresh concrete by distinct element method. In: *Proceedings of the Japan Concrete Institute*, Vol. 16(1), 1994, pp. 479–484
- [86] NEOPHYTOU, M.K.-A.; POURGOURI, S.; KANELLOPOULOS, A.D.; PETROU, M.F.; IOANNOU, I.; GEORGIU, G.; ALEXANDROU, A.: Determination of the rheological parameters of self-compacting concrete matrix using slump flow test. *Applied Rheology*, Vol. 20 (62402), 2010, pp. 1-20
- [87] NEVILLE, A.: Properties of Concrete. John Wiley & Sons, New York, 1996
- [88] NGUYEN, T.L.H.; ROUSSEL, N.; COUSSOT, P.: Correlation between L-box test and rheological parameters of a homogeneous yield stress fluid. *Cement and Concrete Research*, Vol. 36(10), 2006, pp. 1789-1796
- [89] NOOR, M.A.; UOMOTO, T.: Three-dimensional Discrete Element Simulation of rheology tests of Self-Compacting Concrete. In: *Proceedings of the 1st international RILEM Symposium on SCC*, Stockholm, Sweden, 1999, pp. 35-46
- [90] PASHIAS, N.; BOGER, D.V.; SUMMERS, J.; GLENISTER, D.J.: A fifty-cent rheometer for yield stress measurement. *Journal of Rheology*, Vol. 40, 1996, pp. 1179-1189
- [91] PETERSSON, Ö.: Simulation of Self-Compacting Concrete – laboratory experiments and numerical modeling of testing methods, JRING and L-box Tests. In: *Proceedings of international RILEM symposium on Self-Compacting Concrete*, Reykjavik, Iceland, 2003, pp. 202-207
- [92] PETERSSON, Ö.; HAKAMI, H.: Simulation of self-compacting concrete - laboratory experiments and numerical modeling of slump flow and L-box tests. In: *Proceedings of 2nd international symposium on Self-compacting Concrete*, Tokyo, 2001, pp. 79–88

- [93] PIAU, J.M.: Carbopol gels: Elastoviscoplastic and slippery glasses made of individual swollen sponges meso- and macroscopic properties, constitutive equations and scaling laws. *Journal of Non-Newtonian Fluid Mechanics*, Vol. 144(1), 2007, pp.1–29
- [94] RAHAMAN, M.N.: Ceramic processing and sintering (Second Edition). CRC Press, 2003, pp. 330-342
- [95] RAJANI, B.; MORGENSTERN, N.: On the yield stress of geotechnical materials from the slump test. *Canadian Geotechnical Journal*, Vol. 28, 1991, pp. 457–462
- [96] RAMACHANDRAN, V.S.: Concrete admixtures handbook – properties, science, and technology (Second Edition), Noyes Publications, New Jersey, 1995
- [97] REINER, M.: Deformation, strain and flow: an elementary introduction to rheology (Second Edition). Interscience, London, 1960, p. 347
- [98] REINER, M.: Rheologie in elementarer Darstellung. Fachbuchverlag, Leipzig, 1972, pp. 128-141
- [99] RITCHIE, A.G.B.: The triaxial testing of fresh concrete. *Magazine of Concrete Research*, Vol. 14(40), 1962, pp. 37-41
- [100] ROUSSEL, N.: Correlation between yield stress and slump: Comparison between numerical simulations and concrete rheometers results. *Materials and Structures*, Vol. 37(4), 2006, pp. 469-477
- [101] ROUSSEL, N.: Rheology of fresh concrete: from measurements to predictions of casting processes. *Materials and Structures*, Vol. 40, 2007, pp. 1001–1012
- [102] ROUSSEL, N.: The LCPC BOX. A cheap and simple technique for yield stress measurements of SCC. *Materials and Structures*, Vol. 40(9), 2007, pp. 889-896
- [103] ROUSSEL, N.; COUSSOT, P.: Fifty-cent rheometer for yield stress measurements: from slump to spreading flow. *Journal of Rheology*, Vol. 49(3), 2005, pp. 705-718
- [104] ROUSSEL, N.; CUSSIGH, F.: Distinct-layer casting of SCC: The mechanical consequences of thixotropy. *Cement and Concrete Research*, Vol. 38(5), 2008, pp. 624-632
- [105] ROUSSEL, N.; GEIKER, M.R.; DUFOUR, F.; THRANE, L.N.; SZABO, P.: Computational modeling of concrete flow: General overview. *Cement and Concrete Research*, Vol. 37(9), 2007, pp. 1298-1307
- [106] ROUSSEL, N.; STAQUET, S.; SCHWARZENTRUBER, L. D'ALOIA; LE ROY, R.; TOUTLEMONDE, F.: SCC casting prediction for the realization of prototype VHPC-precambered composite beams. *Materials and Structures*, Vol. 40, 2007, pp. 877-887
- [107] SAAK, A.W.; JENNINGS, H.M.; SHAH, S.P.: The influence of wall slip on yield stress and viscoelastic measurements of cement paste. *Cement and Concrete Research*, Vol. 31(2), 2001, pp. 205–212
- [108] SCHOWALTER, W.R.; CHRISTENSEN, G.: Toward a rationalization of the slump test for concrete: Comparisons of calculations and experiments. *Journal of Rheology*, Vol. 42(4), 1998, pp. 865-870

- [109] SCHUTTER, G.: Guidelines for testing fresh self-compacting concrete. European research project: Measurement of properties of fresh self-compacting concrete, 2005
- [110] SCHWABE, J.-H.; KUCH, H.: Development and controlling of concrete mix processing procedures. Vortrag zum Congress BIBM 2005, Amsterdam
- [111] SHYSHKO, S.; MECHTCHERINE, V.: Simulating the workability of fresh concrete. In: SCHLANGEN, E.; DE SCHUTTER, G. (Eds.): Proceedings of the international RILEM symposium of concrete modelling – CONMOD '08, *RILEM Publications SARL*, Delft, Netherlands, 2008, pp. 173–181
- [112] SIMS, J. S.; MARTYS, N.: Simulation of Sheared Suspensions With a Parallel Implementation of QDPD. *Journal of Research of the National Institute of Standards and Technology*, Vol. 109(2), 2004, pp. 267-277
- [113] STROEVEN, P, HE, H, GUO Z, STROEVEN, M.: Particle packing in a model concrete at different levels of the microstructure: Evidence of an intrinsic patchy nature. *Materials Characterization*, Vol. 60(10), 2009, pp. 1088-1092
- [114] STROEVEN, P, HE, H, GUO, Z, STROEVEN, M.: Discrete element modelling approach to assessment of granular properties in concrete. *Journal of Zhejiang University Science A*, Vol. 12(5), 2011, pp. 335-344
- [115] STRUBLE, L.J.; PURI, U.; Ji, X.: Concrete rheometer. *Advances in Cement Research*, Vol. 13(2), 2001, pp. 53–63
- [116] SUJIVORAKUL, C.; NAAMAN, A.E.: Modeling bond components of deformed steel fibres in FRC composites. In: REINHARDT, H.W.; NAAMAN, A.E. (Eds.): Proceedings of the international RILEM workshop high performance fibre reinforced cement composites, *RILEM Publications SARL*, 2003, pp. 35–48
- [117] SULSKY, D.; SCHREYER, H.: Antisymmetric form of the material point method with applications to upsetting and Taylor impact problem. *Computational Methods in Applied Mechanics and Engineering*, Vol. 139, 1996, pp. 409-429
- [118] TANAKA, K.; SATO, K.; WATANABE, S.; ARIMA, I.; SUENAGA, K.; ZIA P. (Ed): Development and utilization of high performance concrete for the construction of the Akashi Kaikyo Bridge. In: SP-140: High Performance Concrete in Severe Environments, Detroit, MI, 1993, pp. 147-161
- [119] TANIGAWA, Y.; MORI, H.: Rheological analysis of slumping behavior of fresh concrete. In: Proceeding of the 29th Japan Congress on Materials Research, Society of Materials Science, Kyoto, 1986, pp. 129-136
- [120] TANIGAWA, Y.; MORI, H.; NODA, Y.; WATABE, T.: Analytical study on pumping behaviour of fresh concrete. In: Proceedings of the Japan Concrete Institute, Vol. 14(1), 1992, pp. 421–426
- [121] TANIGAWA, Y.; MORI, H.; UMEMOTO, M.; WATANABE, K.: Flow simulation of fresh concrete by suspension element method. *Materials Science*, Transactions of the Society of Materials Science, Japan, Vol. 38(431), 1989, pp. 26–31

- [122] TANIGAWA, Y.; MORI, H.; WATANABE, K.: Computer simulation of consistency and rheology test of fresh concrete by visco plastic finite element method. In: Wierig H.-J. (Eds.): Proceedings of the RILEM Colloquium on Properties of Fresh Concrete, Chapman & Hall, London, 1990, pp. 301-308
- [123] TANNER, R.I.: Engineering rheology (Second Edition). *Oxford University Press*, USA, 2002, pp. 1-30
- [124] TATTERSALL, G.H.: The workability of concrete. *Cement & Concrete Association of Great Britain*, 1976
- [125] TATTERSALL, G.H.: Workability and Quality Control of Concrete. *E&FN Spon.*, London, 1991
- [126] TATTERSALL, G.H.; AND BAKER, P.H.: An investigation on the effect of vibration on the workability of fresh concrete using a vertical pipe apparatus. *Magazine of Concrete Research*, Vol. 41(146), 1989, pp. 3-9
- [127] TATTERSALL, G.H.; BANFILL, P.F.G.: The rheology of fresh concrete. *Pitman Advanced Publishing Program*, London, 1983
- [128] THRANE, L. N.; PADE, C.; NIELSEN, C. V.: Determination of rheology of Self-Consolidating Concrete using the 4C-rheometer and how to make use of the results. *Journal of ASTM International*, Vol. 7(1), 2010
- [129] THRANE, L.H.; SZABO, P.; GEIKER, M.; GLAVIND, M.; STAND, H.: Simulation of the test method “L-box” for self-compacting concretes. In: Annual transactions of the Nordic Rheology Conference, Reykjavik, Iceland; Vol. 12, 2003, pp. 47–54
- [130] THRANE, L.N.: Simulation and verification of form filling with Self-Compacting Concrete. In: Proceedings of Nordic Concrete Research Meeting, Vol. 1, 2005, pp. 89-91
- [131] THRANE, L.N.; SZABO, P.; GEIKER, M.; GLAVIND, M.; STANG, H.: Simulation and verification of flow in SCC test methods. In: Proceedings of the 4th international RILEM Symposium on SCC, Chicago, 2005
- [132] TOMAS, J.: Adhesion of ultrafine particles - A micromechanical approach. *Chemical Engineering Science*, 2007, Vol. 62(7), pp. 1997-2010
- [133] VAN ZIJL, G.: Optimisation of the composition and fabrication methods; Applications for precast concrete members. In: MECHTCHERINE, V. (Eds.): Ultra-ductile concrete with short fibres – Development, Testing, Applications, *Ibidem Verlag*, Stuttgart, 2005, pp. 37-54
- [134] VINCENT, M.: *Etude de l'orientation des fibres de verre courtes lors de la mise en oeuvre de thermoplastiques chargés*. Doctoral Thesis, Ecole Nationale Supérieure des Mines, Paris, 1984
- [135] WALLEVIK, J.E.: *Rheology of particle suspensions - fresh concrete, mortar and cement paste with various types of lignosulfonates*. Doctoral Thesis, Department of Structural Engineering, The Norwegian University of Science and Technology, 2003
- [136] WALLEVIK, O.H.; NIELSSON, I.: Self-compacting concrete – a rheological approach. In: International Workshop on SCC, Kochi, Japan, 1998, pp. 136-159

- [137] WALLEVIK, O.H.: Practical description of rheology of SCC. SF Day at the Our World of Concrete, Singapore, August, 2002
- [138] WALLEVIK, O.H.: Rheology – a scientific approach to develop self-compacting concrete. In: WALLEVIK, O.H. (Eds.): Proceedings of International RILEM Symposium on Self-Compacting Concrete, *RILEM Publications SARL*, Reykjavik, Iceland, 2003
- [139] WALLEVIK, O.H.: *The rheology of fresh concrete and its application on concrete with and without silica fume*. Doctoral Thesis, NTH Trondheim, 1990
- [140] WALLEVIK, O.H.; GJORV, O.E.: Development of a coaxial cylinder viscometer for fresh concrete. In: Proceedings of the RILEM Colloquium on properties of fresh concrete, *Chapman & Hall*, Hanover, 1990, pp. 213-224
- [141] WANG, K.; JANSEN, D.C.; SHAH, S.P.; KARR, A.: Permeability study of cracked concrete. *Cement Concrete Research*, Vol. 27 (3), 1997, pp. 381–393
- [142] WEIPERT, D.: Rheologie der Lebensmittel. *Behrs Verlag*, Hamburg, 1993, pp. 51-98
- [143] WESSELING, P.: Principles of Computational Fluid Dynamics. *Springer*, 2000
- [144] WUSTHOLZ, T.: Fresh properties of self-compacting concrete (SCC). *Otto-Graf-Journal*, Vol. 14, 2003, pp. 179-188
- [145] YILDIRIM, O.E.; BASARAN, O.A.: Deformation and breakup of stretching bridges of Newtonian and shear-thinning liquids: comparison of one- and two-dimensional models. *Chemical Engineering Science*, Vol. 56; 2001, pp. 211-233
- [146] ZHUGUO, L.: State of workability design technology for fresh concrete in Japan. *Cement and Concrete Research*, Vol. 37(9), 2007, pp. 1308-1320

Appendix A - Abbreviations, Symbols and Indices

Capital Letters

A	Accelerating component
F_i^n	Normal component vector
F_i^s	Shear component vector
\dot{H}_i	Angular momentum of the particle
F_i^{s-old}	Old value of the shear force vector
ΔF_i^S	Shear elastic force increment
$D_{n,s}$	Damping force
E	Young's modulus
F^n	Normal force
F^s	Shear force
H	Height of the slump cone
I	Principal moments of inertia of the particle
K^n	Normal stiffness at the contact
L	Circumference of the bottom surface of the slump cone
M_i	Resultant moment acting on the particle i
Q	Flow rate
R_{100}	Fixed radius, equal to 100 mm
R_i	Slump flow radius
S	Final slump value
S_f	Slump flow value
T	Slump time
T_{500}	Time T_{500}
U^n	Overlap
V_c	Volume of the slump cone
V_i	Volume of the particle

Lower case letters

Δt	Timestep
$c_{n,s}$	Damping constant
d	Distance between objects
g	Acceleration of gravity
g_i	Body force acceleration vector
$h(r)$	Fluid depth at stoppage as a function of the distance
h_0	Height of unyielded region
h_1	Height of yielded region
h_{100}	Height at the fixed radius R_{100}
h_i	Height at the slump flow radius R_i

A Abbreviations, Symbols and Indices

k_n	Normal stiffness of the particle
k^s	Shear stiffness at the contact
k_s	Shear stiffness of the particle
l_0	Length of the side surface of unyielded region
m	Mass of the particle
n_i	Unit normal vector
p_z	Vertical stress acting on any horizontal layer at the height z
r	Radius
r_{sp}	Radius of spreading
r_z	Radius of the cone at the height z
t	Time
x_i	Position of i -particle
\dot{x}_i	Velocity of i -particle
\ddot{x}_i	Acceleration of i -particle
z	Height, distance from the bottom of the cone

Greek letters

α	Non-dimensional damping constant
$\dot{\gamma}$	Shear strain rate
$\beta_{n,s}$	Critical damping ratio
ε	Strain
η	Dynamic viscosity
μ	Plastic viscosity, coefficient of friction
ρ	Material density
τ	Shear stress
τ, σ	Stress
τ_0, σ_y	Critical stress value, yield stress
ω_i	Angular velocity of i -particle
$\dot{\omega}_1$	Angular acceleration of i -particle

Indexes and prefixes

0	Initial
$1, 2$	Object 1, object 2
$1, 2, 3$	Principal axes
$2D, 3D$	Two dimensional, three dimensional
A, B	Particle A, particle B
$crit$	Critical
e	Elastic
max	Maximum
n	Normal
$perp$	Perpendicular

<i>rot</i>	Rotational
<i>s</i>	Shear
<i>t</i>	Top
<i>b</i>	Bottom
<i>tran</i>	Translational
<i>v</i>	Viscous
<i>y</i>	Yield

Abbreviations

<i>ASTM</i>	American Society for Testing and Materials
<i>CFD</i>	Computational Fluid Dynamic
<i>DEM</i>	Discrete Element Method
<i>DOF</i>	Degree of Freedom
<i>DPD</i>	Dissipative Particle Dynamics
<i>FDL</i>	Force-Displacement Law
<i>FDR</i>	Force-Displacement Relation
<i>FEA</i>	Finite Element Analysis
<i>FEM</i>	Finite Element Method
<i>FEMLIP</i>	Finite Element Method with Lagrangian Integration Point
<i>LCPC</i>	Laboratoire Central des Ponts et Chaussées
<i>MD</i>	Molecular Dynamics
<i>NIST</i>	National Institute of Standards and Technology
<i>OC</i>	Ordinary Concrete
<i>PA</i>	Passing Ratio
<i>PFC</i>	Particle Flow Code
<i>SCC</i>	Self-Compacting Concrete
<i>SCLC</i>	Self-Compacting Light weight Concrete
<i>SP</i>	Superplasticizer
<i>UDM</i>	User-Defined Model
<i>UHPC</i>	Ultra-High Performance Concrete
<i>VDEM</i>	Viscoplastic Divided Element Method
<i>VFEM</i>	Viscoplastic Finite Element Method
<i>VSEM</i>	Viscoplastic Suspension Element Method

Appendix B - Mixing procedures for fresh concretes

The fresh concretes were mixed using ELBA or EIRICH mixers. The OC, SCC and SCLC were mixed in ELBA mixer. UHPC was mixed using EIRICH mixer.

The ordinary concretes were mixed following the procedure given in Table B.1.

Table B.1: *Mixture procedure for OC (ELBA Mixer)*

Action	Duration [s]	Speed of mixing [rpm]
Addition of all solid components: cement, sand and gravel	Not defined	
Homogenization	30	25
Addition of total water	Not defined	25
Homogenization	60	25
Final mixing with high speed	120-180	45

The mixing procedure for the self-compacting concrete is shown in Table B.2.

Table B.2: *Mixture procedure for SCC (ELBA Mixer)*

Action	Duration [s]	Speed of mixing [rpm]
Addition of all solid components: cement, sand, fly-ash and gravel	Not defined	
Homogenization	30	25
Addition of total water	Not defined	25
Homogenization	60	25
Addition of superplasticizer	15	25
Mixing with moderate speed	120	45
Final mixing with high speed	60	25

The mixing procedure for SCLC is presented in Table B.3. Before mixing the expanded clay was moistured with 18.5 M.-% water (relating to the weight of expanded clay) for 30 minutes. The watering attends by mixing for 30 seconds with 5 rpm.

Table B.3: *Mixture procedure for SCLC (ELBA Mixer)*

Action	Duration [s]	Speed of mixing [rpm]
Addition of all solid components: expanded clay, cement, sand, fly-ash and stabilizer	Not defined	5
Homogenization	60	25
Addition of 2/3 of total water	20	5
Addition of 1/3 total water premixed with superplasticizer	Not defined	5
Final mixing with high speed	60	45

The mixing procedure for high-strength concrete mixes UHPC1 and UHPC2 is presented in Tables B.4 and B.5, respectively.

Table B.4: *Mixture procedure for UHPC1 (EIRICH Mixer)*

Action	Duration [s]	Speed of mixing [rpm / m/s]	
		Drum	Agitator
Addition of quartz sand and silica fume	Not defined	3 / 0.1	43 / 0.6
Homogenization	120	18 / 0.5	338 / 5.0
Addition of quartz flour and cement	Not defined	3 / 0.1	43 / 0.6
Homogenization	120	18 / 0.5	338 / 5.0
Addition of total water premixed with 50% of superplasticizer	Not defined	18 / 0.5	338 / 5.0
Homogenization	120	31 / 0.9	338 / 5.0
Pause (mixing with minimal velocity)	120	3 / 0.1	43 / 0.6
Addition of rest of superplasticizer (50%)	Not defined	3 / 0.1	43 / 0.6
Mixing with moderate speed	10	31 / 0.9	104 / 1.5
Mixing with high speed	150	31 / 0.9	433 / 6.4
Final mixing with high speed	60	31 / 0.9	87 / 1.3

Table B.5: *Mixture procedure for UHPC2 (EIRICH Mixer)*

Action	Duration [s]	Speed of mixing [rpm / m/s]	
		Drum	Agitator
Addition of basalt split, quartz sand and silica fume	Not defined	3 / 0.1	43 / 0.6
Homogenization	60	18 / 0.5	338 / 5.0
Addition of quartz flour and cement	Not defined	3 / 0.1	43 / 0.6
Homogenization	60	18 / 0.5	338 / 5.0
Addition of total water premixed with 50% of superplasticizer	Not defined	18 / 0.5	338 / 5.0
Homogenization	120	31 / 0.9	338 / 5.0
Pause (mixing with minimal velocity)	120	3 / 0.1	43 / 0.6
Addition of rest of superplasticizer (50%)	Not defined	3 / 0.1	43 / 0.6
Mixing with moderate speed	40	31 / 0.9	104 / 1.5
Mixing with high speed	50	31 / 0.9	433 / 6.4
Final mixing with high speed	60	31 / 0.9	87 / 1.3

Appendix C – Results of the slump flow test

Self-compacting concretes (SCC)

The density of the fresh SCC is 2.361 kg/dm³.

The photo of the slump “cake” and experimental spreading vs. time curves for SCC are presented in Figure C.1. The test was performed with inverted cone and dry table.

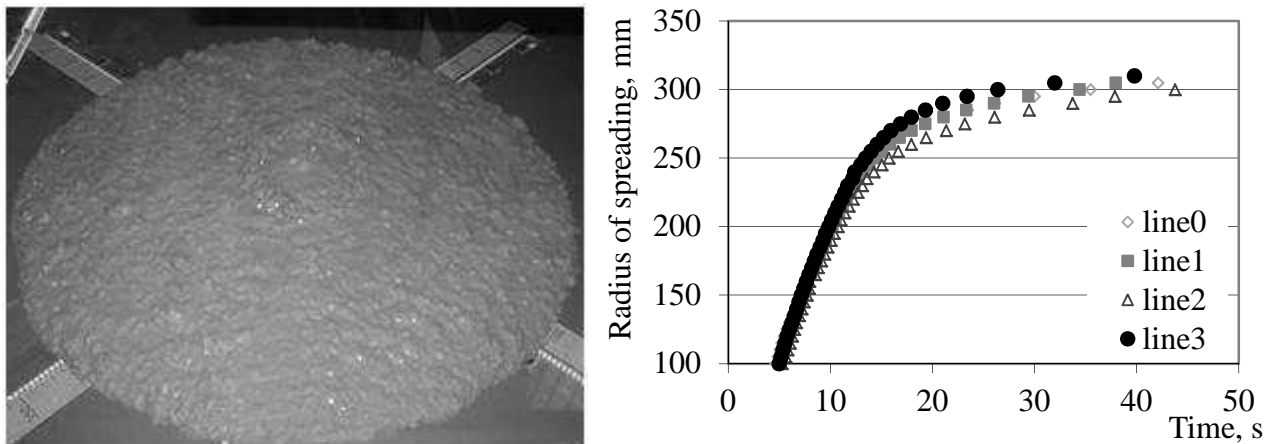


Figure C.1: The results of slump flow test (inverted cone orientation) with SCC on a dry table

The final slump flow value recorded by software is 615 mm. The time T_{50} is 16 s. On the top surface of the slump “cake” the impression of the bottom surface of the cone can be observed.

The slump “cake” and experimental spreading vs. time curves for SCC with wet table are presented in Figure C.2. The test was performed with inverted orientation of the slump cone.

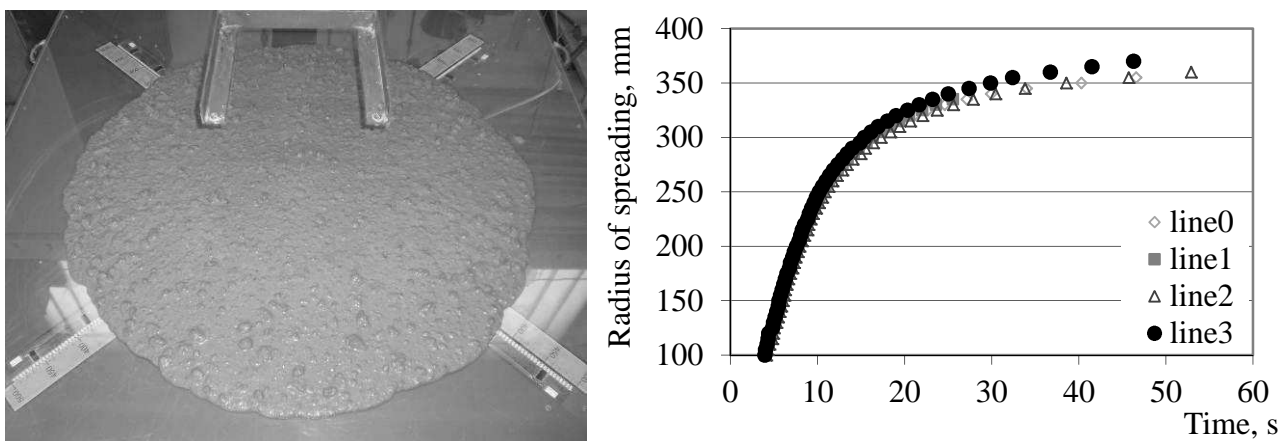


Figure C.2: The results of slump flow test (inverted cone orientation) with SCC on a wet table

The final spreading is 720 mm, time T_{50} 10.5 s.

Ultra-high performance concrete (UHPC1)

The density of the fresh UHPC1 is 2.353 kg/dm³.

The photo of the slump “cake” and experimental spreading vs. time curves for UHPC1 are presented in Figure C.3. The test was performed with inverted cone and dry table.

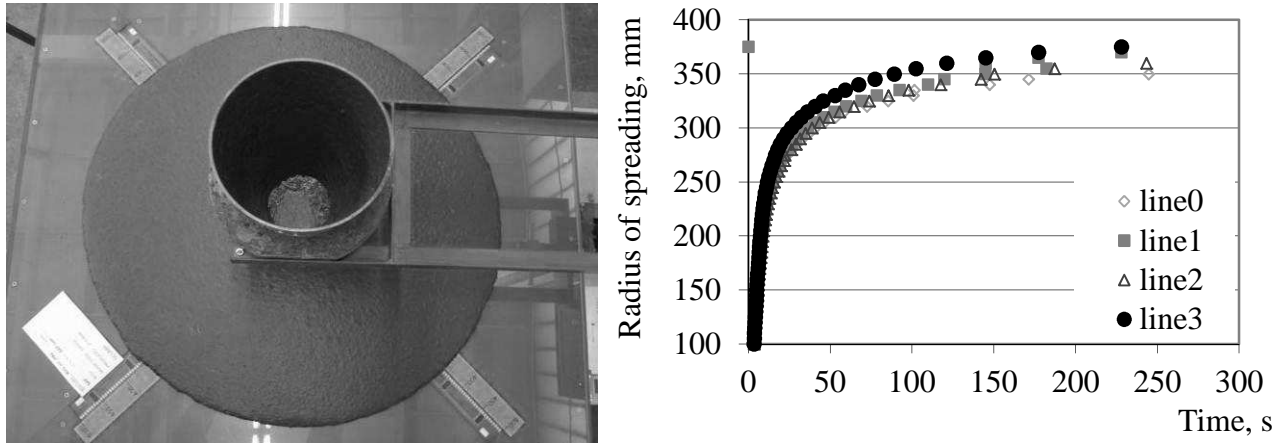


Figure C.3: The results of slump flow test with UHPC1 (inverted cone orientation) on a dry table

The final slump flow value recorded by software is 715 mm. The time T_{50} is 15 s.

On the wet table the same concrete has the following slump flow and the time-spreading diagram, see Figure C.4.

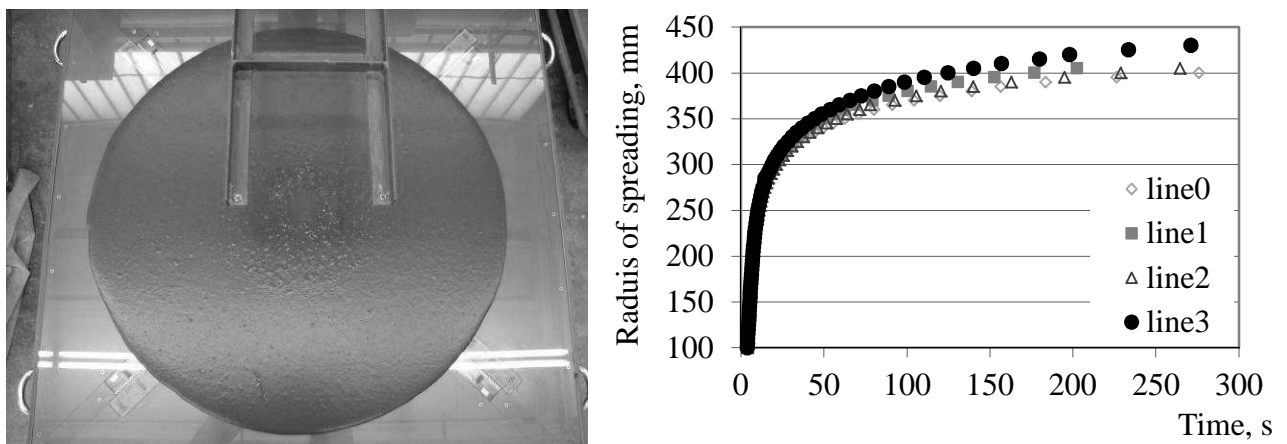


Figure C.4: The results of slump flow test with UHPC1 (inverted cone orientation) on a wet table

The slump flow is 805 mm; the time T_{50} is 10.5 s.

Ultra-high performance concrete (UHPC2)

The density of the fresh UHPC2 is 2.495 kg/dm³.

The photo of the slump “cake” and experimental spreading vs. time curves for UHPC2 are presented in Figure C.5. The test was performed with inverted cone and dry table.

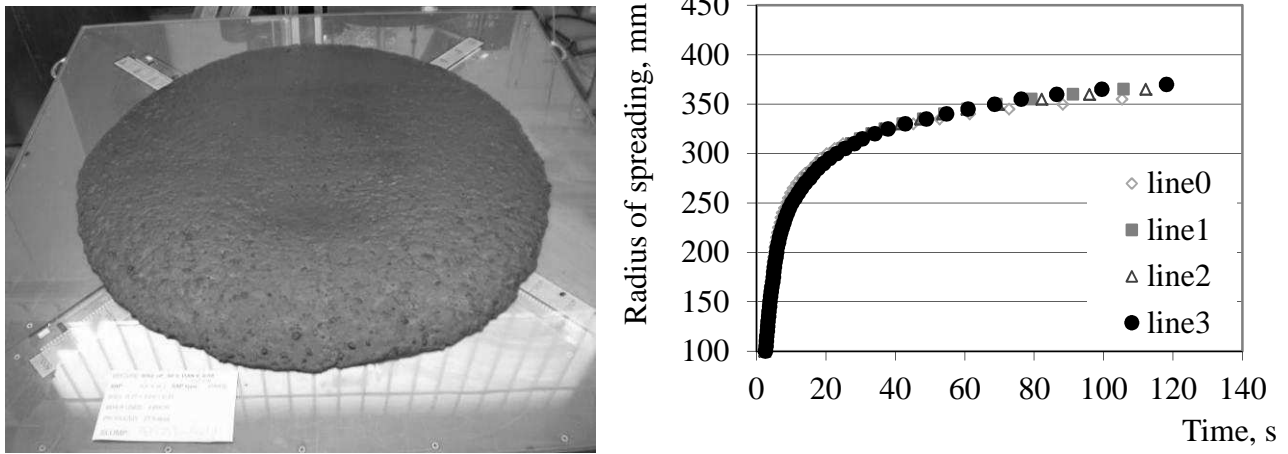


Figure C.5: The results of slump flow test with UHPC2 (inverted cone orientation) on a dry table

The slump flow is 722 mm, the time T_{50} is 11 s.

The final slump flow and the experimental spreading vs. time curves from the computer controlled slump flow table are presented in Figure C.6. The surface of the slump flow table is wet; the orientation of the slump cone is inverted.

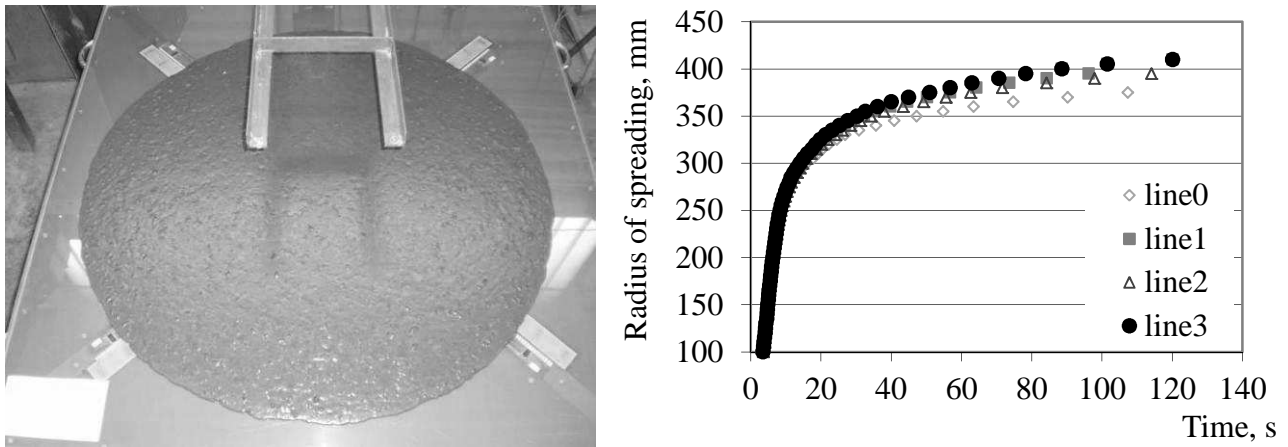


Figure C.6: The results of slump flow test with UHPC2 (inverted cone orientation) on a wet table

The final slump flow value is 790 mm. The time T_{50} is 9 s.

Self-compacting light-weight concrete (SCLC)

The density of the fresh light concrete is 1.758 kg/dm^3 .

The photo of the slump “cake” and experimental spreading vs. time curves for SCLC are presented in Figure C.7. The test was performed with inverted cone and dry table.

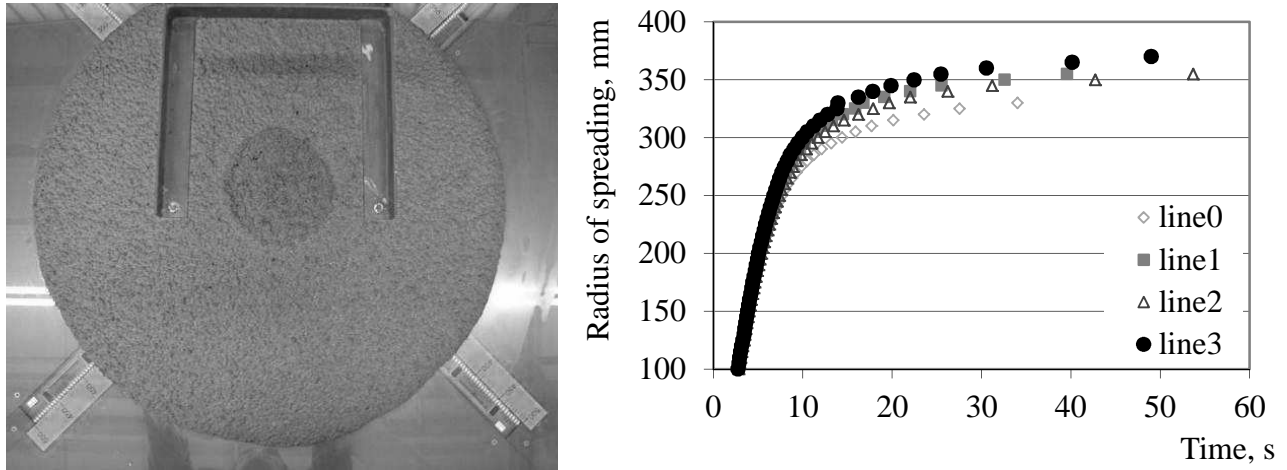


Figure C.7: The results of slump flow test with SCLC (inverted cone orientation) on a dry table

The final slump flow value is 690 mm. The time T_{50} is 7.5 s.

The final slump flow and the experimental spreading vs. time curves are presented in Figure C.8. The test was performed with inverted cone and wet table.

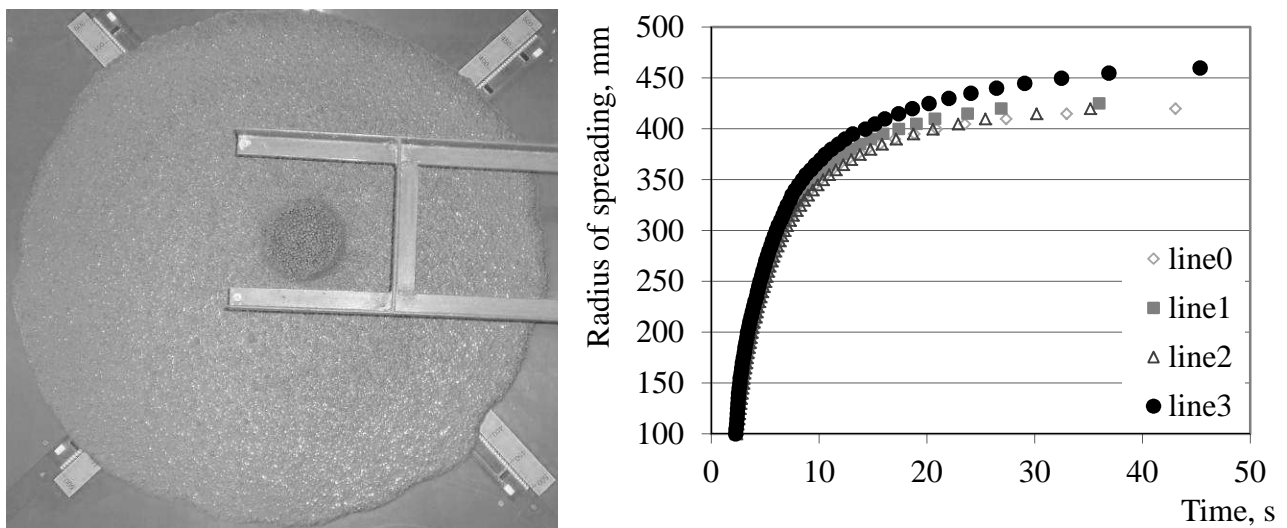


Figure C.8: The results of slump flow test with SCLC (inverted cone orientation) on wet table

The final slump flow is 870 mm; the time T_{50} is 5 s.

Appendix D - Results of meso-level tests on Carbopol polymer 0.3 M%

Appendix D presents the results of the experiments with a water solution containing 0.3 M% of Carbopol. Figure D.1 shows the results of the experiments for a “ball – wall” contact with 100% covering of the equipped ball.

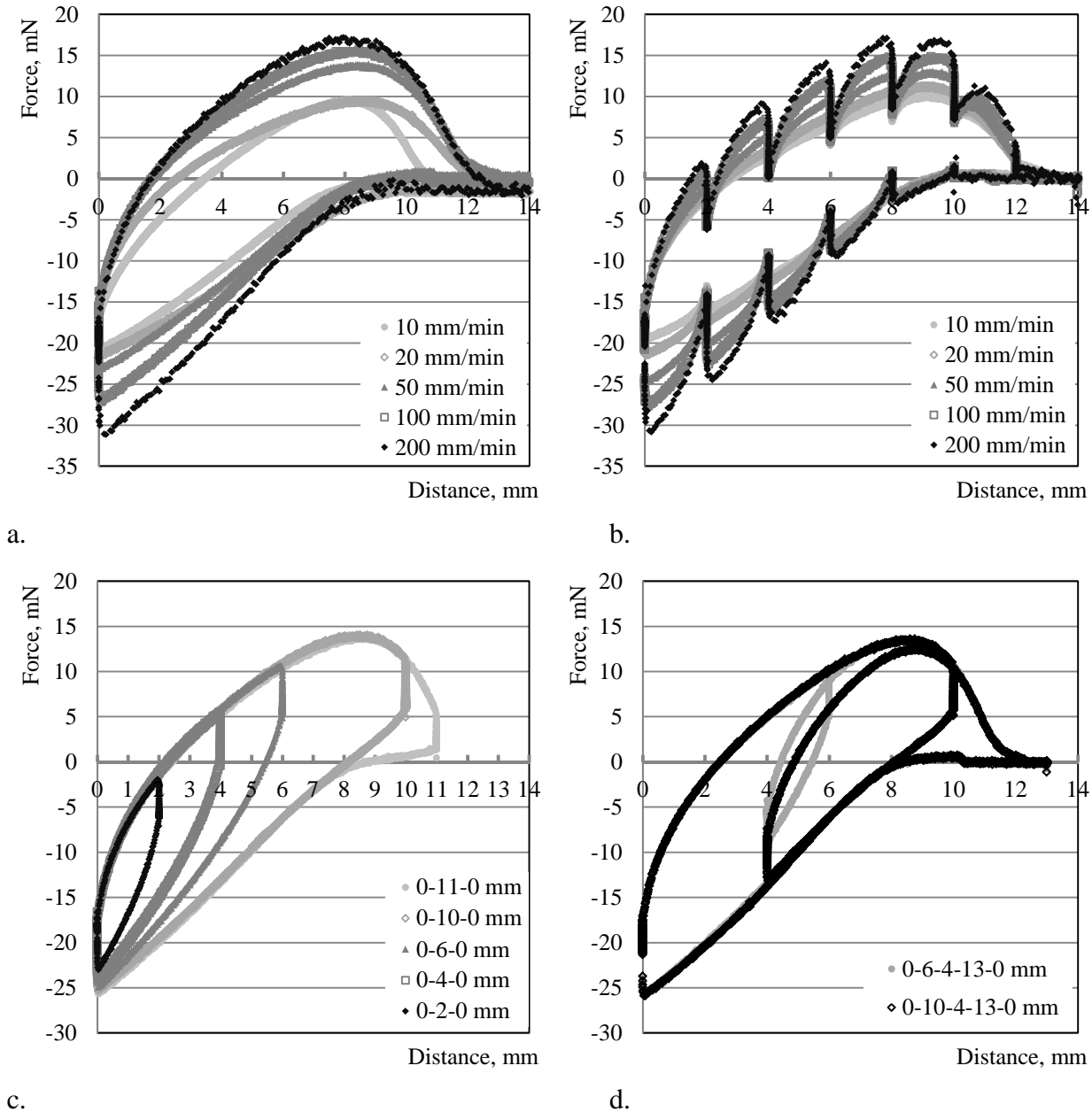


Figure D.1: Force-displacement diagrams for “ball-wall” contact: a) motion with various velocities; b) motion with various velocities and with stops; c) motion with one change in the direction of motion (velocity is 50 mm/min); d) motion with several changes in the direction of motion (velocity is 50 mm/min)

Figure D.2 presents the results of the experiments for a “ball – wall” contact with 50% covering of the equipped ball.

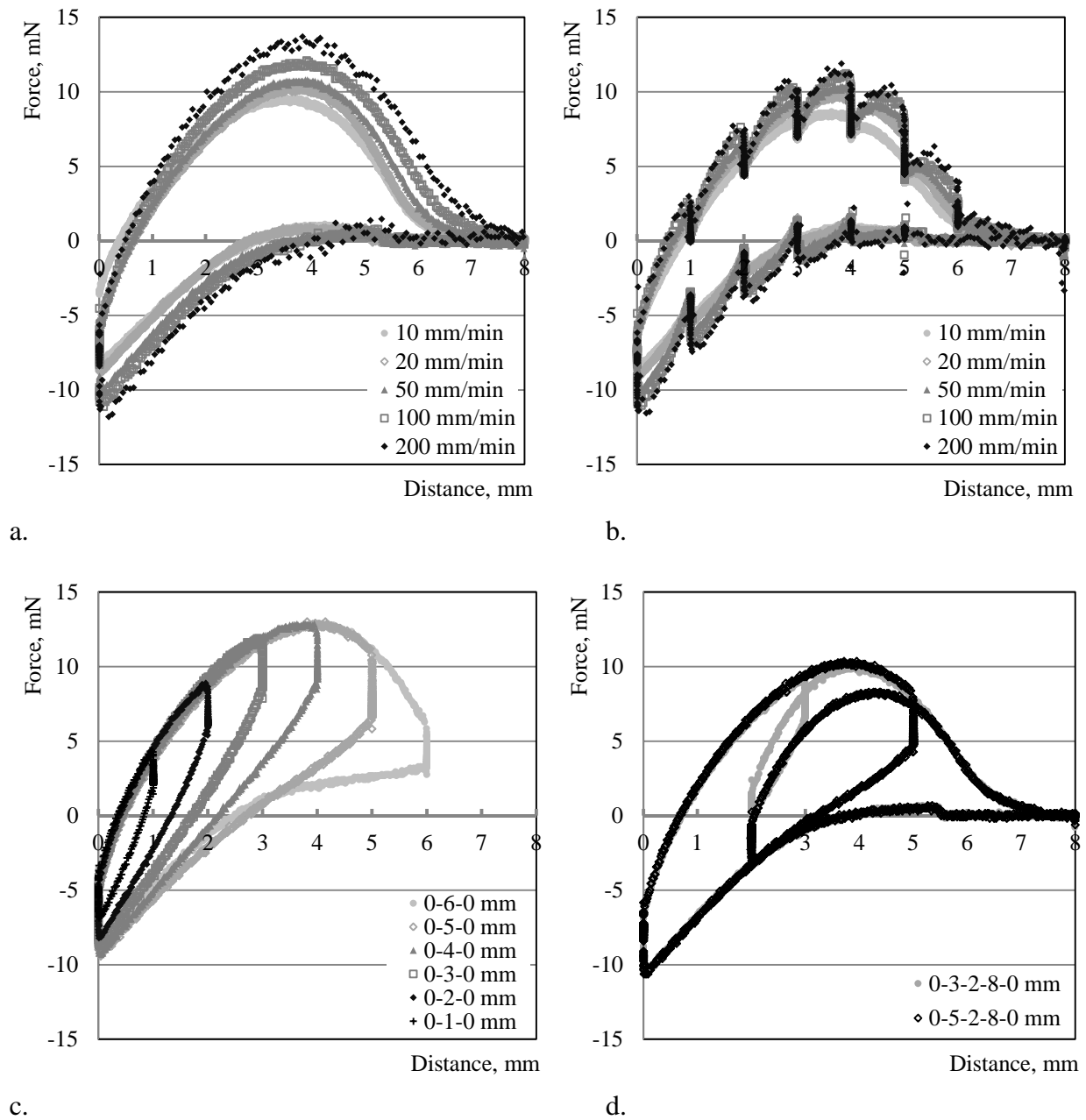
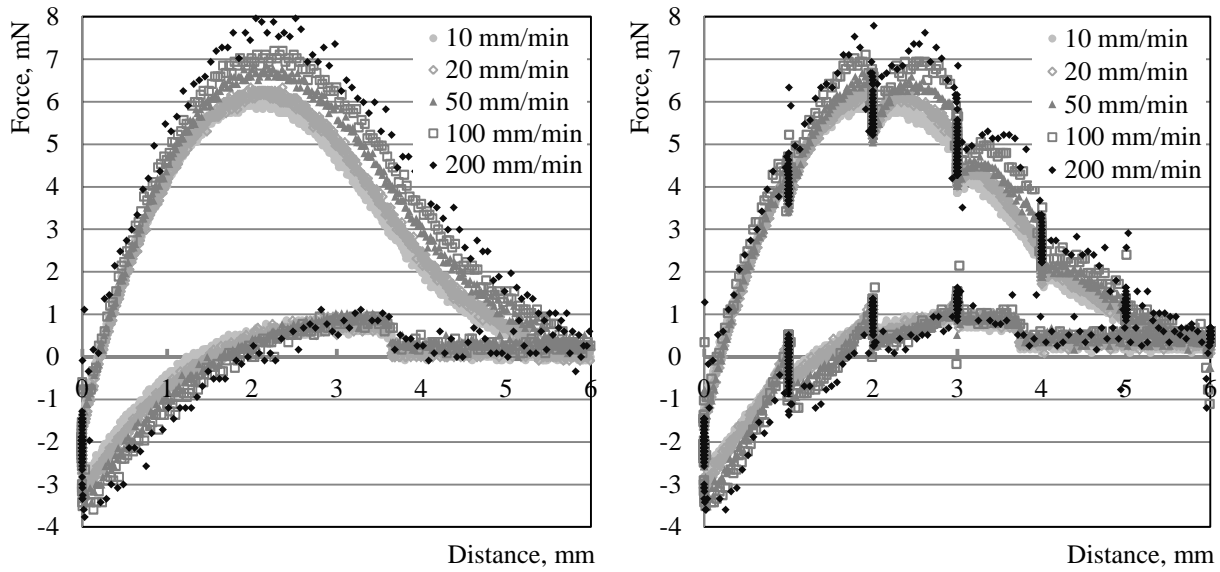


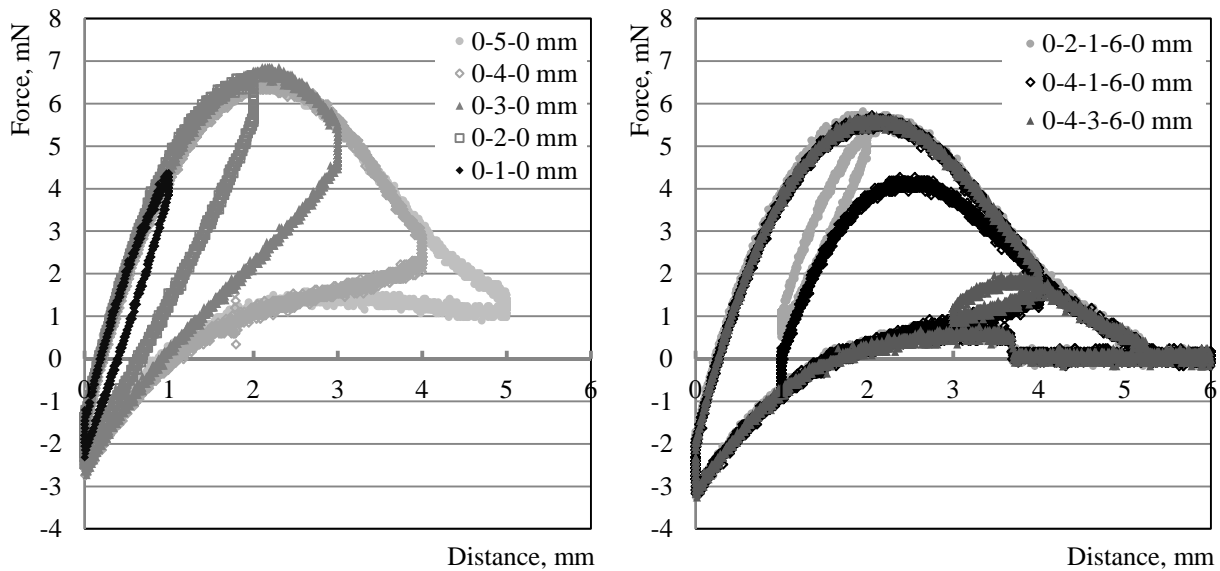
Figure D.2: Force-displacement diagrams for “ball-wall” contact: a) motion with various velocities; b) motion with various velocities and with stops; c) motion with one change in the direction of motion (velocity is 50 mm/min); d) motion with several changes in the direction of motion (velocity is 50 mm/min)

Figure D.3 presents the results of the experiments for a “ball – wall” contact with 25% covering of the equipped ball.



a.

b.



c.

d.

Figure D.3: Force-displacement diagrams for “ball-wall” contact: a) motion with various velocities; b) motion with various velocities and with stops; c) motion with one change in the direction of motion (velocity is 10 mm/min); d) motion with several changes in the direction of motion (velocity is 10 mm/min)

The results of the experiments for the contact “ball-ball” with a transparent ball (10 mm in diameter) are presented in Figure D.4. Covering of the equipped ball is 50%.

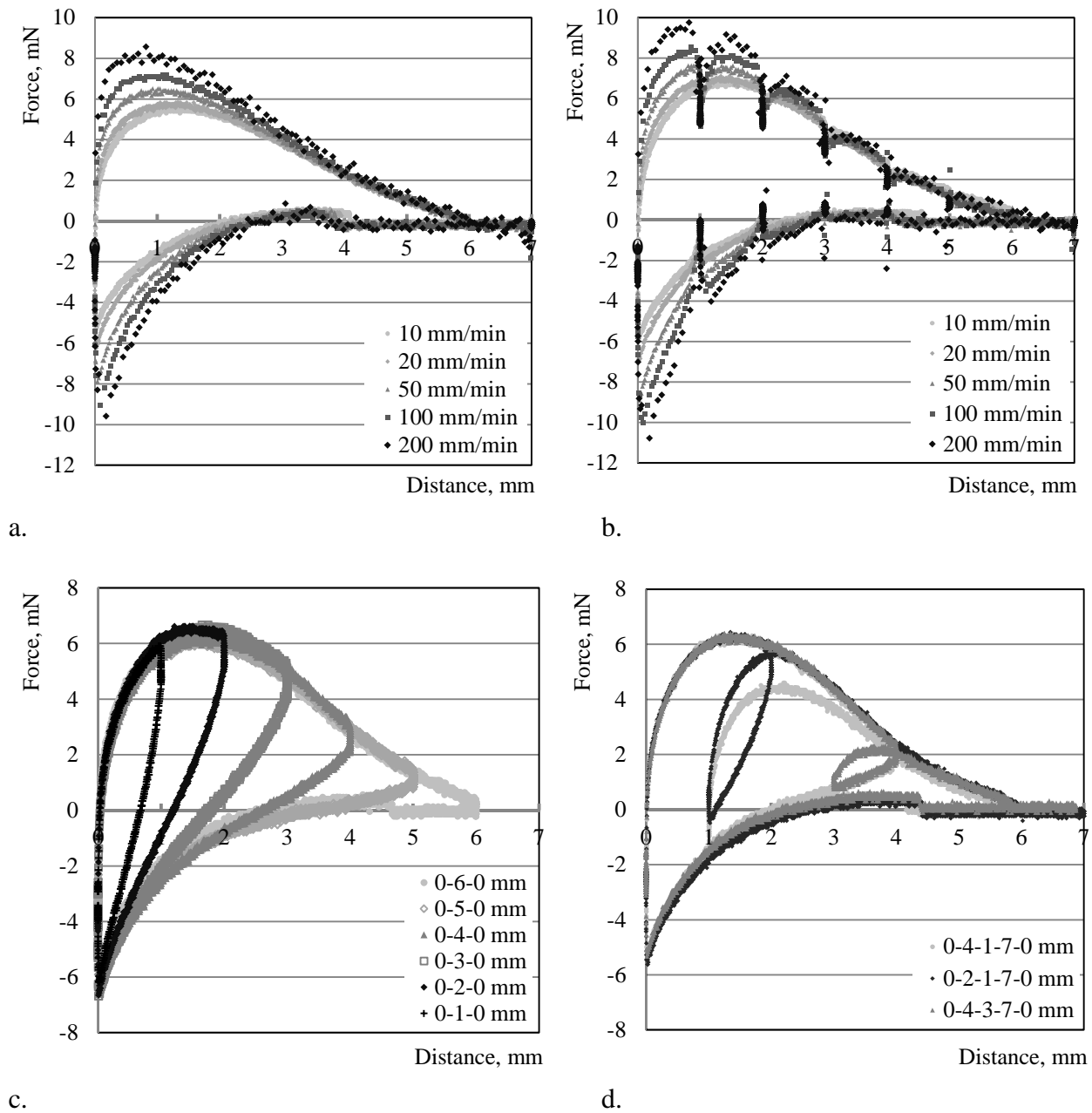
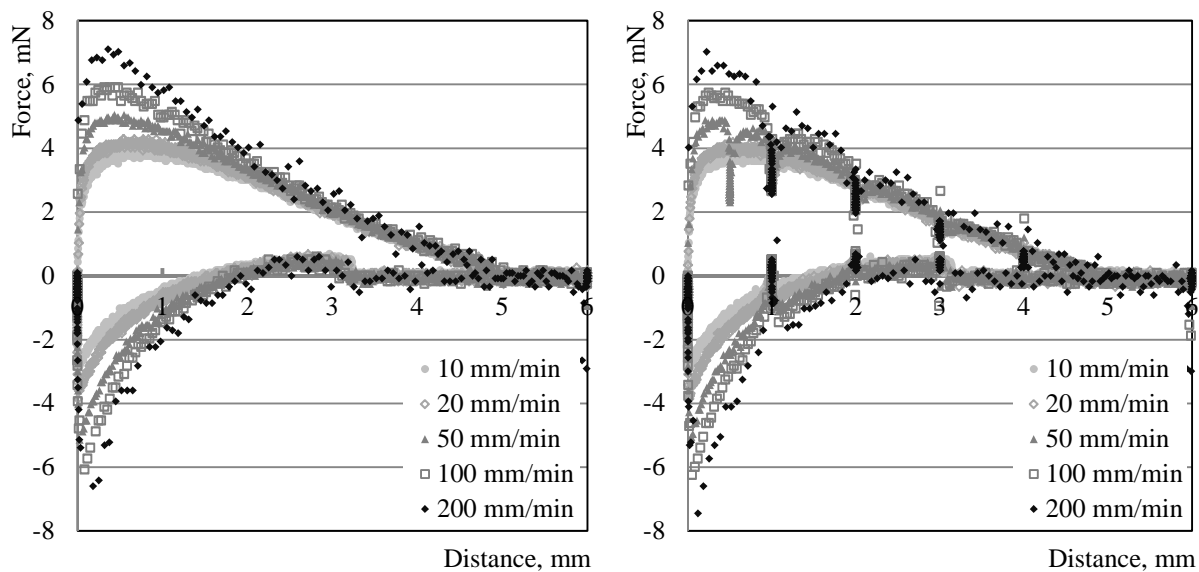


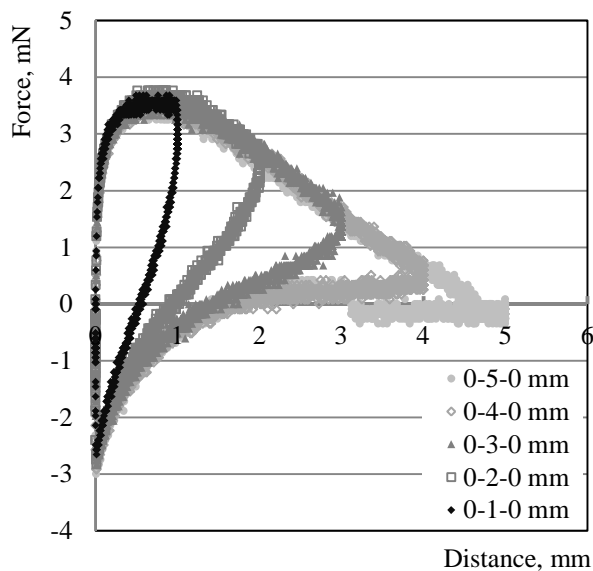
Figure D.4: Force-displacement diagrams for “ball-ball” contact (transparent ball: 10 mm in diameter): a) motion with various velocities; b) motion with various velocities and with stops; c) motion with one change in the direction of motion (velocity is 50 mm/min); d) motion with several changes in the direction of motion (velocity is 50 mm/min)

Figure D.5 presents the results of the experiments for “ball-ball contact” with a transparent ball (10 mm in diameter) and 25% covering.

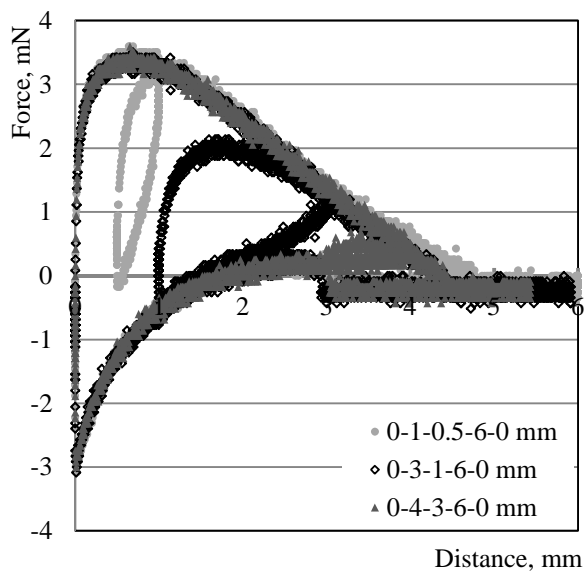


a.

b.



c.



d.

Figure D.5: Force-displacement diagrams for “ball-ball” contact (transparent ball: 10 mm in diameter): a) motion with various velocities; b) motion with various velocities and with stops; c) motion with one change in the direction of motion (velocity is 10 mm/min); d) motion with several changes in the direction of motion (velocity is 10 mm/min)

The results of the experiments with “ball-ball” contact with a green ball (8 mm in diameter) are presented in Figure D.6.

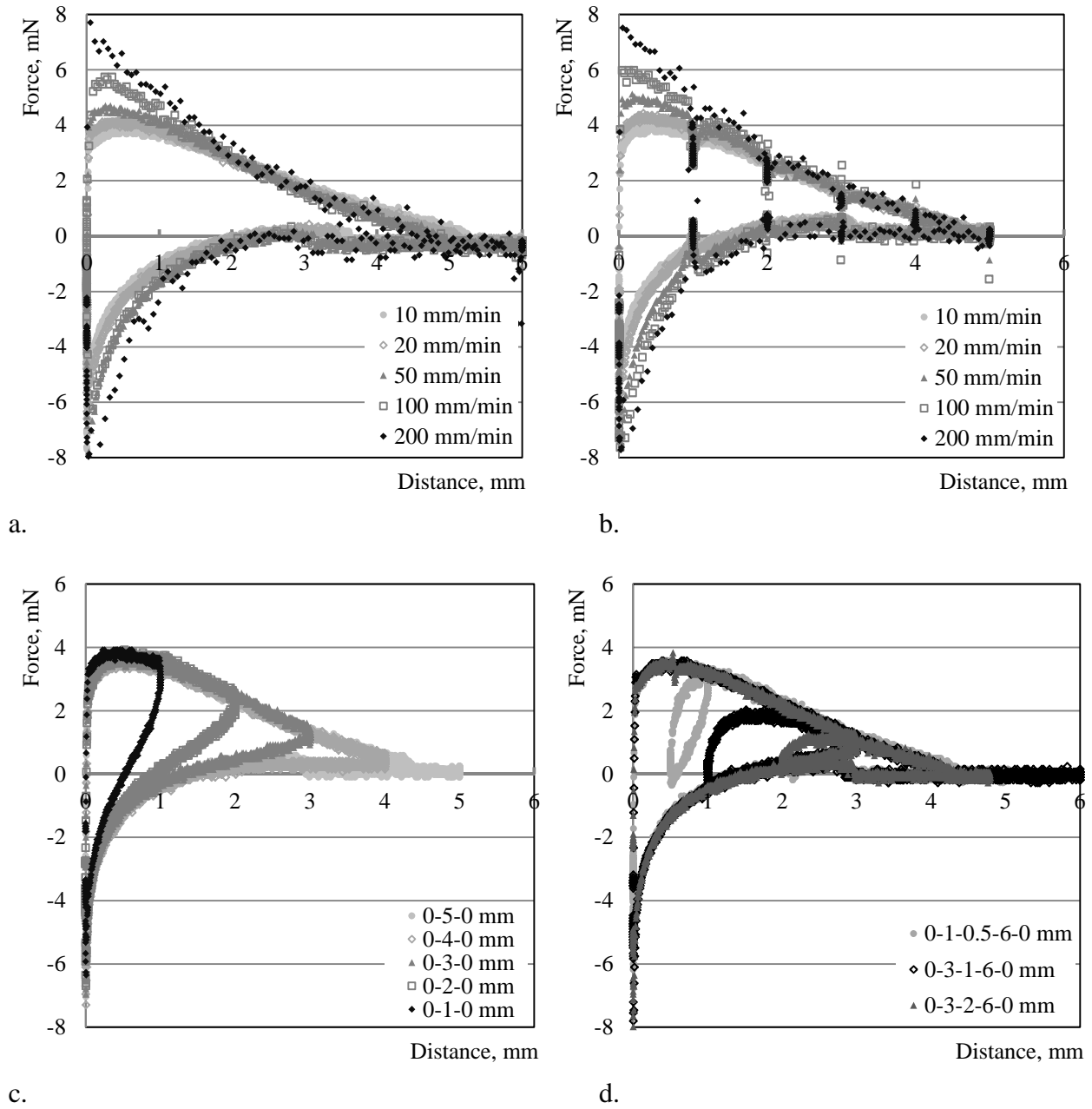
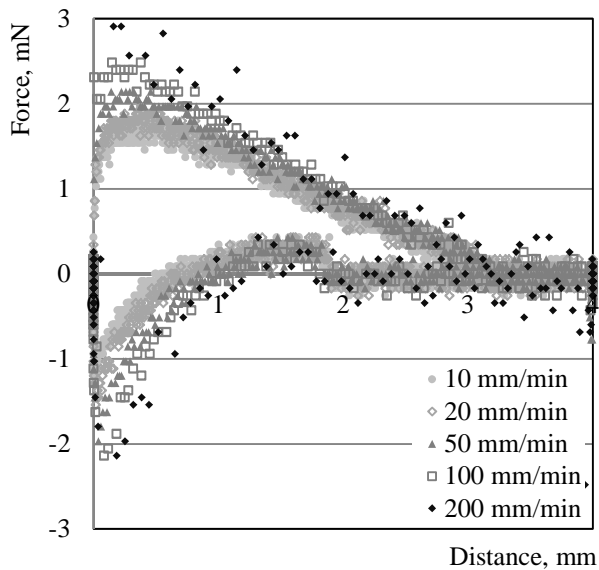
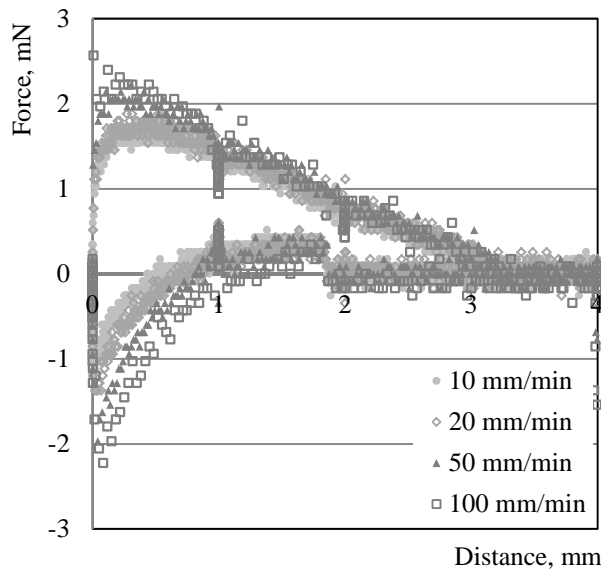


Figure D.6: Force-displacement diagrams for “ball-ball” contact (green ball: 8 mm in diameter): a) motion with various velocities; b) motion with various velocities and with stops; c) motion with one change in the direction of motion (velocity is 10 mm/min); d) motion with several changes in the direction of motion (velocity is 10 mm/min)

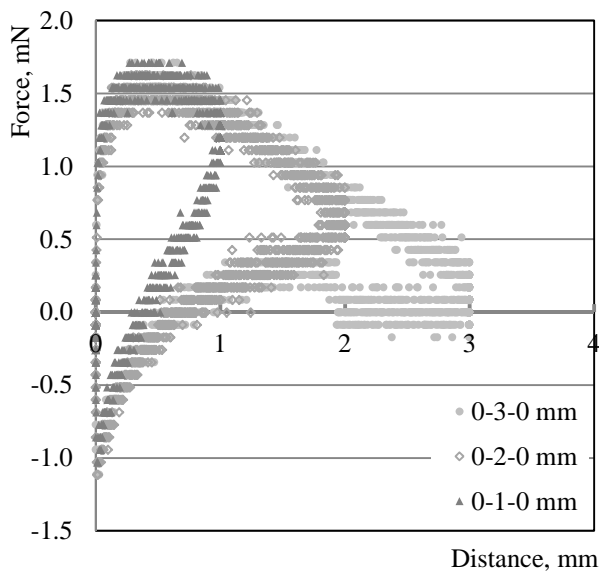
The results of the experiments with “ball-ball” contact with a red ball (4 mm in diameter) are presented in Figure D.7.



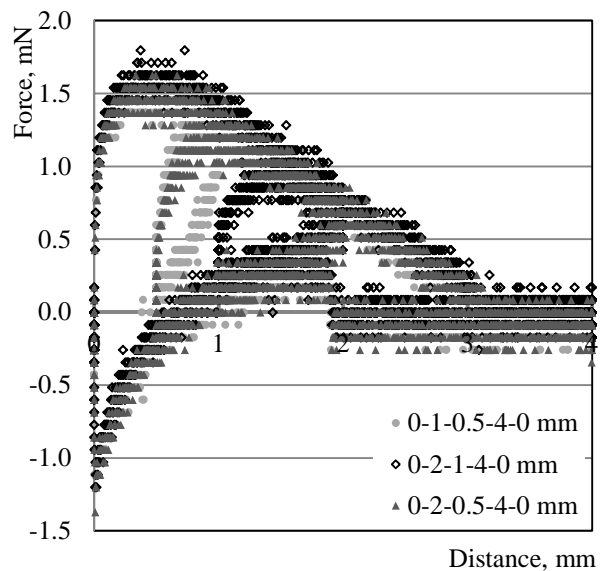
a.



b.



c.



d.

Figure D.7: Force-displacement diagrams for “ball-ball” contact (red ball: 4 mm in diameter):
 a) motion with various velocities; b) motion with various velocities and with stops;
 c) motion with one change in the direction of motion (velocity is 10 mm/min);
 d) motion with several changes in the direction of motion (velocity is 10 mm/min)

The results of the experiments with “ball-ball” contact with a white ball (2 mm in diameter) are presented in Figure D.8.

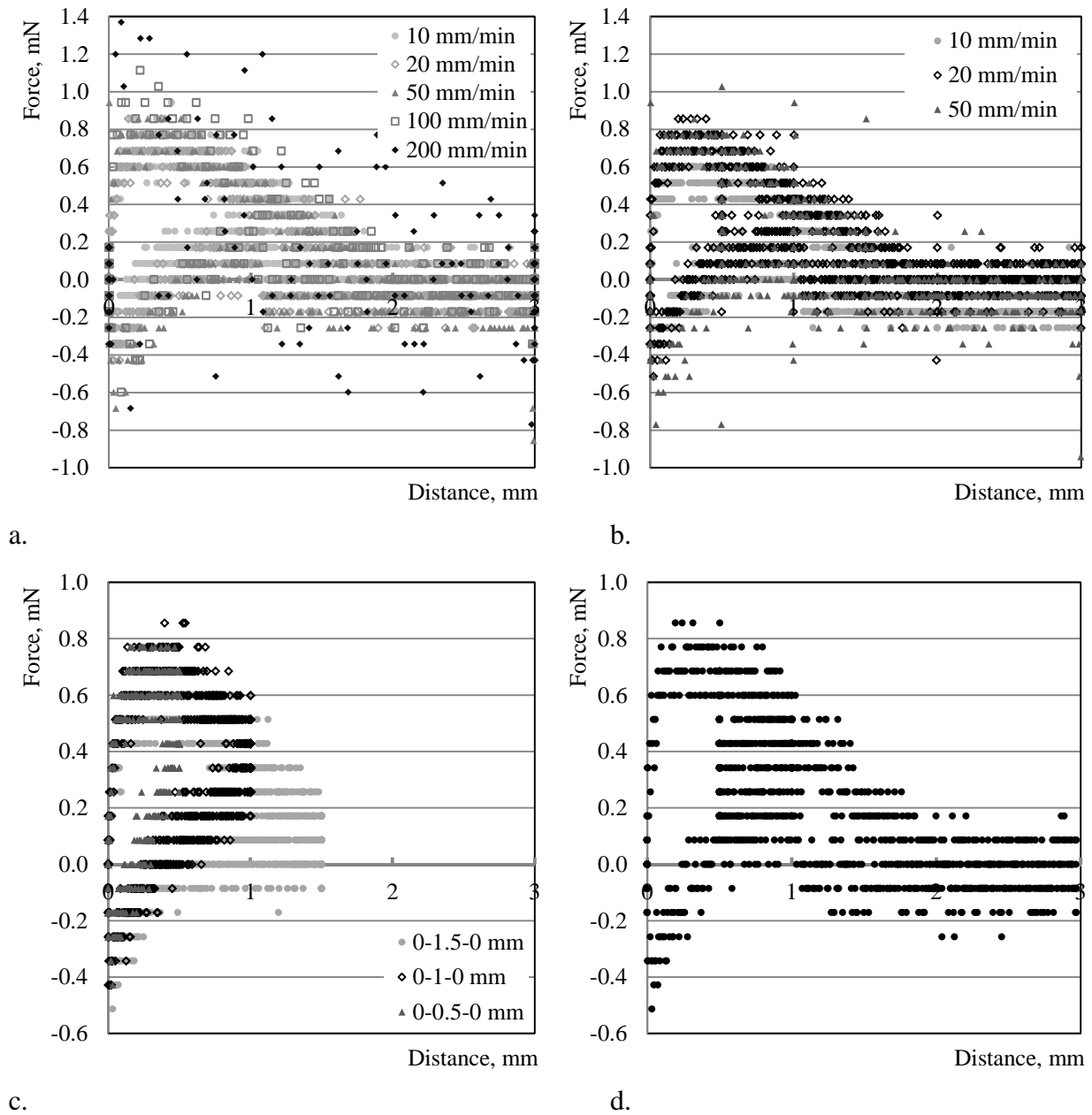


Figure D.8: Force-displacement diagrams for “ball-ball” contact (white ball: 2 mm in diameter):
 a) motion with various velocities; b) motion with various velocities and with stops;
 c) motion with one change in the direction of motion (velocity is 10 mm/min);
 d) motion with several changes in the direction of motion (velocity is 10 mm/min)

In contrast to the previous experiments with bigger balls where the velocity of the movement was 50 mm/min the velocity of the ball movement in these experiments is 10 mm/min. The reduction of the equipped ball velocity is needed in order to reduce the spread of the measured values.

D - Carbopol polymer solution 0.3 M%

The results of the experiments for the contact ball-several balls (with 3 transparent balls) are presented in Figure D.9. The balls are located in the apexes of the triangle.

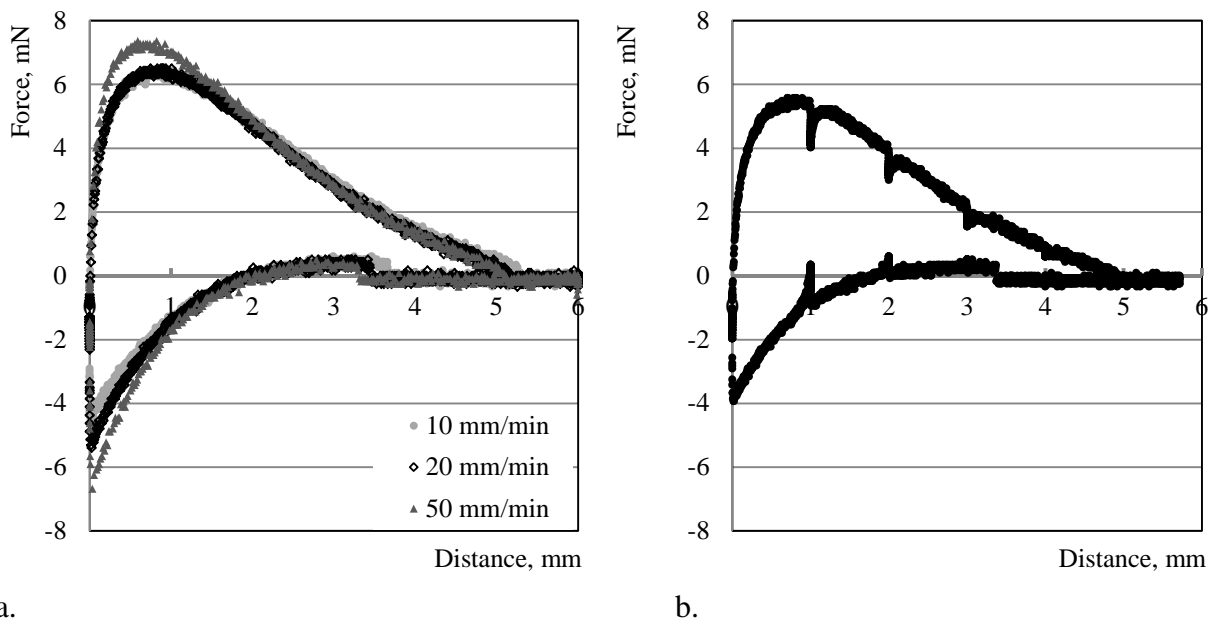


Figure D.9: Force-displacement diagrams for “ball – several balls” contact (3 transparent balls: 10 mm in diameter): a) motion with various velocities; b) motion with stops (velocity is 10 mm/min)

The results of the similar experiments but with 4 balls which located in the apexes of the square are presented in Figure D.10.

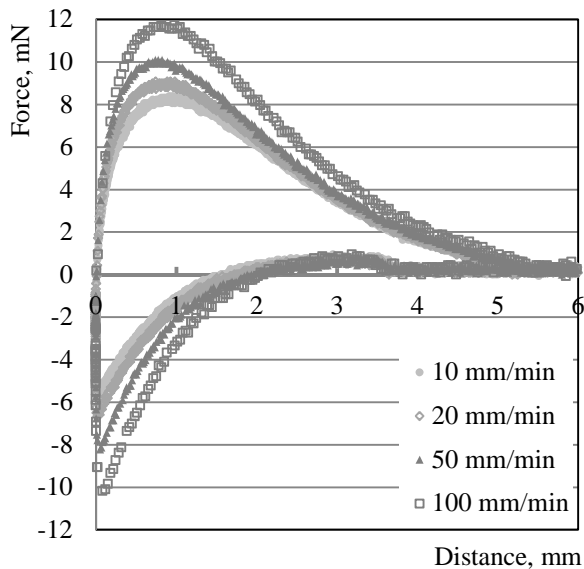


Figure D.10: Force-displacement diagrams for “ball – several balls” contact (4 transparent balls: 10 mm in diameter): motion with various velocities

The results of the experiments with 7 balls located around of the equipped ball are presented in Figure D.11.

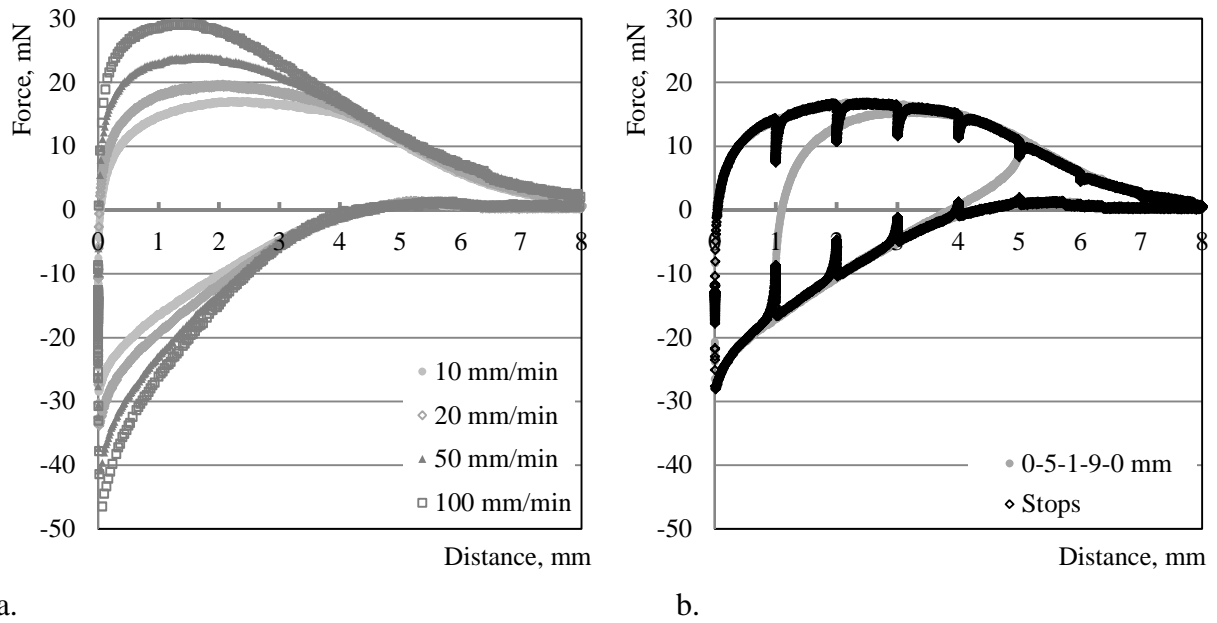


Figure D.11: Force-displacement diagrams for “ball – several balls” contact (7 green balls: 8 mm in diameter): a) motion with various velocities; b) motion with stops and motion with several changes in the direction of motion (velocity is 10 mm/min)

Appendix E - Results of meso-level tests on Carbopol polymer 0.5 M%

Appendix E presents the results of the experiments with a water solution containing 0.5 M% of Carbopol. Figure E.1 presents the results of the experiments for a “ball – wall” contact with 100% covering of the equipped ball.

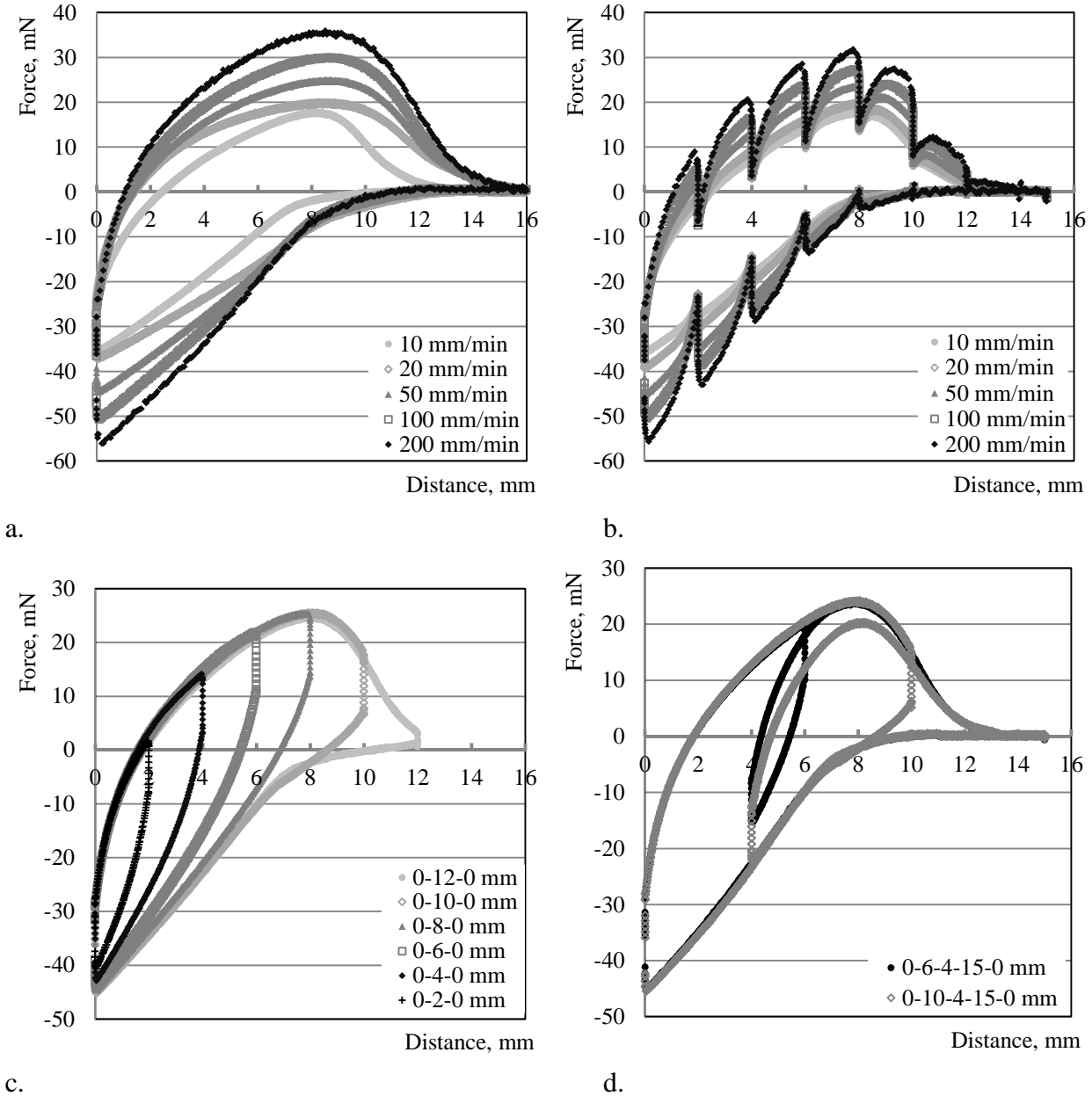


Figure E.1: Force-displacement diagrams for “ball-wall” contact: a) motion with various velocities; b) motion with various velocities and with stops; c) motion with one change in the direction of motion (velocity is 50 mm/min); d) motion with several changes in the direction of motion (velocity is 50 mm/min)

Figure E.2 presents the results of the experiments for a “ball – wall” contact with 50% covering of the equipped ball.

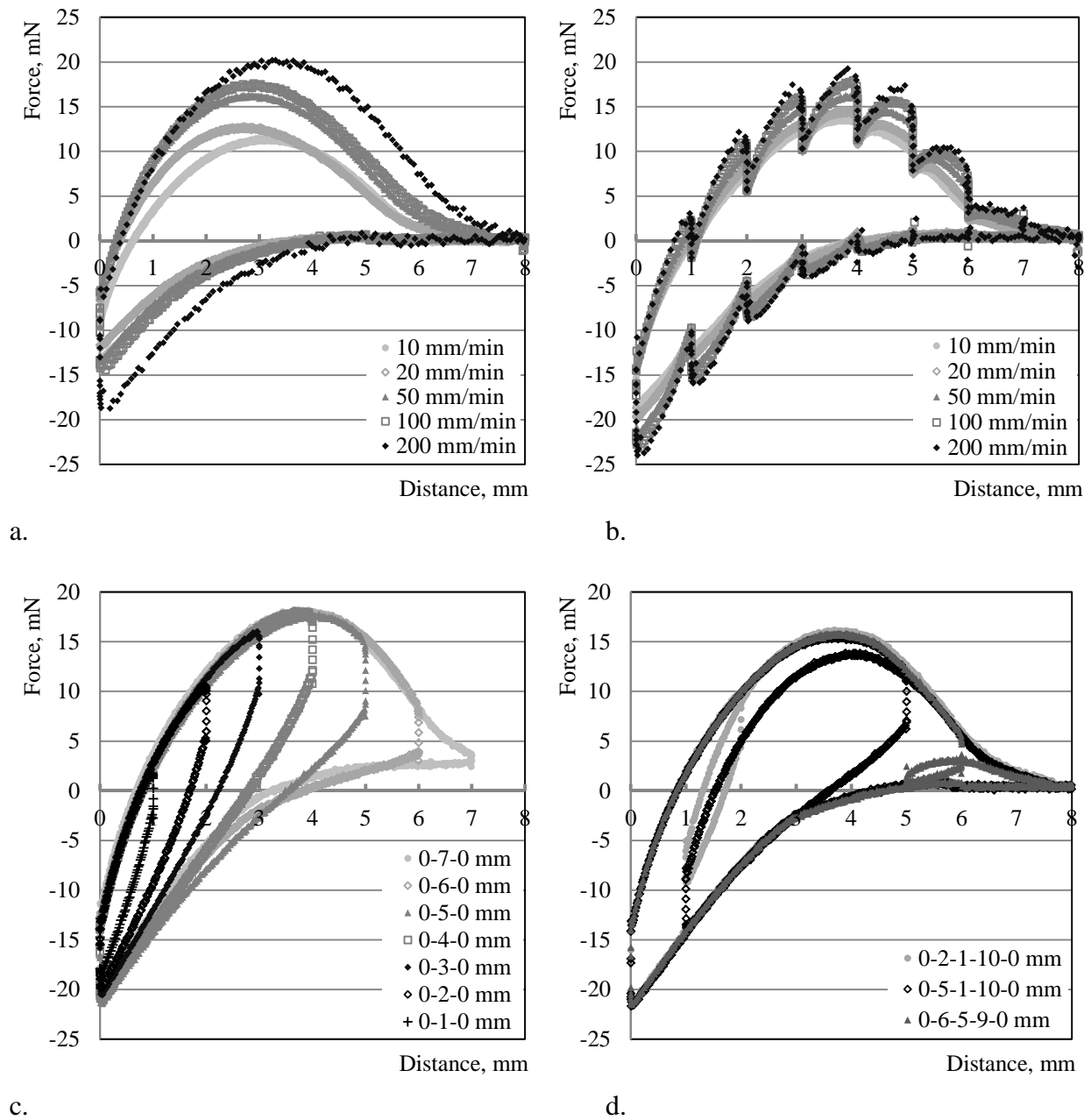


Figure E.2: Force-displacement diagrams for “ball-wall” contact: a) motion with various velocities; b) motion with various velocities and with stops; c) motion with one change in the direction of motion (velocity is 50 mm/min); d) motion with several changes in the direction of motion (velocity is 50 mm/min)

Figure E.3 presents the results of the experiments for a “ball – wall” contact with 25% covering of the equipped ball.

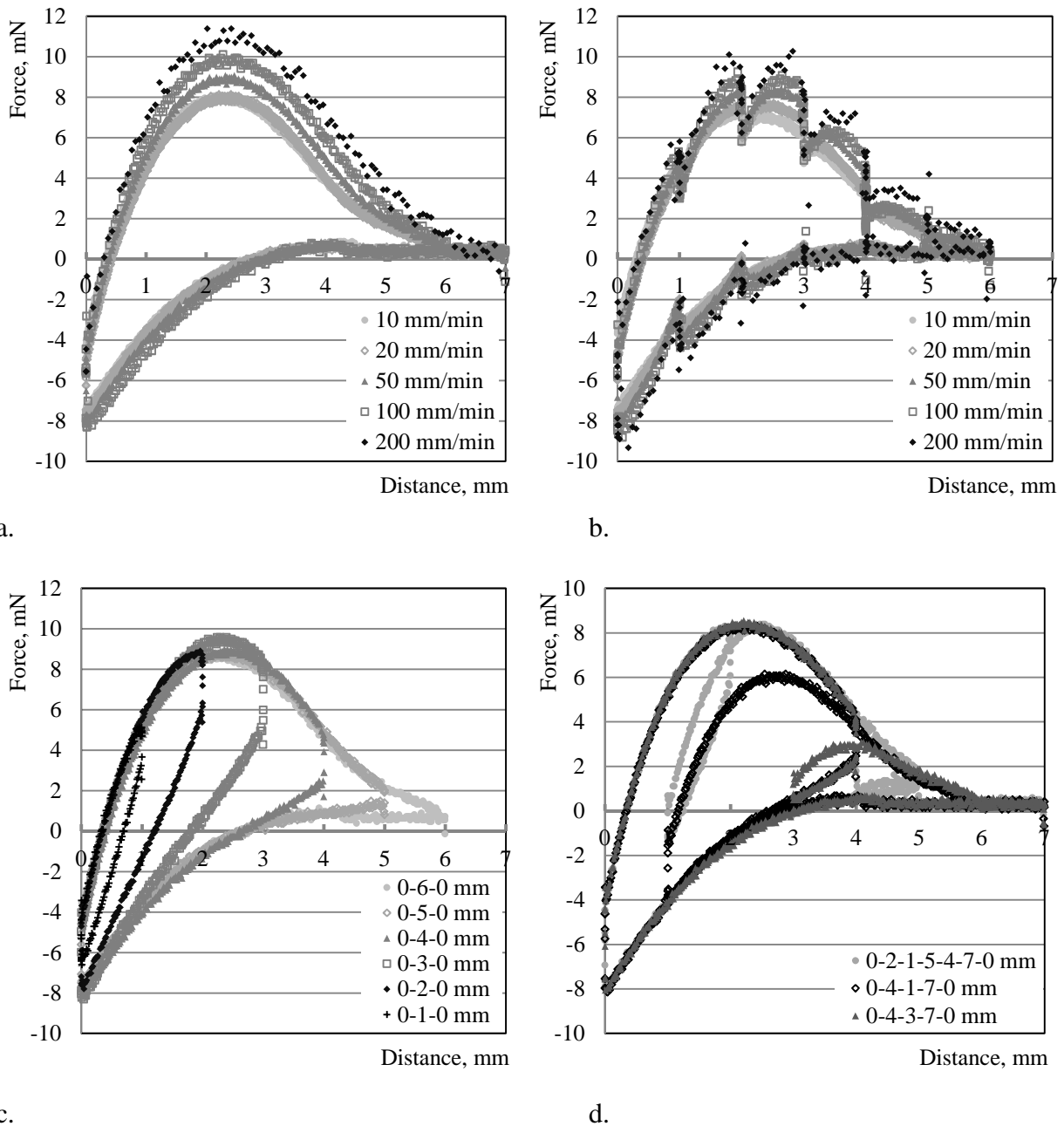


Figure E.3: Force-displacement diagrams for “ball-wall” contact: a) motion with various velocities; b) motion with various velocities and with stops; c) motion with one change in the direction of motion (velocity is 50 mm/min); d) motion with several changes in the direction of motion (velocity is 50 mm/min)

The results of the experiments for the contact “ball-ball” with a transparent ball are presented in Figure E.4. Covering of the equipped ball is 50%.

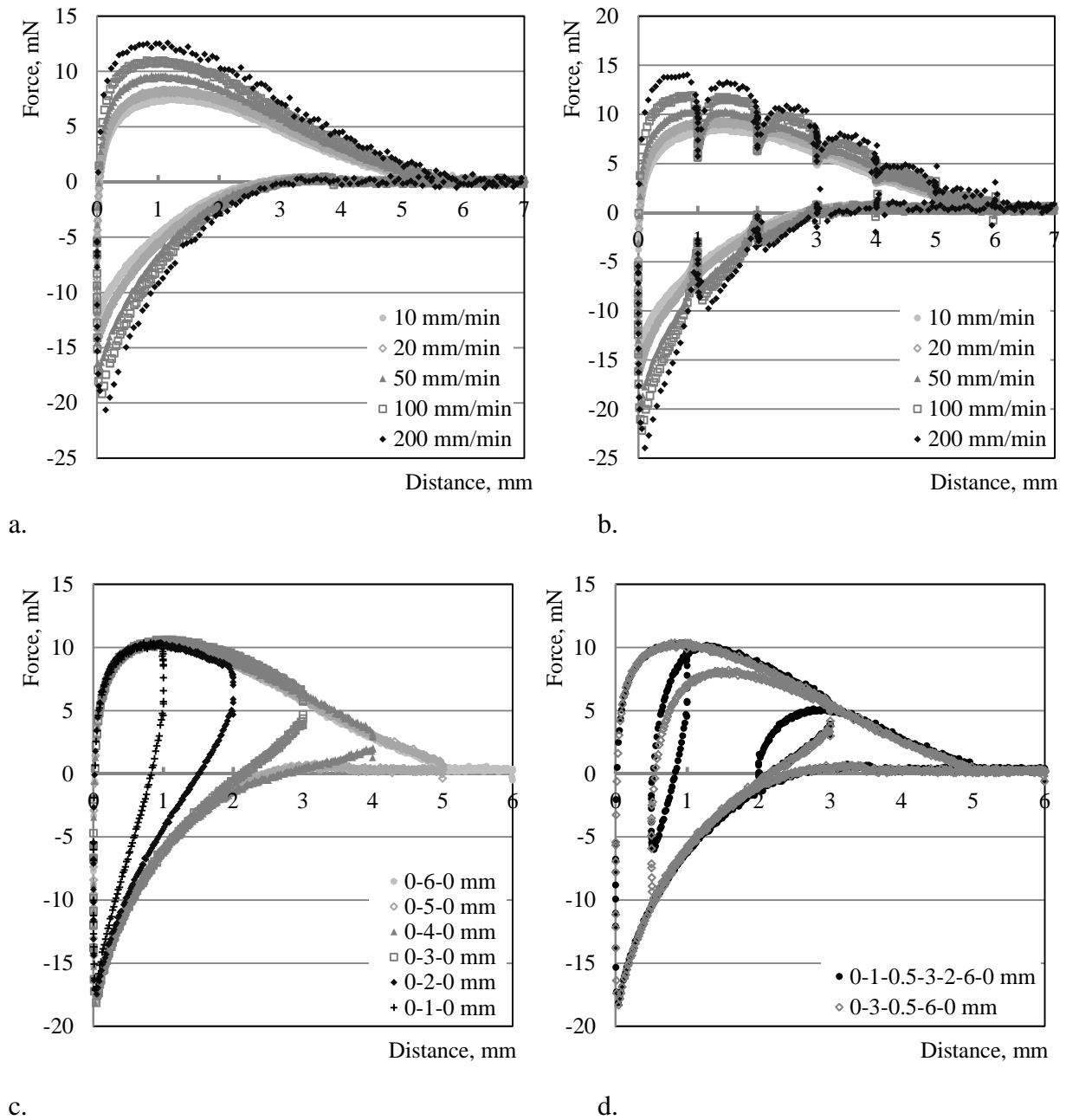
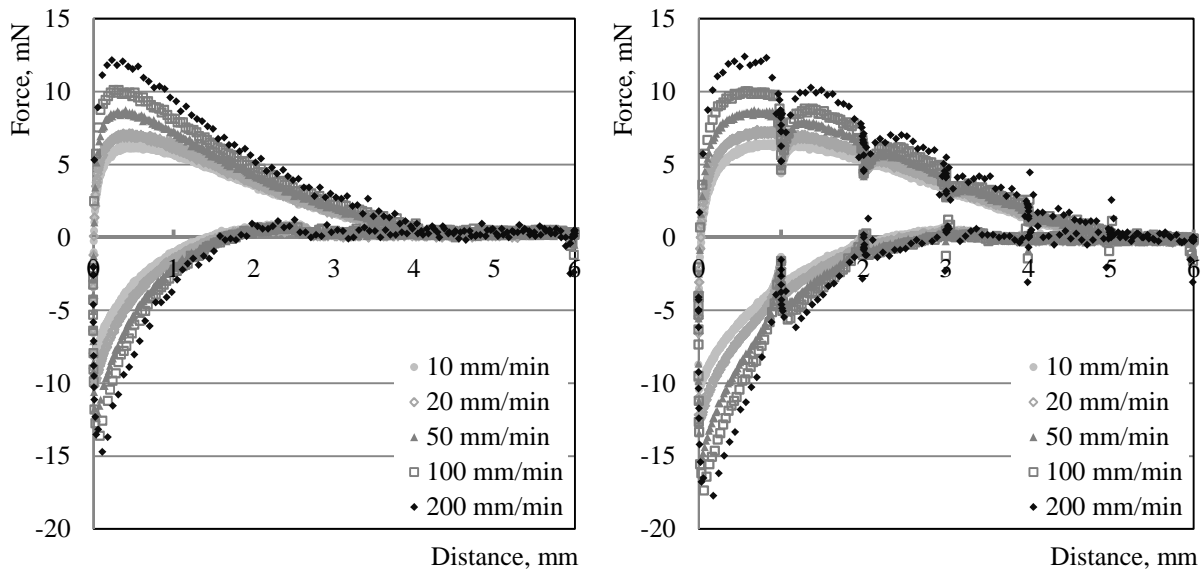


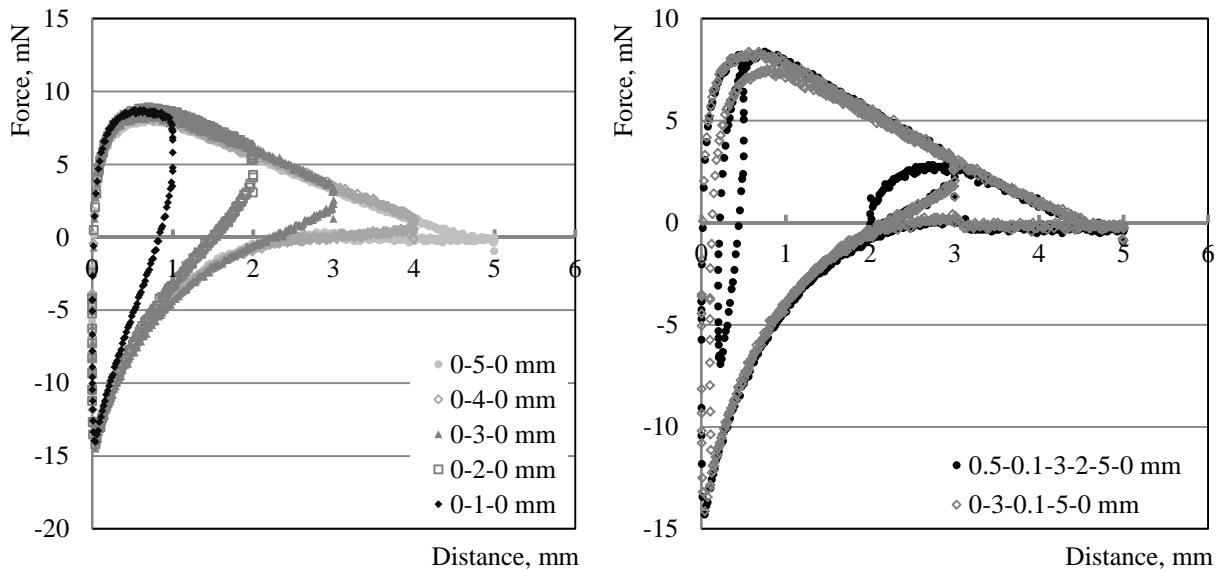
Figure E.4: Force-displacement diagrams for “ball-ball” contact (transparent ball: 10 mm in diameter): a) motion with various velocities; b) motion with various velocities and with stops; c) motion with one change in the direction of motion (velocity is 50 mm/min); d) motion with several changes in the direction of motion (velocity is 50 mm/min)

The results of the experiments for “ball-ball contact” with a transparent (10 mm in diameter) ball by 25% covering of the equipped ball are presented in Figure E.5.



a.

b.



c.

d.

Figure E.5: Force-displacement diagrams for “ball-ball” contact (transparent ball: 10 mm in diameter): a) motion with various velocities; b) motion with various velocities and with stops; c) motion with one change in the direction of motion (velocity is 50 mm/min); d) motion with several changes in the direction of motion (velocity is 50 mm/min)

The results of the experiments with “ball-ball” contact with a green ball (8 mm in diameter) are presented in Figure E.6.

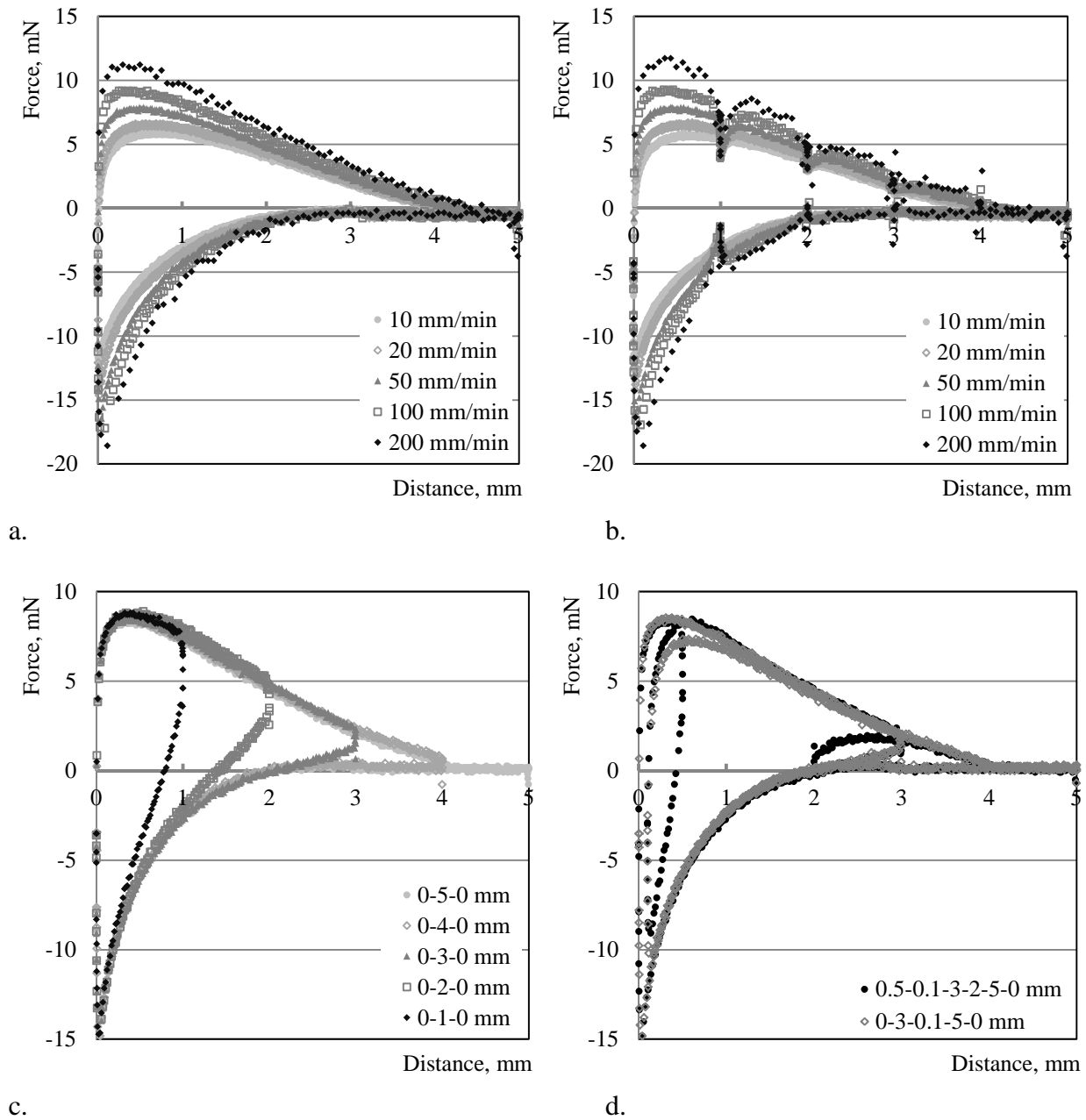
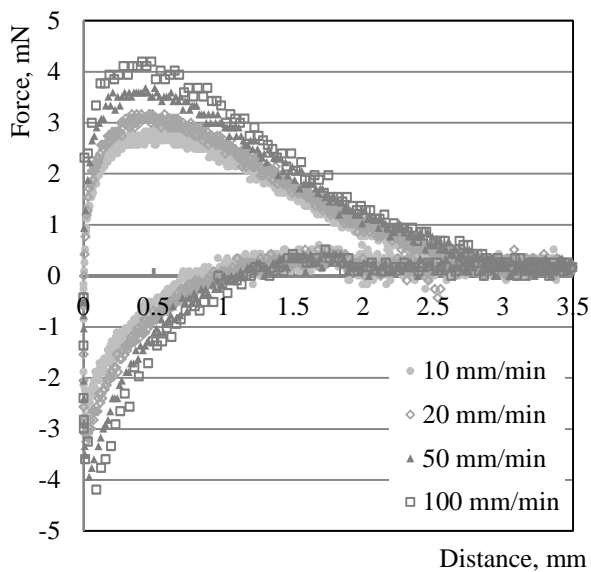
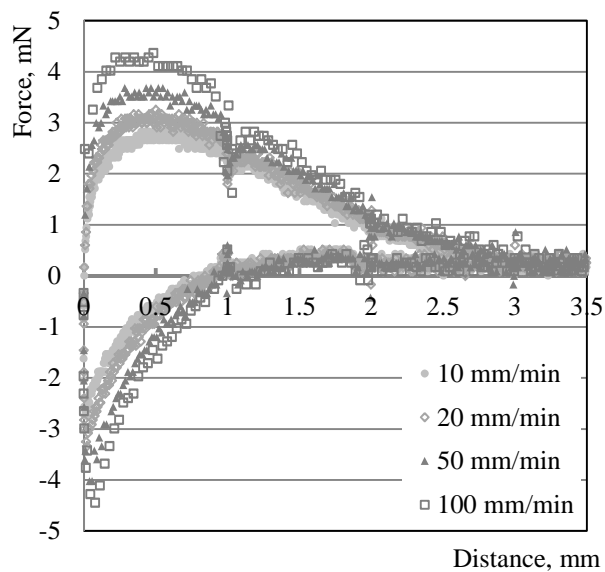


Figure E.6: Force-displacement diagrams for “ball-ball” contact (green ball: 8 mm in diameter): a) motion with various velocities; b) motion with various velocities and with stops; c) motion with one change in the direction of motion (velocity is 50 mm/min); d) motion with several changes in the direction of motion (velocity is 50 mm/min)

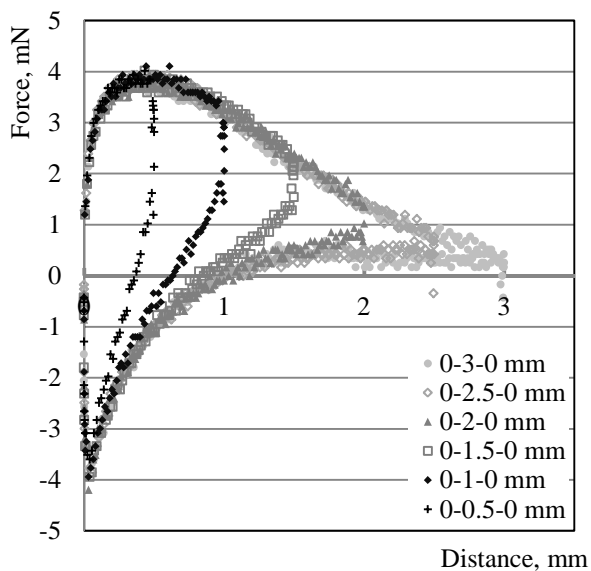
The results of the experiments with “ball-ball” contact with a red ball (4 mm in diameter) are presented in Figure E.7.



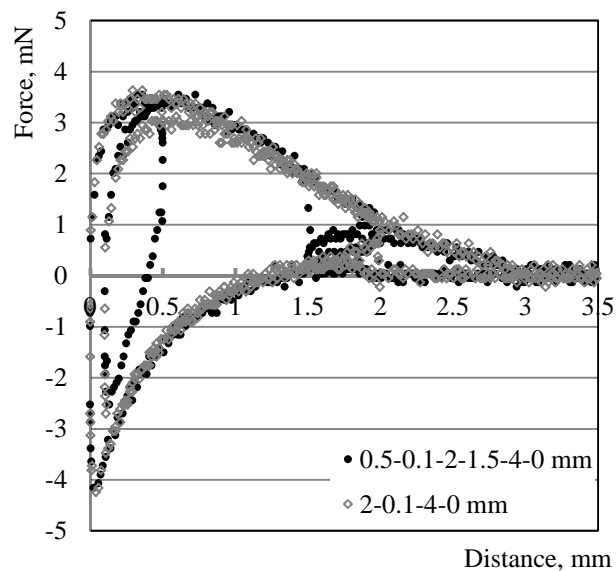
a.



b.



c.



d.

Figure E.7: Force-displacement diagrams for “ball-ball” contact (red ball: 4 mm in diameter):
 a) motion with various velocities; b) motion with various velocities and with stops;
 c) motion with one change in the direction of motion (velocity is 50 mm/min);
 d) motion with several changes in the direction of motion (velocity is 50 mm/min)

The results of the experiments with “ball-ball” contact with a white ball (2 mm in diameter) are presented in Figure E.8.

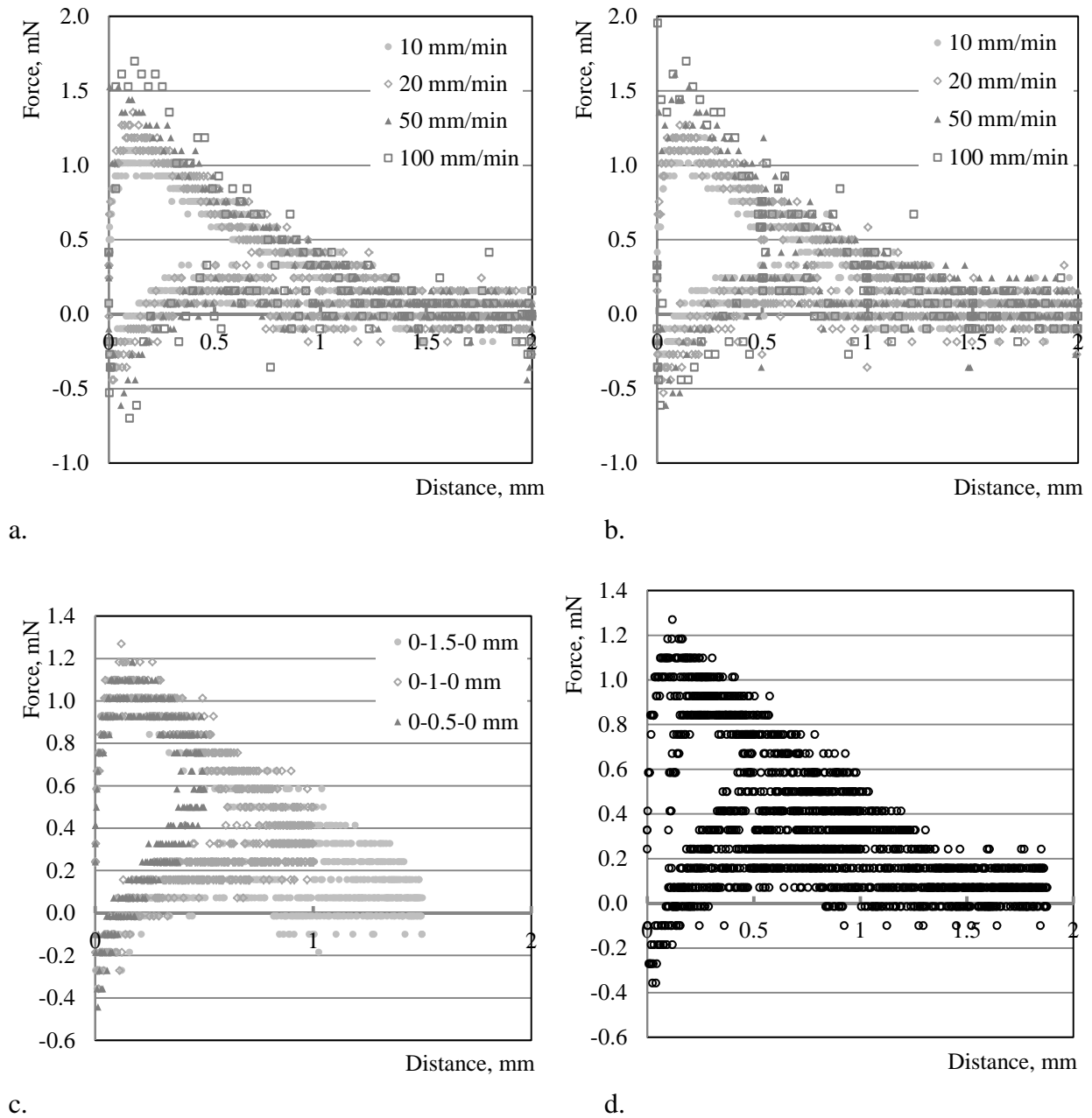


Figure E.8: *Force-displacement diagrams for “ball-ball” contact (white ball: 2 mm in diameter): a) motion with various velocities; b) motion with various velocities and with stops; c) motion with one change in the direction of motion (velocity is 10 mm/min); d) motion with several changes in the direction of motion (velocity is 10 mm/min)*

In contrast to the previous experiments with bigger balls where the velocity of the movement was 50 mm/min the velocity of the ball movement in these experiments is 10 mm/min. The reduction of the equipped ball velocity is needed in order to reduce the spread of the measured values.

The results of the experiments for the contact ball-several balls (with 3 transparent balls) are presented in Figure E.9. The balls are located in the apexes of the triangle.

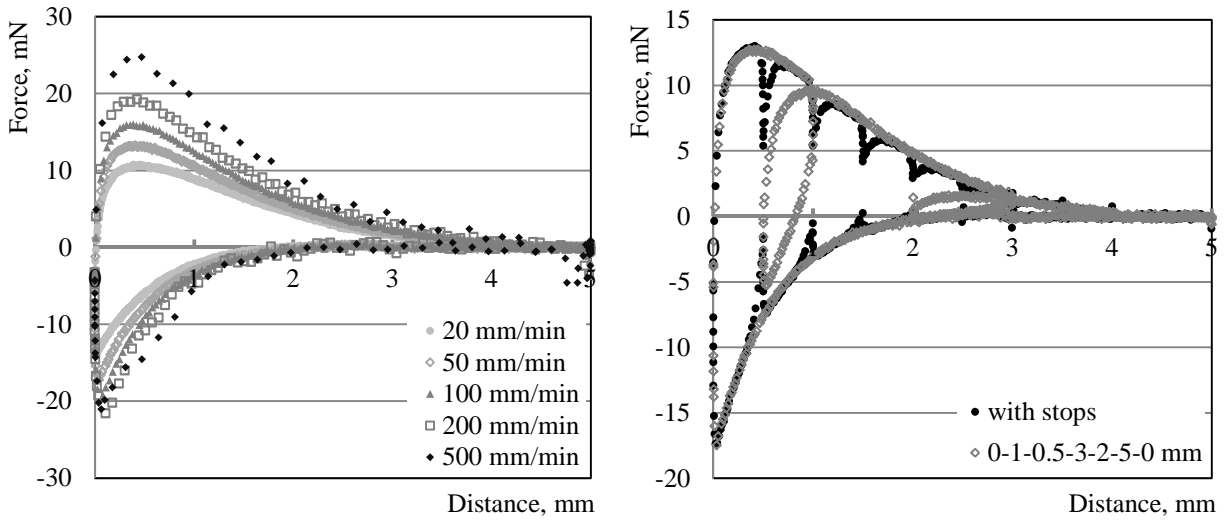


Figure E.9: Force-displacement diagrams for “ball – several balls” contact (3 transparent balls: 10 mm in diameter): a) motion with various velocities; b) motion with stops and motion with several changes in the direction of motion (velocity is 50 mm/min)

The results of the similar experiments but with 4 balls which located in the apexes of the square are presented in Figure E.10.

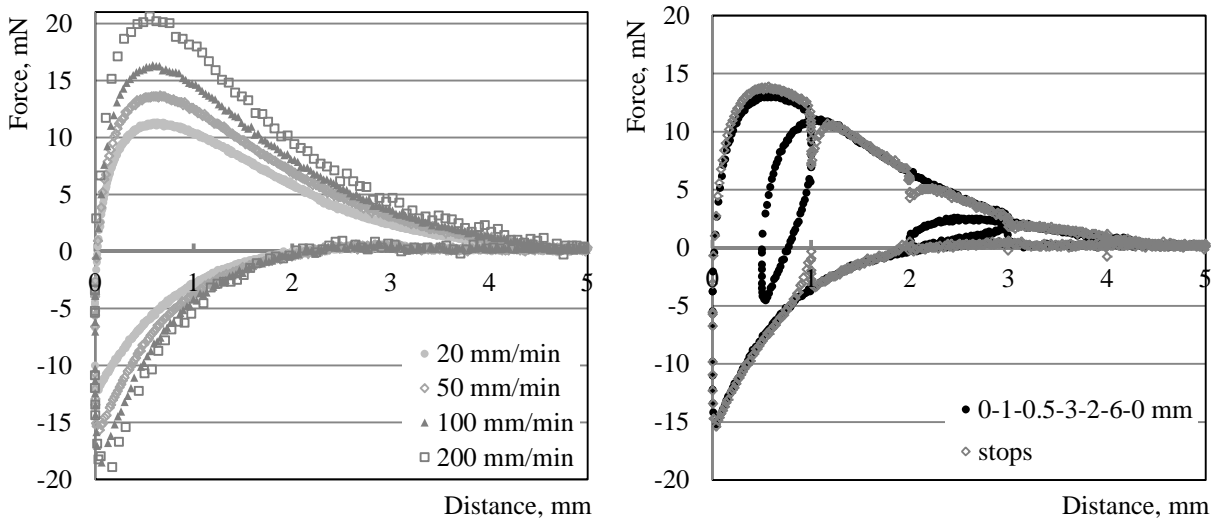


Figure E.10: Force-displacement diagrams for “ball-- several balls” contact (4 transparent balls: 10 mm in diameter): a) motion with various velocities; b) motion with stops and motion with several changes in the direction of motion (velocity is 50 mm/min)

The results of the experiments with 7 balls located around of the equipped ball are presented in Figure E.11.

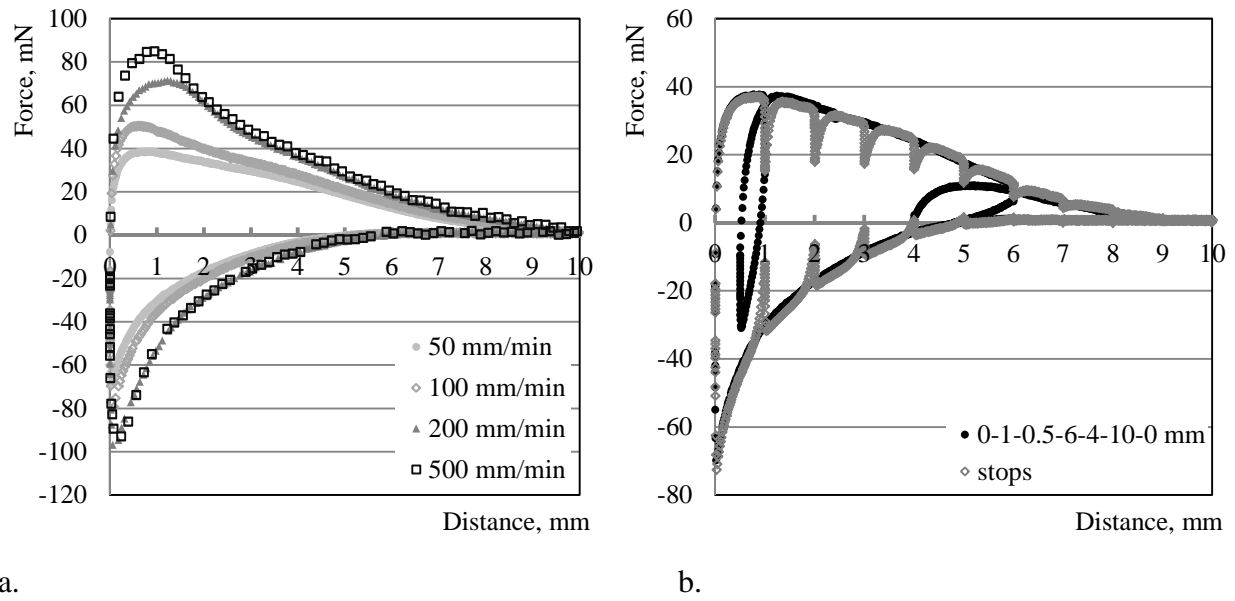


Figure E.11: Force-displacement diagrams for “ball-- several balls” contact (7 green balls: 8 mm in diameter): a) motion with various velocities; b) motion with stops and motion with several changes in the direction of motion (velocity is 50 mm/min)

Appendix F - Results of meso-level tests on SCC mortar

The results of the test with stops on SCC mortar are presented in Figures F.1 and F.2.

Figure F.1 shows the results of the test for a “ball-wall” contact which was performed with 100% covering of the equipped ball. The magnitudes of the contact force which were used for calculation of the components of the contact force are presented in the Table below.

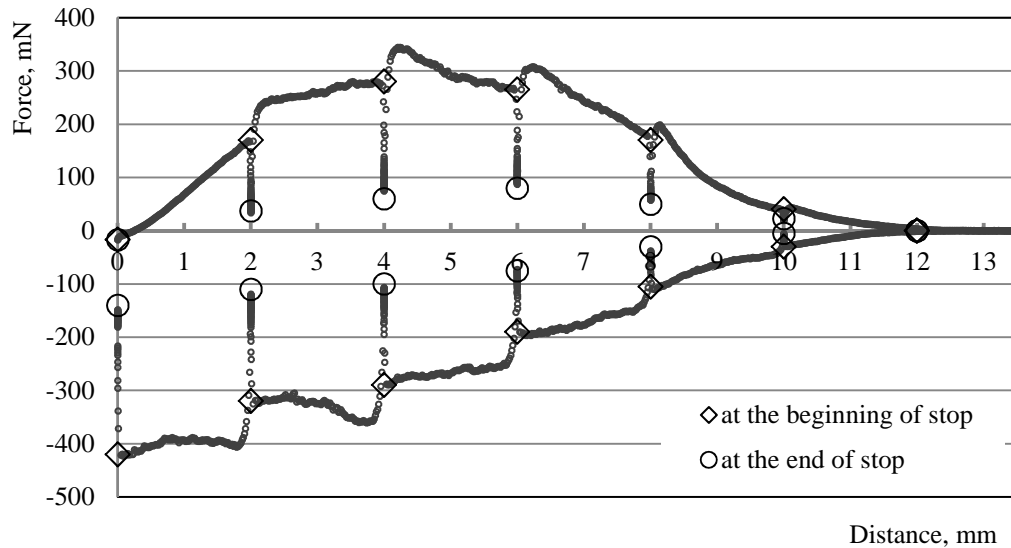


Figure F.1: Force-displacement diagrams obtained from ball-wall tests with stops on SCC mortar; covering of the equipped ball was 100%, displacement rate 50 mm/min, age of the concrete 12 min

Distance, mm	Force before stop, mN		Elastic force, mN		Viscous force, mN	
	moving away	approaching	moving away	approaching	moving away	approaching
0	-17	-420	-17	-140	0	-280
2	160	-320	37	-110	123	-210
4	290	-290	75	-100	215	-190
6	280	-210	80	-75	200	-135
8	190	-110	50	-30	140	-80
10	40	-40	23	-5	17	-35
12	0	0	0	0	0	0

Figure F.2 presents the results of the test for a “ball-wall” contact which was performed with 50% covering of the equipped ball. The magnitudes of the contact force which were used for calculation of the components of the contact force are presented in the Table below.

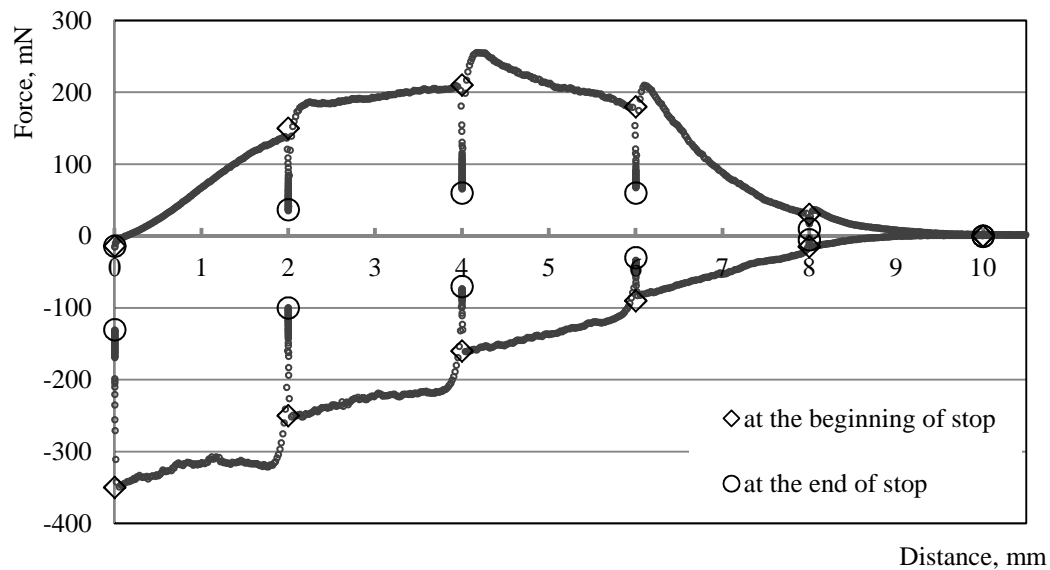


Figure F.2: Force-displacement diagrams obtained from ball-wall tests with stops on SCC mortar; covering of the equipped ball was 50%, displacement rate 50 mm/min, age of the concrete is 11 min

Distance, mm	Force before stop, mN		Elastic force, mN		Viscous force, mN	
	moving away	approaching	moving away	approaching	moving away	approaching
0	-14	-350	-14	-130	0	-220
2	160	-250	37	-100	123	-150
4	210	-160	60	-70	150	-90
6	180	-90	60	-30	120	-60
8	30	-15	10	-5	20	-10
10	0	0	0	0	0	0

Appendix G - Results of meso-level tests on UHPC

The results of the test with stops UHPC are presented in Figures G.1 and G.2.

Figure G.1 shows the results of the test for a “ball-wall” contact which was performed with 100% covering of the equipped ball. The magnitudes of the contact force which were used for calculation of the components of the contact force are presented in the Table below.

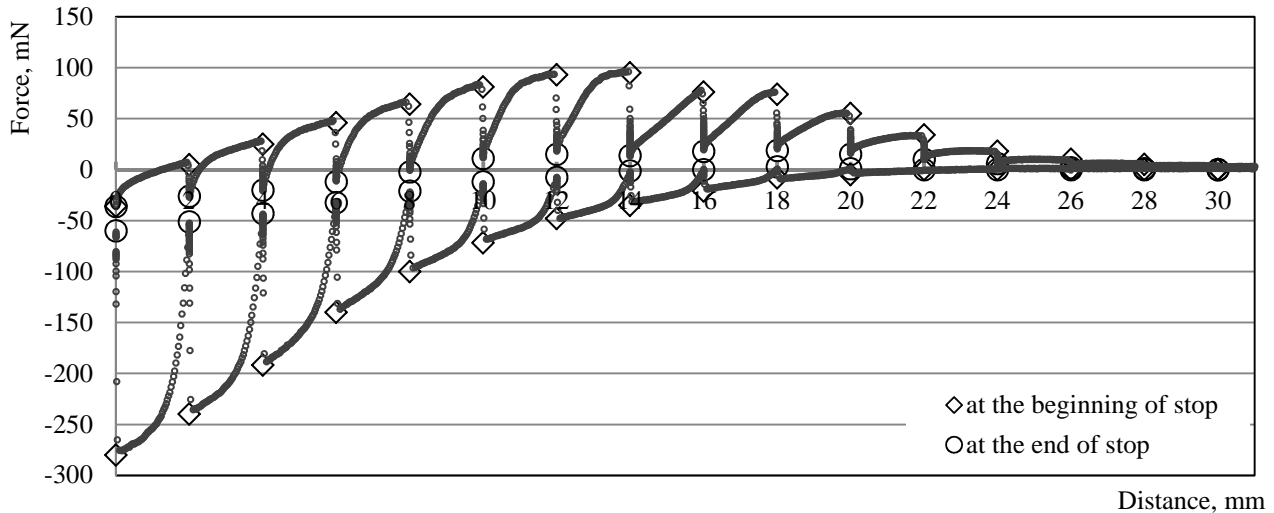


Figure G.1: Force-displacement diagrams obtained from ball-wall tests with stops on UHPC; covering of the equipped ball was 100%, displacement rate 50 mm/min, age of the concrete 12 min

Distance, mm	Force before stop, mN		Elastic force, mN		Viscous force, mN	
	moving away	approaching	moving away	approaching	moving away	approaching
0	-36	-280	-36	-60	0	-220
2	4.8	-240	-26	-51	30.8	-189
4	25	-192	-20	-43	45	-149
6	46	-140	-13	-32.3	59	-107.7
8	64	-100	-3	-21	67	-79
10	81	-72	11	-12	70	-60
12	93	-48	15	-7.5	78	-40.5
14	95	-35	14	-1.2	81	-33.8
16	76	-21	18	0.1	58	-21.1
18	74	-8	19	3	55	-11
20	55	-5	15	1	40	-6
22	34	0	10	0	24	0
24	18	0	6	0	12	0
26	10	0	2	0	8	0
28	5	0	1	0	4	0
30	0	0	0	0	0	0

Figure G.2 shows the results of the test for a “ball-wall” contact which was performed with 50% covering of the equipped ball. The magnitudes of the contact force which were used for calculation of the components of the contact force are presented in the Table below.

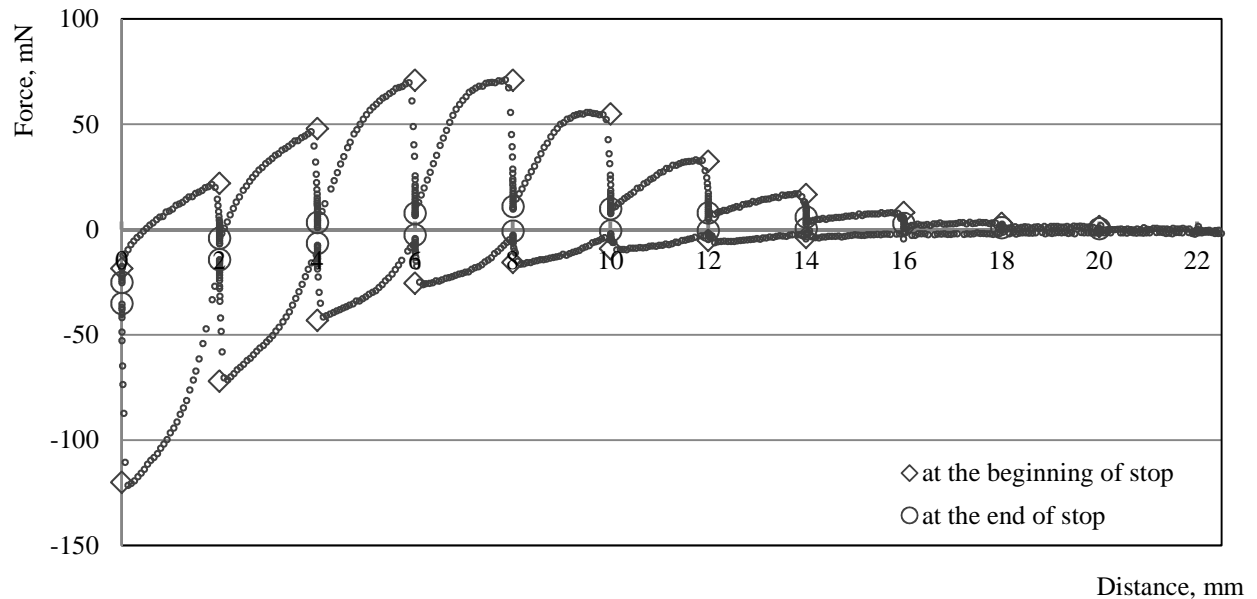


Figure G.2: Force-displacement diagrams obtained from ball-wall tests with stops on UHPC; covering of the equipped ball was 50%, displacement rate 50 mm/min, age of the concrete is 11 min

Distance, mm	Force before stop, mN		Elastic force, mN		Viscous force, mN	
	moving away	approaching	moving away	approaching	moving away	approaching
0	-18.5	-120	-25	-35	-10	-85
2	22	-72	-4	-14.2	26	-57.8
4	48	-43	3.5	-6.5	44.5	-36.5
6	71	-25.5	7.8	-2.5	63.2	-23
8	71	-15.6	11	-0.64	60	-14.96
10	55	-9	10	-0.52	45	-8.48
12	32.5	-5	8	-0.3	24.5	-4.7
14	16.7	-3.7	6	0.5	10.7	-4.2
16	8.1	0	3	0	5.1	0
18	3	0	1	0	2	0
20	1.5	0	0.5	0	1	0